

**Plasma Channel Guided Laser Wakefield Accelerator**

by

Cameron Guy Robinson Geddes

B.A. (Swarthmore College) 1997

M.A. (University of California, Berkeley) 2003

A dissertation submitted in partial satisfaction  
of the requirements for the degree of

Doctor of Philosophy

in

Physics

in the

GRADUATE DIVISION

of the

UNIVERSITY OF CALIFORNIA, BERKELEY

Committee in charge:

Dr. Wim Leemans, Co-chair  
Professor Jonathan Wurtele, Co-chair  
Professor Roger Falcone  
Professor Edward Morse

Spring 2005

The dissertation of Cameron Guy Robinson Geddes is approved.

---

Co-chair

Date

---

Co-chair

Date

---

Date

---

Date

University of California, Berkeley

Spring 2005

Plasma Channel Guided Laser Wakefield Accelerator

Copyright © 2005

by

Cameron Guy Robinson Geddes

## Abstract

Plasma Channel Guided Laser Wakefield Accelerator

by

Cameron Guy Robinson Geddes

Doctor of Philosophy in Physics

University of California, Berkeley

Dr. Wim Leemans, Co-chair

Professor Jonathan Wurtele, Co-chair

High quality electron beams (several  $10^9$  electrons above 80 MeV energy with percent energy spread and low divergence) have been produced for the first time in a compact, high gradient, all-optical laser accelerator by extending the interaction distance using a pre-formed plasma density channel to guide the drive laser pulse. Laser-driven accelerators, in which particles are accelerated by the electric field of a plasma wave (wake) driven by the radiation pressure of an intense laser, have over the past decade demonstrated accelerating fields thousands of times greater than those achievable in conventional radio-frequency accelerators. This has spurred interest in them as compact next-generation sources of energetic electrons and radiation. To date, however, acceleration distances have been severely limited by the lack of a controllable method for extending the propagation distance of the focused laser pulse. The ensuing short acceleration distance resulted in low-energy beams with 100 percent electron energy spread, which has limited potential applications.

Optical guiding of relativistically intense (  $> 10^{18}$  W/cm<sup>2</sup> ) laser pulses over

distances greater than 10 diffraction lengths is demonstrated herein using plasma channels, which have a density minimum on the axis of propagation, formed by hydrodynamic shock. Laser modes with peak powers of up to 4 TW - twice the self-guiding threshold - were guided without aberration by tuning the plasma density profile. The transmitted optical spectrum showed that the pulse remained in the channel over the entire length, and no accelerated electrons were observed at these powers. Simulations indicated that a large plasma wave was driven by the 4 TW pulse, indicating a possible dark current free structure for a laser wakefield accelerator using controlled injection. The presence of a large plasma wave was verified by increasing laser power and observing electron acceleration.

At a guided drive pulse power of 9 TW (500 mJ in 50 fs), electrons were trapped from the background plasma and accelerated. Tuning of the plasma density, laser power, and channel shape produced electron bunches with several  $10^9$  electrons within a few percent of a single high energy and with an emittance (focusability) competitive with state of the art conventional accelerators. Electron bunch energy was above 80 MeV using a 2 mm plasma channel, and energies as high as 150-170 MeV were observed. The presence of high energy electrons was highly correlated to well guided optical pulses. Measurements in pre-ionized plasmas with no channel structure confirmed that the enhancement was due to channeling not ionization.

Particle in cell simulations showed that the important physics of the new operating regime is that trapping of an initial bunch of electrons loads the wake, suppressing further injection and forming a bunch of electrons isolated in phase space. At the dephasing point, as the bunch begins to outrun the wake, the particles are then concentrated near a single energy, and hence a high quality bunch is obtained by terminating the plasma at this length. These simulations show that only a single wake period contributes to the high energy bunch, and hence the electron bunch length is near 10 fs, indicating that a compact ultrafast electron source with high beam quality

has been developed. High numerical resolution as well as three-dimensional effects were found to be important to the convergence of such simulations.

To experimentally verify the mechanism producing the high quality electron bunches observed, the energy distribution (spectrum) of electrons was measured using plasmas of variable length and density, produced by different gas jet targets. High quality electron bunches were produced by matching the gas jet length to the length over which electrons were accelerated by and outran (dephased from) the wake.

Gas target as well as experimental and control system development efforts supported these experiments and provided the required infrastructure.

The experiments and simulations in this dissertation indicate that the guiding of intense laser pulses in pre-formed plasma channels is an important building block for laser plasma accelerators, facilitating scaling to higher energies and beam quality.

---

Dr. Wim Leemans  
Dissertation Committee Co-chair

---

Professor Jonathan Wurtele  
Dissertation Committee Co-chair

# Contents

<b>Contents</b>	<b>i</b>
<b>List of Figures</b>	<b>v</b>
<b>List of Tables</b>	<b>ix</b>
<b>Acknowledgements</b>	<b>x</b>
<b>1 Introduction</b>	<b>1</b>
1.1 Laser Wakefield Accelerators . . . . .	2
1.2 Guided Laser Wakefield Acceleration . . . . .	7
1.3 Summary and Outline . . . . .	10
<b>2 Theoretical and Experimental Foundations</b>	<b>13</b>
2.1 Ponderomotive Force and Plasma Oscillation . . . . .	14
2.2 Wake Generation . . . . .	16
2.3 Particle Trapping . . . . .	21
2.4 Plasma Refractive Index and Laser Propagation . . . . .	24
2.5 Laser Guiding and Self-Modulation in Plasmas . . . . .	28
2.5.1 Plasma Channel Guiding . . . . .	29
2.5.2 Relativistic Guiding . . . . .	31
2.5.3 Plasma Wake and Self-Modulation . . . . .	33
2.5.4 Guiding Summary . . . . .	35
2.6 Accelerator Scaling and Design . . . . .	36
2.7 Additional Plasma Requirements . . . . .	39

2.8	Summary . . . . .	41
<b>3</b>	<b>Experimental Arrangement</b>	<b>43</b>
3.1	Channel Formation . . . . .	45
3.1.1	Plasma Ionization . . . . .	47
3.1.2	Plasma Heating and Channel Expansion . . . . .	50
3.2	Laser and Optical Configuration . . . . .	53
3.3	Diagnostics . . . . .	57
3.3.1	Plasma Interferometer . . . . .	57
3.3.2	Laser Mode and Spectrum . . . . .	60
3.3.3	Electron Diagnostics . . . . .	61
3.4	Summary . . . . .	68
<b>4</b>	<b>Laser Guiding in Plasma Channels</b>	<b>71</b>
4.1	Channel Formation and Tuning . . . . .	72
4.2	Laser Guiding in Plasma Channels . . . . .	75
4.3	Simulations of Laser Guiding . . . . .	81
4.4	Summary . . . . .	84
<b>5</b>	<b>Channel Guided Laser Wakefield Acceleration</b>	<b>85</b>
5.1	Guiding at High Power and Density . . . . .	86
5.2	Electron Acceleration in Plasma Channels . . . . .	88
5.3	Correlation of Accelerated Electron Yield and Laser Pulse Properties	93
5.4	Unchanneled Acceleration . . . . .	97
5.5	Summary . . . . .	100
<b>6</b>	<b>Simulations of Channeled Wakefield Acceleration</b>	<b>101</b>
6.1	Two-Dimensional Considerations . . . . .	103
6.2	Wake and Electron Bunch Formation . . . . .	105
6.3	Particle Tracking . . . . .	110
6.4	Laser Pulse Modulation . . . . .	112
6.5	Summary . . . . .	114
<b>7</b>	<b>Simulation Numerical and Physical Parameters</b>	<b>117</b>

7.1	Initial Simulation Design . . . . .	118
7.2	Checks Against Analytic Fluid Models . . . . .	121
7.3	Numerical Convergence and Parameters . . . . .	124
7.4	Physical Parameters . . . . .	129
7.5	Summary . . . . .	132
<b>8</b>	<b>Optimization of Beam Quality at Dephasing</b>	<b>135</b>
8.1	Acceleration and Dephasing Lengths . . . . .	137
8.2	Electron Spectra versus Acceleration Length . . . . .	138
8.3	Comparison of Channeled and Unchanneled Results . . . . .	142
8.4	Summary . . . . .	144
<b>9</b>	<b>Conclusions</b>	<b>145</b>
9.1	Summary . . . . .	145
9.2	Prospects and Future Work . . . . .	148
<b>A</b>	<b>Control System</b>	<b>151</b>
A.1	Control System Architecture . . . . .	152
A.2	Diagnostics and Controls . . . . .	155
A.3	Acquisition and Analysis . . . . .	159
A.4	Summary . . . . .	161
<b>B</b>	<b>Gas Target Development</b>	<b>163</b>
B.1	Target Requirements . . . . .	164
B.2	Supersonic Nozzles and Flow . . . . .	165
B.3	Gas Jet Characterization . . . . .	171
B.4	Cylindrical Nozzle Designs and Results . . . . .	176
B.5	Cylindrical Nozzle Shape, Surface, and Environmental Variations . . . . .	181
B.6	Slit Gas Jet . . . . .	186
B.7	Summary . . . . .	189
	<b>Bibliography</b>	<b>191</b>



# List of Figures

1.1	Laser accelerator schematic. . . . .	3
1.2	Wake density and electric fields. . . . .	5
1.3	Laser diffraction and guiding. . . . .	10
2.1	Wake longitudinal and transverse fields. . . . .	21
2.2	Preliminary unguided wakefield acceleration experiments. . . . .	23
2.3	Self-modulation. . . . .	35
3.1	Laser channeling experimental setup. . . . .	46
3.2	Channel formation ionization calculation. . . . .	49
3.3	Simple model of channel formation. . . . .	51
3.4	Target chamber and accelerator setup. . . . .	55
3.5	Folded wave plasma interferometer. . . . .	58
3.6	Magnetic spectrometer. . . . .	64
3.7	Magnetic spectrometer phosphor calibration. . . . .	66
4.1	Channel plasma profile versus time. . . . .	73
4.2	Channel temperature. . . . .	73
4.3	Plasma channel tuned for 4 TW guiding. . . . .	75
4.4	Plasma profile after drive pulse passage. . . . .	76
4.5	Mode images of laser propagation at 4 TW. . . . .	77
4.6	Mode images of laser propagation at various powers. . . . .	79
4.7	Transmitted optical spectrum. . . . .	80
4.8	Laser guiding simulation. . . . .	82
4.9	Energy depletion and accelerating field versus propagation distance. . . . .	83

5.1	Plasma channel for acceleration experiments. . . . .	87
5.2	Laser propagation interferograms and mode images at 9 TW. . . . .	88
5.3	Electron beam spatial profile. . . . .	89
5.4	Single shot 55 <sup>0</sup> electron energy spectrum of the channeled accelerator.	90
5.5	Single shot 5 <sup>0</sup> electron energy spectrum of the channeled accelerator.	92
5.6	Electron yield above 100 MeV versus guided mode intensity. . . . .	94
5.7	Channeled accelerator performance with channel tuning. . . . .	95
5.8	Normalized optical spectrum at 9 TW. . . . .	96
5.9	Shot averaged electron spectrum of the unchanneled accelerator. . . .	99
5.10	Electron spectrum for unchanneled accelerator with and without pre- ionization of the target plasma. . . . .	99
6.1	Simulation momentum phase space and laser envelope of the channeled accelerator. . . . .	106
6.2	Simulated electron density of the channeled accelerator. . . . .	107
6.3	Particle tracking in simulations shows details of channeled acceleration.	112
6.4	Electric fields experienced by representative tracked particles. . . . .	113
6.5	Simulated laser mode evolution at 9 TW. . . . .	114
7.1	Comparison of low intensity simulation with fluid calculations. . . . .	122
7.2	Numerical dispersion. . . . .	125
7.3	Trapped particle number versus simulation resolution. . . . .	127
7.4	Electron phase space density for runs with opposite laser polarizations.	130
7.5	Electron density and longitudinal field for runs with opposite laser polarizations. . . . .	130
8.1	Gas jet plasmas for testing effect of variable acceleration length. . . .	136
8.2	Electron energy spectra at density of $4 \times 10^{19} \text{ cm}^{-3}$ . . . . .	140
8.3	Electron energy spectra at density of $2 \times 10^{19} \text{ cm}^{-3}$ . . . . .	141
8.4	Channeled and unchanneled accelerator electron energy spectra at den- sity of $2 \times 10^{19} \text{ cm}^{-3}$ . . . . .	143
A.1	Control system interfaces to the experiment. . . . .	153
A.2	Control system layout. . . . .	154
A.3	Master control program. . . . .	156

A.4	Video camera control program. . . . .	156
A.5	Digital CCD camera control program. . . . .	157
A.6	Online plotting program. . . . .	158
A.7	Shot correlated data. . . . .	161
B.1	Converging - diverging gas jet nozzle and code schematic. . . . .	167
B.2	Gas jet test stand. . . . .	172
B.3	Interferometer noise and gas jet fluctuation. . . . .	173
B.4	Neutral and plasma interferometer gas jet density measurements. . .	175
B.5	Gas jet overall schematic. . . . .	177
B.6	Gas jet density profiles - initial nozzles. . . . .	177
B.7	Supersonic nozzle design. . . . .	178
B.8	Supersonic nozzle density profile. . . . .	179
B.9	Unchanneled accelerator performance with different gas jets. . . . .	181
B.10	Effect of gas jet nozzle surface finish. . . . .	183
B.11	Effect of gas jet shape variation. . . . .	184
B.12	Slit gas jet. . . . .	187
B.13	Slit gas jet density profile. . . . .	189



# List of Tables

3.1	Summary of major diagnostics and physical observables. . . . .	57
-----	--	----

## Acknowledgements

I have benefitted from the counsel and support of many colleagues, family, and friends without whom this work would not have been possible.

Wim Leemans provided me the opportunity to work at LBNL, and has been a constant source of inspiration and motivation. His earlier work laid the foundation these experiments. From providing good ideas to practical help in the lab, he has as a supervisor provided me a combination of independence and support which made graduate school a great experience.

Jonathan Wurtele has always been an interested and engaging advisor, and I thank him for taking the time to supervise a student outside his group. His close attention and reading have helped me find many new angles on the problem.

I had the privilege of being part of a collaborative and collegial group in L'OASIS at Lawrence Berkeley National Laboratory. Together with Wim, Jeroen van Tilborg, Csaba Toth, Gerry Dugan, Jerome Faure, Bob Nagler, Kei Nakamura, Palma Catravas, and Ned Saleh were of great help with the experiments. Eric Esarey, Carl Schroeder, Brad Shadwick, and Gwenael Fubiani were of great assistance with theory. Thank you all for making graduate school enjoyable.

A productive collaboration with the University of Colorado and Tech-X corporation facilitated the simulations. Thanks to John Cary and David Bruhwiler for good advice and assistance with the simulations, and to Chet Nieter, Peter Stoltz, and others for code development.

I appreciate the support of the faculty at U.C. Berkeley in pursuing an external research project. Roger Falcone assisted me both on my qualifying examination and dissertation committees, and as department chair. Ed Morse served on both my

qualifying examination and dissertation committees, and Joel Fajans on the qualifying examination committee.

No experiment goes forward without support, and Leon Archambault, Michael Dickinson, Scott Dimaggio, Don Syversrud, Joe Wallig, and Nathan Ybarrolaza provided great assistance technically. Anne Takazawa, Donna Sakima, Olivia Wong, and Joy Kono kept administration on track.

In my thesis work, I was supported by the Fannie and John Hertz foundation. My thanks to the foundation and its staff both for financial support and for the opportunity to interact with a unique group of fellows. The experiments and simulations were funded by the United States Department of Energy.

I have benefitted from many teachers who inspired and helped me. Special thanks to Dr. Love at Reed for my first exposure to science, to Sally Scholz and Doug Foster for the IB program at Lincoln, and to Lynne Molter and Mike Brown at Swarthmore for my research there.

Research experiences at many laboratories have enriched my professional life. Thanks especially to the PPPL plasma fellowship and Ray Fonck for my start in plasma physics. Bob Kirkwood, Siegfried Glenzer, and others in the Nova plasma physics group at Livermore Lab for a great experience in fusion. Bedros Afeyan for further fusion-related work at Polymath Research.

My parents have always given support and encouragement to explore and inquire, which underlies much of my fascination with science, and I am very grateful. They have been ever supportive of endeavors they may not have always understood, from re-building toys and appliances as a child through the current work.

Friends and team-mates have provided a sounding board for ideas and a source of sanity always. Among many, I thank Sonya Smallets, Robert Richardson, Alex Montgomery, Tom Kornack, and Evan Dorn. Fog, Buzzards, Baracus, and Earthquakes:

with you. Likewise, thanks to others whom I've been lucky to have in my life but whom space does not allow me to include here.

# Chapter 1

## Introduction

Particle and radiation beams from electron accelerators are an enabling technology in a broad range of scientific fields including physics, medicine, biology, and chemistry. Present electron accelerator technology [1] relies on resonantly excited radio frequency (RF) cavities to obtain high accelerating fields. These cavities typically are limited to accelerating electric fields around 50 MV/m to avoid material breakdown, which occurs when the field is sufficiently large to induce emission of electrons from the metal cavity walls. This limit on field means that study of fundamental particle physics at the energy frontier (at and beyond a TeV) requires facilities 10s of km in scale. A technology capable of higher gradients will hence be required in order to prevent machines from becoming excessively large. High gradients would also open new applications for moderate energy accelerators in medicine, materials science, and other fields by rendering such machines of laboratory scale.

A promising candidate for the next generation of compact high-energy electron sources is the laser wakefield accelerator (LFWA), which has demonstrated accelerating gradients thousands of times those obtained in conventional accelerators using the electric field of a plasma wave (the wakefield) driven by an intense laser [2, 3].

Plasmas are not subject to the electrical breakdown that limits conventional accelerators, and plasma based accelerators hence offer a path to more compact machines. Previous wakefield acceleration experiments [4–10] (Section 1.1) have demonstrated high accelerating gradients, but the electron beams produced had 100% energy spread and an exponentially small fraction of electrons at high energy, unsuitable for most applications.

This dissertation demonstrates the production of high quality electron beams (several  $10^9$  electrons above 80 MeV energy with percent energy spread and low divergence) for the first time in a high gradient laser wakefield accelerator. This was achieved by extending the interaction distance using a pre-formed plasma density structure, or channel, to guide the drive laser pulse over many diffraction ranges. Such beams allow laser-plasma accelerators to be considered seriously as alternatives to conventional accelerators for a wide variety of applications that demand high-quality electron bunches. A qualitative outline of compact accelerators using laser driven plasma waves is presented in this Chapter, followed by an outline of this dissertation. The detailed theory follows in Chapter 2. Experiments and simulations which demonstrated the use of a pre-formed plasma to control laser propagation at high intensity, extending acceleration length and producing high quality electron beams, are described in the Chapters that follow.

## 1.1 Laser Wakefield Accelerators

Laser driven plasma wakefield accelerators [2] obtain high accelerating gradients using the plasma wave driven by the radiation pressure of an intense laser pulse. This Section introduces the physics of wake excitation and particle acceleration, and the state of the field at the inception of the present experiments, in order to motivate the work herein.

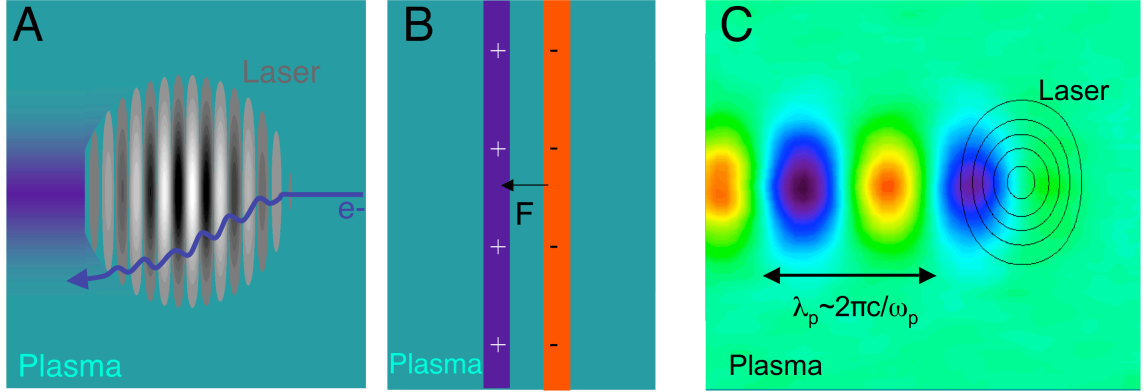


Figure 1.1. Interaction between an intense laser pulse (traveling from left to right) and a plasma creates a high gradient accelerating structure. The radiation, or ponderomotive, force of a laser pulse results from the oscillation of the electrons in the laser field (A). This plows electrons to the side and ahead of the pulse, forming a depletion of electron density (dark color) following (to the left of) the laser pulse, while the heavier ions remain stationary. This charge separation results in a restoring force (B), and an oscillation in density ensues at a characteristic frequency  $\omega_p$ . This leads to an oscillation of electron density (color: black to red) following the laser pulse, and moving along with it in analogy to the wake of a boat (C). The density oscillation was calculated by numerical simulation (Chapter 6).

As illustrated in Fig. 1.1, the radiation (or ponderomotive) pressure of a laser pulse moving through the plasma pushes electrons ahead of the pulse and to the side [11–13]. An electron initially on the axis of a focused laser spot experiences a push outward by the laser electric field then, when the field reverses, a smaller push inward because the laser intensity is highest near the center. Over several cycles, the electron migrates further outward. Interaction of this oscillation with the laser magnetic field also results in an axial force which plows electrons ahead of the pulse (see quantitative derivation, Section 2.1). This movement of the electrons creates a low electron density region in the plasma following the pulse. To drive a significant wake (Section 2.2), electron oscillation in the laser field must be relativistic, which requires laser intensities of  $10^{18} - 10^{19}$  W/cm<sup>2</sup> at a wavelength of 810 nm (typical of current high power solid state lasers). Ions, being much heavier than electrons, are not significantly displaced for the parameters of these experiments.

The electric field of the ponderomotively driven density perturbation causes the electron density to oscillate behind the laser pulse, creating a plasma wave which co-moves with the laser pulse in analogy to the wake behind a speedboat. Consider displacement of a slab of plasma electrons with thickness  $L$  as illustrated in Fig. 1.1B, while the ions remain fixed [11, 12]. Displacement by a distance  $\delta \ll L$  produces positive charge on one side of the slab, negative on the other. The electric field of these charges,  $E = 4\pi n e \delta$ , where  $e$  is the electron charge magnitude and  $n$  the density, exerts a restoring force on the slab. Letting the force per area equal the mass per area times the acceleration:

$$-4\pi n^2 e^2 L \delta = nmL \frac{\partial^2 \delta}{\partial t^2} \Rightarrow \frac{\partial^2 \delta}{\partial t^2} + \frac{4\pi n e^2}{m} \delta = 0 \quad (1.1)$$

This is simply the form of a harmonic oscillator with frequency  $\omega_p = (4\pi n e^2 / m)^{1/2}$ , where  $m$  is the electron mass. As a result, the charge separation induced by the laser ponderomotive force sets up an oscillation in the plasma density at a frequency  $\omega_p$ , referred to as the electron plasma frequency. Because the laser travels through the plasma near the speed of light, this oscillation creates a wave following the laser pulse [2, 3], with spatial wavelength  $\lambda_p \approx 2\pi v_p / \omega_p$  and wavenumber  $k_p = \omega_p / v_p$ , with  $v_p \sim c$  the phase velocity of the wave ( $\sim$  group velocity of the laser) and  $c$  the speed of light. The plasma response is maximized for laser pulselengths  $c\tau_L$  approximately equal to  $\lambda_p$ , since if the laser pulse is longer its ponderomotive force inhibits the rebound of plasma density.

The plasma wave density oscillation has an electric field as shown in Fig. 1.2. Electrons placed in the indicated phase range are both accelerated longitudinally and focused in the transverse direction. This allows confinement and acceleration of the particles over long distances.

The accelerating field of the wake is limited by breaking of the wave, which occurs when the wake reaches an amplitude sufficient to trap background plasma electrons

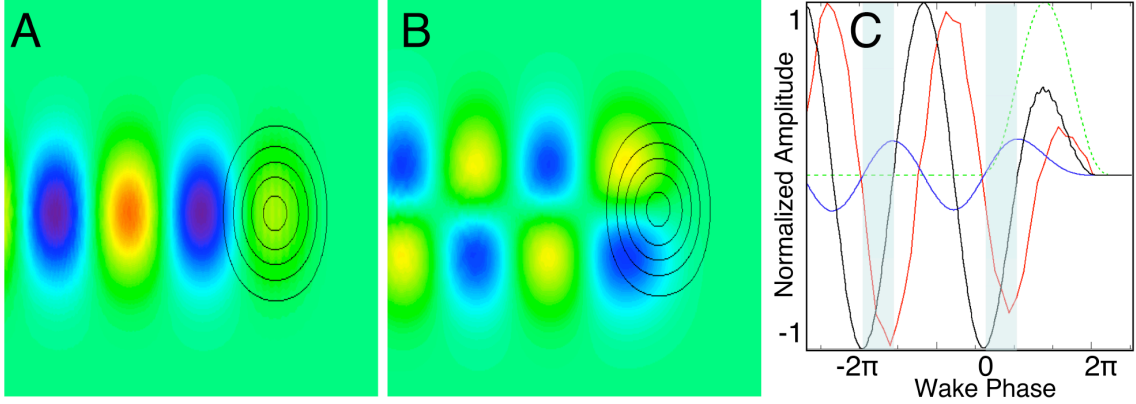


Figure 1.2. The density perturbation and electric fields driven by a laser pulse propagating in a plasma from a numerical simulation (Chapter 6). The accelerating (A) and transverse (B) field contours (color: purple negative, red positive) are shown with the laser envelope overplotted (lines). Lineouts (C) of density (red) and accelerating field (black) on axis, and peak focusing field (blue) show accelerating and focusing regions. The shaded regions, where radial field is positive and longitudinal field negative, are both accelerating and focusing for electrons. Electrons in these regions can be accelerated over long distances while remaining focused. Laser intensity is plotted in green.

from rest [14, 15] and is subsequently damped by that trapping [16, 17]. In the one-dimensional non-relativistic limit, this condition is:

$$\frac{eE_0}{m\omega_p} = v_p \approx c \Rightarrow E_0 = \frac{m\omega_p c}{e} \quad (1.2)$$

where  $m$  is the electron mass, and  $e$  is the magnitude of the charge. This field amplitude is known as the cold wave-breaking limit, which in convenient units can be expressed as:  $E_0 = 0.96\sqrt{n_0}[\text{cm}^{-3}]$  Volts per centimeter, with  $n_0$  ambient the electron density. For typical experimental densities of a few  $10^{19} \text{ cm}^{-3}$ ,  $E_0 \sim 500 \text{ GV/m}$ , allowing very high accelerating fields. More detailed calculations including nonlinear, relativistic, and multi-dimensional effects (Section 2.1, Chapter 6) show that fields of several hundred GV/m are indeed possible for such plasma parameters, allowing use of a much shorter acceleration distance than required by facilities using RF technology.

The wake is driven by the laser field, and hence its phase velocity is approximately equal to the group velocity of the laser driver in the plasma (Section 2.4). For low

plasma densities ( $\omega_p \ll \omega$ , i.e.  $10^{18} - 10^{19} \text{ cm}^{-3}$  for  $\lambda=810 \text{ nm}$ ), this is close to the speed of light, allowing acceleration of relativistic particles moving with the wake over long distances. Acceleration will be limited by the shorter of the distance over which the electrons outrun (dephase from) the wake, or the distance over which the wake can be driven. We consider these limits further below.

The wake can be driven by laser pulses longer than  $\lambda_p$  due to the self-modulation of such pulses by the response of the plasma. The small wake driven by the (initially unmatched) laser modulates the pulse at  $\lambda_p$  due to the variation of the plasma refractive index with density [18–22] (Section 2.5.3). The wake then grows, further modulating the pulse, and instability results. This can lead to complete modulation of the laser pulse into sub-pulses at  $\lambda_p$ , and generation of a large plasma wave. This is experimentally important, as high power laser pulses short enough to match the plasma period are not available for regimes of interest to the present experiments (Section 2.3).

Experiments have demonstrated that fields of hundreds of GV/m are obtainable in practice, but the electron beams produced previously have been of poor quality [4–10] due to limited acceleration distance. The experiments used a single laser pulse of  $10^{18} - 10^{19} \text{ W/cm}^2$  intensity, driving a wake through self-modulation in the plasma formed when the front edge of the pulse ionized a neutral gas jet. In distances on the order of a mm at plasma densities of a few  $10^{19} \text{ cm}^{-3}$ , electrons were trapped and accelerated from the background plasma, and peak energies of more than 100 MeV have been observed. The electron beams produced had 100% energy spread and an exponentially small fraction of electrons at high energy. For example, using a 32 TW laser pulse, beams with more than  $10^{10}$  electrons were produced but less than  $10^8$  were above 60 MeV [9]. The beam divergence was typically greater than 50 mrad full-width at half maximum (FWHM).

No external guiding of the laser beam was used in these experiments, limiting acceleration to little more than the vacuum diffraction range,  $Z_R \approx \pi w_0^2/\lambda$ , over which the laser remains focused without guiding [23, 24] (Fig. 1.3). Here  $w_0$  is the laser spot size and  $\lambda$  the wavelength. Some self-guiding [20, 21, 25–27] (Section 2.5.2) of the pulse can be obtained from the modification of the plasma refractive index that occurs when oscillation of plasma electrons in the laser field relativistically changes their mass, but this is unstable, eventually destroying the pulse [18, 22, 23, 27]. Due to the limits on propagation, the best results in previous experiments had been obtained by increasing  $w_0$  to increase  $Z_R$ , requiring ever greater laser power to maintain the laser intensity, but this approach was still limited to distances of a few hundred  $\mu\text{m}$  [23].

While the electron beams demonstrated by the experiments above can be acceptable for some users [28, 29] many applications, including high-energy physics and some radiation sources, require monoenergetic beams (1% energy spread or less) with at least  $10^9$  electrons [29–35]. The challenge was hence to produce high quality electron beams while retaining the high accelerating field demonstrated in previous experiments.

## 1.2 Guided Laser Wakefield Acceleration

To obtain higher quality and energy electron beams, the limits on laser propagation distance discussed above should be overcome by controlling the propagation of the laser pulse (i.e. laser guiding) [36–41]. For optimum acceleration, accelerator length should be matched to the dephasing length, which is the distance over which the electrons are accelerated to above the plasma wave velocity, and slip from the accelerating phase region shown in Fig. 1.2 into the decelerating phase of the wake [2, 3, 37, 42, 43] (Section 2.6). This slippage occurs because the wake phase ve-

locity matches the group velocity of the laser, which is sub-luminal in the plasma. At the dephasing length, electrons have their maximum energy, since further propagation results in deceleration.

Extending acceleration length to the dephasing point can result not only in higher energies, but also in small energy spread electron beams. As we shall see in Chapter 6, the highest energy electrons typically outrun the wake first, so that they are decelerated while the low energy tail is still accelerating. This can result in the electrons being bunched near a single energy at the dephasing length. The result is that a high quality electron bunch with low divergence, low energy spread, and high energy can be extracted. The final energy spread is limited by the region of wake phase covered by the electrons. To achieve close to the same energy, the electrons must all see nearly the same accelerating field, and due to the oscillatory nature of the wake injection of the electrons over a small phase range is therefore important [44].

The dephasing length is determined by the phase velocity of the wake, and hence the group velocity of the laser driver, which rises with decreasing density. Higher wake velocity allows longer dephasing lengths and higher energies, but makes trapping electrons from the plasma more difficult [43]. Hence for experiments where the electrons are self-trapped by the wake, as described herein, the plasma density that allows the highest electron energies is the lowest density that allows self-trapping. For our laser parameters (10 TW, 50 fs), this was a few times  $10^{19} \text{ cm}^{-3}$ , in the self-modulated regime [18–20, 22] (Section 2.5.3). In a distance of the order of 2 mm, peak energy gain can be of the order of fifty to a few hundred MeV in this regime [3–10, 45, 46]. With controlled injection [44, 47–50], lower densities could be used in the future. Accelerator lengths of several cm and energies up to several GeV per stage are then possible [3]. To reach the high intensities required for optimal wake excitation with a typical 10 TW peak power laser system operating at 810 nm, the laser pulse should be focused to spot sizes near  $8 \mu\text{m}$  (Section 2.3) [10], giving a  $Z_R \approx 200 \mu\text{m}$  and

making guiding over many  $Z_R$  desirable in order to reach the dephasing condition and high energies.

A stable waveguide for a laser pulse can be produced using a pre-formed plasma that has a cylindrically symmetric density profile with a minimum on the laser propagation axis (i.e., a plasma channel) [18] (Section 2.5.1). This occurs because the phase velocity of light in a plasma increases with density. Hence a light wave seeing a minimum of density on axis experiences curving of its phase fronts in a focusing direction (Fig. 1.3). For example, a parabolic density profile can be matched to guide a Gaussian laser mode without distortion in the low intensity limit, circumventing the diffraction limit [18, 51]. Previous experiments have demonstrated controlled guiding using such channels for input pulse intensities at up to  $2 \times 10^{17}$  W/cm<sup>2</sup>, where relativistic effects are unimportant [51–54]. Monomode guiding of low powers has also been demonstrated in capillary waveguides [55, 56]. Powers in these experiments were below the self-guiding threshold, and too low to trap and accelerate particles. High powers have been focused into hollow capillary guides, but with poor mode structure and at low density. Guided intensity was either not analyzed [57] or remained low [58].

Guiding of high quality modes at high intensity and power, where both diffraction and relativistic modification of the plasma refractive index [22] are important, would enable the wakefield to be driven over long distances, accelerating particles to higher energies and potentially producing high quality electron beams. Such guiding had not been demonstrated prior to the current work.

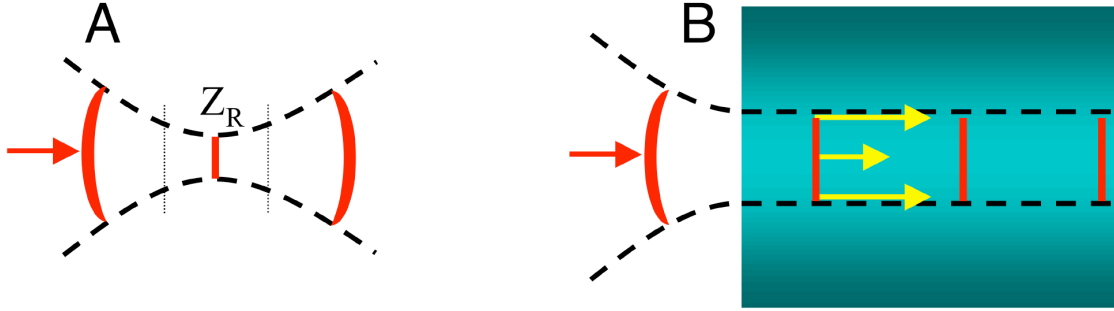


Figure 1.3. Laser diffraction and guiding. A laser beam in vacuum (A) diffracts, maintaining a small spot only over a diffraction length  $Z_R$ . Variation of refractive index (B) (blue color) can cause higher phase velocity (yellow) off axis, which bends the phase fronts in the opposite direction of diffraction. A suitable refractive index profile can then guide the laser, maintaining its spot size over long distances. In a plasma, guiding is obtained with a minimum of plasma density on axis.

### 1.3 Summary and Outline

This dissertation describes a laser-plasma wakefield accelerator in which the drive laser pulse was guided using a plasma channel in order to extend the interaction length and match it to the dephasing length, resulting in the production of high energy, high quality electron beams [45,59,60]. Chapter 2 details the basic physics of laser plasma interactions relevant to wakefield acceleration, elaborating on the overview in this Chapter, and describes the previous experiments which underlie the current work.

The setup of the experiments and diagnostics is described in Chapter 3. New diagnostics were built, and the laser system was modified to bring multiple beams on target in order to form the channel and drive the wake.

Chapter 4 describes experiments and simulations on plasma channel guiding of intense laser pulses. A relativistically intense laser pulse has been guided for the first time using a plasma channel in these experiments, and propagation over  $10Z_R$  without aberration was demonstrated [46,60]. Input powers up to twice the threshold for relativistic self-focusing were guided. No electrons were accelerated, providing a

long scale length high gradient structure for wakefield acceleration experiments using external injection of electrons.

Chapter 5 describes the experiments on channel guided wakefield acceleration, where the laser intensity was increased until electrons were self-trapped by the wake from the background plasma, and accelerated. It is demonstrated that as a result, high energy high quality electron beams were produced which have, for the first time in a compact laser driven accelerator, small energy spread and good emittance (focusability) as well as fs duration and high charge [45,59,60]. Bunches with several  $10^9$  electrons above 80 MeV energy and 2 percent energy spread as well as 3 mrad divergence were produced (Fig. 5.4), and energies up to 170 MeV were observed.

Chapter 6 describes simulations conducted with the experimental parameters which indicate that the high quality electron beams were formed when the electron bunch trapped by the wake loaded the wake [16,17], reducing its amplitude. This suppressed further injection, self-consistently limiting injection to a small range of phase in the wake. These particles were then concentrated within a few percent of the same high energy at the dephasing point, when the front of the beam outran the wake and began to decelerate, while the tail of the beam was still accelerating [45,59,60].

Bunching of electrons near a single energy has also been observed by two other groups, and published concurrently [61,62]. These groups used a large focal spot to produce a long  $Z_R$ , and varied plasma density to match the dephasing condition. The larger spot size resulted in reduced intensity, and accelerated less electron bunch charge per laser power than channeled experiments [45,62], but confirms the physics of accelerator length optimization. Structure in the energy distribution has also been observed in other experiments [57]. Other simulations have also observed the bunching of electrons at a single energy over long acceleration distance [41,63,64]. These results are discussed in relation to the present experiments in Chapters 6, 8.

Chapter 7 describes tests and validation of the simulations, and their response to variation of parameters. Numerical parameters were varied in order to understand the stability of the simulations. Physical parameters were also changed to shed light on the variability in the experimental results. Both high numerical resolution and three-dimensional effects appear to be important for convergence of the simulations.

Chapter 8 describes unchanneled experiments and simulations varying the gas jet (plasma) length. These confirmed that particles were bunched in energy when the accelerator and dephasing lengths were matched, producing high quality electron beams with few percent of the same energy [59,60]. Bunch energy and quality were however never as good as in the channeled experiments described in Chapter 5 (Fig. 5.4), indicating the advantages of controlling laser propagation with the channel.

The experimental and numerical work in this dissertation is summarized in Chapter 9. Conclusions and directions for future work are presented. With the demonstration of high quality electron beams, laser accelerators offer bright prospects for future accelerators, and higher energy and controlled injection experiments will be among the next steps.

The accelerator experiments were underlain by supporting developments of gas targets used to form the plasmas in the accelerator, and of control systems used to acquire data and optimize performance. Experimental control and data collection work is described in Appendix A. Gas target development is detailed in Appendix B.

## Chapter 2

# Theoretical and Experimental Foundations

The channeled laser wakefield accelerator described in this dissertation was motivated by previous experiments and theory, as described in this Chapter. These indicated that wakefield accelerators can produce high accelerating gradients, and predicted that their performance could be greatly enhanced by guiding the laser pulse. On this basis, the present experiments and simulations were designed and executed. The considerations below are further motivated by the availability of the L'OASIS laser at Lawrence Berkeley National Laboratory (LBNL) which delivers pulses of 10 TW power, 50 fs duration, and 0.8  $\mu\text{m}$  wavelength, and are directed at optimizing the accelerator performance with this driver. The experiments were designed for this laser based on both theoretical scalings and state of the art experimental evidence as of 2000, when this dissertation was initiated. We now consider the physics of wake excitation, particle trapping, and laser guiding.

## 2.1 Ponderomotive Force and Plasma Oscillation

We begin with a quantitative description of the ponderomotive force of the laser and the oscillation of the plasma. As noted qualitatively in the Introduction, the ponderomotive force results from the oscillation of the particles in a laser field with spatial dependence (i.e. a peak in intensity on axis, as is typical of focused laser spots, or finite pulselength). To derive the resulting force [11–13], we expand the fields about a central location  $\mathbf{r}_0$  in displacement  $\delta\mathbf{r}$ :

$$\mathbf{E} = \mathbf{E}_s(\mathbf{r})\cos(\omega t) = [\mathbf{E}_s(\mathbf{r}_0) + (\delta\mathbf{r}_1 \cdot \nabla)\mathbf{E}_s(\mathbf{r})|_{\mathbf{r}_0} + \dots]\cos(\omega t) = \mathbf{E}_1 + \mathbf{E}_2 + \dots \quad (2.1)$$

where  $\mathbf{E}_s(\mathbf{r})$  is the envelope and the cosine contains the oscillation at the laser frequency. Vector quantities are bold. The wave equation [12] gives  $\partial\mathbf{B}/\partial t = -c(\nabla \times \mathbf{E})$  so that  $\mathbf{B}_1 = [\nabla \times \mathbf{E}_s(\mathbf{r}_0)]\sin(\omega t)$  and similarly for higher orders. Now, at first order in velocity we have simply the motion in the oscillating electric field:

$$m \frac{d\mathbf{v}_1}{dt} = -e\mathbf{E}_1 \Rightarrow \begin{cases} \mathbf{v}_1 = -\frac{e}{m\omega}\mathbf{E}_s(\mathbf{r}_0)\sin(\omega t) \\ \delta\mathbf{r}_1 = \frac{e}{m\omega^2}\mathbf{E}_s(\mathbf{r}_0)\cos(\omega t) \end{cases} \quad (2.2)$$

where  $m$  is the electron mass,  $e$  the magnitude of the charge,  $\mathbf{v}$  the velocity, and  $\delta\mathbf{r}$  the displacement. At second order, there is a  $\mathbf{v}_1 \times \mathbf{B}_1$  contribution as well as an electric field  $\mathbf{E}_2$ . We average the motion over a laser period to obtain the slow motion (denoted by  $\langle \rangle$ ) and hence the ponderomotive force  $\mathbf{F}_p$ :

$$\begin{aligned} m \frac{d\mathbf{v}_2}{dt} &= -e[\mathbf{E}_2 + \mathbf{v}_1 \times \mathbf{B}_1] = -e[(\delta\mathbf{r}_1 \cdot \nabla)\mathbf{E} + \mathbf{v}_1 \times \mathbf{B}_1] \\ \mathbf{F}_p = \langle m \frac{d\mathbf{v}_2}{dt} \rangle &= -\frac{1}{2} \frac{e^2}{m\omega^2} [(\mathbf{E}_s \cdot \nabla)\mathbf{E}_s + \mathbf{E}_s \times (\nabla \times \mathbf{E}_s)] = \frac{e^2}{4m\omega^2} \nabla E_s^2(\mathbf{r}) = \frac{mc^2 \nabla a_0^2(\mathbf{r})}{4} \end{aligned} \quad (2.3)$$

where the identity  $\mathbf{E}_s \times (\nabla \times \mathbf{E}_s) = \frac{1}{2}\nabla E_s^2 - \mathbf{E}_s \cdot \nabla \mathbf{E}_s$  has been used, and the factor of 1/2 results from averaging  $\cos(\omega t)^2$  over the laser period. The wave equation has been used to substitute for  $\mathbf{B}$ . The normalized vector potential  $a_0$  has been used in

the last step, and is defined by:

$$a_0 = \frac{eE_s}{\omega mc} \approx 8.5 \times 10^{-10} \lambda[\mu m] \sqrt{I[\frac{W}{cm^2}]} \quad (2.4)$$

This is an important quantity as, by conservation of canonical momentum:

$$a_0 = \gamma v_{\perp}/c \quad (2.5)$$

where  $\gamma = (1 - v^2/c^2)^{-1/2}$ ,  $c$  is the speed of light, and  $v_{\perp}$  is the quiver velocity in the laser field [3]. Note that due to the contribution of the magnetic field, there is an axial ponderomotive force as well as a radial one. The ponderomotive force expels electrons from regions of high laser intensity, and the result is that plasma density is depressed following the passage of an intense laser pulse. The ponderomotive force is stronger for electrons than for ions because the ions' larger mass results in smaller oscillations in the laser field, and the resulting displacement is smaller by  $(m/M)^2 \approx 10^6$ , where  $M$  is the ion mass. As we shall find below, this means that the ions are not influenced directly by the ponderomotive force for our laser parameters.

The ponderomotive displacement of electrons results in oscillation of the plasma density, as shown in Eq. 1.1 (Fig. 1.1), where it was found that the electron density oscillates at a characteristic frequency:

$$\omega_p = (4\pi n e^2/m)^{1/2} \quad (2.6)$$

Because the laser travels through the plasma near the speed of light, this oscillation creates a wave following the laser pulse. The spatial wavelength is  $\lambda_p \approx 2\pi v_p/\omega_p$  and the wavenumber is  $k_p = \omega_p/v_p$ , with  $v_p \sim c$  the phase velocity of the wave ( $\sim$  group velocity of the laser) and  $c$  the speed of light. The corresponding frequency for ions is slower due to their increased mass:  $\omega_{pi} = (4\pi e^2 n/M)^{1/2}$ .

The limit on the accelerating field of the wave can be calculated by demanding that the wave amplitude be large enough to accelerate the particles to the wave

phase velocity  $v_p$  in one cycle [14, 15]. In the one-dimensional non-relativistic limit this condition is (Eq. 1.2):

$$\frac{eE_0}{m\omega_p} = v_p \approx c \Rightarrow E_0 = \frac{m\omega_p c}{e} \quad (2.7)$$

This is known as the cold wave-breaking limit, which can be written as:  $E_0 = 0.96\sqrt{n_0[cm^{-3}]}$  Volts per centimeter, with  $n_0$  the electron density. Using the non-linear relativistic cold fluid equations, it can be shown that the one-dimensional non-linear relativistic limit is [14]:

$$E_{WB} = \sqrt{2(\gamma_p - 1)}E_0 \quad (2.8)$$

where  $\gamma_p = (1 - \beta_p^2)^{-1/2}$  with  $\beta_p = v_p^2/c^2$  and  $v_p$  the wake phase velocity (Section 2.4, below). Trapping will hence be easiest when the wake velocity is low, and its amplitude high. Transverse wave-breaking [65], where particles are injected from the sides of the wave rather than along its axis, can reduce the threshold. However, multi-dimensional trapping solutions for the experimental parameters do not exist so that the one-dimensional theory remains useful. Detailed modeling of experiments often requires numerical simulations (Chapter 6).

## 2.2 Wake Generation

Much of the physics of wakefield acceleration can be described by the cold fluid model of laser plasma interaction [3, 11, 12, 37]. The plasma is described as an electron fluid with zero temperature, and the ions are immobile. This model is appropriate to wakefield acceleration, as the plasma temperature ( $\sim 10$  eV) is typically small compared to the oscillation velocity in the laser field ( $\sim$ hundreds of eV-MeV). Because of their greater mass, the ions are slower to move, and  $\omega_{pi}$  is much longer than the driver duration. As a result, the ions are effectively immobile, as confirmed below.

Collisional effects are also neglected since the characteristic collision times are much longer than the driver duration. The model was used in combination with previous experiments to give scalings for the experiments described herein.

We begin with the fluid force and continuity equations in one dimension. We write the variables as the sum of a constant background plus a (small) perturbation  $\mathbf{v} = \mathbf{v}_0 + \tilde{\mathbf{v}}$ , and discard quantities that are higher order in  $\tilde{\mathbf{v}}$ . This is suitable for considering small departures from stasis:

$$\frac{\partial \tilde{\mathbf{v}}}{\partial t} = -\frac{e}{m}(\mathbf{E}_\perp + \frac{\mathbf{v}}{c} \times \mathbf{B}_\perp + \mathbf{E}_P) \quad (2.9)$$

$$\frac{\partial \tilde{n}}{\partial t n_0} = -\nabla \cdot \tilde{\mathbf{v}} \quad (2.10)$$

where  $\mathbf{v}$  is the fluid velocity,  $n$  the density,  $e$  and  $m$  are the electron charge magnitude and mass, and  $c$  is the speed of light.  $\mathbf{E}_\perp, \mathbf{B}_\perp$  are the (transverse) laser fields and  $\mathbf{E}_P$  is the plasma field which is longitudinal:  $\mathbf{E}_P = E_z$  for laser propagation along the  $z$  axis. Recalling that the high frequency electron motion in the laser field is (Eq. 2.5)  $\mathbf{v}_\perp = \mathbf{a}c$  for small  $\mathbf{a}$ , we write the velocity  $\tilde{\mathbf{v}} = \mathbf{v}_s + \mathbf{a}c$  where  $\mathbf{v}_s$  is the slow contribution. Averaging over a laser period, we then obtain for the force equation:

$$\frac{\partial \mathbf{v}_s}{\partial t} = -\frac{e}{m}(\nabla \Phi_P + \mathbf{E}_P) \quad (2.11)$$

where  $\Phi_P$  is the potential from the ponderomotive force derived in Section 2.1. Taking the time derivative of the continuity equation and  $\nabla \cdot$ (force Eqn.):

$$\frac{\partial^2 \tilde{n}}{\partial t^2 n_0} = -\frac{\partial}{\partial t} \nabla \cdot \mathbf{v}_s = -\frac{e}{m}(\nabla^2 \Phi_P + \nabla \cdot \mathbf{E}_P) \quad (2.12)$$

Then, making use of the Poisson equation  $\nabla \cdot E = -4\pi e\tilde{n}$ , we find the response of the plasma to the laser driver:

$$\left(\frac{\partial^2}{\partial t^2} + \omega_p^2\right) \frac{\tilde{n}}{n_0} = -\frac{e}{m} \nabla^2 \Phi_P = \frac{c^2}{4} \nabla^2 a^2 \quad (2.13)$$

It can often be useful to take a frame of reference (nearly) co-moving with the laser

at  $c \approx v_g$ . Hence we transform  $\xi = z - ct$ ,  $t = t$  and find:

$$\left(\frac{\partial^2}{\partial \xi^2} + k_p^2\right) \frac{\tilde{n}}{n_0} = (\nabla_{\perp}^2 + \frac{\partial^2}{\partial \xi^2}) \frac{a^2}{4} \quad (2.14)$$

The equation is that of a driven harmonic oscillation, with  $\tilde{n}/n$  as the oscillation variable and the ponderomotive potential as the driver, just as one would expect from the discussion of the plasma oscillation and ponderomotive force in Section 2.1.

The Green's function solution for such an oscillator is [3, 16, 66]:

$$\frac{\tilde{n}}{n_0} = \frac{1}{\omega_p} \int_{-\infty}^t \sin(\omega_p(t-t')) \nabla^2 \frac{c^2 a^2(\mathbf{r}, t')}{4} dt' \quad (2.15)$$

Using the Poisson equation to relate density to electric field and potential, the solutions for these quantities are:

$$\begin{aligned} \Phi &= \frac{mc^2 \omega_p}{4e} \int_{-\infty}^t \sin(\omega_p(t-t')) a^2(\mathbf{r}, t') dt' \\ E_z &= -\frac{mc^2 \omega_p}{4e} \int_{-\infty}^t \sin(\omega_p(t-t')) \nabla a^2(\mathbf{r}, t') dt' \end{aligned} \quad (2.16)$$

Solutions of this equation are obtained by integrating over the laser pulse shape. For a sine pulse ( $a_0 \propto \sin(\xi/(c\tau_L))$  for  $0 \leq \xi/(c\tau_L) \leq \pi$  and  $a_0 = 0$  elsewhere) we find that the largest plasma response is obtained for a pulse length  $c\tau_L = \lambda_p$ , and the plasma wave electric field behind the laser pulse is then:

$$\frac{E_z}{E_0} = -\frac{\pi a_0^2}{8} \cos(k_p \xi) \quad (2.17)$$

and as noted above the potential and the density perturbation:

$$\frac{\tilde{n}}{n} = -\frac{\pi a_0^2}{8} \sin(k_p \xi) \quad (2.18)$$

again follow from Poisson. Similarly, for a square laser pulse, ( $a_0 = \text{constant}$  for  $0 \leq \xi \leq \lambda_p/2$  and  $a_0 = 0$  elsewhere),  $E_z/E_0 = (a_0^2/2) \sin(k_p \xi)$  and  $\tilde{n}/n = (-a_0^2/2) \cos(k_p \xi)$ . Note that the square pulse excites a larger wake, due to its sharper rise/fall times, for a given pulse amplitude or energy.

The laser pulse hence excites a copropagating plasma wave with wavelength  $\lambda_p$  and phase velocity equal to the group velocity of the laser [2, 67, 68]. Its amplitude is proportional to the ponderomotive potential of the laser pulse. For modest  $a_0 = 0.5$  and a plasma density of  $1 \times 10^{18}$ , chosen to match  $L = \lambda_p$  for a 50 fs laser pulse, the wake electric field is 10 GV/m. The electron bunch produced will also be shorter than half the plasma wavelength in order to fit in the accelerating region of the field, so that 10 fs electron bunches may be produced, providing for ultrafast applications. The electron density perturbation is approximately 10% for this example, and recalling the relative size of the ponderomotive displacement for ions ( $10^{-6}$ ), it is hence clear that the stationary ion approximation used was valid. The field scales up as  $a_0^2$  and  $\sqrt{n}$  so that much higher fields are available. For example, a 10 TW laser can produce  $a_0 \approx 2$  in a reasonable focal spot of 8  $\mu\text{m}$ , and densities of a few  $10^{19}$  can be used with self modulation, allowing fields of hundreds of GV/m. The desirable parameter ranges are discussed further in the following sections.

Analytic solution for the wake in the non-linear case ( $a_0 \gtrsim 1$ ), where the wake is a large perturbation, is available only for a few cases. For a square laser pulse profile, this has been calculated, yielding:  $E_{z,max}^2/E_0^2 \approx 2a_0^2/(1 + \beta_p)$  for  $a_0^2 > 1$  and  $a_0^2 \ll \gamma_p^2\beta_p^2$  [43, 69] for circular polarization. For linear polarization (as used above), replace  $a_0^2$  in the solution with  $a_0^2/2$ . Analytic solutions are not available in the multidimensional non-linear regime or for realistic pulse shapes, so that numerical simulations are used to obtain the plasma response and particle behavior. Such simulations are described in Chapters 6, 7 [21, 61–64, 70–74]. Even such simulations do not fully predict the behavior of experiments due to the highly non-linear nature of the problem. The linear and one-dimensional non-linear theory do however provide a useful general guide to establish the operating regime, and can be used in conjunction with both simulations and scaling from previous experiments to choose appropriate parameters for and interpret the data from experiments.

If the wake is not one-dimensional, the radial wake can be derived from the Panofsky-Wenzel theorem [3, 16, 75, 76]. This will be most important for laser spot size (and hence wake radial dimension)  $\lesssim \lambda_p$ . We make use of:

$$\mathbf{E} = -\nabla\Phi \Rightarrow \frac{\partial E_r}{\partial z} = \frac{\partial^2 \Phi}{\partial z \partial r} = \frac{\partial E_z}{\partial r} \quad (2.19)$$

assuming azimuthal symmetry in cylindrical coordinates, as is reasonable for typical round laser driver spots ( $\partial\phi/\partial\theta = 0$ ). For a laser with a Gaussian radial envelope (Section 2.4), the fluid solution (Eq. 2.17) yields:

$$E_z = -\frac{\pi a_0^2 E_0}{8} \exp(-2r^2/w_0^2) \cos(k_p \xi) \Rightarrow E_r = \frac{\pi a_0^2 E_0}{8} \frac{4r}{w_0^2 k_p} \exp(-2r^2/w_0^2) \sin(k_p \xi) \quad (2.20)$$

Hence there is a wake region where the fields are both accelerating and focusing:  $E_z < 0$  and  $E_r > 0$  for  $-2\pi < k_p \xi < -3\pi/2$ , and this repeats in each wake period. This allows particles to be accelerated over long distances. The size of the focusing region is extended by wake curvature in non-linear wakes, such as used for these experiments, and in plasma channels [3, 77] (Chapter 6, Section 2.5.1). Variation of the plasma period due to wake nonlinearity in the former case, or density variation in the second, causes the wake fronts to bend, creating a horseshoe shaped wake whose field points inward as well as along the laser propagation direction, increasing focusing.

The availability of the high fields indicated here offers an attractive alternative to conventional accelerators. The presence of a focusing region in the wake additionally indicates that particles can be confined radially as well as accelerated, facilitating acceleration over long distance. Trapping and acceleration of particles by the wake can then be analyzed.

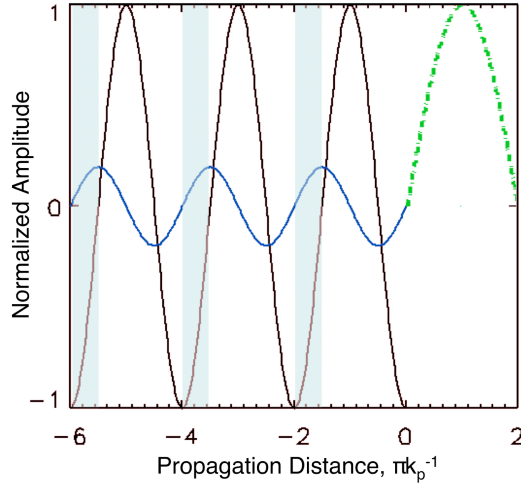


Figure 2.1. Wake longitudinal (red) and peak radial (blue) fields driven behind a laser pulse with a sine envelope (green dotted), from Eq.'s 2.17 and 2.19 for  $w_0 \sim \lambda_p$ . The shaded regions, where radial field is positive and longitudinal field negative, are both accelerating and focusing for electrons. Electrons in these regions can be accelerated over long distances while remaining focused. The wake under the laser pulse is not shown, but can be calculated numerically (for example Fig 1.2, Section 7.2).

## 2.3 Particle Trapping

The experiments described here used self-trapping from the bulk plasma to inject electrons into the wake field for acceleration. This avoids the need for an external injector, but requires high wake amplitude in order to trap electrons. Evaluation of the wake model and wave-breaking thresholds in this Chapter, as well as previous experiments, indicate that a wake field large enough to trap and accelerate electrons from the bulk plasma can be generated by self-modulation [18–20, 22](Section 2.5.3) in a plasma of a few  $10^{19} \text{ cm}^{-3}$  density using a 10 TW, 50 fs laser pulse at  $0.8 \mu\text{m}$ . Particle self-trapping is facilitated in these high density plasmas, where the laser group velocity and hence wave phase velocity is low.

From the expression for non-linear relativistic wave-breaking (Eq. 2.8) and the plasma wave model (Eq. 2.2) above we anticipate that  $a_0 \sim 1.9(\gamma_p - 1)^{1/4} > 1$  will be

required to trap particles from the background plasma in one dimension. The linear wake model is not valid for  $a_0 \gtrsim 1$  however, so that this formula does not accurately predict the value of  $a_0$  needed. Using the non-linear one-dimensional model for  $E_z$  (Section 2.2) indicates  $a_0 \sim 2(\gamma_p - 1)^{1/2} > 1$  ( $\beta_p \sim 1$  has been used since  $v_p \sim c$ ). This indicates the need for large  $a_0$  in order to trap particles by wave-breaking, since a fast wake velocity ( $\gamma_p \gg 1$ ) is required to obtain high electron energies. If the wake velocity is slow, electrons quickly outrun the wake and are not accelerated (see Section 2.6 for details). However, the scaling of wave-breaking with  $\gamma_p$  also indicates that the wake phase velocity must be kept low enough to allow trapping. Compromise is required. The laser group (and wake phase) velocity is derived in Section 2.4, where we find that  $\gamma = \omega/\omega_p$  with  $\omega$  the laser frequency (Eq. 2.29). At densities of a few  $10^{19} \text{ cm}^{-3}$ ,  $\gamma \sim 10$ , and  $a_0$  of a few will hence satisfy the wave breaking criteria above, and this is attainable with our 10 TW laser. At densities of a few  $10^{18} \text{ cm}^{-3}$  the required  $a_0$  is likely too high for our system, and this is confirmed by experiments (below). Transverse wave-breaking [65] reduces the trapping threshold for three-dimensional wakes, so that numerical modeling [21,61–64,70–74] (Chapter 6) or experimental scaling is needed for more accurate projections.

Experiments at several laboratories [4–9] including preparatory experiments by researchers including the author at LBNL [10,28], have provided data on wave-breaking and acceleration of electrons. Data from our experiments are presented in Fig. 2.2. These experiments used a pulse of  $<10$  TW power and  $> 50$  fs duration incident on a gas jet target to drive the wake and self-trap/accelerate electrons. No guiding was used. The experiments indicated that  $a_0 \sim 1 - 2$  is required for such pulses at densities of a few  $10^{19} \text{ cm}^{-3}$  (where  $\gamma_p \sim 10$ ) in order to self-trap and accelerate electrons. Trapped charge and energy generally increased with  $a_0$ , indicating the desirability of high intensities. Trapping and acceleration of electrons was not observed at densities below approximately  $2 \times 10^{19} \text{ cm}^{-3}$  for these pulse parameters. As expected, the

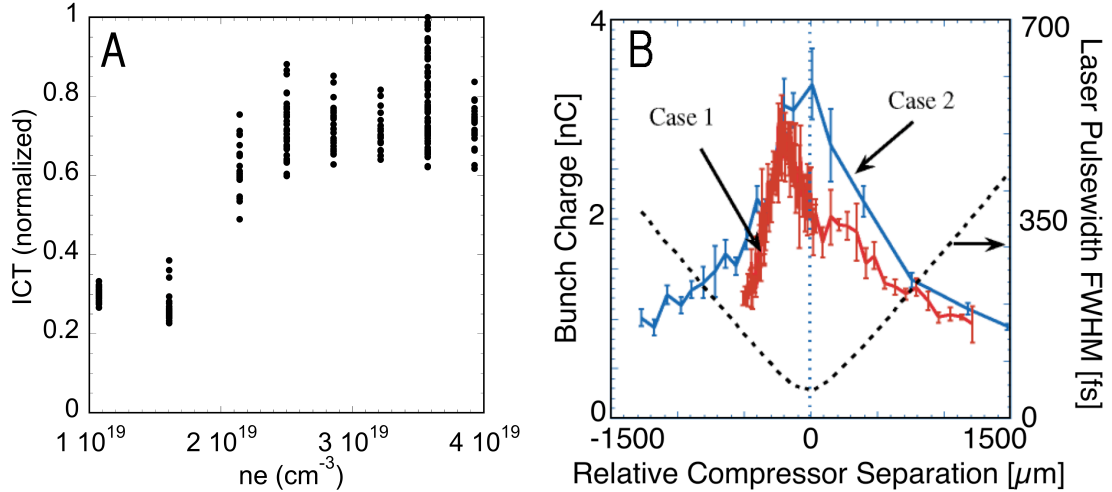


Figure 2.2. (A) Normalized electron yield versus plasma density. Significant trapping is observed for densities  $\gtrsim 2 \times 10^{19} \text{ cm}^{-3}$ . The laser pulse energy was 460 mJ, the duration 50 fs and spot size  $7 \mu\text{m}$  FWHM resulting in  $a_0 \approx 2$ . (B) Electron yield for two runs (cases 1 and 2) and pulse duration (dashed line) vs. compressor setting at a plasma density of  $4 \times 10^{19} \text{ cm}^{-3}$  [10]. Little trapping is evident for pulse lengths longer than 200 fs, corresponding to  $a_0 < 1$ , indicating that high intensity is required to self-trap and accelerate particles.

experimental values are somewhat lower than the one-dimensional predictions, which indicate  $a_0 \approx 5 - 6$ , but both confirm the need for high  $a_0$  and high density in order to self-trap.

The charge of the trapped and accelerated electron beam can be limited by beam loading of the wake [16, 17]. The electric field of the electron bunch being accelerated by the wake induces its own wake, pushing electrons aside just as the laser ponderomotive force does. This wake interferes destructively with the wake driven by the laser, reducing its amplitude [16]. As electrons are trapped and accelerated, this loading eventually reduces the wake amplitude below the trapping threshold, preventing injection of further electrons. As we shall see in Chapter 6, under certain conditions this can result in the loading of electrons over a small range of wake phase, and hence in the production of small energy spread electron bunches, because all electrons loaded near the same phase experience similar accelerating field.

Both the theoretical and experimental scalings indicate that a laser with  $a_0 \gtrsim 2$  is needed for efficient trapping, even in high density plasmas of a few  $10^{19} \text{ cm}^{-3}$ . For a laser power of 10 TW, as available for these experiments, this indicates a laser spot size  $w_0 \sim 7 \mu\text{m}$ . Hence the diffraction range over which the laser remains focused without guiding is  $Z_R \sim 200 \mu\text{m}$  (see Eq. 2.21, below). These parameters were taken as the basis for the experiments described in this thesis. As we shall see in the following sections, this regime indicates guiding of the laser pulse will be desirable to optimize performance. We next consider the propagation of the laser pulse in the plasma to determine how the driver can be optimized.

## 2.4 Plasma Refractive Index and Laser Propagation

The propagation of the laser is modified by the plasma refractive index, which in turn can be modified by the presence of the laser in a non-linear interaction. This interaction is important for wake generation and laser guiding. Here we consider laser propagation with and without plasma interaction to obtain the group and phase velocities. The former determines the velocity of the accelerating structure, while the latter leads to consideration of how the plasma can be shaped to control the laser pulse.

Without guiding, the laser diffracts according to vacuum optics. The experimental laser pulses have nearly Gaussian radial intensity profiles, with  $I = I_0 \exp(-2r^2/w_0^2)$  at focus where  $w_0$  is the spot size. For such a beam, the laser spot size  $w_0$  varies with propagation distance  $z$  as:

$$w(z) = w_0 \sqrt{1 + z^2/Z_R^2} \quad (2.21)$$

For a distance  $Z_R = \frac{\pi}{\lambda} w_0^2$  on either side of the focus, the spot size remains with in

$\sqrt{2}$  of the minimum value, and the intensity within a factor of 2 [24]. This is referred to as the diffraction range, and is the range over which an unguided pulse remains intense. Acceleration in the absence of laser guiding is limited to this length, as the intensity falls off rapidly after  $Z_R$  as the beam expands. We found in Section 2.3 above that for a 10 TW laser such as available for these experiments,  $w_0 \sim 7\mu\text{m}$  and hence  $Z_R \sim 200\mu\text{m}$  must be used to obtain  $a_0 \sim 2$ , which is needed to self-trap particles in the wake. Such a short acceleration distance will limit the final energy to 10's of MeV even given the high fields derived in Section 2.2. Guiding the laser, through interaction with the plasma refractive index, can extend interaction length and offer higher energies [36–41].

We begin by considering the propagation of a plane electromagnetic wave in a homogeneous plasma [11, 12]. The plasma affects the laser through its conductivity, which can be modeled by considering the oscillation of the electrons in the laser field. Assuming that  $\omega > \omega_p$  (required for propagation, as we shall see), ions can be treated as stationary. Similarly to the ponderomotive force derivation, we take the laser field to be of the form  $\mathbf{E} = \mathbf{E}(\mathbf{r})\exp(-i\omega t)$  and consider the first order electron motion in the field, yielding:

$$\frac{\partial \mathbf{v}}{\partial t} = -\frac{e}{m}\mathbf{E}(\mathbf{r})\exp(-i\omega t) \quad (2.22)$$

$$\mathbf{v} = -\frac{ie}{m\omega}\mathbf{E} \quad (2.23)$$

$$\mathbf{J} = -nev = \frac{i\omega_p^2}{4\pi\omega}\mathbf{E} = \sigma\mathbf{E} \quad (2.24)$$

where  $\sigma = i\omega_p^2/(4\pi\omega)$  is the high frequency conductivity of the plasma. By using the non-relativistic mass, we assume a regime where  $a_0 \ll 1$ , i.e. the quiver velocity in the laser field is much less than  $c$ . If  $a_0 \gtrsim 1$ , the substitution  $m \rightarrow \gamma m$  is made (Eq. 2.30).

The wave equation for the electromagnetic wave follows from Faraday's and Am-

per's laws. For a wave of the form given above, we find from Ampere's law:

$$\begin{aligned}
\nabla \times \mathbf{B} &= \frac{4\pi}{c} \mathbf{J} + \frac{1}{c} \frac{\partial \mathbf{E}}{\partial t} \\
&= \left( \frac{4\pi}{c} \sigma - \frac{i\omega}{c} \right) \mathbf{E} \\
&= \frac{i\omega}{c} \left( \frac{\omega_p^2}{\omega^2} - 1 \right) \mathbf{E} \\
&= -\frac{i\omega}{c} \epsilon \mathbf{E}
\end{aligned} \tag{2.25}$$

where  $\epsilon = 1 - \omega_p^2/\omega^2$  is the plasma dielectric function. Applying the curl to Faraday's equation and using Eq. 2.25 to substitute  $-\frac{i\omega}{c}\epsilon\mathbf{E}$  for  $\nabla \times \mathbf{B}$  we obtain the wave equation for  $\mathbf{E}$ :

$$\begin{aligned}
\nabla \times (\nabla \times \mathbf{E}) &= \nabla \times \left( -\frac{1}{c} \frac{\partial \mathbf{B}}{\partial t} \right) = -\frac{1}{c} \frac{\partial}{\partial t} \nabla \times \mathbf{B} \\
\nabla^2 \mathbf{E} - \nabla(\nabla \cdot \mathbf{E}) + \frac{\omega^2}{c^2} \epsilon \mathbf{E} &= 0
\end{aligned} \tag{2.26}$$

where the vector identity  $\nabla \times (\nabla \times \mathbf{E}) = \nabla(\nabla \cdot \mathbf{E}) - \nabla^2 \mathbf{E}$  has been used. Similarly, applying the curl to Eq. 2.25 and using Faraday's equation to eliminate  $\mathbf{E}$  we obtain:

$$\nabla^2 \mathbf{B} + \frac{1}{\epsilon} \nabla \epsilon \times (\nabla \times \mathbf{B}) + \frac{\omega^2}{c^2} \epsilon \mathbf{B} = 0 \tag{2.27}$$

which is the wave equation for  $\mathbf{B}$ .

For a plane wave in a homogeneous plasma,  $\nabla \epsilon = 0$  and  $\nabla \cdot \mathbf{E} = 0$ , so that the wave equations become identical. Inserting the spatial dependence of a plane wave ( $\exp(ik \cdot r)$ ) into either equation then yields the dispersion relation for electromagnetic waves in a plasma:

$$\begin{aligned}
\nabla^2 \mathbf{E} + \frac{\omega^2}{c^2} \epsilon \mathbf{E} &= 0 \\
k^2 + \epsilon \frac{\omega^2}{c^2} &= 0 \\
\omega^2 &= \omega_p^2 + k^2 c^2
\end{aligned} \tag{2.28}$$

Note that the density where  $\omega_p = \omega$  is the maximum density of plasma through which the wave can propagate without attenuation, since above this density  $k$  is imaginary.

Physically, this corresponds to the ability of the electrons to shield any field with  $\omega < \omega_p$ . This maximum density for propagation is referred to as the critical density,  $n_{cr}[cm^{-3}] \approx 1.1 \times 10^{21} \lambda[\mu m] \approx 9 \times 10^{20}$  for 0.8  $\mu m$  light. This also validates the assumption of stationary ions, as  $\omega_{pi} \ll \omega_p$ .

The group velocity of the laser pulse,  $v_g$ , determines the phase velocity of the wake that forms the accelerating structure. Differentiating the dispersion relation Eq. 2.28 we obtain:

$$v_g = \frac{\partial \omega}{\partial k} = \frac{\partial}{\partial k} \sqrt{\omega_p^2 + k^2 c^2} = c \sqrt{1 - \frac{\omega_p^2}{\omega^2}} \quad (2.29)$$

This determines the wave-breaking threshold (Section 2.3), which increases for high wake phase velocity. It also affects the available energy gain, since relativistic particles will take longer to outrun a wake traveling near  $c$ , resulting in high energy gain (Section 2.6). To obtain  $v_g \approx c$  for higher energy gain, we choose  $n/n_{cr} \ll 1$ , and in this limit it is often more convenient to refer to  $\gamma_g = (1 - v_g^2/c^2)^{-1/2} = \omega/\omega_p$ .

The phase velocity  $v_p$  of the laser pulse describes focusing and modulation, which affect propagation properties in the plasma. Using the dispersion relation, we obtain the refractive index for a homogeneous plasma in the low  $a_0$  limit:  $\eta_0 = ck/\omega = c/v_p = \sqrt{1 - \omega_p^2/\omega^2} = \sqrt{\epsilon}$ . Including variation of the plasma density (for instance due to the plasma wave or a pre-formed structure in the plasma), and using the substitution  $m \rightarrow \gamma m$  to account for the relativistic mass increase of the electron due to oscillation in the laser field, we find that:

$$\eta(\mathbf{r}) = \sqrt{1 - \frac{\omega_p^2}{\omega^2} \frac{n(\mathbf{r})}{\gamma(\mathbf{r})n_0}} \quad (2.30)$$

where  $n_0$  is the bulk plasma density, and  $(\mathbf{r})$  indicates spatially dependent quantities. Suitable manipulation of Eq. 2.5 shows that  $\gamma \approx 1 + (1/2)a_0^2$  for small  $a_0$ . Using this expression for  $\gamma$  and expanding Eq. 2.30 for small changes in density and modest

relativistic effects, we obtain:

$$\eta(\mathbf{r}) = c/v_p = 1 - \frac{\omega_p^2}{2\omega^2} \left( 1 + \frac{\Delta n(\mathbf{r})}{n} + \frac{\delta n(\mathbf{r})}{n} - \frac{a_0(\mathbf{r})^2}{2} \right) \quad (2.31)$$

where  $\Delta n$  is the density variation due to a pre-existing structure in the plasma, and  $\delta n$  is the change in plasma density due to the wake response. It is clear that phase velocity increases for increasing  $n$  and for decreasing  $a_0$ . Hence non-uniform transverse densities or intensity profiles will focus or defocus the laser pulse by bending the phase fronts due to the difference in phase velocity.

By considering the laser interaction with the plasma fluid, we have obtained the group and phase velocities. The group velocity of the laser pulse, and hence the wake structure, influences self-trapping of electrons (Eq. 2.8) and also the energy that electrons can obtain from the wake (see Section 2.6 below). The structure of the refractive index (and phase velocity) indicate that the laser pulse focusing can be affected by the plasma structure and by the laser intensity distribution. We now turn to how this can be used to guide the laser pulse.

## 2.5 Laser Guiding and Self-Modulation in Plasmas

Guiding of the laser pulse results when the phase velocity on the propagation axis is lower than that off axis. In this case, faster propagation off axis bends the phase fronts in a focusing direction (Fig. 1.3). From the form of the refractive index (Eq. 2.31), it is evident that this can occur either due to a preformed plasma density variation with a minimum on the propagation axis (channel guiding), or due to a peaked laser amplitude  $a_0$  on axis (self-guiding). In both cases, the refractive index change must be sufficient to counter diffraction in order for guiding to occur.

### 2.5.1 Plasma Channel Guiding

Solution of the wave equation with the refractive index given in (Eq. 2.31) indicates that a parabolic transverse plasma density profile, or ‘channel,’ can be matched to guide a Gaussian laser pulse [18, 51]. We begin with the wave equation for  $\mathbf{E}$ :  $\nabla^2 \mathbf{E} + \frac{\omega^2}{c^2} \epsilon \mathbf{E} = 0$  (Eq. 2.28), which reads:

$$\nabla^2 \mathbf{E} + \frac{\omega^2}{c^2} \eta^2 \mathbf{E} = 0 \quad (2.32)$$

with the substitution:  $\eta = \sqrt{1 - \omega_p^2/\omega^2} = \sqrt{\epsilon}$ . We next write  $\mathbf{E} = E_{\perp} \exp(-i\beta z) \hat{\mathbf{E}}$  where  $\beta$  is the wavenumber in the propagation direction,  $E_{\perp}$  is the transverse envelope of the pulse,  $\hat{\mathbf{E}}$  is the transverse field polarization vector, and  $k = \omega/c$  is the total wavenumber. The wave equation then becomes:

$$\nabla^2 E_{\perp} + (\eta^2 k^2 - \beta^2) E_{\perp} = 0 \quad (2.33)$$

This is a scalar wave equation, which applies to the components of  $\mathbf{E}$ , and can be solved for the appropriate refractive index distribution.

With a parabolic plasma density distribution  $n = n_0 + \Delta n r^2/w_0^2$  (neglecting relativistic effects and the wake response for now), Eq. 2.31 can be written in the form  $\eta = \eta_0(1 - cr^2)$  with  $c$  a constant:

$$\begin{aligned} \eta(r) &= 1 - \frac{\omega_p^2}{2\omega^2} \left(1 + \frac{\Delta n(r)}{n}\right) = 1 - \frac{\omega_p^2}{2\omega^2} \left(1 + \frac{\Delta n r^2}{n w_0^2}\right) \\ &\approx \left(1 - \frac{\omega_p^2}{2\omega^2}\right) \left(1 - \frac{\omega_p^2}{2\omega^2} \frac{\Delta n r^2}{n w_0^2}\right) = \eta_1 \left(1 - 2\Delta \frac{r^2}{w_0^2}\right) \end{aligned} \quad (2.34)$$

where higher order terms in  $\omega_p^2/\omega^2$  have been discarded since we are considering low plasma densities where  $\omega_p^2 \ll \omega^2$ . This form indicates a parabolic index of refraction, which can be inserted in the wave equation.

We now solve the wave equation with the refractive index profile Eq. 2.34 using a Gaussian beam:  $E_{\perp} = E_0 \exp(-r^2/w_0^2)$ . Note that the laser spot size and channel

scale length  $w_0$  were taken to be the same: this imposes no restriction as  $\Delta n$  can be adjusted to provide any desired channel density rise. Inserting these forms into Eq. 2.33 in cylindrical geometry yields:

$$\begin{aligned}
0 &= \left[ \frac{1}{r} \frac{\partial}{\partial r} r \frac{\partial}{\partial r} \right] E_{\perp} + [\eta^2 k^2 - \beta^2] E_{\perp} \\
0 &= \left[ \frac{1}{r} \frac{\partial}{\partial r} r \frac{\partial}{\partial r} \right] e^{(r^2/w_0^2)} + [\eta^2 k^2 - \beta^2] e^{(r^2/w_0^2)} \\
0 &= \left[ -\frac{4}{w_0^2} + \frac{4r^2}{w_0^4} \right] e^{(r^2/w_0^2)} + \left[ k^2 \left( 1 - \frac{\omega_p^2}{2\omega^2} \right)^2 \left( 1 - 2 \frac{\omega_p^2}{2\omega^2} \frac{\Delta n r^2}{n w_0^2} + \left[ \frac{\omega_p^2}{2\omega^2} \frac{\Delta n r^2}{n w_0^2} \right]^2 \right) - \beta^2 \right] e^{(r^2/w_0^2)}
\end{aligned} \tag{2.35}$$

The second to the last term on the right is neglected as it is higher order in  $\omega_p^2/\omega^2$ . Equating terms that are quadratic in  $r$ , we obtain the matching condition for guiding.

$$\begin{aligned}
\frac{4r^2}{w_0^4} &= k^2 \left( 1 - \frac{\omega_p^2}{2\omega^2} \right)^2 \frac{2\omega_p^2}{2\omega^2} \frac{\Delta n r^2}{n w_0^2} \\
\frac{4}{w_0^2} &= k^2 \left( 1 - \frac{\omega_p^2}{\omega^2} \right)^2 \frac{2\omega_p^2}{\omega^2} \frac{\Delta n}{n} \\
\frac{4}{w_0^2} &= \frac{1}{c^2} \frac{4\pi e^2 n}{m_e} \frac{\Delta n}{n}
\end{aligned} \tag{2.36}$$

where Eq. 1.1 has been used for the plasma frequency. This yields a formula for the change in density required to guide a spot of size  $w_0$ :

$$\Delta n = 1/\pi r_e w_0^2 \tag{2.37}$$

over the laser spot size  $w_0$  is sufficient to guide the pulse, where  $r_e = e^2/mc^2$  is the classical electron radius [18, 51]. In convenient units,  $\Delta n [cm^{-3}] \sim 1.1 \times 10^{20}/w_0^2 [\mu m]$ . For the experimental parameters, this is a small fraction of the plasma density, so that the homogeneous plasma solution for the group velocity obtained above remains approximately valid. A more precise solution of the group velocity is noted in Section 7.2, and for parameters of these experiments the difference is  $\sim 0.1\%$ .

Further analysis shows that a family of modes can be guided [78]. In general, the solutions are:

$$E_{\perp}(r) = \left( \sqrt{2} \frac{r}{w_0} \right)^m L_p^m \left( 2 \frac{r^2}{w_0^2} \right) e^{-im\theta} e^{-r^2/w_0^2} \tag{2.38}$$

where  $L_p^m$  is the generalized Laguerre polynomial of order  $m$  and degree  $p$  (both integers). These reduce to the Gaussian beam for  $m=p=0$ . These modes solve the wave equation when:

$$\beta = \eta_1 k \left(1 - \frac{\sqrt{2\Delta}}{\eta_1 k w_0} (4p + 2m + 2)\right)^{\frac{1}{2}} \quad (2.39)$$

For the current experiment, the Gaussian beam is of primary interest as it closely approximates the laser transverse envelope near focus, but the higher order modes may be excited in mismatched structures [79].

The infinite parabolic density distribution used for the solution found here will accurately reproduce (finite) experimental channels if the channel radius  $r_0$  is much greater than the spot size, so that the mode does not see the drop off in density at large radius. This is the desirable regime in any case, as modes which approach the channel radius will be attenuated due to leakage, and those that are larger than it simply are not guided since they do not see a guiding profile. The experimental modes in this dissertation are order of 1/10th the channel radius, well satisfying this condition. Leakage of the mode from the guide has also been analyzed [52], and should be negligible for such modes. This is confirmed by simulations (Section 4.3) and by the experimental observations (Chapter 4). Parabolic channels are the form of interest for the present experiments because there are demonstrated experimental methods for forming them [51,52] (Chapter 3). However, hollow channels (zero plasma density out to a radius  $r_0$  and constant outside that) also have advantages for future experiments [80–83] if they can be formed.

## 2.5.2 Relativistic Guiding

Relativistic guiding is obtained when the quiver momentum of the electrons of the laser field causes their mass to increase, lowering the plasma frequency where the laser is most intense [20, 25–27]. This has the same effect on the refractive index as

a drop in plasma density; both reduce the plasma frequency. Hence, guiding can be obtained if the power is large enough for the relativistic effect to overcome diffraction, and a threshold condition in power (similar to that in density for the channel) can be obtained.

The change in refractive index in the relativistic case follows the laser envelope, rather than being externally specified. This means that in order to obtain an exact solution, we must find a mode which produces the right index variation to guide itself. This has been done using a source dependent expansion over all of the Laguerre-Gaussian modes [22, 84]. Here we present an approximate derivation of self-guiding for a Gaussian mode. As we shall find, the Gaussian mode is not exactly matched to self-guide. Although the resulting solution is therefore not exact, it conveys concisely the correct physics.

For the case of relativistic self-guiding,  $\eta$  takes the form (from Eq. 2.31):

$$\eta(r) = 1 - \frac{\omega_p^2}{2\omega^2} \left(1 - \frac{a_0(r)^2}{2}\right) \quad (2.40)$$

Here the plasma response  $\delta n$  has been neglected. This is appropriate for a long pulse, since such a pulse does not drive a large wake. The plasma response for pulses matched to the plasma period is considered below. We expand the intensity distribution to order  $r^2$ :  $a_0(r)^2 = a_0^2 \exp(-r^2/w_0^2) \approx a_0^2(1 - 2r^2/w_0^2)$ , valid for  $r \ll w_0$ . Inserting this into Eq. 2.40 and neglecting higher order terms in  $\omega_p^2/\omega^2$ , we find that:

$$\eta(r) \approx \left(1 - \frac{\omega_p^2}{2\omega^2} - \frac{\omega_p^2}{2\omega^2} \frac{a_0^2}{2}\right) \left(1 - \frac{\omega_p^2}{2\omega^2} \frac{a_0^2 r^2}{w_0^2}\right) \quad (2.41)$$

which is of the same form,  $\eta = \eta_1(1 - Cr^2)$  with C a constant, as found in Eq. 2.34 for the plasma channel wave guide.

With a quadratic refractive index profile, the solution takes the same form as for channel guiding, and the solution is the same with the substitution of  $a_0^2$  for  $\Delta n/n$ .

Making this substitution, Eq. 2.36 becomes:

$$\frac{4}{w_0^2} = \frac{1}{c^2} \omega_p^2 a_0^2 \rightarrow 1 = \frac{w_0^2 a_0^2 k_p^2}{4} \quad (2.42)$$

This indicates that self-guiding will occur for powers greater than a critical power at a given plasma density ( $k_p$ ).

The solution above over-estimates self-focusing because the Gaussian mode is not a matched solution with an intensity dependent refractive index and also because the quadratic expansion of the intensity over-estimates self-focusing. However, the scaling is correct. An accurate derivation using the source dependent expansion finds:

$$1 = \frac{w_0^2 a_0^2 k_p^2}{32} \quad (2.43)$$

i.e., self-guiding occurs for powers greater than a critical power  $P_c[GW] = 17\omega^2/\omega_p^2$  [20, 25–27].

### 2.5.3 Plasma Wake and Self-Modulation

The wake density perturbation driven by the laser pulse (Eq. 2.18) affects laser guiding, reducing the effectiveness of relativistic guiding for short pulses, and modulating the envelope of long pulses. Because the ponderomotive force tends to push electrons forward ahead of the pulse, creating a high density region under the first  $\lambda_p/2$  of the pulse (Fig. 1.2), the wake response tends to counteract the effect of relativistic self-focusing and is defocusing for this portion of the pulse. For pulses matched to the plasma period (as in Eq. 2.17), the wake perturbation is strong and can negate the effect of relativistic guiding for the leading edge of the pulse so that channel guiding is needed [18, 22].

The wake density perturbation also causes evolution of the laser pulse shape, and this ‘self-modulation’ of the laser by the wake it drives allows driving of a large wake

with a laser pulse longer than  $\lambda_p$  [18–20, 22]. As a long pulse enters a plasma, it drives a relatively weak wake because it is not matched to the optimal length derived in Eq. 2.17. The density modulation of this wake in turn modulates the pulse as shown in Fig. 2.3. Where the wake is high in density, the pulse is defocused, and conversely for low density. There is also axial transport of energy due to the varying group velocity and this too bunches the laser in regions of low density. This self-modulation process modulates the pulse at  $\omega_p$ , driving a larger wake. The feedback can lead to complete modulation of the pulse into sub pulses separated by  $\lambda_p$  and the generation of large wakes. This is experimentally important since experiments without controlled injection must operate at high density to provide low  $\gamma_p$  and hence facilitate trapping through wave-breaking. High power laser pulses matched in length to the (short) plasma period at these high densities were not available at the time of these experiments, so that self-modulation is typically used for acceleration experiments. Shorter pulses can also be self-modulated by the plasma response, and in this case the principal effects include changing of the pulshape and laser spectrum [37, 83, 85].

Analytic solutions of self-modulation have been obtained for long pulses with near-Gaussian radial profiles and  $a_0 \ll 1$ , and these indicate that modulation typically requires several  $Z_R$  to occur [20]. Solutions at high intensity with arbitrary pulse evolution, as required for the present experiments, are not available so that numerical or experimental scalings are used. Simulations (Fig. 4.9, Chapter 6) have typically indicated that the pulse self-modulates over a distance of a few hundred  $\mu\text{m}$ –one mm for parameters similar to those available for our experiments (10 TW, 50 fs, few  $10^{19} \text{ cm}^{-3}$ ). This adds to the length required for acceleration, since the wake is only driven efficiently after the pulse is modulated. Hence optimum acceleration should require 1-2 mm plasmas ( $\approx 10Z_R$  for our laser), making guiding desirable.

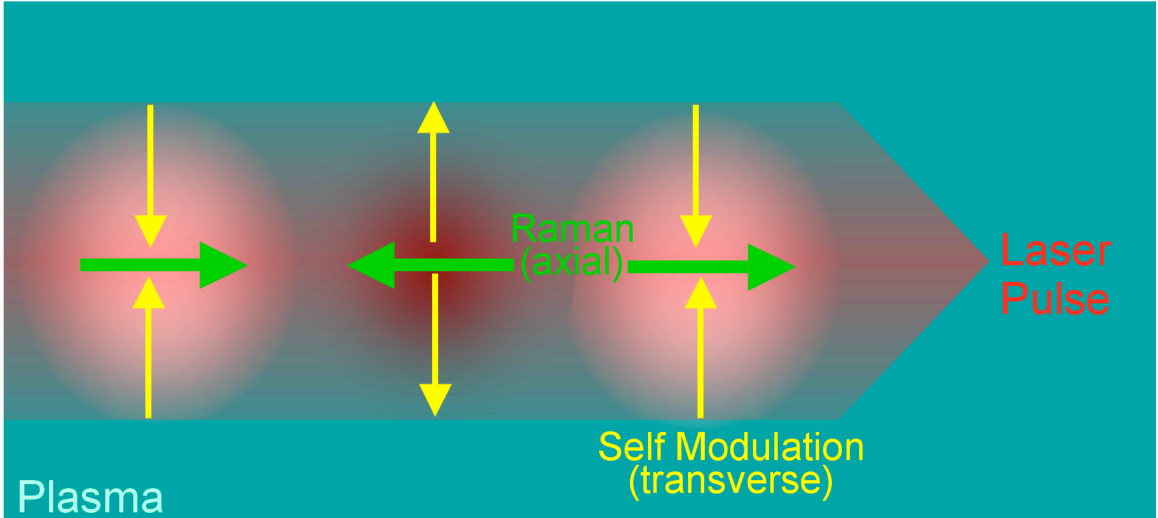


Figure 2.3. A laser pulse not matched to the plasma period drives a small wake, and this wake in turn modulates the pulse to the plasma period. The low density (light) part of the wake focuses the laser while the high density part defocuses it. This radially self-modulates the laser intensity. At the same time, the slower group velocity in the denser part of the plasma (faster in the less dense part) causes axial energy transport (forward Raman) which also modulates the pulse.

#### 2.5.4 Guiding Summary

Modulation of the laser phase fronts by the plasma makes guiding possible, and hence acceleration over long distances, while modulation of the laser envelope allows use of high densities where the laser pulse may not match the plasma period (through self-modulation).

Previous experiments have explored channel guiding for low power pulses and self-guiding for higher powers. Experiments have demonstrated guiding with preservation of the Gaussian input mode over many  $Z_R$  by plasma density channels for input pulse intensities at up to  $2 \times 10^{17}$  W/cm<sup>2</sup>, where relativistic effects are unimportant and a parabolic transverse density profile can be matched to guide the low intensity pulse [51–55, 86]. Channel guiding of high intensity pulses, where compensation for self-guiding is important, had however not been demonstrated experimentally prior to the present work.

The relativistic self-guiding effect has been observed to provide some guiding but is unstable, eventually destroying the pulse and limiting propagation distance to little more than diffraction range [22,23,87]. Because of the instability, pulses may be subject to break up (filamentation) into multiple spots [12] or steering (hosing) [3,88,89]. These limits are most severe for pulses not much longer than the plasma period, as used for most laser acceleration experiments, since relativistic self-guiding is less effective for such pulses [18]. Hence the good guided mode properties obtained in channeled experiments were not obtained using self-guiding.

In order to better control propagation at the intensities needed for acceleration, this dissertation describes experiments in which relativistically intense pulses were guided by plasma channels, and the effect of such guiding on acceleration was evaluated. Together with the derivation of the wake structure in Section 2.2, the guiding formulae of this section form a basic model of the guided wakefield accelerating structure. The performance of this structure, and the potential benefits of guiding, can now be evaluated.

## 2.6 Accelerator Scaling and Design

We now consider the accelerator performance that can be obtained from electron bunches accelerated by a wake with and without laser guiding [37]. Some fundamental limits on acceleration are evaluated. These include: depletion of the laser energy, dephasing of the particles from the structure, and acceleration length limits due to diffraction. We continue reference to the case of our 10 TW 50 fs laser, with  $Z_R \sim 200 \mu\text{m}$  to provide high enough  $a_0$  to allow self-trapping of particles at a density near  $2 \times 10^{19} \text{ cm}^{-3}$  (as indicated in Section 2.3).

The laser will deplete its energy into the wake over a distance where the energy

deposited in the wake equals the pulse energy [42, 90]. Evaluating the wake energy from the fluid result (Eq. 2.17) and expressing the fields in terms of the normalized vector potential  $a_0$ , this gives:

$$\begin{aligned}
 L_{pump} &= \frac{E_{laser}^2 c \tau_L}{E_{wake}^2} \\
 &= \frac{(\omega m c a_0 / e)^2 c \tau_L}{(\omega_p m c / e)^2 (a_0^4 / 4)} \\
 &= 2 \frac{\lambda_p^3}{a_0^2 \lambda^2}
 \end{aligned} \tag{2.44}$$

where  $c \tau_L$  is the laser pulse length,  $\omega$  the laser frequency, and  $\omega_p$  the plasma frequency. The laser pulse length is taken as the matched pulse length derived in Section 2.2,  $\approx \lambda_p$  for a sine pulse, and the average value of the envelope is 1/2 for such a pulse. For our reference case, the pump depletion length is near 500  $\mu\text{m}$ , though this (linear) result is at best approximate in this regime. For a pulse of  $c \tau_L > \lambda_p$ , as used in self-modulated experiments such as those described here, the pump depletion length will be longer, since pump depletion will only begin once the laser has self-modulated and is driving a large wake. This emphasizes the need for propagation well beyond  $Z_R \approx 200 \mu\text{m}$  in order to efficiently use the laser energy (i.e. deposit a significant fraction of it into the wake).

Since the wake travels at the group velocity of the laser,  $v_g < c$ , electrons accelerated by the wake eventually outrun it and slip into decelerating phase over a length called the dephasing length [2, 3, 37, 42]. The details of this length depend on the exact acceleration dynamics, but a useful lower limit is obtained by considering the propagation distance  $L_d$  it takes a hypothetical test particle to travel across the accelerating bucket. The slippage is just the difference in velocity times the time taken, yielding (for velocities close to  $c$  so that time  $\approx$  distance/ $c$ ):

$$\Delta v \frac{L_d}{c} = \frac{\lambda_p}{2} \tag{2.45}$$

where  $\Delta v$  is the velocity differential between the particle and the wave. For a particle

moving close to  $c$ , and using the group velocity of the laser obtained in Eq. 2.29, this becomes:

$$c\left[1 - \left(1 - \frac{\omega_p^2}{2\omega^2}\right)\right]\frac{L_d}{c} = \frac{\lambda_p}{2} \quad (2.46)$$

$$L_d = \frac{\lambda_p^3}{\lambda^2} = \frac{a^2}{2}L_{pump} \quad (2.47)$$

For our parameters, where  $a_0 \approx 1 - 2$ , the dephasing and pump depletion lengths are nearly equal. The length above is valid only for particles already injected and at an energy of several rest masses (hence velocity  $\approx c$ ). Therefore, once again, for self-modulated and self-trapped experiments where the laser must first modulate to the laser period and drive an intense enough wake to trap electrons, the required length will be longer. This indicates that acceleration of electrons over the longest possible distance also requires guiding of the drive pulse beyond  $Z_R$  for our laser parameters.

The maximum energy a particle can gain from the wakefield is on the order of the wake amplitude times the dephasing length. Evaluating the wake field from the fluid model of Section 2.2 yields the dephasing energy [3, 37, 91]:

$$E_{deph}[eV] = \frac{\pi a_0^2}{8} E_0 \frac{\lambda_p^3}{\lambda^2} \quad (2.48)$$

Recalling that  $E_0 = m\omega_p c/e$ , the maximum energy scales as the reciprocal of the density. To obtain maximum energy we then wish to operate at low densities. Low densities also require longer acceleration lengths, since the dephasing length increases with decreasing density. However, self-trapping requires high densities in order to bring the trapping threshold down, so that self-trapped experiments are necessarily a compromise. Using the lowest density which allows self-trapping will optimize beam energy if the wake can be driven over this distance (for instance using guiding to maintain the laser focus). On the other hand, if the wake length is limited to the diffraction range (no guiding), peak energy is limited to the product of the amplitude times  $Z_R$ :  $E_{unguided}[eV] = (\pi a_0^2/8)E_0 Z_R$ , which is typically much lower than the dephasing energy [3, 37, 91].

In the experiments described in this dissertation, a plasma channel was used to guide the drive beam of a self-modulated accelerator. This allowed the wake to be driven over long distance and hence allowed the dephasing and depletion conditions to be met near the lowest density that provided self-trapping, increasing particle energy. Previous experiments (Section 2.3) indicated that densities as low as  $2 \times 10^{19} \text{ cm}^{-3}$  allowed self-trapping near 10 TW. For such densities, the dephasing and depletion distances are several  $Z_R$  for the laser parameters available. Additional distance on the order of a millimeter is needed to allow self-modulation, so that guiding over  $\sim 10Z_R$  is desired to attain the dephasing length and optimize performance of self-trapped experiments using 10 TW lasers. For such a guided self-modulated accelerator, Eq. 2.47 indicates dephasing energies up to a few hundred MeV are possible. As indicated, without guiding acceleration is limited to  $\approx Z_R$ , and this results in energies of 10's of MeV, so that channeling may offer a potential improvement of several-fold over unguided experiments at the same power.

The required  $a_0 \sim 2$  could alternatively be achieved without a channel over the required  $\sim 1 - 2$  mm for optimal acceleration at these densities by using a laser with a larger spot size, but this would require a power of approximately 40 TW, a large increase in laser power and cost. As density is reduced to increase energy in future experiments, channel guiding will become increasingly beneficial due to the long dephasing lengths. The power required to obtain long distance by using a large laser spot increases as the square of the distance, and this eventually becomes prohibitive.

## 2.7 Additional Plasma Requirements

Several additional requirements for the target plasma follow from the considerations of this Chapter. We have already noted (Section 2.3) the requirements on

plasma density for self-trapping of particles. Here we consider the effect of gas outside the target region and of density fluctuation. This will set requirements on how the plasma is generated.

At the high intensities used for wakefield acceleration, the presence of gas upstream from the desired interaction region must be minimized in order to avoid ionization induced refraction of the laser pulse [92, 93], requiring the use of gas jets or similar targets to localize the target gas to the desired region. Ionization induced refraction occurs as the laser pulse approaches focus, and the center region of the pulse exceeds the intensity for ionization of the gas in which the laser propagates. This results in a plasma with highest density on the axis of propagation, which acts as a defocusing lens, preventing the pulse from focusing to the higher intensity which is required to drive the wake. For low  $Z$  gasses such as hydrogen the plasma is ionized out to many  $w_0$  near the focus of an intense pulse (ionization intensity  $\approx 10^{14}$ , pulse intensity  $\approx 10^{19}$  for these experiments) so that ionization refraction is negligible there. Away from focus however, intensity drops and ionization refraction is problematic. High  $Z$  gasses have ionization stages at high intensities that would produce ionization refraction even at focus. For efficient interaction then, a low  $Z$  (hydrogen or helium) plasma must then be used which rises from near zero density to the desired interaction density over less than  $\approx 2Z_R$ , where  $Z_R$  is the diffraction range over which the laser pulse remains focused (Eq. 2.21).

The plasma should be maintained at a fixed density over a region long enough for acceleration to occur, this length ideally being matched to the dephasing length for production of high electron beam energy and quality [37, 45](Section 2.6). For the conditions used, this indicated plasma lengths of 600-2000  $\mu\text{m}$ , according to the simulations in Chapters 6, 8 and ref. [3]. The tolerance to density non-uniformity is given by the phase condition on the plasma wake. Changing density alters the wavelength of the plasma wake, which can dephase the electrons and hence spoil

acceleration. In order to keep such dephasing at less than 10 degrees of wake phase for an electron traveling in the first wake bucket, we require that  $\lambda_p$  not vary by more than 10 parts in 360. Since  $\lambda_p \propto 1/\sqrt{n}$ , density must be maintained within  $\pm 5\%$  tolerance, or within 10% of the maximum value. Note that the requirement is more severe for bunches in trailing buckets.

These considerations illustrate that, in addition to a specific plasma density, the plasma must be localized, of a selected length, and uniform in density. This requires localization and uniformity of the gas from which the plasma is ionized, for instance using a gas jet orthogonal to the laser beam. Such targets were developed for the experiments and are described in Appendix B.

## 2.8 Summary

The models presented in this Chapter for wake generation, particle trapping, and laser propagation, together with previous experiments, established the desired regime of operation for a channel guided accelerator operating with self-trapped electrons and a 10 TW driver. Self-trapping necessitates high intensity and high plasma density so that the wake has high enough field to trap background plasma electrons. This indicated density near  $2 \times 10^{19} \text{ cm}^{-3}$  and  $a_0 \sim 2$ . In turn, for the 10 TW laser available,  $a_0 \sim 2$  indicated  $Z_R \sim 200 \mu\text{m}$ . This is much shorter than the dephasing or depletion conditions which govern the optimum acceleration length, so that guiding of the laser pulse to maintain its intensity over many  $Z_R$  could potentially increase electron beam energy several fold. Calculations and previous experiments at low intensities indicated that a suitably shaped plasma channel can guide a laser pulse, but compensation for relativistic effects is required for the high intensity pulses used in these experiments.

For future experiments, controlled optical injection techniques [44, 47–50] have also been proposed in order to circumvent the compromise in density necessitated by self-trapping, and to allow placement of electrons at controlled phase in the wake. These techniques place electrons in the wake by giving them an initial kick to match the wake phase velocity, allowing lower densities and higher energies in the future. Because of the low densities and hence long dephasing lengths used, such techniques require a long scale accelerating structure without self-trapping to accelerate the injected electrons, and have not been fully demonstrated experimentally in part due to lack of such a structure. By allowing controlled propagation of the drive pulse at an amplitude or plasma density below the self-trapping threshold, channeling will also enable such experiments in the future.

We now turn to the experimental design and to the experiments and simulations on guiding of relativistically intense laser pulses, and the effect of guiding on acceleration of self-trapped electrons.

# Chapter 3

## Experimental Arrangement

The calculations and recent experiments described in Chapter 2 indicated a parameter regime where the physics of channel guided self-modulated laser wakefield accelerators with self-trapped electron bunches could be explored using the facilities of the 10 TW L'OASIS laser at LBNL [91,94]. Guiding over  $10Z_R \sim 2$  mm in plasmas near  $2 \times 10^{19} \text{ cm}^{-3}$  at  $a_0 \sim 2$  (therefore spot size  $w_0 \sim 7 \mu\text{m}$ , or  $8.5 \mu\text{m}$  full width half max (FWHM)) was required. This Chapter describes the configuration of the laser, and the construction of diagnostics and supporting systems, for such experiments.

The 10 TW L'OASIS laser [91,94] features a single master oscillator driving several amplifiers to deliver four or more pulses at up to 10 Hz with intrinsic synchronization. Chirped pulse amplification [95] in a Ti:Sapphire medium is used to provide pulses as short as 45 fs, as measured by an autocorrelator and checked using a Frequency Resolved Optical Gating (FROG) system [96]. In chirped pulse systems, the fs pulse from a mode-locked oscillator is stretched by a grating pair; different colors in the pulse take different paths off the grating resulting in dispersion and stretching the pulse to  $\approx 250\text{ps}$ . The pulse is then amplified while stretched to high energy in an optically pumped Ti:Sapphire crystal, and re-compressed by a second grating pair.

Amplifying the pulse while stretched allows high energies, while avoiding undesirable non-linear effects in the crystal that occur at high powers. The architecture of the L'OASIS system features a common front end where the pulses from the oscillator are amplified to 1 mJ by a regenerative amplifier, then to 30 mJ by a 3 pass pre-amplifier. The beam is then split and sent to two final amplifiers. At the inception of the experiments described in this dissertation, a single 10 TW (0.5 J, 50 fs after compression) pulse from the main amplifier was available in a target chamber allowing experiments on self-modulated laser wakefield acceleration without channeling or injection [97]. The beams from a secondary amplifier- 150 and 250 mJ respectively before compression- and a 1/2 mJ probe beam split from the regenerative amplifier, had been used for initial experiments on laser guiding [52] in a smaller target chamber which was not radiation shielded. Compression incurs an approximately 50% energy loss due to the transmission of the gratings. Hence in addition to the 10 TW beam already on target, additional beams were available with 150(75) mJ, 250(125) mJ, and 1/2(1/4) mJ of uncompressed (compressed) energy.

The laser system was re-configured to bring all beams to the radiation shielded experimental area, allowing experiments on plasma channel guided wakefield acceleration. Section 3.1 reviews calculations which indicated how the additional beams could be used both to form a plasma channel and for controlled injection experiments. Section 3.2 describes the laser modifications and new vacuum chambers, transport optics, and compressors that were built to bring the beams to target with the appropriate focus, astigmatism compensation, and repetition rate. Part of the first (75 mJ compressed) beam from the secondary amplifier was used to form the plasma, and was called the ignitor. The second beam (up to 250 mJ uncompressed) was used to heat the plasma and referred to as the heater beam. The 10TW (500 mJ compressed) beam was retained as the beam which drove the plasma wake.

Diagnostics were built to analyze guiding of the laser pulse and the resulting

accelerated electron bunches (Section 3.3). These included a plasma interferometer, laser mode imagers, and modifications to the magnetic electron spectrometer. Other diagnostics used are also described.

Supporting experimental developments are described in the Appendix. A control system was developed to provide automated control and data acquisition for the experiments, which must be operated remotely due to radiation hazards, as described in Appendix A. Gas targets were developed to provide the plasma required, and these are described in Appendix B.

### 3.1 Channel Formation

A variation of the ignitor-heater method [52], using hydrodynamic shock to shape the plasma [51], was used to produce plasma channels to guide the drive laser pulse. The plasma channel was formed in a supersonic hydrogen gas jet (Appendix B) by two pulses fired before the drive pulse; a short intense ignitor pulse was used to efficiently ionize a long thin plasma column, and a longer heater pulse provided efficient heating. The resulting hot plasma filament on axis expanded outward at the sound speed,  $c_s \approx \sqrt{T_e/M}$  where  $T_e$  is the electron temperature and  $M$  the ion mass [11], driving a shock wave in the cold surrounding gas. This shock resulted in a density depletion on axis and a nearly parabolic transverse density profile [51, 52, 98, 99] which was tuned by adjusting the timing and energies of the beams. Here, calculations are presented which indicated the required beam energies and configurations.

To optimize performance with the available gas jets, and to provide compatibility with other accelerator components, an ignitor pulse colinear with the wake drive pulse was used [45]. Previous experiments [52] had both ignitor and heater orthogonal to the drive beam and to one another. With the ignitor and heater at 90 degrees to one

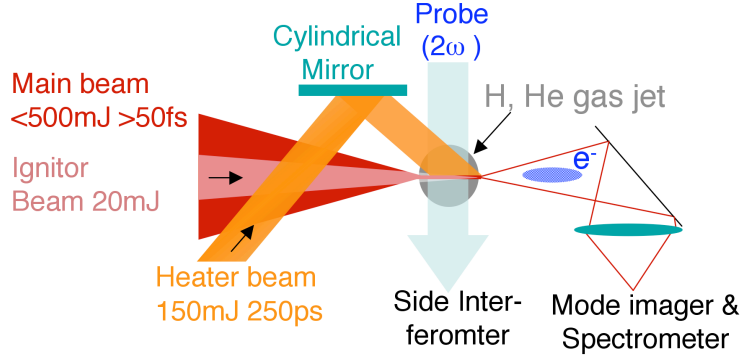


Figure 3.1. Channels were formed by a colinear ignitor-heater method using hydrodynamic shock. A cylindrical filament of plasma was ionized in the neutral gas plume from a jet by an ignitor beam copropagating with the drive beam. This plasma was then heated by a heater beam for 250 ps. The hot plasma expanded into the surrounding neutral gas, creating a shock wave and a density depletion on axis. This density depletion, or channel, guided the drive laser pulse. The plasma channel was analyzed by interferometry, and the transmitted laser light by a mode imager and optical spectrometer.

another, allowing for the beam  $f$ /numbers leaves a clear angle of  $\sim 45 - 60^\circ$  available. This requires the gas jet be placed approximately a jet diameter from the interaction region in order to clear the beams. For jets such as those used for these experiments, this distance is  $\sim 2$  cm. This makes it difficult to obtain the desired constant plasma density (Section 2.1) due to spreading of the gas plume, as described in Appendix B. As a result, constant plasma density along the axis of propagation was not obtained with this arrangement [52]. The crossing beams also consumed space in the target area. In the present experiments, the ignitor beam was therefore colinear with the wake drive beam, while the heater was incident from the side as shown in Fig. 3.1. This arrangement keeps all the beams in one plane, and the gas jet can then be much closer ( $\sim 1$  mm, governed by beam  $f$ /number as described in Appendix B) to the interaction region, allowing the jets described in Appendix B to produce flat density profiles.

### 3.1.1 Plasma Ionization

Plasma formation was calculated using both barrier suppression ionization and the Keldysh model for tunneling ionization [51, 52, 93, 98, 100–103]. The ionization mechanism can be understood as a modification of the Coulomb potential of the atom by the laser field:  $V(x) = -Ze/|x| - E_x x$  where the first term is the ordinary Coulomb potential and the second is the modification due to an external field in the x direction. As a result, the potential is increased on one side and decreased on the other. Sufficiently strong external field can bring the maximum potential on the low side below the binding energy of an electron, resulting in barrier suppression ionization. The required field to meet this condition can be calculated using this condition and is:  $E = U_i^2/(4eZ)$ , and the corresponding laser intensity is  $I = 4 \times 10^9(U_i^4[eV]/Z^2)$ , where  $U_i$  is the ionization potential and  $Z$  the charge state. The important intensities are  $1.4 \times 10^{14}$  W/cm<sup>2</sup> for hydrogen, or 1 and  $9 \times 10^{15}$  W/cm<sup>2</sup> for the first and second electron in helium. For intensities less than the barrier suppression value, ionization can be described by a model of tunneling through the potential barrier, as done by Keldysh [101].

The beam requirements to obtain the desired plasma,  $\approx 2$  mm long at a few  $10^{19}$  cm<sup>-3</sup>, were obtained analytically and with numerical modeling. To produce a uniform plasma, we want the waist size of the ionizing beam to remain roughly constant over this length, hence requiring  $2Z_R \gtrsim 2$  mm, or  $w_0 \gtrsim 15$   $\mu$ m from the expression for  $Z_R$  (Eq.2.21). For a perfect Gaussian beam, this indicates a beam of f/25, measured at the  $1/e^2$  intensity contour. In practice, an iris was used to restrict the f/number of the beam, and the resulting beam was not Gaussian. Focusing at f/15, measured at the diameter of the hard aperture, hence provided the desired spot diameter and  $Z_R$ . Ionization induced diffraction [92, 93], where partial ionization creates a plasma of highest density on the axis of propagation where laser intensity is high, tends

to defocus the pulse. To minimize this effect, the intensity of the beam should be above the ionization intensity out to  $\gtrsim 1.9w_0$ , where  $I/I_0 \approx 10^{-3}$ . Hence  $I_0 \approx 10^{17}$  W/cm<sup>2</sup> is appropriate for hydrogen, and the resulting plasma will be about 60  $\mu$ m in diameter. Hydrogen was used in these experiments since it has the lowest intensity for full ionization, allowing use of the lowest intensity laser pulses. The energy in the pulse should be much greater than the ionization energy of the atoms in the ionized volume to prevent depletion effects. For a hydrogen plasma  $60 \times 60 \times 2000$   $\mu$ m in dimension at a density of  $2 \times 10^{19}$  cm<sup>-3</sup>, this indicates a pulse energy well above 0.3 mJ. The shortest pulses available from our compressors are 40-60 fs long, and a pulse at the required intensity and waist size hence has an energy of 15 mJ, which easily satisfies this condition.

A more complete model of the plasma shape was obtained by characterizing the laser as a Gaussian spatial and temporal envelope, and applying the barrier suppression and tunneling ionization models. For barrier suppression ionization, the plasma is ionized completely to a given ionization state if the intensity at any time exceeds the ionization intensity. Due to the variation of the spot size with propagation distance (Eq. 2.21), the peak intensity as a function of spatial coordinates can be written:

$$I(r, z) = I_0 \frac{w_0^2}{w_z^2} \exp(-2r^2/w_z^2) \quad (3.1)$$

with  $w_z$  given by Eq. 2.21 and  $I_0$  the peak intensity at focus. The plasma profile is then the contour of intensity = ionization intensity. For tunneling, the laser pulse was propagated numerically according to Gaussian vacuum diffraction (Section 2.4) through a initially neutral gas. The pulse was advanced a small fraction of a pulse-length (typically 1/10th) per time step providing good resolution, and the transverse grid was similarly selected to resolve the laser spot size with at least 10 grid points. At each time step the Keldysh ionization model was applied, with the probability of

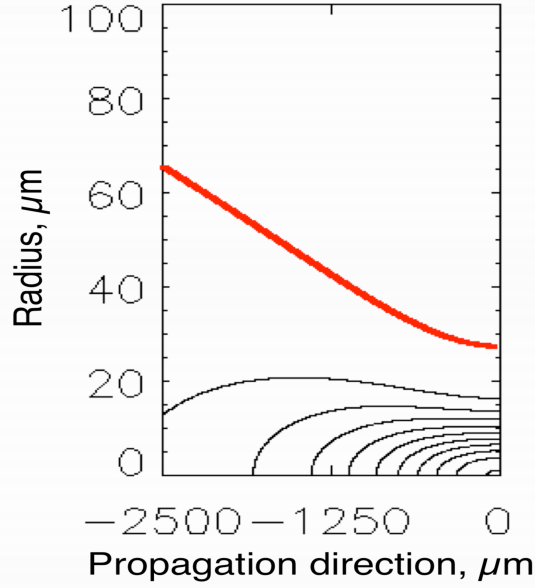


Figure 3.2. Iso-intensity contours for a Gaussian laser pulse with  $I_0 = 1e17$ ,  $w_0 = 15$   $\mu\text{m}$ . The thick contour (red) represents the barrier suppression intensity for hydrogen. Only the upper left quadrant is shown due to symmetry.

ionization given by:

$$W(|E|) = 4\left(\frac{3}{\pi}\right)^{1/2}\Omega_0 U_i^{7/4} \left(\frac{E_H}{E}\right)^{1/2} \exp\left(-\frac{2}{3}U_i^{3/2}\frac{E_H}{E}\right) \quad (3.2)$$

Here  $E$  is the electric field,  $E_H = 5.2$  GV/cm is the atomic field of Hydrogen,  $U_i$  is the ionization potential divided by the Hydrogen ionization potential (13.4 eV), and  $\Omega_0 = 4.1 \times 10^{16} \text{s}^{-1}$  the characteristic atomic frequency [22, 93, 100–103]. Depletion of laser pulse energy was neglected in both models since the calculation above indicated it was not significant.

The plasma density produced by a 15  $\mu\text{m}$  laser spot with  $I_0 = 1 \times 10^{17}$  is shown in Fig. 3.2. In practice, use of tunneling ionization made little difference to the calculation since peak intensities were far above barrier suppression. For a plasma 2 mm long with symmetry about the origin,  $r_{\text{plasma}} = 32 \pm 5$   $\mu\text{m}$ . Based on these calculations, ionization of the required plasma using a 15 mJ, 60 fs pulse focused at  $f/15$  -  $f/25$  was feasible. With up to 75 mJ from the compressed ignitor beam, ample flexibility was

available to tune f/number and energy to optimize the plasma, making the coaxial method reasonable. Un-needed energy can be diverted for other experiments. Ionization induced diffraction (above) was neglected in these calculations, but should be mild for the intensities selected. By appropriately tuning intensity, this effect may be used to counteract convergence of the beam, hence making the profile more uniform. Experimental optimization confirmed the smoothing effect of ionization refraction, and demonstrated production of acceptable plasmas (Chapter 4).

### 3.1.2 Plasma Heating and Channel Expansion

The requirements for plasma heating were set by calculations and by previous experiments which indicated that expansion to approximately 1.5 times the initial plasma radius would be necessary in order to obtain the desired plasma density profile. A simple model explains this: imagine that the initial plasma has a flat top density profile, and a temperature sufficient to fully ionize neutral gas it encounters as it expands. Assume this plasma expands uniformly outward at the sound speed, maintaining its flat top shape. Neglecting flow of the newly ionized gas, this results to first order in a stair step profile as illustrated in Fig. 3.3. After expansion to 1.5 times initial radius, the initially ionized region has a density  $n = n_0 * A/A_0 = 0.45n_0$  where  $n$  is the density,  $A$  is the area, and the subscript  $_0$  indicates initial conditions. The density has decreased due to expansion. The density in the region outside the initial ionization volume is  $0.45n_0 + n_0 = 1.45n_0$ , the sum of the expanded plasma and newly ionized gas. Choosing the center density of the channel to be  $2 \times 10^{19} \text{cm}^{-3}$  the density rise (which is equal to the initial density) is hence  $n_0 \approx 4 \times 10^{19} \text{cm}^{-3}$ , over the initial plasma radius  $\approx 35 \mu\text{m}$  taken from the ionization calculation of Section 3.1.1. This is the matched rise for a parabolic channel to guide a spot of  $w_0 \approx 7 - 8 \mu\text{m}$  (Section 2.4), as desired to obtain  $a_0 \approx 2$  for wave-breaking with a 10 TW laser in

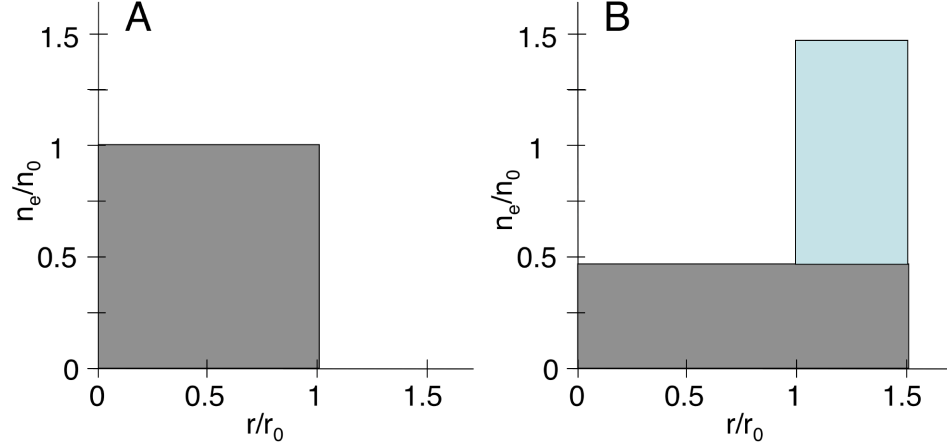


Figure 3.3. A simple model of plasma expansion. A plasma (dark grey), initially ionized with radius  $r_0$  (A), expands outward(B), ionizing additional gas (light blue). As a result, the density at the outside, where the new plasma is ionized, is higher than at the center. Neglecting flow of the newly ionized gas and modeling the expansion as a uniform flat top, the zero'th order expansion required to obtain the matched rise in density to guide a laser pulse can be estimated. For an initial plasma  $32 \mu\text{m}$  in radius at  $4 \times 10^{19}$ , expansion to  $r = 1.5r_0$  is required to guide an  $8 \mu\text{m}$  laser spot at  $0.8 \mu\text{m}$  wavelength. This is confirmed by more detailed simulations and by experiments.

a plasma of this density (Section 2.3). In the real plasma, flow does exist and the profile will be smooth so that this is only an approximation. Both fluid calculations and previous experiments confirmed the basic scaling indicated however, and showed that near parabolic guides are formed [51, 52, 98].

The expansion ratio of 1.5 requires that the initial plasma temperature be at least 20 - 30 eV, so that the plasma will have sufficient energy to ionize the neutral gas it expands into, given the 13 eV ionization potential of hydrogen. Laser heating was accomplished via inverse Bremsstrahlung, in which the electrons oscillating in the laser field undergo collisions with ions, transferring part of their oscillation energy into thermal energy [51, 52, 98, 104, 105]. As a result of these collisions, when the laser turns off, the electrons are left with a non-zero temperature. This heating can be expressed as:

$$\frac{3}{2}K_B \frac{\partial T}{\partial t} = \frac{1}{2}\nu_{ei} \frac{mv_{os}^2}{2} \quad (3.3)$$

where  $T$  is the temperature of the electrons. The term  $mv_{os}^2/2$  is the kinetic energy of an electron oscillating with a quiver velocity  $v_{os} = ca_0$  in the laser field, and  $\nu_{ei}$  is the electron-ion collision rate. The factor of  $1/2$  at right is due to averaging the oscillation velocity over the laser period. Note that electron-electron collisions do not contribute since the Debye length  $\lambda_d = \sqrt{T_e/(4\pi ne^2)} \approx 740\sqrt{T_e[eV]/n[cm^{-3}]}$  [cm]  $\approx 5 - 10$  nm [11] is much shorter than the wavelength of the laser. Since the plasma shields out the field for lengths longer than  $\lambda_d$ , this means that the electric field is invariant over the collision length. Hence, electrons colliding with one another are at the same oscillation velocity so that oscillation velocity is not transferred to thermal velocity by electron-electron collisions [105]. When  $v_{os} < v_t$ , the thermal velocity in the plasma, the electron-ion collision rate is well described by the thermal collision rate:

$$\nu_{ei} = \frac{8\pi nZe^4 \ln(\Lambda)}{6.4m^2v_t^2} \approx \frac{Z \ln(\Lambda)}{13\Lambda} \omega_p \quad (3.4)$$

where  $\Lambda = n\lambda_d^3$  is the plasma parameter and  $n$  the density. Because the collision frequency decreases with increasing velocity, the collision rate falls off for  $v_{os} > v_t$ , so that low intensity laser pulses are most efficient for heating. For hydrogen plasmas near  $2 \times 10^{19} \text{ cm}^{-3}$  and 10 eV, as used in these experiments,  $\lambda_d \sim 5 \times 10^{-7} \text{ cm}$  and  $\Lambda \sim 3$  while  $\omega_p \sim 2.5 \times 10^{14}$ . Intensities below  $5 \times 10^{13} \text{ W/cm}^2$  are most efficient at these temperatures. Using the collision rate Eq. 3.4 indicates heating at a rate of  $\partial E/\partial t \sim (1/2)(\omega_p/40)(mv_{os}^2/2) \sim 1.51 \times 10^{12} mc^2 a_0 \sim 0.4I[W/cm^2] \text{ eV/s}$  for these parameters, so that a pulse length near 0.5 ps is required to heat by 10 eV at  $5 \times 10^{13} \text{ W/cm}^2$ . Because heating is linear for low intensities, a longer pulse at lower intensity but containing the same energy will work equally well, provided it is short compared to the expansion time  $\sim r_0/c_s \sim 1 \text{ ns}$ . Assuming the pulse covers the initial plasma specified above, 2 mm by 60  $\mu\text{m}$ , a laser energy of 30 mJ is required. Note that the plasma will be heated isotropically since the laser coupling efficiency to the plasma is  $\sim 1\%$ , so that absorption is not a concern. The heating rate goes down linearly with

decreasing density, so that heating of low density plasmas requires more energy. With up to 250 mJ available in the 250 ps uncompressed arm of the laser for heating, these calculations indicated that there was ample ability to heat the required plasmas, with room for experimental optimization by changing the heater intensity and energy.

## 3.2 Laser and Optical Configuration

The calculations in Section 3.1 indicated that the available beams from the secondary amplifier were sufficient to form the required plasma channel using the co-axial ignitor heater method. The 10 TW beam used in unchanneled experiments was retained as the wake drive beam [28]. The laser, transport system, and target chamber were then modified from those of Ref. [28,52] to accommodate channeled acceleration and injection experiments.

Transport and compression optics and a new target chamber with optics were built, and modifications to the secondary amplifier were carried out in order to bring its beams to the target area used by the 10 TW beam. A new vacuum beam pipe from the laser bay allowed routing of the extra beams, and the drive beam was re-routed to facilitate co-axial combination with the ignitor. Because the full energy of the 75 mJ compressed beam from the secondary amplifier was not needed to pre-ionize the plasma, this beam was split and two independent compressors were built to provide each beam with independent control. The first, made coaxial with the main beam using a polarizing beam combiner, provided the ignitor beam to pre-ionize the plasma. The second was routed to nearly counter-propagate with the drive beam, allowing for injection [44, 49] and scattering experiments in the future. The second, 250 mJ uncompressed, beam from the secondary amplifier was used as the plasma heating beam. The general layout of the target chamber and compressor optics are shown in Fig. 3.4. Delay lines were built to bring the beams to target at the same time.

The secondary amplifier mode was adjusted using internal and external telescopes to provide improved mode quality over the longer propagation distance to the new target chamber.

Each of the three pulse compressors was fitted with a delay stage allowing independent remote adjustment of beam timing with 5 fs precision over a 500 ps range. Additional adjustments were possible using secondary stages in the laser bay, which are also remote adjustable. Combined, this allowed adjustment of relative beam timing by as much as 1 ns without manual intervention. This timing adjustment was used to optimize channel formation and injection, and to adjust the interferometer probe beam that was used to characterize the plasma evolution (Section 3.3).

Astigmatism in the focal spot of the ignitor was compensated using a telescope mounted before the compressor in the ignitor line. Since the ignitor and drive pulses were coaxial, they were focused onto the target by the same off axis parabolic mirror. Differences in propagation line and amplifier crystal meant that the beams had different amounts of astigmatism, and because of the common parabola, this optic could not be used to remove the difference. Telescopes were used to expand the beam before compression at the final gratings in order to avoid damage associated with high fluence. While reflective telescopes were used for the high power drive beam, a refractive system was adequate to handle the power of the ignitor beam. The refractive telescope provided straightforward adjustment of astigmatism by rotating one of the lenses [106]. Rotation means that a ray in the plane of rotation a distance  $d$  from the center of the beam is a distance  $h = d/\cos(\theta)$  from the center of the lens, where  $\theta$  is the angle of rotation. This shortens the focal length  $f_t$  in the plane of rotation, and lengthens it in the orthogonal plane ( $f_s$ ). For small angles, the focal lengths in the two planes are approximately  $f_t \sim f\cos(\theta)$  and  $f_s \sim f/\cos(\theta)$  where  $f$  the initial focal length, while for larger angles the correction due to bending of light at the glass-air boundary must be included [106]. The difference between the focal lengths for the two

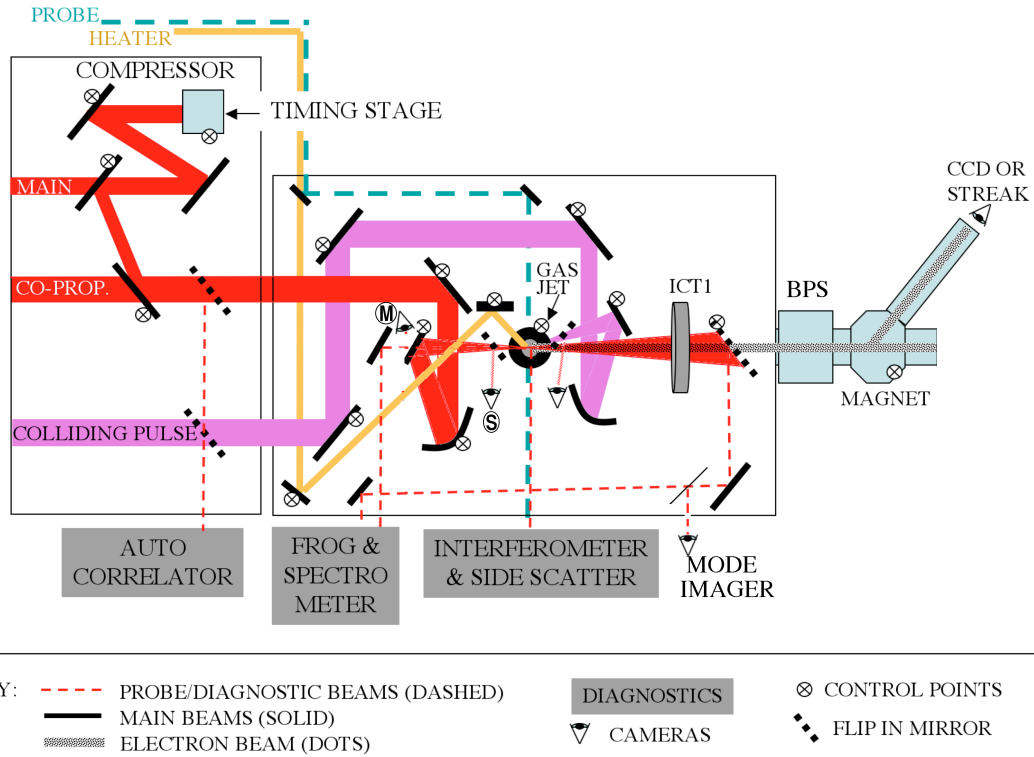


Figure 3.4. Experimental arrangement of the target chamber (center) and one compressor chamber, showing the major beams, optics, and detectors. To form a channel to guide the main beam, the gas from a jet (center) is pre-ionized by the ignitor beam copropagating with the main beam (both red) and heated by the heater beam (orange). A near counterpropagating beam is provided for injection experiments (purple). Diagnostics are detailed in Section 3.3. Major diagnostics include a plasma interferometer using a frequency doubled beam (blue) and an autocorrelator to measure laser pulse length. The incident laser spot is measured by high resolution spot cameras (S) at low power and an online monitor camera (M) at high power. A mode imager and spectrometer characterize transmitted radiation. The electron beam is characterized using an integrating charge transformer, phosphor screen (BPS), and a magnetic spectrometer. Radiation detectors are distributed around the area. Nuclear activation targets and THz detectors are not shown.

axes allowed introduction of astigmatism to cancel that in the beam. Beam pointing was minimally affected by this rotation, and was compensated using the mirror just after the telescope. Use of a separate telescope also allowed the ignitor to be expanded to a different diameter than the drive beam, yielding the desired f/number (above). An iris after the telescope was used to set the final f/number.

The plasma heating beam was incident from the side, focused from an f/1.5 cylindrical mirror in the vertical direction and partially focused in the horizontal direction by a pair of fused silica cylindrical lenses located before the cylindrical mirror. The lenses allowed the axial length of the heater line focus produced by the cylindrical mirror to be adjusted. For these experiments, the beam formed a line focus approximately 8 mm long. The heater beam was typically tuned to produce 150 mJ (less than the 250 mJ maximum output), and hence from the geometry, approximately 50 mJ of this energy overlapped the  $\approx 2.4$  mm gas jet, consistent with the calculated energy requirements above. The focused vertical spot size of the heater was much smaller than the ignitor plasma ( $\sim 2 \mu\text{m}$  from the f/number), and the beam was defocused to cover the whole plasma. Focusing the beam tightly resulted in heating of a sub volume, and a distorted channel.

A shutter was installed at the input of the main amplifier to regulate the firing rate of the laser and hence avoid distortion of the laser spot. Measurements of the laser spot during shots at full system energy using the spot monitor camera (Section 3.3.2) showed that the laser spot distorted over a period of a few minutes of operation at 10 Hz. This may be due to heating of the gratings, which absorb a substantial fraction of the laser energy. Reducing firing rate below  $\approx 3$  Hz maintained reproducible input spots and substantially improved accelerator performance. The yield of electrons above 13 MeV produced by the single beam (unguided) accelerator was measured using  $\gamma$ -n reactions (Section 3.3.3), and using the shutter increased yield three-fold. This indicates the importance of the laser mode shape and intensity.

Diagnostic	Observable	Parameter
<b>Optical Diagnostics</b>		
$2\omega$ transverse interferometer	Phase shift of probe beam Ionization outside channel	Plasma profile Confinement of laser to channel
Transmitted light spectrometer	Blue shifting of laser Red shifting of laser	Confinement of laser to channel Depletion of laser to plasma waves
Mode imager CCD	Laser mode image	Mode change with propagation
<b>Electron Diagnostics</b>		
Integrating current transformer	Induced current	Bunch charge
Beam phosphor (BPS)	e-beam spatial profile	Divergence, ballistic emittance
Electron spectrometer $55^0$	e-beam momentum distribution	Structure in distribution
Electron spectrometer $5^0$	Electrons above given energy	High energy electrons
<b>Laser Diagnostics</b>		
Spot camera	Laser focal mode at low power	Intensity, alignment, astigmatism
Spot monitor	Laser focal mode at full power	Change in focal mode over time
Autocorrelator	Self-correlation in time of laser	Laser pulselength, power
FROG	Frequency/time resolved spectrum	Laser pulse shape

Table 3.1. Summary of major diagnostics and physical observables.

### 3.3 Diagnostics

The target plasma, guiding of the optical beam, and the resultant accelerated electron bunches were characterized by an array of diagnostics (table 3.1). The plasma shape and size indicated both channel density profile and the extent of laser diffraction. Cameras monitored the input laser spots both for alignment and on target shots. The guided laser spot and spectrum of the pulse were also characterized. These optical measurements indicated the effectiveness of the channel in maintaining the focus of the drive pulse through the plasma and, in the case of the spectrum, also its coupling to plasma waves. The electron beam charge, spatial profile, and spectrum were measured, indicating the effectiveness of the drive pulse in driving the plasma wave and accelerating particles.

#### 3.3.1 Plasma Interferometer

A ‘folded wave’ interferometer [107] was used to characterize the plasma, and to measure its temporal evolution with fs resolution (Fig. 3.5). The compact folded wave design allows operation using a single beam passed through the target chamber. The beam is split, one arm is inverted spatially by a roof mirror, and the two are

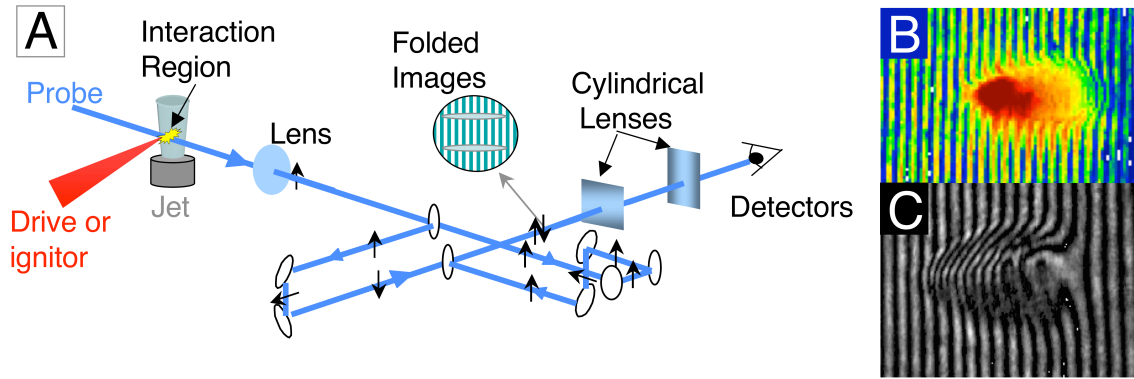


Figure 3.5. A folded wave interferometer was used to measure the plasma density profile on system shots (A). The beam was split and one arm was inverted, allowing the plasma image to be interfered with the (relatively unperturbed) area of the beam which did not pass through plasma. Cylindrical lenses provided higher resolution in the vertical plane for imaging of long narrow plasma channels. The probe beam was frequency doubled to 405 nm to reduce stray light. An image from this diagnostic (C) shows better resolution and less contamination from scattered light than the previous configuration using cylindrical optics and a 810 nm beam (B).

recombined to interfere. The result is interference of the top of one arm with the bottom of the other. The pointing was arranged so that the plasma is, for instance, near the top of the beam and the bottom of the beam passes through free space or gas. Each arm then provides the reference for the other, and the phase shift due to the plasma refractive index derived above is measured.

The interferometer imaging and probe beam were selected to provide the best possible imaging of the channels. The interferometer used either an 810 nm pulse split from the drive beam, or a 405 nm pulse frequency doubled from the 1/4 mJ compressed probe pulse diverted from the output of the first (regenerative) amplifier. Operation at 405 nm dramatically reduced contamination of the data by side-scatter from the plasma, allowing the plasma to be seen on full energy laser shots. Preserving the 810 nm option provides high phase sensitivity for lower density experiments in the future, where there should be less side scatter, but was not used for the present experiments. To provide high resolution viewing of the long narrow plasma channels

an imaging system using aspherical and cylindrical optics was constructed. The plasma is imaged to a primary focus near the beam combiner by an f/7 achromat. Cylindrical optics were then used to image this onto a Photometrics CCD providing a resolution of  $17\ \mu\text{m}$  in the horizontal plane and  $4\ \mu\text{m}$  in the vertical. This is well suited to the experimental channels, which were  $\approx 2000 \times 200\ \mu\text{m}$  in size. Resolution was optimized by ray tracing the system for various lens locations and focal lengths. The configuration was chosen to minimize the clipping due to the mirrors and optics in order to maximize the effective f/number and hence provide optimal resolution. These optimizations were important in order to obtain accurate recovery of plasma density, as insufficient transverse resolution leads to increased error in the Abel transform. A second, wide field, CCD using a spherical lens provided a view of the plasma and jet, and was used for alignment.

The plasma density was recovered from the interferogram using a phase recovery routine written for the purpose (Appendix B.3) which allowed automatic analysis of multiple interferograms, returning average density as well as RMS fluctuations. Use of Abel inversion then determined the density from the phase shift [108, 109], assuming cylindrical symmetry of the plasma. Symmetry was confirmed by observing the structure of the guided laser mode (Chapter 4, below); a round input mode will remain round in cylindrically symmetric plasma, but will become elliptical in an asymmetric plasma due to asymmetric plasma focusing. The density profile of the plasma could then be tuned with immediate feedback, allowing adjustment of the formation beams to optimize the profile. The plasma size after the propagation of the drive pulse also showed the radial extent of ionization, which indicated the extent of diffraction of the laser as it propagated through the plasma. This gave an indication of how well collimated the pulse was over the plasma length.

### 3.3.2 Laser Mode and Spectrum

The laser mode and spectrum were characterized both in vacuum and during plasma interactions by three cameras and an optical spectrometer. These provided alignment as well as characterization of the guided mode and spectrum.

The ignitor and drive beams were aligned and monitored using two spot cameras, as pictured in Fig. 3.4. The high resolution spot camera used a mirror flipped in just before the beam focus to divert the beam to a microscope objective and CCD with 1  $\mu\text{m}$  resolution. To use this camera, the beam was attenuated by a flip-in attenuator upstream. This attenuator was inserted at a point where the beam is collimated, and is also at close to zero degrees angle of incidence, to avoid inducing astigmatism. Online monitoring of the spot was provided by a ‘spot monitor’ camera which looked through the final turning mirror before the target. Because the beam is incident on this mirror off normal incidence, the transmitted beam passes through the mirror glass off axis, causing astigmatism. This astigmatism was balanced by placing a ‘compensator’ plate just behind the mirror, tilted in the opposite plane. Compensation was imperfect, but sufficient to allow online monitoring of the positions of the beams, and to determine whether the mode shape changed over time. It was this monitoring which indicated the distortion of the spot over time at high power, and motivated the installation of the rep rate shutter described in the previous Section.

In order to characterize the effectiveness of the guide in maintaining the laser mode, a mirror was inserted into the beamline and an f/10 achromatic lens imaged the mode directly onto a CCD (mode imager) camera. The lens could be translated to image the entry or exit of the channel. Because of mounting constraints on its f/number, the mode imager resolution was slightly larger than the focused spot size of the laser, so that only a lower limit on guided intensity is obtained directly from the image intensity. To overcome this problem, the resolution and imaging properties

of this system were characterized using known laser spots which were independently measured with a high resolution camera, and also with backlit USAF resolution targets [110]. The imaging properties were consistent with diffraction for a circular aperture at  $f/10$  [24]. This allowed deconvolution of spot sizes for laser modes that are near the resolving power of the lens. To do this, the known diffraction delta function response was deconvolved from the measured spot, yielding the spot at the guide. For electron beam measurements, the mode imager mirror was removed to minimize scattering of the electron beam by the mirror. Guiding of the laser pulse was then monitored using the interferometer. For experiments correlating electron production to mode image quality, the mirror inserted into the beamline was replaced by a  $10\ \mu\text{m}$  thick nitrocellulose pellicle coated with silver. This pellicle had insignificant attenuation for the electron beam. By mounting it in a stress free holder, optical quality was acceptable, though somewhat worse than the solid mirror.

Simultaneous analysis of the transmitted laser spectrum was obtained by diverting part of the light sent towards the mode imager to an optical spectrometer using a beam splitter. As discussed below, red or blue shifting of the laser pulse can yield information about the interaction of the pulse with plasma waves or ionizing media.

### 3.3.3 Electron Diagnostics

The accelerated electron bunch was characterized using two commercial integrating current transformers (ICTs) to measure charge, a beam phosphor screen (BPS) for spatial profile, and an electron spectrometer for energy distribution. The electron spectrometer could be configured to observe two different bend angles. The first provided high resolution, while the second allowed detection of electrons up to higher energies.

The ICTs measured the total bunch charge within an  $f/8$  (110 mrad) cone 40

cm from the gas jet. The first ICT was a Bergoz 10:1 transformer with a sensitivity of 0.4 Vs/C and a 1.9" inner diameter (ID). The second was 20:1 with a sensitivity of 0.2 Vs/C and a 4.9" ID. The two ICT's were cross calibrated by placing them immediately following one another inside the target chamber. Accounting for the solid angle subtended by each, and the number of turns, the charge measured on the two ICT's agreed. This provided two mutually calibrated detectors, and ensured that the indicated charge was free of systematic errors due to detector impedance, sensitivity to short electron bunches, or other factors, since these varied between the two units. Sensitivity of the ICT's to radiation in the chamber and to beam electrons hitting the coils themselves was also tested by shielding them with varying thicknesses of material. No change was observed, indicating that the ICTs were not affected by such issues. Due to the electromagnetic noise from the plasma, the detection threshold was near  $0.5 \times 10^9$  electrons.

The BPS (Kodak LANEX Fast phosphor backed by an aluminum pellicle to reject laser light) was placed at 45 degrees to the electron beam 72 cm from the jet, also subtending  $f/8$ . The BPS was imaged onto a CCD camera, producing an image of the electron beam spatial distribution at this plane integrated over all energies. Use of a CCD camera and phosphor allowed the electron beam to be clearly differentiated from X-ray hits, which showed up as single bright pixels and could therefore be rejected. To measure the charge of beams below the detection threshold of the ICT, the ICT was used to calibrate the BPS and magnetic spectrometer phosphor for charge per count. The phosphor signal could then be used to determine the beam charge.

The energy distribution of the electron beam and its divergence as a function of energy were measured by a magnetic spectrometer. With the BPS removed, the beam propagated through a slit 82 cm from the gas jet, through a bend of  $55^\circ$  in a dipole magnet to provide dispersion, and onto a phosphor screen (LANEX Fast backed by an aluminum foil to reject laser light) imaged onto a CCD camera. The angle subtended

by the screen gives a  $\pm 15\%$  energy range in a single shot about a central value, selectable from 1 to 80 MeV by setting the magnet current (hence the maximum energy detectable was 92 MeV in this configuration). This allowed observation of structure in the energy distribution. The vertical beam size is obtained in the undispersed direction, allowing the simultaneous determination of (vertical) divergence and energy. Since electron beams observed on the BPS were typically round in shape, this vertical divergence measurement is representative. A full spectrum from 0-92 MeV averaged over many shots was obtained by scanning the magnet current. The multi-shot spectrum allowed determination of the peak energy achieved and shot-to-shot statistics at a given energy. The slit used at the input of the spectrometer gave  $\pm 2\%$  energy resolution. Alternatively, using no slit allowed the spectrometer to intercept all beams over a  $0.9^\circ$  half cone angle. This allowed the statistics of how often a beam was formed at a particular energy to be observed with less convolution to pointing, but limited resolution. The spectrometer acceptance then indicated a resolution of  $\pm 8\%$ , so that structure in the spectrum could still be observed in this case. To detect electrons above 92 MeV, a separate phosphor screen observing bend angles of  $0-5^\circ$  was used. Because of the small bend angle and observation down to  $0^\circ$ , this diagnostic could observe electrons of arbitrarily high energy, but could not resolve the energy spread of the beam. In either configuration, the beam divergence was obtained in the undispersed direction. Both configurations are shown in Fig. 3.6.

The magnetic spectrometer dispersion was calculated [111, 112] in detail using a field map obtained using a magnetic probe. The trajectories of electrons were then traced through this field, determining the energy observed at a given angle and the resolution. Here we present a simple model that conveys the important points. The bend radius of a relativistic electron in the magnetic field is [111]:

$$\rho[m] = \frac{p[\frac{GeV}{c}]}{0.2998B[T]} \quad (3.5)$$

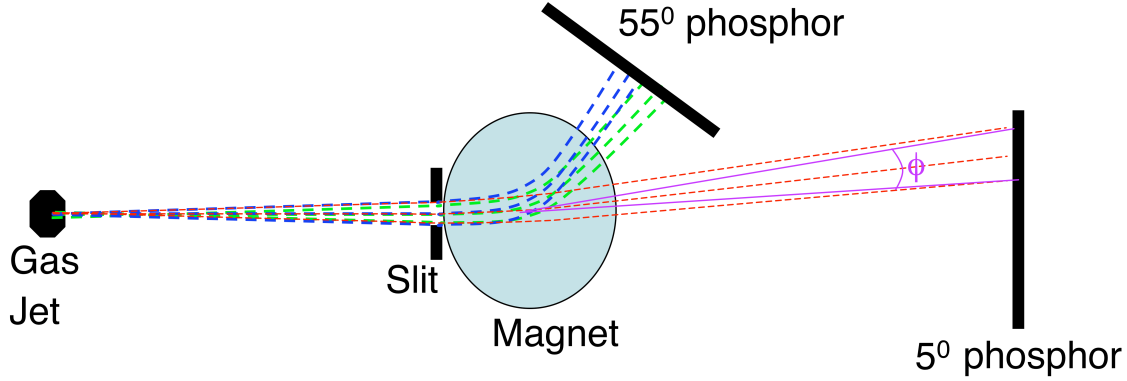


Figure 3.6. Electrons (dashed lines) emerging from the gas jet are collimated by a slit and bent by a dipole magnet whose field points out of the page. Different energies are bent by different amounts. Resolution is then determined by the bend angle  $\phi$  subtended by the slit. In the diagram, Blue is an energy  $E_0$ , and green is approximately  $1.04E_0$ , which is just distinguished given the slit size (rays do not overlap). Red is  $10E_0$ , and is observed on the 0-5° phosphor. Because very high energies are only slightly deflected, high energies are compressed together near 0°, leading to reduced resolution for the small angle phosphor.

High energy particles are bent less than low energy particles. For a magnetic field of length  $L$ , a particle is bent by an angle  $\theta = L/\rho \propto 1/p$ . For our magnet, the pole diameter is about 20 cm so that  $L = 20\text{-}30$  cm depending on the path through the field, and  $B$  is up to  $\sim 1\text{T}$ . Eq. 3.5 then indicates we can observe energies up to about 60-90 MeV at 55°, which is compatible with the 80 MeV obtained from the detailed calculation. Resolution is roughly determined by the fraction of the bend angle subtended by the image of the spectrometer slit on the phosphor ( $\phi$  in Fig. 3.6). Our 55° configuration had a slit width  $w = 1$  cm at  $L_1 = 82$  cm from the gas jet, magnet centered at  $L_2 = 110$  cm from the jet, and a phosphor at  $L_3 = 140$  cm from the jet. Hence neglecting focusing the slit image on the phosphor is  $w' = d L_3/L_1 = 1.7\text{cm}$  wide. This subtends a bend angle  $\phi = w'/(L_3 - L_2) = 3^\circ$ . This is 6% of the 55° bend angle, implying a  $\pm 3\%$  energy resolution, close to the 2% from the full calculation. At 5°, the slit angle is nearly the bend angle, so that there are only one or two completely resolvable bins. Since  $\theta \rightarrow 0^\circ$  as  $p \rightarrow \infty$  high energies are compressed

together near  $0^\circ$  leading to further reduced resolution on axis, but allowing detection of arbitrarily high energies. However, this operating mode of the spectrometer is still useful as, using the full calculation, one can determine the minimum energy required for an electron to appear at any point on the screen. This gives a lower limit on the energy of the beam. The simple model presented here shows the essential aspects of operation. The full trace of the fields includes focusing effects, fringe fields, and other non-uniformities, and hence gives a much more detailed picture.

The magnetic spectrometer was calibrated against the integrating charge transformer, located before the slit, to obtain the charge in the electron beam. To do this, the average overlap of the electron beam with the magnetic spectrometer slit (if present) over many shots was calculated using the beam position data from the BPS. Multiplication by the beam charge, as indicated by the ICT, then yielded average charge through the slit. The averaged spectrum over many shots and over all energies was then calibrated to the average charge through the slit (or within the spectrometer acceptance if no slit was used) to obtain the charge per energy on any given shot.

The sensitivity of the magnetic spectrometer phosphor as a function of electron beam energy was determined by calibration of the phosphors against the ICT. The first (1.9" ID) ICT was placed inside the beam tube of the magnetic spectrometer just before the  $5^\circ$  phosphor screen. This ICT was shielded from direct exposure to the beam by 1" of aluminum on the upstream side, and was isolated from contact with the beam pipe by a Kapton film. By adjusting the magnet current, the ratio of phosphor counts to charge as observed on the ICT could be calculated for various energies. Normalizing the sensitivity to 1 at low energy, a best fit to the data over 3 runs was obtained as:  $Q = (1 + E/10) * C$  where  $Q$  is charge,  $E$  is the beam energy in MeV, and  $C$  is normalized phosphor counts. One such run is displayed in Fig. 3.7.

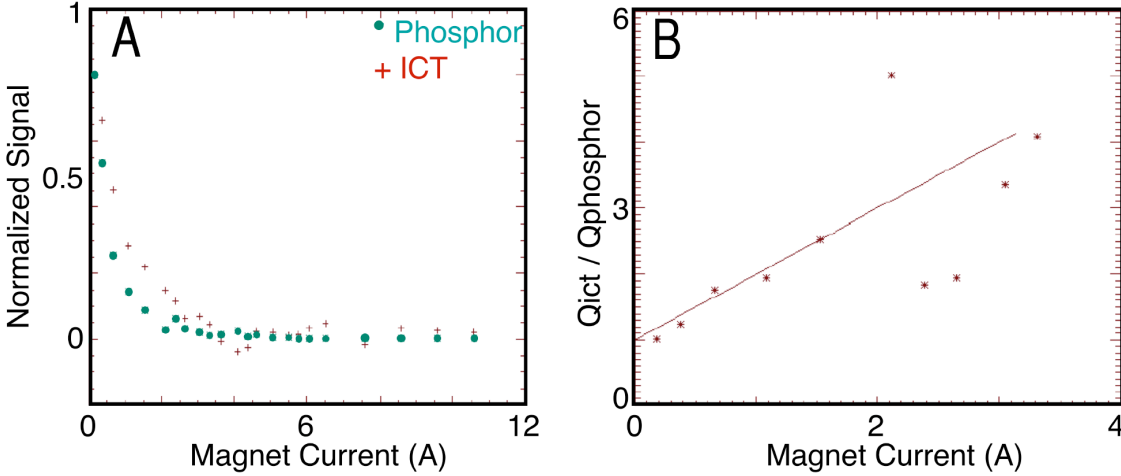


Figure 3.7. The magnetic spectrum at 0-5 degrees allowed calibration of the ICT and phosphor. (A) The spectrum taken with the ICT(+) and phosphor ( $\bullet$ ), averaged over many shots and binned by magnet current for each detector. For this spectrometer configuration, electrons at energy  $E > 10I$  are observed at a current  $I$ . (B) the ratio of signal on the ICT to that on the phosphor, showing that phosphor sensitivity decreases for higher energy electrons.

ICT signal to noise ratio restricted the calibration to energies below 40 MeV, where there was highest charge.

The calibration of the phosphor was verified by applying it to the multi shot spectra taken over the full energy range. As indicated above, the charge in the averaged magnetic spectrum was calibrated to the ICT by observing the average overlap of the beam with the magnetic spectrometer slit using the BPS. Without accounting for energy sensitivity of the phosphor, it was found that the calibration factor differed by a factor of 10 for beams with higher or lower average energy. Applying the energy dependent calibration derived above produced consistent charge readings within a factor of two, indicating that the calibration was reasonably accurate. The direction of the remaining discrepancy suggests that the phosphor is even less sensitive at high energies than the calibration above would indicate (perhaps a quadratic term in energy is present, not visible at the low energies for which the calibration could be performed). If true, that would increase the charge at high energy, but because

it could not be quantified, this additional factor was not applied in the analysis of the beam. Hence the indication from the averaged spectra is that, if anything, the calibration used will under-estimate the charge at high energy.

A further check of the phosphor calibration was done by examining the integrated signal observed on the beam phosphor screen, and correlating it to the charge observed on the ICT. As on the integrated magnetic spectrum, the ratio of counts changed with beam energy. The changes were consistent with lower phosphor sensitivity at high energy, also consistent with the calibration above.

The magnetic spectrometers were further benchmarked against nuclear activation [28]. To do this, single beam self-modulated wakefield acceleration experiments were conducted in which stable operation was obtained for several hours. The energy spectrum of the beam was measured with the magnetic spectrometer. The electron beam was then terminated in a lead-copper sandwich target. Gamma radiation was produced by Bremsstrahlung when the electrons slowed in the target, and for electron energies greater than  $\sim 13$  MeV, depending on isotope, these  $\gamma$ 's have sufficient energy to knock neutrons out of nuclei in the target, causing activation [28]. During activation, accelerator stability was monitored using the ICT (above) and radiation detectors (below) to ensure consistent performance. The target was removed from the accelerator and transferred to a remote counting facility, where the isotope abundances were determined by observing the decay rates of the various  $\gamma$  emission peaks. The code MCNP [113] was used to calculate the production of various isotopes from the observed magnetic spectrum, and the calculated abundances were compared with the observations. Conversely, the electron beam spectrum was inferred from the ratio of isotope abundances. These measurements were consistent with each other and with the spectrometer phosphor calibration above [28].

Direct neutron yield from the  $\gamma$ -n reactions described above was used as a final

check on the magnetic spectrometers. In these experiments,  $\gamma$ -ray and neutron detectors were placed around the chamber. The  $\gamma$  detectors measured the radiation produced by Bremsstrahlung when the electrons slowed in the target, yield from which increases with increasing electron energy. As above, electron energies greater than  $\sim 13$  MeV produced  $\gamma$ 's with sufficient energy to knock neutrons out of nuclei in the target [28]. Hence, the ratio of neutron signals for various accelerator conditions is roughly proportional to the yield of electrons above 13 MeV. This yield ratio was also consistent with the ICT/phosphor calibration above within a factor of two for various energy spectra, and once again, the direction of the discrepancy indicated that the calibration taken is conservative, and hence represents a lower limit when calculating charge of beams at high energies. Signal on these neutron detectors was also used to roughly tune the accelerator for high energies, with detailed optimization then done using the magnetic spectrometer.

### 3.4 Summary

In this Chapter, the experimental setup required to implement the plasma channel guided laser wakefield accelerator was described. Calculations (Section 3.1) showed that available laser beams could be used to form a plasma channel, with the parameters required by the calculations of Chapter 2, using a co-axial variant of the ignitor heater method. The laser transport was modified and new chambers and transport optics were built to bring the beams to target and manipulate them (Section 3.2). The setup for future injection experiments was also developed. Diagnostics were built to analyze guiding of the laser pulse and the resulting accelerated electron bunches (Section 3.3), a control system was built to control the experiment and collect data (Appendix A), and gas targets were built to supply the plasma required (Appendix B).

We now turn to the experiments on laser guiding and electron acceleration using this setup.



# Chapter 4

## Laser Guiding in Plasma Channels

The experiments on guiding described in this Chapter demonstrated that suitable plasma channels could be formed, and could guide the drive laser pulse at acceleration relevant intensities [46]. The plasma channel was created as described in Section 3.1 using the coaxial ignitor-heater method shown in Fig. 3.1. For these experiments, a 2.4 mm long supersonic hydrogen gas jet (Appendix B) provided a target at an atomic density of  $3 \times 10^{19} \text{ cm}^{-3}$ . The drive laser was focused to a spot size of  $7 \mu\text{m}$  FWHM ( $w_0 = 6 \mu\text{m}$ ), and compressed to a pulsewidth of 55 fs. The plasma was hence  $\approx 12Z_R$  long. Timing and energy of the guide formation pulses was adjusted to form the desired guides. The energy of the guided drive pulse was then varied to evaluate guiding at different powers, and the effectiveness of the guide was evaluated using laser mode profiles and spectra as well as plasma interferograms. Simulations compatible with the experimental results indicate formation of a long scale length accelerating structure without self-trapping of electrons at 4 TW guided power.

## 4.1 Channel Formation and Tuning

Appropriate plasmas were created to guide the drive pulse by choosing the timing and energy of the guide formation pulses. As predicted by the ionization model of Section 3.1.1, a 15 mJ ignitor pulse effectively ionized the full length of the jet. By adjusting the energy, pulse length, focal position and f/number, the plasma ionized was reasonably uniform. Optimum performance was found using an ignitor pulse 60 fs in duration (FWHM) and focused at f/15 between the center and the downstream edge of the gas jet. As anticipated, suitable tuning of the beam energy and focus position allowed ionization diffraction to balance laser convergence, producing plasmas of nearly uniform radius. The plasma density of the ignitor produced plasma, recovered from side interferometer images by Abel inversion [108, 109] (Appendix B.3), is shown in the ‘0 ps’ case of Fig. 4.1.

Heater energy and focus were adjusted to control the beam intensity and hence the plasma temperature, and channel formation over time was observed by scanning the timing of the interferometer probe beam. The initial plasma formed by the ignitor at time=0 ps was heated by the heater until  $\approx 200$  ps, and subsequently expanded to form a channel at 500 ps whose profile then evolved with further expansion (Fig. 4.1). Plasma temperature was derived from the expansion velocity of the plasma by observing the radius of the shock front as the timing of the interferometer probe beam was scanned [51, 52, 99]. With approximately 50 mJ of the heater energy overlapping the gas jet, the plasma was heated to approximately 30 eV, consistent with the calculations in Section 3.1.2 (Fig. 4.2). The heater beam was defocused to cover the whole plasma, since focusing the beam tightly resulted in heating of a sub volume, and a distorted channel. There is structure in the recovered density on the propagation (Z) axis at 500 - 700 ps in Fig. 4.1, which appears to result from the inaccuracy of the Abel inversion near the axis of symmetry (Appendix B.3). Smoothing of the inter-

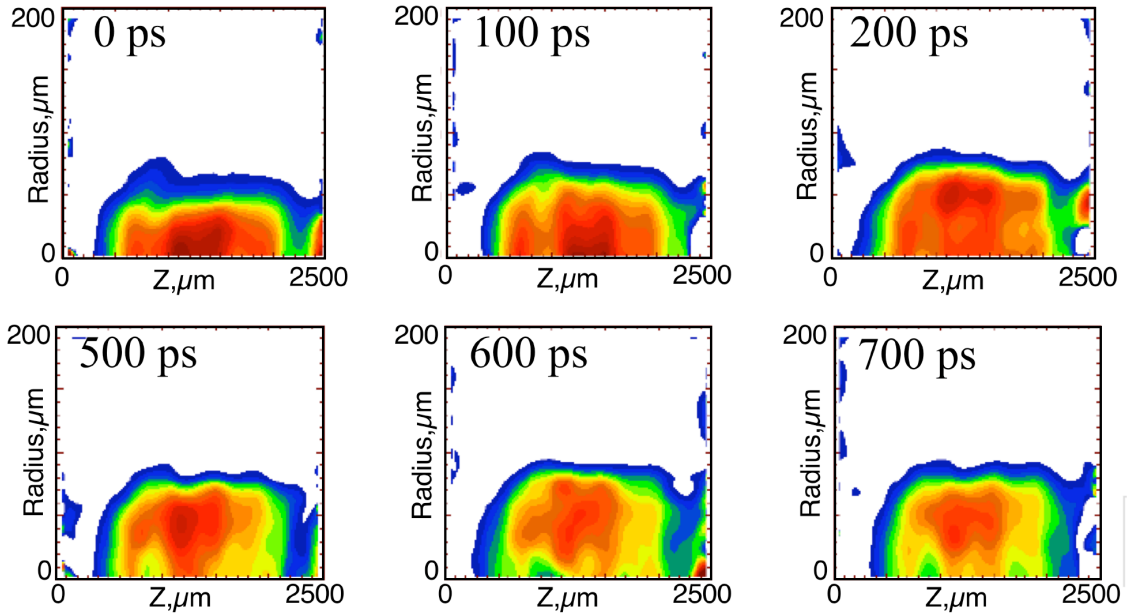


Figure 4.1. Plasma profile measured by the side interferometer versus time after the ignitor pulse. Plasma density (color: blue to red) shown was obtained by Abel inversion of the phase map. The initial plasma formed by the ignitor (0 ps) was heated by the heater until 200 ps. Subsequent expansion formed a channel with a density depletion along the axis, whose profile varies with time (500-700 ps). Further adjustment was accomplished by varying beam energies.

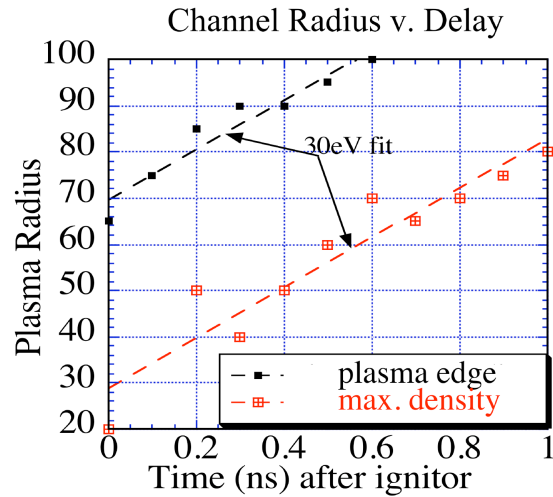


Figure 4.2. Plasma radius versus time indicates plasma temperature. Measurement of the location of the density peak or plasma edge produced compatible measurements, indicating a temperature of 30 eV. This temperature is consistent with the expected Bremsstrahlung heating for the heater beam energy applied.

ferogram to eliminate high frequency noise (above the fringe frequency) and careful attention to selecting the axis of symmetry results in a more uniform profile. This is done when the details of the density profile are important (Fig. 4.3). However, errors remain, and comparing shots indicates that the density is known within  $\sim 10\%$ .

The optimum channel profile for guiding was found by observing the interferometer plasma profile as well as the guided mode image as the formation beam timings and energies were adjusted. This was typically done for a drive beam energy of 50 mJ on target, or a power of 1 TW, to avoid creation of radiation from accelerated electrons. The energy was then ramped up, and the channel was adjusted using the timing and energy of the formation beams to compensate for changing guide requirements with varying power. This was done remotely using the control system (Appendix A) for powers where electron trapping and acceleration was observed.

The interferogram and profile of a guide tuned for optimum performance at 4TW are shown in Fig. 4.3. The density was obtained by Abel inversion with cylindrical symmetry, and this symmetry was confirmed by the mode structure of the guided laser pulse (Fig. 4.5 and Section 3.3.1). The profile shows that the axial density was within 10% of  $1.4 \times 10^{19} \text{ cm}^{-3}$  over the central 1.7 mm of the jet. The length of the wake drive laser pulse (50 fs = 15  $\mu\text{m}$ ) was thus longer than the linear plasma period (9  $\mu\text{m}$  from Eq. 1.1), providing operation in the self-modulated regime [20]. This allows the channels to extend laser propagation distance and enhance the acceleration performance in current wakefield accelerators, which operate in the self-modulated regime to allow self-trapping of electrons [40, 45]. The critical power for self-guiding in such a plasma is 2 TW (Section 2.5.2), so that the drive beam power is about  $2P_c$ . The profile of the channel shown in Fig. 4.3 had a 40% reduced rise in density over the laser spot size of 6  $\mu\text{m}$  compared to the matched profile for a low intensity pulse [52](Section 2.5.1). This detuning was required to compensate for the presence of self-guiding at 4 TW, or two times the self-guiding threshold  $P_c$  at this density

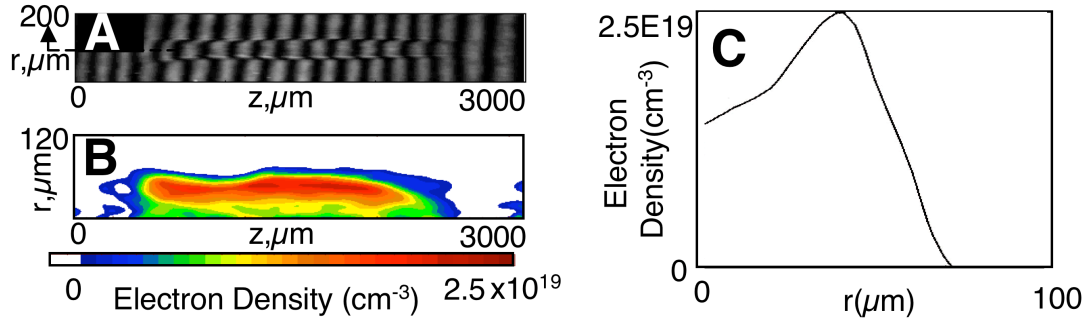


Figure 4.3. The plasma profile at the time of arrival of the drive pulse was measured with an interferometer. The interferogram of the plasma channel (A) was Abel inverted with symmetry about the  $z$  axis to obtain the density profile (B). A lineout (C) shows a rise in density with radius detuned by 40% from the low power guiding condition in order to account for the presence of self-guiding at 4 TW.

(next section). The channel is slightly flared open at the laser entrance (left) side, as a result of the convergence of the coaxial ignitor beam used to form it, which provides good incoupling of the guided mode. Obtaining this open end region has previously required use of additional laser pulses to [53].

## 4.2 Laser Guiding in Plasma Channels

Propagation of the drive pulse in the plasma was analyzed using the interferometer as well as the mode imager and the spectrometer. The interferometer image of the plasma when the drive pulse propagated in the channel at 4 TW (Fig. 4.4b) is very similar to that of the channel alone (Fig. 4.4a). The absence of additional plasma ionized outside the channel when the drive pulse is on demonstrates good confinement and minimal leakage over the length of the guide, as laser energy leaked outside the guide would ionize additional plasma. By contrast, the unguided drive beam diffracts rapidly, creating a larger plasma which expands as the laser propagates (Fig. 4.4c).

Using the channel tuned as described in the previous section, the guided laser mode

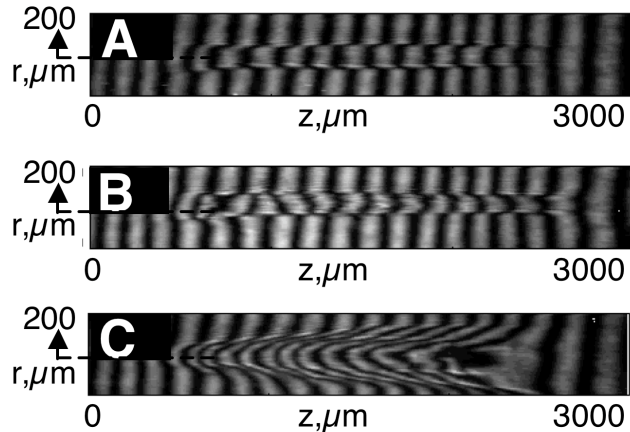


Figure 4.4. The plasma profile after the passage of the drive pulse was measured with an interferometer. The interferogram of the plasma channel alone is shown in (A). When the drive pulse propagated in the channel at 4 TW (B), there was no change in the interferogram, indicating good confinement of the mode inside the channel. Without the guiding channel (C), the drive pulse diffracted, spreading out as it propagated from left to right.

for an input power of 4 TW and intensity of  $7 \times 10^{18}$  W/cm<sup>2</sup> showed no detectable aberration or change in spot size when compared to the input mode (Fig. 4.5A,B). This demonstrates control of laser propagation over more than 10 diffraction ranges at a power two times  $P_c$ , and at an intensity useful for acceleration. The output mode was cylindrically symmetric, indicating that the assumption of channel symmetry (above) was valid. The effectiveness of the guide can be seen by comparison to the vacuum propagated mode, which displayed diffraction, and to the beam propagated through the gas jet without channeling, where diffraction was further increased by ionization [92, 93] effects (Fig. 4.5C,D). The energy transmission was near 35%. Deconvolution of the image using the measured imaging system response to various spot sizes (Section 3.3.2) indicated that since input and output measured mode sizes were identical, the output mode was within 1 μm of the 7 μm input, yielding an output intensity of  $2.5 \times 10^{18}$  W/cm<sup>2</sup> or  $a_0 = 1$  (the lower limit on intensity from the direct image gives  $I > 1 \times 10^{18}$  W/cm<sup>2</sup>), well into the relativistic regime relevant to wakefield acceleration. For a pulse long compared to  $\lambda_p$ , linear fluid theory predicts

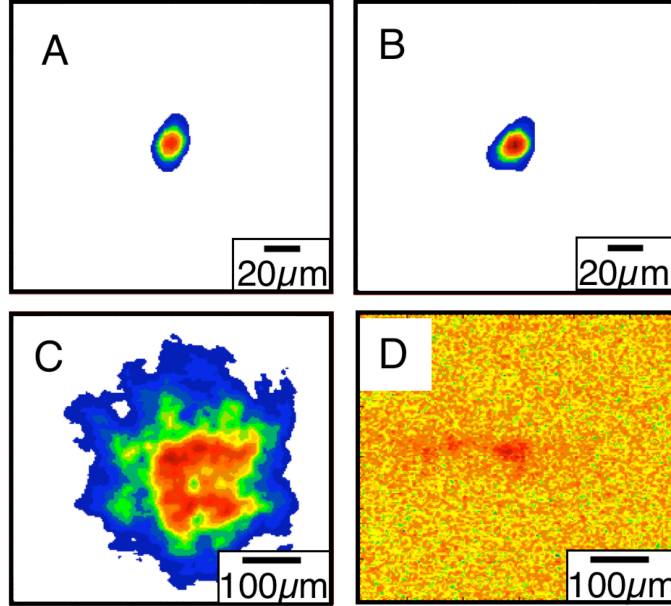


Figure 4.5. Mode images of laser propagation at 4 TW, or four times the critical power for self-focusing (color: blue to red, each mode normalized to its own maximum). Using the channel tune shown in Fig 4.3, the input mode (A) is reproduced without distortion or change in spot size at the output after 2.4 mm (10 diffraction ranges) of propagation (B). Vacuum propagation over the same distance results in a large output mode due to diffraction (C). With gas jet on but without the guide displays enhanced diffraction (D), indicating that self-guiding is not effective. Note enlarged spatial scale in (C),(D).

self-guiding at this power without a channel, though this is subject to instabilities which can disrupt propagation [3, 12, 18, 22, 23, 27, 88, 89]. For the  $\leq 10\lambda_p$  long pulses used in these experiments however, self-guiding alone was never sufficient to guide the pulse over  $10 Z_R$ . The channel density rise over the spot diameter required to guide the high intensity pulses was 60% of the low power rise, indicating that channeling was important even for high power beams.

Adjusting channel plasma profiles allowed guiding of modes at various powers by compensating for the changing effect of relativistic self-guiding. Figs. 4.4 and 4.5 showed guiding of a 4 TW pulse for which the channel profile was flattened, relative to the low power tune, to allow for the relativistic contribution. Fig. 4.6 shows the

guiding of modes at various input powers by a channel which has been tuned to guide a low power ( $0.5 \text{ TW} < P_c$ ) beam. Energy throughput was up to 50% at 0.5 TW, compared to 35% at 4 TW, indicating that a substantial amount of the laser energy was depleted into the wake at high powers. The low power beam was well guided by this channel, while pulses exceeding  $P_c$  were distorted. Indeed, the guided intensity saturated for input power  $> P_c$ . This indicates the importance of tuning the channel profile to compensate for the focusing effect of relativistic self-guiding, and demonstrates that this can be done for  $P \geq 2P_c$ . Above this power, pulses have been guided up to 9 TW, and the interferometer shows good confinement of the laser energy at all powers. However, at 9 TW some distortion of the mode was always observed, with typical output spots near  $20 \mu\text{m}$ , probably due to the very strong self-focusing and coupling to plasma waves in this case [22, 45](Chapter 5). Note that the images of Fig. 4.6 were taken with a different camera than those of Fig. 4.5, which is the reason for the difference in noise levels.

The transmitted spectrum of the laser light serves as a check of the channeling efficiency and a diagnostic of plasma wave production. An intense laser pulse propagating in an un-ionized gas suffers a blue shifting in spectrum due to the time dependent index of refraction as the gas is ionized by the laser [10, 114]. Hence the extent of such ionization blue shifting is an indicator of the laser escaping confinement in the pre-formed channel. On the other hand, coupling of the laser to plasma waves (as used for laser plasma accelerators) results in red shifting of the laser pulse as energy is depleted into the plasma wave [37, 83, 85]. Fig. 4.7 shows the normalized transmitted spectrum at 4 TW for the vacuum, unchanneled, and channeled case. In the unchanneled case, nearly all of the laser energy is blue shifted, and transmission of the 810 nm fundamental is a few percent. In contrast, the channeled spectrum shows a very small blue shifted shoulder, likely caused by residual neutral gas at the channel ends. The transmission of the 810 nm feature is  $\approx 30\%$ , compatible with

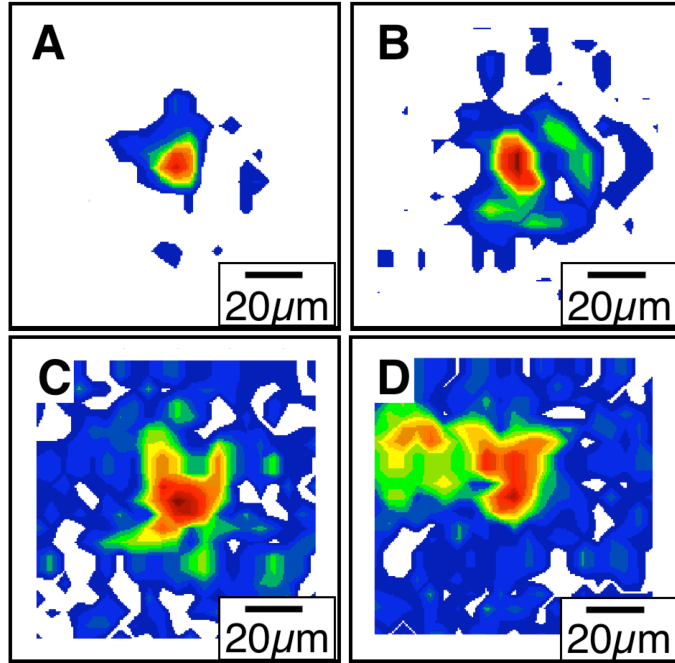


Figure 4.6. Tuning of the channel to compensate for self-guiding. The effect of self-guiding on mode structure in the channel is shown by varying the input power in a channel tuned to guide low intensity pulses (color: blue to red, each mode normalized to its own maximum). For pulses at 0.5 TW, below the critical power for self-guiding, the output mode is undistorted (A). As power is increased to 2 TW (B), some distortion is evident and this becomes more severe as power is further increased to 4 TW (C) and 8 TW (D). The ignitor-heater produced guide was tuned to guide modes up to 4 TW without distortion by adjusting the density profile to account for the presence of self-guiding (Fig. 4.5).

the transmission numbers from the mode imager, indicating that the transmitted beam is largely unaberrated spectrally as well as spatially. A red shifted shoulder can also be seen beginning to appear in the channeled case, and the energy in this shoulder increased to more than 20% of the fundamental with increasing laser intensity (Chapter 5, Fig. 5.8), indicating coupling to plasma waves. Self-modulation of the laser pulse into shorter sub pulses may also contribute to spectral broadening in both directions [23], again indicating coupling to plasma waves. This should broaden the spectrum proportional to the change in pulse length, about a factor of 1.5 for our parameters, which is consistent with the observed red and blue shifts in the channeled

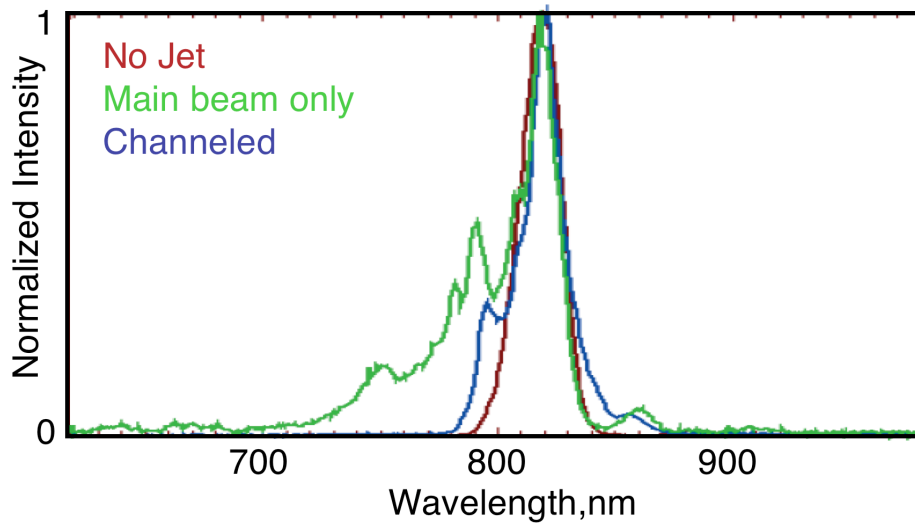


Figure 4.7. Normalized transmitted optical spectrum of the drive pulse. The drive pulse propagating in the gas jet has most of its energy blue shifted away from the fundamental by ionization, impairing its usefulness for applications. The channeled beam shows almost undistorted propagation, with the appearance of a red shifted side band indicating depletion of some of the laser energy into plasma waves. The absence of significant blue shifting indicates propagation through ionized plasma, and hence that the pulse remains within the channel.

case. The blue shift in the unguided case is far beyond this bandwidth, indicating that ionization is dominant there.

The presence of an intense plasma wave was verified by observing the trapping and acceleration of electrons. For drive pulse powers above 4TW, electrons were self-trapped and accelerated [45, 59, 60] (Chapter 5), indicating that the wave is close to the wave breaking field at 4TW. At intensities just below the trapping threshold, where no electrons are self-trapped but laser intensity and hence plasma wave amplitude were maintained over a long scale length, the wave produced enables experiments on controlled injection into laser wakefields. Such experiments have the potential to both stabilize and increase quality of beams from laser accelerators [44, 47–50], but require a long plasma wake structure without dark current to accelerate the injected electrons, which has not been available until now.

### 4.3 Simulations of Laser Guiding

Two dimensional simulations using the particle in cell code VORPAL [74] reproduced many of the features of the guiding experiment, and also indicated good coupling of the laser to plasma waves in the channel. Simulations were performed for the experimental density and laser parameters, using a moving window copropagating with the laser pulse  $90 \mu\text{m}$  long in the longitudinal direction by  $80 \mu\text{m}$  transversely, with  $1800 \times 300$  cells and 10 particles per cell. Further numerical details of these simulations are presented in Chapters 6, 7. Because laser transmission in the experiments at 0.5 TW was 50%, and simulations and theory at this power indicate little laser energy should be depleted into plasma waves, this value was assumed for the coupling of laser energy into the waveguide. Hence to simulate guiding of the 4 TW laser pulse, 2 TW was injected into the guide in the simulation. In practice this may underestimate the injected power, since self-guiding present at  $4 \text{ TW} > P_C$  may improve coupling by aiding transport over the few hundred micron of gas at the nose of the guide. This assisting effect is seen in the simulations at high intensity, where the beam couples well even for plasma ramp lengths longer than  $Z_R$ . Hence, the simulations shown here indicate a lower limit on coupled energy and on the wave excited.

Simulated mode and energy transmission are compatible with the experiments. The laser envelope, fields, and particle phase space after 1.5 mm propagation, where the plasma wave is intense, are shown in Fig. 4.8. The guided spot size is  $\sim 1 \mu\text{m}$  smaller than the input in these simulations, consistent with the experimental observation. Approximately 20–25% of the laser energy is depleted into plasma waves over the 1.7 mm length of the experimental plasma flat top, close to the experimentally observed decrease in transmission between 0.5 and 4 TW. The smaller depletion in the simulations is likely due to a combination of under-estimation of injected power

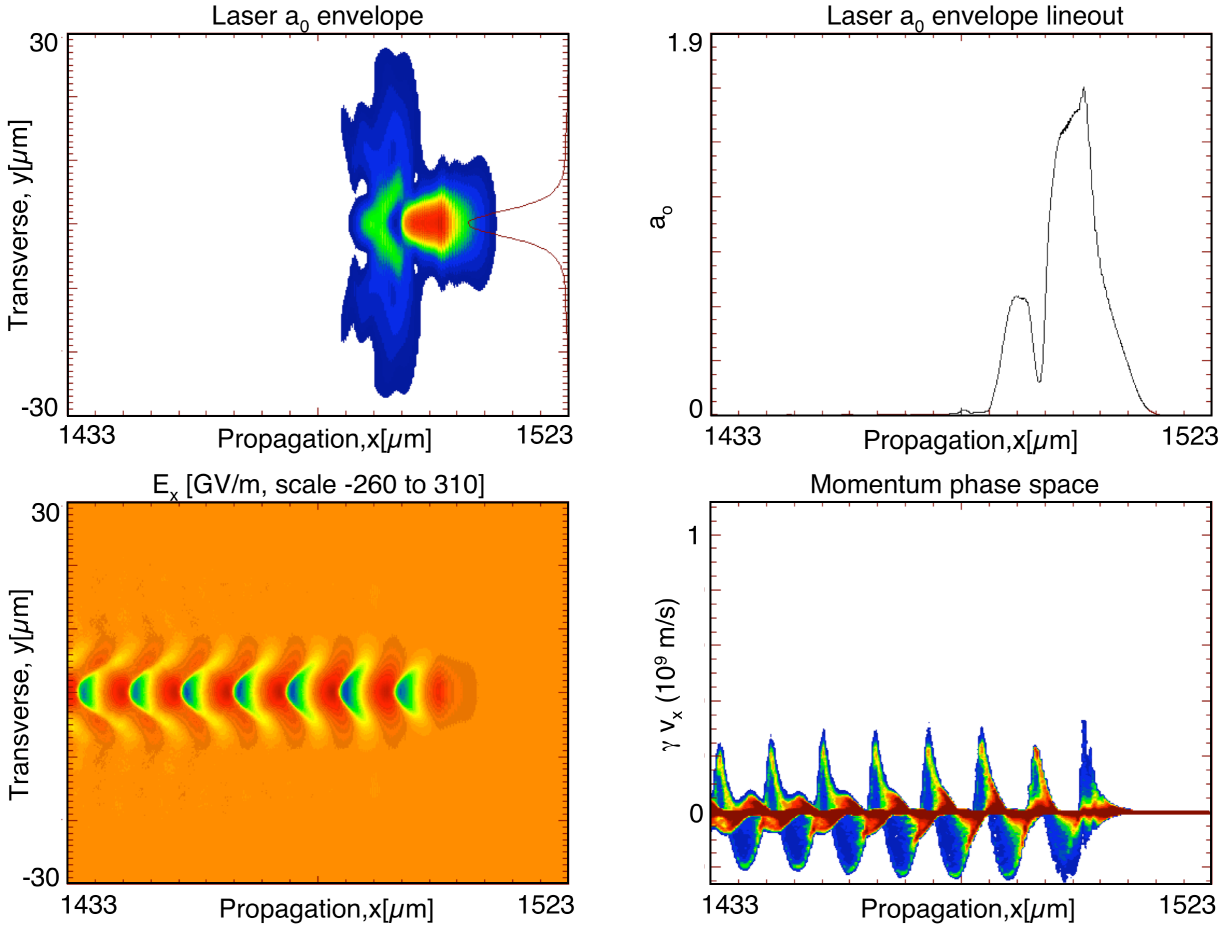


Figure 4.8. Particle in cell simulation of laser guiding. At a laser power of 4 TW (2 TW coupled to the guide), a large wake ( $E_x$ =longitudinal field) is excited by self-modulation of the laser pulse (top panels), but no particles are trapped (phase space, bottom right). The pulse is well guided over the length of the jet, and approximately 20 – 25% of the laser energy is depleted into plasma waves. The long scale length wake produced will be useful for controlled injection experiments.

(above) and three-dimensional effects (Chapter 6). The simulations appear to be converged numerically, with variation of resolution changing results only a few percent (see Chapter 7 for details on convergence).

A large wake is excited by self-modulation of the laser pulse. Little energy is depleted over the first millimeter of the guide, since the laser has not yet modulated to match the plasma period, and the wave driven is weak. Self-modulation becomes strong after approximately 1 mm propagation. Once self-modulated, the laser drives

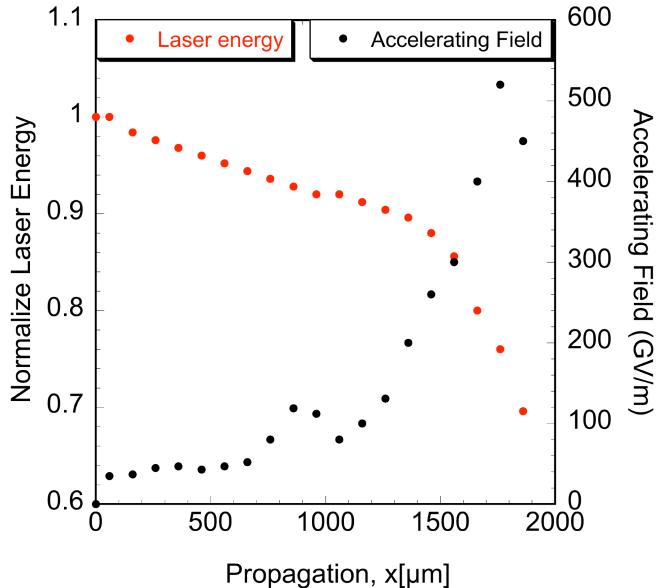


Figure 4.9. Energy in the laser pulse and accelerating field versus propagation distance in the simulation of Fig. 4.8. Accelerating field rises after 1 mm propagation as the laser pulse modulates to the plasma period, and the laser energy is depleted into this wave. After 1.9 mm propagation, depletion of the laser pulse causes accelerating field to drop.

a large plasma wave, into which the laser deposits significant energy, with a field averaging  $\sim 300$  GV/m over the last 0.5 mm of the guide. This is illustrated in Fig. 4.9. This wave amplitude is also consistent within 25% with the estimate obtained by equating the energy in the wake ( $\sim 1.5E^2w_0^2L$ ) over the last  $L=0.5$  mm of the guide to the energy depleted from the laser in the experiment. The wave is below the self-trapping threshold, so that there is no dark current, and could provide significant energy gain for injected particles. Evaluating Eq. 2.47 indicates the dephasing length is  $\sim 1$  mm, greater than the length of the excited wake. Electrons could therefore be accelerated over the whole 0.5mm, providing energy gains of  $\sim 150$  MeV. The accelerating field varies strongly as the laser self modulates then depletes its energy over a short distance (Fig. 4.9).

The simulations show no significant leakage of the laser from channels similar in diameter to the experimental channels, indicating that the losses observed in the

experiment may be primarily due to incoupling mismatch. This is supported by interferometer data above, which showed no ionization outside the channel. These results are consistent with analytic evaluations of guide performance [52], which also show negligible leakage for the experimental guide parameters. As a result, improvement of guiding efficiency may be obtainable by reducing the scale length of the ramp in density at the edge of the jet (Appendix B) to improve coupling, and by further tuning the channel.

## 4.4 Summary

These experiments demonstrated guiding of relativistically intense laser pulses over many  $Z_R$  in plasmas, and tailoring of the radial plasma profile provided guiding without detectable aberration up to several times the relativistic self-guiding threshold. Intensities near  $10^{19}$  W/cm<sup>2</sup> were guided without self-injection of electrons. Experiments as well as simulations show that a substantial plasma wave is excited in the channel, offering energy gains of up to  $\sim 150$  MeV. This provides a platform for future experiments on controlled injection of electrons [44, 47–50], which offer the possibility of further stabilizing and improving the beam quality of laser driven accelerators. Yet higher energies are available at lower densities, as indicated by Eq. 2.48, and GeV accelerator stages are possible using this channeling technique [37, 40]. As described in the following Chapter, we have used these channels to enhance the performance of self-modulated laser wakefield accelerators where the electrons are self-trapped from the background plasma [45, 59, 60].

# Chapter 5

## Channel Guided Laser Wakefield Acceleration

The experiments of the previous Chapter demonstrate that the intensity and mode of a relativistically intense laser pulse can be maintained over many  $Z_R$  by a plasma channel, and we now turn to the resulting enhancement in acceleration. To trap electrons into the wake, the plasma density was increased. Increasing the plasma density reduced the phase velocity of the wake and hence the threshold for self-trapping of electrons (Chapter 2). The drive laser pulse power was also increased to 9 TW, with a pulselength of 55 fs and a spot size of 8.5  $\mu\text{m}$  FWHM, driving the wake to higher amplitude. The channel was then re-tuned to guide the high power pulse, and the density and guiding were optimized for best electron beam performance. The result was self-trapping and acceleration of electrons from the background plasma, and the production of high quality electron bunches from a high gradient wakefield accelerator for the first time [45, 59, 60].

## 5.1 Guiding at High Power and Density

Optimal guiding of the drive pulse at 9TW, and optimal acceleration of self-trapped electron bunches, were observed in channels having an axial density of  $1.9 \times 10^{19} \text{ cm}^{-3} \pm 10\%$  over the central 1.7 mm of the jet. As in Chapter 4, the length of the wake drive laser pulse was thus longer than the linear plasma period, providing operation in the self-modulated regime [20]. This allowed the channels to extend laser propagation distance and enhance the acceleration performance of self-modulated wakefield accelerators, where high densities allow self-trapping and acceleration of electrons [40, 45]. The density and profile were tuned as described in Section 4.1 to optimize electron beam performance. Primary tuning was done using the ICT (charge) and the neutron detectors (yield of high energy electrons, see Section 3.3.3). Fine tuning was then done observing the magnetic spectrometer. This tuning, as shown in the following Chapters, resulted in extraction of the electron bunch close to the dephasing length and the resultant production of high energy high quality beams. Density is higher than in the low power guiding experiments described in Chapter 4, near  $1.8 \times 10^{19} \text{ cm}^{-3}$ . The profile of the channel, shown in Fig. 5.1, had a  $\sim 40\%$  reduced rise in density over a laser spot size compared to the matched profile for a low intensity pulse of  $8.5 \mu\text{m}$  FWHM [52](Eq. 2.37). Detuning was required to optimize guiding of the 9 TW pulse, due to the contribution of self-guiding for this power ( $6P_c$ ).

The plasma channel guided the drive pulse, maintaining its intensity and nearly eliminating diffraction over  $10 Z_R$ , as shown in Fig. 5.2. After the propagation of the 9 TW drive pulse, the side interferometer image showed a plasma only slightly wider than the original channel diameter. This indicates that the drive pulse was well confined within the channel since leakage of the drive pulse from the channel ionizes the surrounding neutral gas. The spatial mode of the laser pulse was characterized

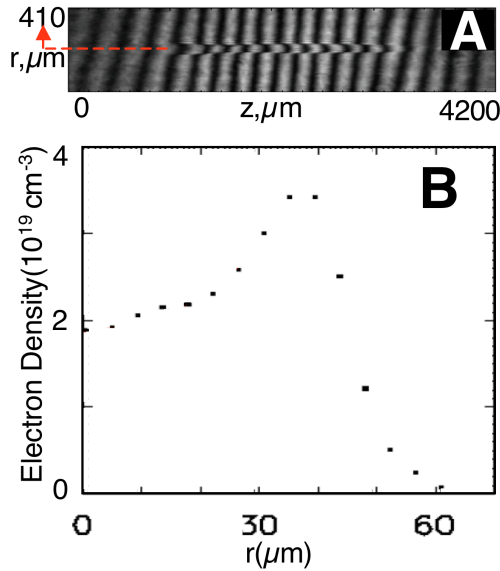


Figure 5.1. Plasma channel formed by the ignitor and heater pulses at the time of arrival of the drive pulse. A frequency doubled interferometer images the plasma transversely (A). The transverse density profile (B) was obtained from Abel inversion of the resulting phase map with cylindrical symmetry about the  $z$  axis (black dots).

using the mode imaging camera, which could be translated to image the input or output of the channel. This mode image showed an intense spot of  $24 \mu\text{m}$  FWHM at the guide output containing 10% of the input energy, confirming that the drive pulse was well guided. The spot is circular, confirming that the guiding channel is cylindrically symmetric. Losses at incoupling to the channel (Chapter 4) may explain as much as a factor of two reduction in energy from the input spot. The remaining factor of 5 is due to depletion of the laser energy to excite the wakefield, and leakage from the channel. Enlargement of the spot compared to the  $8.5 \mu\text{m}$  input and the leakage outside the guide appeared as the input intensity was increased beyond two times the relativistic self-focusing threshold. This is believed to be due to the inability of the channel to perfectly control the spot size in the presence of intense self-guiding (Section 6.4). The enlargement due to this effect is small however compared to the diffraction displayed when the channel is off (Section 5.4, Fig. 5.2). Correlating the

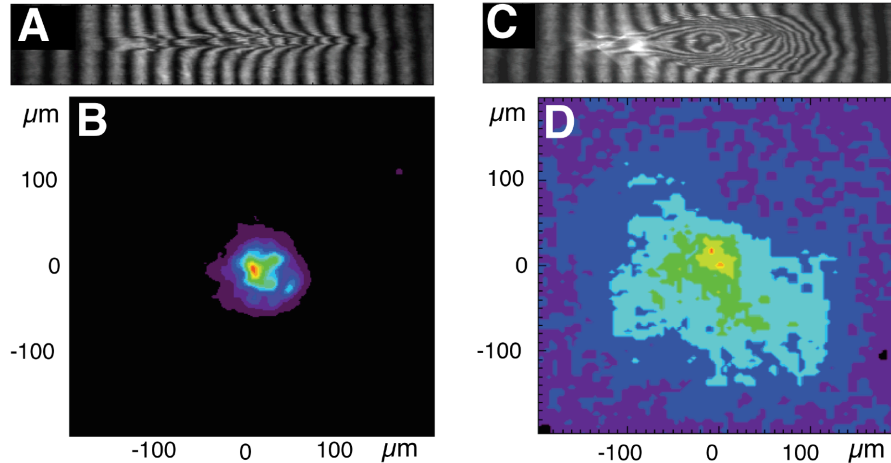


Figure 5.2. Propagation of the laser through the gas jet was measured by the side looking interferometer (A,C) and mode (laser spot) imager (B,D) (color: black to red). In the channel guided accelerator, the plasma interferogram after the passage of the drive beam (A) was similar to the guiding channel (Fig. 5.1), indicating that the drive laser pulse is confined to the channel. The laser mode at the channel exit is a well defined spot of  $24 \mu\text{m}$  FWHM after 2.4 mm of propagation (B). When the channel is off, the interferogram (C) shows a plasma expanding rapidly along the propagation direction (left to right). The mode image (D) shows a diffuse transmitted spot. This indicates the effectiveness of the channel in maintaining the drive beam intensity and mode over many diffraction lengths.

mode imager and interferometer measurements showed that an intense guided mode was present only when the interferometer indicated that the laser was well confined to the channel. We next describe the effect of using a pre-formed plasma channel on the electron acceleration process.

## 5.2 Electron Acceleration in Plasma Channels

Electrons were trapped and accelerated in plasma channels with 9 TW of drive pulse power, and analysis of the electron beam spectrum showed both acceleration of electrons to energies of at least 150 MeV, and the formation of narrow energy spread bunches from appropriately tuned channels.

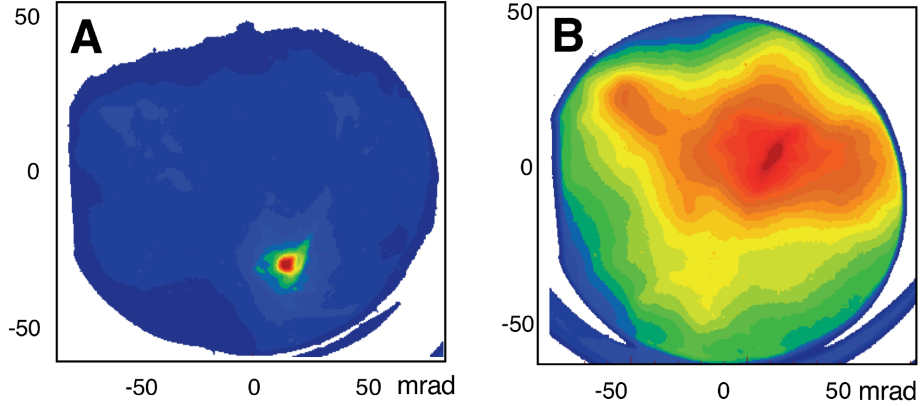


Figure 5.3. Profile of the electron beam, showing the spatial distribution 72 cm after exiting the plasma. The profile was measured using a phosphor screen placed in the beam, imaged by a CCD camera (color: blue to red, each normalized to its own maximum). The channel guided accelerator (A) produces collimated beams with divergence near 6 mrad FWHM. The unchanneled accelerator produced diffuse electron beams with a much wider divergence of 50 mrad FWHM (B).

Associated with improved guiding of the optical pulse was a reduction of the electron beam divergence by nearly a factor of ten in comparison to unguided experiments, to 6 mrad FWHM on well-guided shots (Fig. 5.3). The pointing of the electron beam fluctuated shot-to-shot over a range of 20 mrad RMS, likely caused by laser pointing jitter that changes the overlap between the wake drive pulse and the channel formation pulses (and hence guide quality and incoupling) shot-to-shot.

The channel guided accelerator produced electron bunches with a large fraction of the charge in a well defined bunch at 86 MeV with 3.6 MeV energy spread FWHM and 3 mrad divergence FWHM [45, 59, 60], in contrast to previous experiments which observed beams of continuous energy spread [4–10]. The single shot energy spectrum from the  $55^\circ$  magnetic spectrometer is shown in Fig. 5.4. The energy spread of the peak, at  $\pm 2\%$ , is essentially limited by the spectrometer slit resolution so that the beam may in fact have narrower energy spread. The divergence of the bunch at 86 MeV was half that of the integrated beam observed on the BPS (Fig. 5.3), consistent with previous experiments that have shown that higher energy electrons

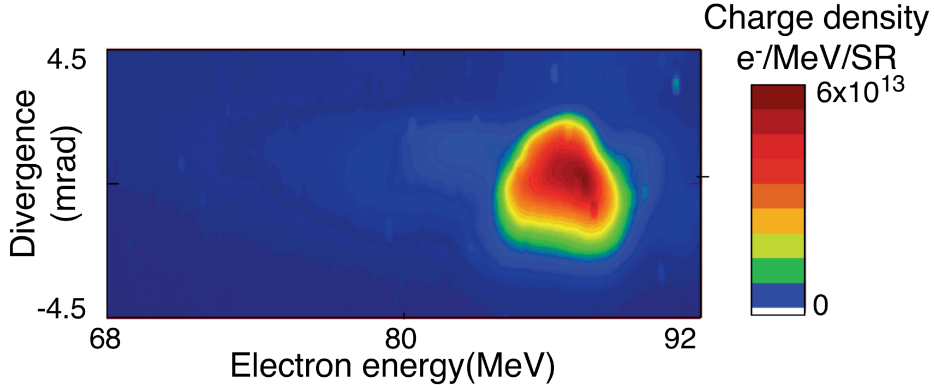


Figure 5.4. Single shot electron beam spectrum of the channel guided accelerator, showing a strongly peaked distribution, in contrast to the exponential distribution of the unchanneled accelerator (Fig. 5.9). A contour plot of electron beam intensity versus energy and divergence shows a bunch containing  $2 \times 10^9$  electrons in a narrow distribution at  $86 \pm 1.8$  MeV and 3 mrad divergence FWHM with contrast  $> 10 : 1$  above background (color: blue to red).

were more collimated [9]. The peak at 86 MeV shows a contrast ratio greater than 10:1 above a broad distribution of charge extending on either side. To determine the charge of this high energy bunch, the spectrometer current was scanned to obtain a full spectrum from 1 to 92 MeV averaged over 300 shots. The integral of this average spectrum was calibrated to the ICT, accounting for the beam size and for the average overlap of the beam with the spectrometer slit as observed on the BPS (Section 3.3.3). This calibration was verified by changing the slit size and observing that the amplitude of the spectrum changed by the expected ratio. The calibration of the magnetic spectrometer has also been verified using an ICT and nuclear activation measurements as described in Section 3.3.3. This provides a lower limit on the charge in the 86 MeV beam of  $2 \times 10^9$  electrons, assuming 100% transmission through the slit.

To obtain an estimate for the emittance, ballistic propagation from a source the size of the laser spot in the channel ( $\sim 8.5 \mu\text{m}$  at entrance,  $\sim 24 \mu\text{m}$  at end) is evaluated. The 3 mrad divergence of the high energy beam then indicates a geometric

RMS emittance  $\epsilon_x$  of 0.005-0.01  $\pi$  mm-mrad and a normalized emittance of 1-2  $\pi$  mm-mrad RMS, comparable to the best state of the art RF accelerators [35]. This estimate was confirmed by evaluation of an envelope model of beam propagation [115] for the parameters of these beams, which indicated that space charge affects emittance less than 10% [116]. Hence the ballistic estimate is very close to correct. The above represents an upper limit, as it is likely the electron beam comes from a source smaller than the initial laser spot size (simulations, discussed in Chapter 6, indicate a source size near 4  $\mu\text{m}$ ) indicating that a normalized emittance as small as  $0.5\pi$  mm-mrad is possible.

The quality of optical guiding as well as the pointing, quality, and charge of the electron beams at high energy fluctuated from shot-to-shot, probably caused by laser pointing jitter that changes the overlap between the wake drive pulse and the channel formation pulses (and hence guide quality and incoupling) as well as laser power fluctuations. Beams with  $3 \times 10^9$  electrons have been observed at similar energies ( $78 \pm 3$  MeV FWHM) [60], and electrons were observed up to the limit of our  $55^\circ$  high-resolution spectrometer (92 MeV). Correlations of guiding and acceleration are discussed further in Section 5.3.

We observed electrons at energies of 150-170 MeV (Fig. 5.5) using the  $5^\circ$  spectrometer, but this diagnostic did not allow the fine resolution required to resolve energy spread (Section 3.3.3). Because of the small bend angle, the distribution of the beam across the slit is important for the energy spectrum, and this distribution is not known. Assuming the beam to be uniformly distributed across the slit, maximum energy is 170 MeV, and charge above 135 MeV is near  $2 \times 10^9$  electrons. A lower limit is obtained by assuming that the whole beam enters along one side of the slit. This indicates a lower limit of 150 MeV and  $1 \times 10^9$  electrons above 135 MeV. This represents nearly 10% coupling of laser energy into the high energy electron beam, an efficiency which will be important for production accelerators.

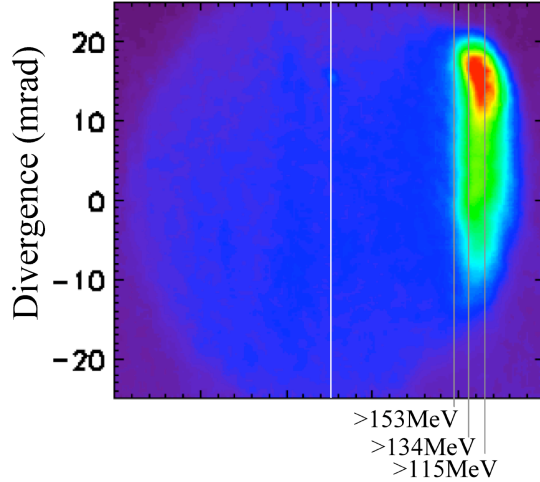


Figure 5.5. Single shot electron beam spectrum of the channeled accelerator from the  $5^\circ$  spectrometer, showing acceleration of electrons to high energy (color: blue to red). Bars on the figure are absolute lower limits on energy assuming the whole beam is incident on the far side of the slit. Assuming uniform distribution across the slit, peak energy is close to 170 MeV and charge above 135 MeV is  $\sim 2 \times 10^9$  electrons.

Structure in the energy spectrum has been seen for electron energies as low as 15 MeV. Below 15 MeV there was an essentially continuous distribution, and total beam charge over all energies was  $1.7 \times 10^{10}$  electrons as measured by the ICT, subtending  $f/8$ . Using a bend magnet, the low-energy contribution can be separated, leaving a high-energy, high-quality beam with a few times  $10^9$  electrons.

Reliance on self-modulation and trapping as well beam loading may introduce a sensitive dependence on laser power and energy as well as plasma density, explaining the variability in the results. In the PIC simulations discussed in Chapters 6 and 7, variations as little as 10 % in laser energy were sufficient to change or broaden the electron distribution. In the experiments, laser power and energy typically fluctuated by approximately 10 %, and we observed fluctuation between continuous and structured energy spectra shot-to-shot, consistent with this explanation. Improvements in laser stability as well as controlled electron injection [44, 47–50] may offer a path to stabilized electron bunches of even higher quality.

The fluctuation of yield is as much as a factor of 20 in spectral density (electrons per MeV) shot-to-shot at a given energy, due in large part to the spectrometer slit. As noted above, the beam fluctuates over a range of  $\pm 20$  mrad RMS, while the spectrometer acceptance is near  $\pm 5$  mrad. Hence only a small fraction of the beams generated make it through the slit. This effect causes greater fluctuation in apparent charge at high energy than at low energy, since the high energy beam is more collimated. The diffuse low energy beam couples to the slit relatively consistently, since its divergence is greater than the RMS pointing fluctuation. For this reason, it is not practical to use the average spectrum to determine the structure of these beams at low energy. In an averaged sense however, there is a roughly exponential distribution of 25 MeV temperature when the slit is used. Experiments (Fig. 8.4) without a spectrometer slit provide a better description of the beam statistics, and these indicate that high energy beams are produced on most shots.

### 5.3 Correlation of Accelerated Electron Yield and Laser Pulse Properties

Well guided optical beams were highly correlated with the acceleration of electrons to high energies. Simultaneous observation of the mode image and the  $5^\circ$  spectrometer over 300 shots allowed measurement of the correlation between guided mode intensity and charge of the electron beam at high energy. Figure 5.6 shows the charge at energy greater than 100 MeV as a function of normalized guided mode intensity. Normalized guided mode intensity is defined as the peak intensity in the mode image on a given shot normalized to the peak observed on any shot in the run, and parameterizes the effectiveness of the guide in maintaining drive amplitude. Charge is measured by integrating the signal on the magnetic spectrometer phosphor screen,

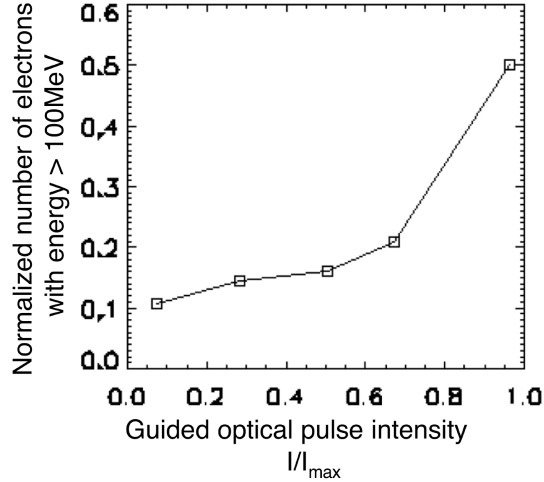


Figure 5.6. Normalized electron bunch charge above 100 MeV versus guided mode intensity. Data are binned from 300 shots, and normalized to the highest values observed during the run. High energy beams are highly correlated with high guided mode intensities, indicating that maintaining the drive laser intensity over the length of the plasma using the channel enhances accelerator performance.

normalized to the maximum charge observed. Data have been binned by guided mode intensity in order to display the dependency. There is a stronger than linear rise of charge with intensity, indicating that good mode transport was very important to high energy electron production, or alternatively, that maintaining drive intensity over long distance is an essential criterion for obtaining high energy electrons.

A further confirmation that guiding is responsible for the enhanced performance observed is obtained by observing the dependence of accelerator performance on channel tune (Fig. 5.7). Neutron detectors were used to indicate the yield of electrons above 13 MeV (Section 3.3.3) and the channel was tuned by adjusting the timing between the drive pulse and guide formation pulses (Fig. 4.1). Highest yield of neutrons was observed for timing near 400 ps. This indicates the importance of channel tuning to the acceleration process. The  $\approx 200$  ps time window over which performance is high roughly corresponds to the evolution timescale over which the guide (and guided

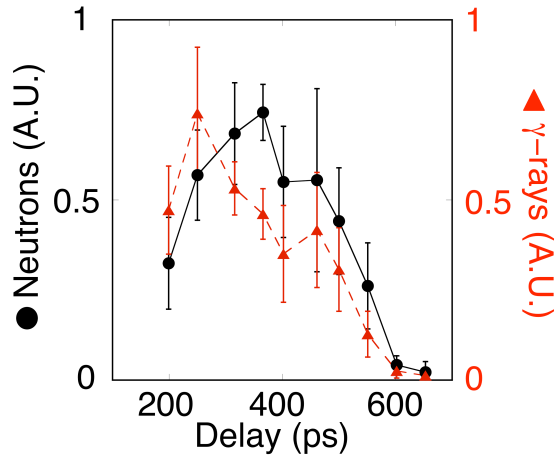


Figure 5.7. Performance of the channel guided accelerator as a function of channel tune. The channel was tuned by scanning the delay of the drive beam with respect to the guide formation beams. Accelerator performance is parametrized by the yield of  $\gamma$ -rays and neutrons. Optimal yield of neutrons, which indicate electrons above 13 MeV, was found near 400 ps delay, indicating that performance is sensitive to channel tuning. Yield of  $\gamma$ -rays was high over a broader range but still sensitive, indicating lower energy electrons are produced in less well tuned channels.

mode) changed significantly, consistent with guiding being the determining factor in accelerator performance.

As guided power was increased from 4 to 9 TW, the red shifted feature in the guided optical spectrum increased to nearly 20% of the fundamental amplitude (Fig. 5.8). Total transmission drops from 35% to 10%. The observation of red shifting and energy depletion are consistent with fluid simulations [117] and with energy conservation, which indicate that the laser must red shift as it deposits energy in the plasma wave [83]. Significant blue shifting also appears in the spectrum, though this remains much less than in the unchanneled case. The blue shifting may be due to the imperfect confinement of the mode to the guide at this power. Fig. 5.2 shows that at 9 TW there is some ionization outside the guide, and this ionization may result in the observed blue shifting [10, 114]. Self-modulation of the laser pulse into shorter sub pulses may also contribute to spectral broadening in both directions [23], again indicating coupling to plasma waves.. This should broaden the spectrum proportional to

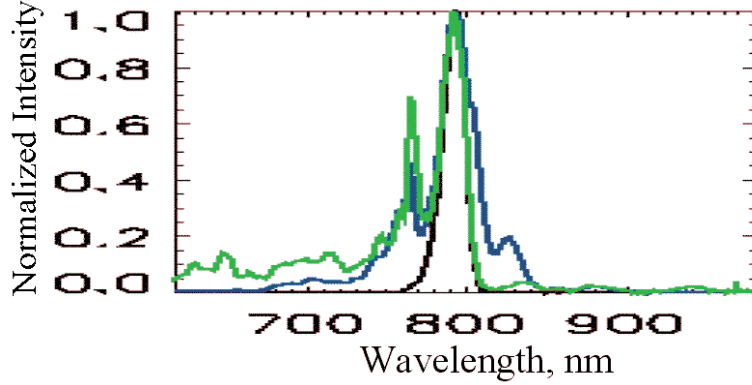


Figure 5.8. Normalized optical spectrum of the transmitted drive laser pulse at 9 TW. Shown are the spectrum in vacuum (black), channeled (blue), and unchanneled (green). The red shifted feature has increased to 20% of the fundamental amplitude in the channeled case, in contrast to a few percent at 4 TW (Fig. 4.7). Significant blue shifting is also evident at this power in the channeled case, though much less than in the unchanneled case.

the change in pulse length, about a factor of two for our parameters. While consistent with the first red and blue shifted shoulders, this does not explain the blue shifting to  $<600$  nm observed, indicating that ionization is still important.

The correlation between the laser spectrum at the exit of the plasma channels and the generation of high energy electron beams was also studied. To analyze the transmitted laser spectra, we divided each measured spectrum into an unshifted (within the laser bandwidth) region, and red shifted and blue shifted bands. The correlation of transmitted energy to high energy electrons was positive, and the correlation was more than twice as strong for red shift as blue shift. Normalizing to spectrally integrated transmission, shots with high charge above 100 MeV had 6% more energy in the red shifted band, and 5% less blue shifted energy. Hence, in contrast to previous reports [9], here we observe that the largest plasma waves (indicated by accelerated electrons) were most strongly correlated with red shifting of the laser light, and were more weakly correlated to blue shifting.

This data reinforces the conclusion that maintaining the drive pulse intensity

using the channel is important for efficient acceleration. Electron spectrometer and neutron data indicate that the highest energy electrons are produced by the best guided beams. The optical transmission and spectrum exhibit features consistent with increased depletion of the laser pulse into the plasma wave under the same conditions.

## 5.4 Unchanneled Acceleration

To provide a baseline for evaluating the effects of guiding, the accelerator was operated without the guiding channel using the same gas jet and laser parameters. Plasma density was independently optimized for the unchanneled accelerator, and highest charge and electron energies were obtained at  $4 \times 10^{19} \text{ cm}^{-3}$ . The high density may allow acceleration before the laser diffracts since self-modulation and dephasing both occur more quickly at high density, but this also reduces the peak energy compared to the channeled case. Operating the unchanneled accelerator at the density used for the channeled accelerator ( $2 \times 10^{19} \text{ cm}^{-3}$ ) produced low-charge low-energy beams, possibly since the intensity of the drive beam was not maintained for sufficient distance to allow acceleration at this density without channeling.

Without channel guiding, the side interferometer showed that the laser pulse diffracted strongly after only a few hundred micron of propagation in the plasma, producing a plasma which flared out from  $100\mu\text{m}$  diameter at the entrance of the jet to  $700\mu\text{m}$  at the exit (Fig. 5.2C). This indicates that relativistic self-guiding did not keep the pulse focused. The mode imager confirmed that the beam is severely defocused after 2.4 mm propagation, showing a diffuse transmitted spot of  $\sim 150\mu\text{m}$  FWHM diameter containing approximately 2% of the input energy with a peak near  $2 \times 10^{15} \text{ W/cm}^2$ , an intensity too low to drive a substantial wake (Fig. 5.2D).

The electron beam had a total charge of  $1.5 \times 10^{10}$  electrons, as measured by the ICT. Beam divergence at the plane of the BPS was near 50 mrad FWHM (Fig. 5.3B). The profile of the beam was nearly circular, consistent with production by a radially symmetric wake, as expected. The electron energy spectrum of the unguided accelerator, obtained by scanning the magnet current, is described by a two-temperature distribution characterized by a 2.6 MeV temperature below 10 MeV and a hot tail with an 8 MeV temperature above 10 MeV (Fig. 5.9). Analysis of individual images from the spectrometer indicated that there is little structure in the distribution, so that the exponential description is appropriate. Structure in the energy distribution was weak and only present in the tail of the distribution above 15 MeV, which contained  $< 2\%$  of the charge, consistent with a beam accelerated over a short distance. The spectrum is also stable, with typical shot-to-shot fluctuations of spectral density less than a factor of four peak to peak. This likely results from the fact that the divergence of the beam is large, so that slit overlap variations are small. The self-modulation instability is also rapid at high density, and there is no effect of varying guide conditions, both of which reduce fluctuation. These results are consistent with previous experiments [4–7, 9, 10].

To differentiate the effects of channeling from pre-ionization, the ignitor pulse was fired 20 or 80 ps before the drive pulse, pre-ionizing a plasma 80  $\mu\text{m}$  in diameter. The plasma did not expand significantly over 80 ps, so there was no shock wave and the transverse density profile was flat and had no guiding properties. We observed no substantial difference between the drive pulse only and pre-ionized cases in laser propagation, electron yield, or energy spectrum. Fig. 5.10 shows that the averaged energy spectra in the pre-ionized case and the single beam case (where the drive beam is incident on neutral gas) are indistinguishable. This indicates that channeling and not pre-ionization was responsible for differences in the electron beams described in Section 5.2, and is also consistent with the expectation that the plasma in the single

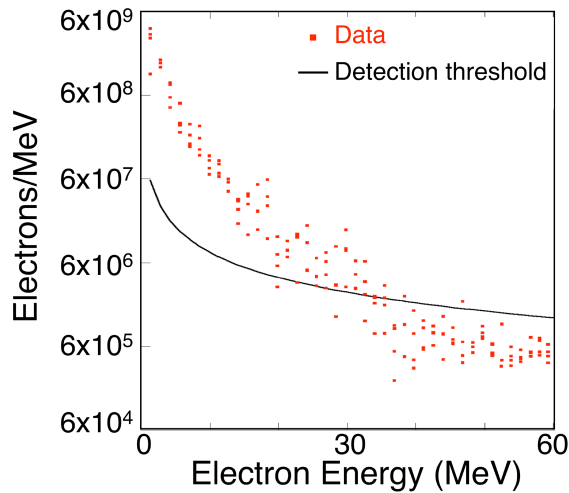


Figure 5.9. Shot averaged electron beam spectrum for the unchanneled accelerator, obtained by scanning the spectrometer magnet current. Each point represents one shot. Typical of such experiments, the energy distribution is essentially continuous and there are very few electrons above 40 MeV. Individual shot images showed little structure in the distribution (not displayed).

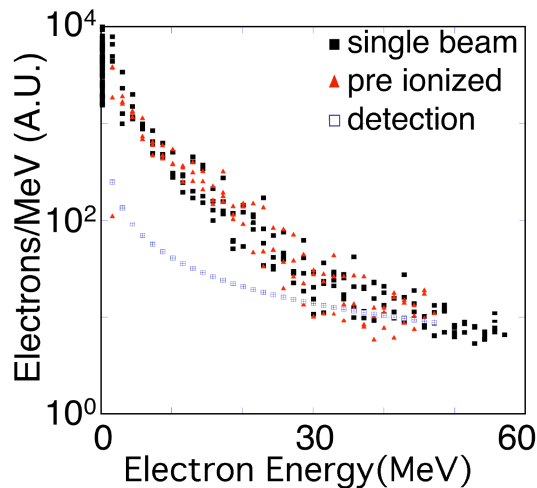


Figure 5.10. Shot averaged electron beam spectrum for the single beam and pre-ionized (unchanneled) accelerators, obtained by scanning the spectrometer magnet current. Each point represents one shot. The spectra are indistinguishable, indicating that pre-ionizing the target gas does not significantly change acceleration. Hence the electron beam enhancements observed in Fig. 5.4 are due to channeling, not pre-ionization. Results are not calibrated to the ICT, so that Electrons/MeV are displayed in arbitrary units.

beam experiment is ionized so early in the pulse that the bulk of the pulse (more than 99.9%) sees an ionized target and is not significantly affected by ionization physics. This is also consistent with the channel tuning data presented in Fig. 5.7, which indicated high energy electron production was well correlated to guiding, and that a particular channel tune was required to obtain high performance.

## 5.5 Summary

These experiments demonstrate for the first time the production of high energy, monochromatic beams from a high gradient laser accelerator. Bunches with  $2 \times 10^9$  electrons at  $86 \pm 1.8$  MeV and with 3 mrad divergence were produced (Fig. 5.4), and energies up to 170 MeV were observed. Beam energy and quality are sensitively dependent on tuning of the channel, and pre-ionization without channeling is not sufficient to improve performance. Undesirable beam qualities observed in previous experiments (which did not use controlled guiding), including 100% energy spread, exponentially small fraction of electrons at high energy, and high beam divergence are overcome by this technique while the high accelerating gradient is retained. The beam produced has an estimated emittance comparable to state-of-the-art RF facilities, and in combination with narrow energy spread this opens new fields of application for laser accelerators. The energy in the present experiments is limited by the need to have the density high enough to allow self-trapping (Section 2.3). Future experiments with controlled injection may reach GeV energy using channels to maintain the laser intensity over cm scales at lower densities near  $10^{18} \text{ cm}^{-3}$  [37, 38, 40]. The following Chapters describe simulations and single beam experiments which elucidate the mechanisms for formation of the high quality electron bunch from self-trapped electrons. The results are compared with other experiments [61, 62] and simulations [41, 63, 64] which have also observed narrow energy spread beams.

# Chapter 6

## Simulations of Channeled Wakefield Acceleration

Two-dimensional particle-in-cell (PIC) simulations [70] using the code VORPAL [74] (jointly developed at U. of Colorado and Tech-X Corp.) were used to evaluate mechanisms of beam formation and to compare to the structure of the experimental electron spectra [45, 59, 60]. In PIC simulations, many electrons are represented by each simulation ‘macroparticle’. Further, instead of calculating binary forces between each particle pair, charge and current are deposited on a grid and used to calculate fields. These fields are used to push the particles, resulting in manageable computation time. Simulations were performed for the experimental densities and laser parameters, and analyzed as a function of propagation distance. These simulations indicate that high quality, low energy spread electron beams are produced when trapping of electrons loads the wake [16, 17], suppressing further injection and forming a bunch of electrons isolated in phase space. At the dephasing length, where the bunch begins to outrun the wake, the particles are concentrated near a single energy, and a high quality bunch is obtained by terminating the plasma at this length.

The simulations used parameters as close as possible to the experiments. The laser pulse had a 55 fs FWHM pulsewidth with a half sine longitudinal envelope,  $a_0 = 2.15$ , and 8.5  $\mu\text{m}$  FWHM spot size. This indicates a power of 9 TW in three dimensions. This laser propagated in a channel of axial density of  $1.8 \times 10^{19} \text{cm}^{-3}$ , and with a transverse density profile fit to the experimental profile using a cosine function which is nearly parabolic near axis. The pulse was polarized out of the plane of the simulation. Numerical parameters included a moving window copropagating with the laser pulse, 90 $\mu\text{m}$  long in the propagation direction (x axis) by 80 $\mu\text{m}$  transversely (y axis). The grid was 2700  $\times$  600 cells with 10 particles per cell. This yielded a grid spacing of 24  $\times$  6 cells/ $\lambda$ . Boundaries were reflecting for EM waves and absorbing for particles. Plasma was loaded over the central 60 $\mu\text{m}$  of the box transversely using a bit-reversed ‘quiet load’ scheme [70]. Variations in plasma density were represented by variable weighting of the simulation macro-particles, so that number of particles/cell did not vary across the simulation other than statistical fluctuations induced by the randomness in the loader. The longitudinal plasma density was represented as a flat top, with a 30  $\mu\text{m}$  ramp up from vacuum to peak density. This allowed the laser (which is launched at the wall at focus) to couple to the channel. Studies varying the the ramp length (Section 7.4) did not show much change in the parameters of the accelerated electron bunch, so that this deviation from the experimental ( $\sim 300\mu\text{m}$  ramp) parameters is not thought to be important.

Numerical and physical parameters, and the effect of variation of these parameters, including plasma ramp, are discussed in detail in Chapter 7. In the present Chapter we describe the results of the simulations and their applications to the experiments.

## 6.1 Two-Dimensional Considerations

Simulations were conducted in two-dimensional slab geometry since three-dimensional simulations would have exceeded available computer time, taking  $\sim 600$  times longer. Use of cylindrical geometry is precluded by the laser polarization vector, which breaks the symmetry. Hence, the relationship between the two-dimensional slab simulations and three-dimensional experiments must be considered.

We use a laser pulse with a Gaussian transverse envelope  $I = I_0 \exp(-2y^2/w_0^2)$ , and many laser and plasma interaction parameters are similar to the three-dimensional form, with the substitution of  $y$  for  $r$ . The diffraction range has the same form,  $Z_R = (\pi/\lambda)w_0^2$ , but since diffraction occurs only in one transverse dimension, the drop off of intensity with diffraction is more gradual in slab geometry. The density rise for a guiding channel is  $\Delta n = 1/\pi r_e w_0^2$  [52], which also matches 2.37. The simulations accurately model this, and matched guiding and vacuum diffraction have both been verified (Section 7.2). Similarly, taking the limit of a slab beam in the envelope equation for self-guiding derived in [88] yields  $1 = \frac{w_0 a_0^2 k_p^2}{32}$ , which is of similar form to Eq. 2.42 but with a different power of  $w_0$  because in two dimensions power density ( $a_0^2 w(z)$ ) is conserved rather than power ( $a_0^2 w^2(z)$ ) as in three dimensions. Laser self-focusing in the simulations also appears to be consistent with this value. Note however that oscillation of mis-matched spots will be different due to the different dependence of intensity on spot size.

For the wake, the longitudinal wake solution Eq. 2.17 is unchanged. The transverse wake is obtained from the Panofsky-Wenzel theorem (Eq. 2.19) in slab geometry which yields:

$$\frac{\partial E_y}{\partial z} = \frac{\partial^2 \Phi}{\partial z \partial y} = \frac{\partial E_z}{\partial y} \quad (6.1)$$

so that the transverse wake has the same form in slab and cylindrical coordinates

with  $E_y$  being given by the expression for  $E_r$  shown in 2.20 with the substitution of  $y$  for  $r$ .

Based on the above, we used the same intensity and waist size for the laser, and the same transverse plasma profile in the simulations as in the experiments. This should give reasonably realistic wake amplitudes. However, differences remain that cannot be rectified, and will influence results. One is that laser intensity is proportional to  $1/w_0$  in slab and  $1/w_0^2$  in three dimensions, so that variation of spot size has greater effect in three dimensions. This means slab geometry will underestimate self-modulation and other laser instabilities.

Estimation of accelerated charge is complex, as each macroparticle in the slab simulation represents a charge density,  $\rho$ , in electrons/meter. A simple estimate is given by multiplying the number of macroparticles in the bunch times  $\rho$  times the transverse spot size laser pulse, which gives the charge accelerated by the two-dimensional slab with the experimental power. Alternatively, the electrons can be revolved around the axis, so that an electron at transverse displacement  $y_0$  from the axis represents a charge  $\pi\rho y_0$ . This gives the charge in a cylindrical electron bunch with the same transverse structure as the slab simulation. However, unlike the slab method above, macroparticles at large radius now represent more charge than those close to axis. This is problematic, especially from the point of view of beam loading - the revolved bunch represents a smaller fraction of the charge in the revolved plasma wake than the slab bunch did. This effectively under-estimates the charge that can be trapped before beam loading would turn off injection. Two and three-dimensional simulations loading controlled bunches into a wake just below the self-trapping threshold indicated that three-dimensional beam loading falls somewhere between the slab and cylindrical estimates. Hence while neither estimate is complete, they provide upper and lower limits on the trapped charge expected in three dimensions, and both are employed below. Particle trapping may also be different between two and three

dimensions, since in slab geometry particles can enter only in one transverse dimension. These considerations indicate two-dimensional simulations may under-estimate trapped charge, and this is reinforced by comparison with other simulations [121] (Section 7.5).

Hence, while there are differences between slab and three-dimensional geometry which necessitate care in interpretation, many parameters can be matched to the experiments. Low resolution three-dimensional simulations have confirmed that the basic features of wake and beam formation are reproduced from two to three-dimensions, and the main differences appear to be faster self-modulation and greater particle trapping in three dimensions, indicating that the two-dimensional simulations may underestimate bunch charge and over estimate the required acceleration length. However, these three-dimensional simulations were not of high enough resolution due to computer time, and hence we use the two-dimensional simulations for analysis. We now discuss what these simulations reveal about electron bunch formation mechanisms and laser propagation.

## 6.2 Wake and Electron Bunch Formation

The simulated laser envelope and particle phase space as a function of propagation distance are shown in Fig. 6.1 , and the wake density is shown in Fig. 6.2. The laser initially entered the plasma with a pulse duration longer than the linear plasma period, and as a result did not excite a large wake or accelerate electrons (Fig. 6.1A). As it propagated, the laser self-modulated to the plasma period. This excited a wake [3] of increased amplitude, which trapped and accelerated electrons. Trapping and acceleration of a high energy high quality beam was observed in the first plasma period of the wake (i.e., bucket) behind the laser, with electrons trapped when the laser has propagated  $\approx 1$  mm (Fig. 6.1B). The field of the initially trapped electrons

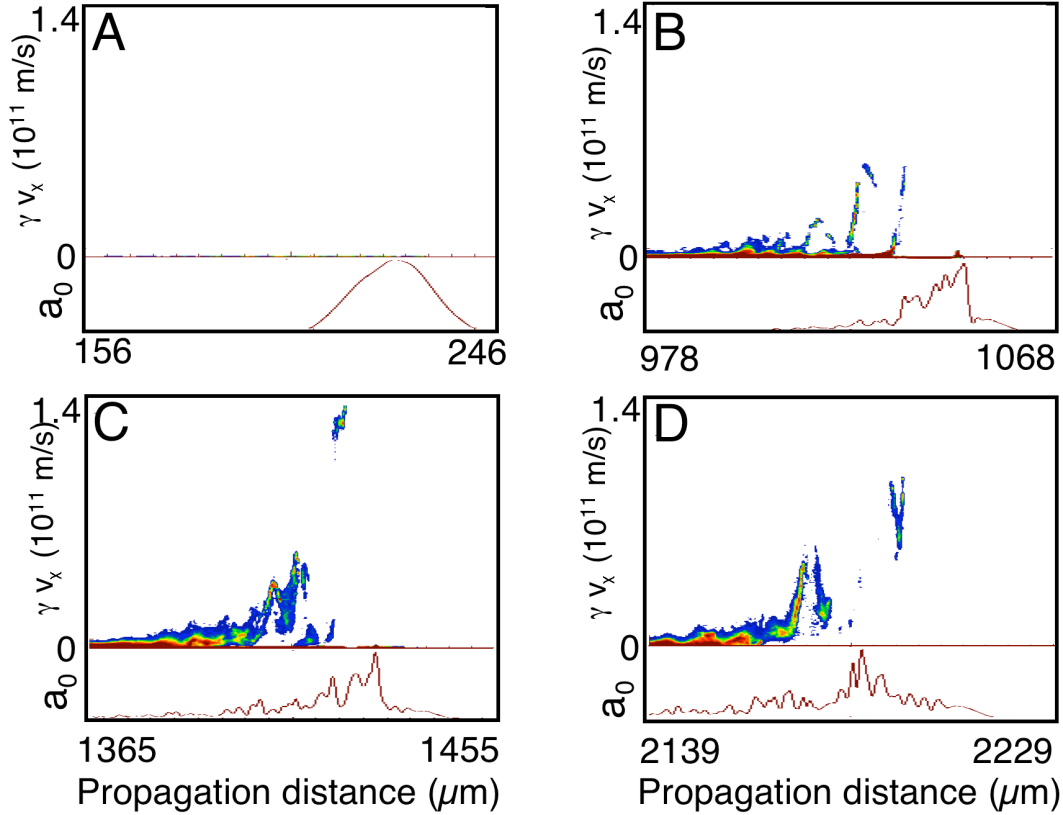


Figure 6.1. Simulation momentum phase space density (top of each panel, color: blue to red) and laser envelope (bottom) as a function of propagation distance ( $x$  [ $\mu\text{m}$ ]). The laser enters the plasma (A), exciting a wake and trapping electrons (B). If trapping turns off after the initial bunch is loaded (Fig. 6.2), these electrons are concentrated in energy at the dephasing length, forming a high energy low energy spread bunch (C) which dissipates with further propagation (D).

interfered with the wake driven by the laser, reducing its amplitude (beam loading) [16]. This effect can be seen in the reduction of wake amplitude from Fig. 6.2A (before trapping) to Fig. 6.2B (after trapping). Further trapping was suppressed by this loading. The initial electrons were then isolated in phase space and able to form a high quality bunch if suitably compressed in momentum space.

The electrons are compressed in momentum to form a high quality beam at the dephasing length [3], the length at which the electrons outrun the wake and slip forward into decelerating wake phase. The leading edge of the bunch has the highest

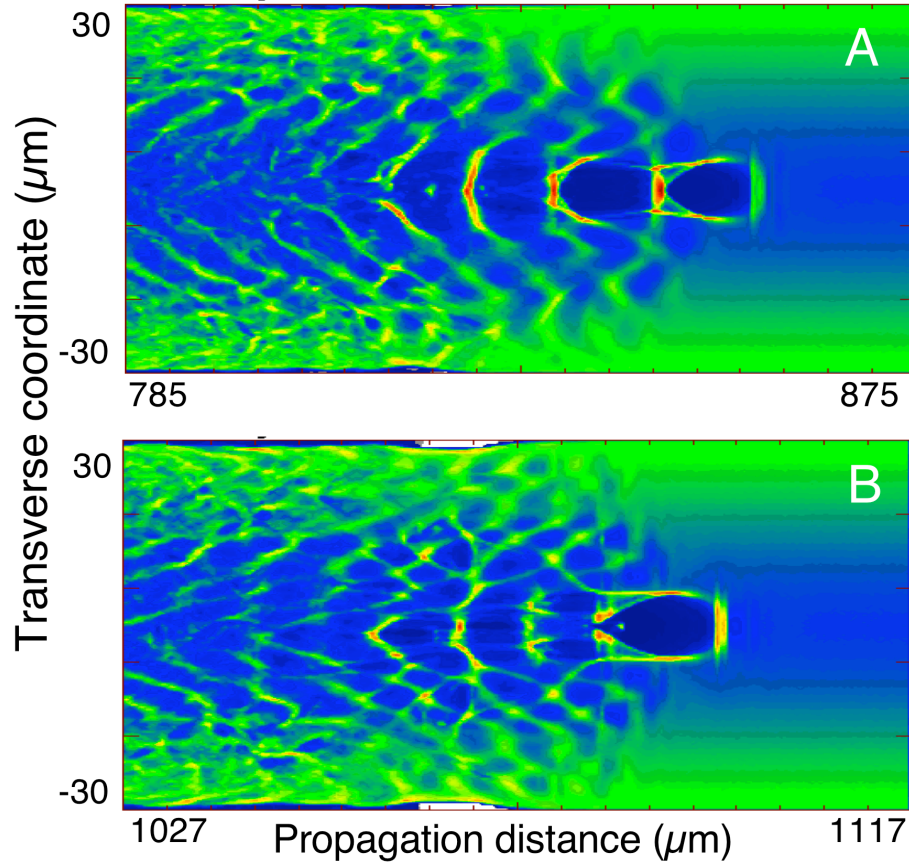


Figure 6.2. Simulated electron density after laser propagation of  $875\mu\text{m}$  (A) and  $1117\mu\text{m}$  (B), showing the wake and the effect of the trapped electrons on it (color: blue to red). Just before trapping in the first bucket behind the laser (A), the wake structure is undisturbed and large in amplitude, allowing self-trapping of electrons. When a bunch is trapped, the wake is damped, suppressing further trapping and hence isolating the initial bunch (B). The bunch is visible in (B) as a small isolated dot in the center of the first bucket, with density comparable to the plasma density (green). These electrons then form a low energy spread bunch when they outrun the wake as the front of the bunch is decelerated and the tail still accelerated. Buckets further behind the pulse trap and dephase earlier; accordingly, bunches are already visible in the trailing buckets before trapping in the first.

energy as seen in Fig. 6.1B, and these high energy electrons outrun the wake and dephase first, beginning to decelerate while the trailing edge is still accelerating. This concentrates the particles at the dephasing energy, and results in the formation of a low energy spread bunch after 1.5 mm propagation (Fig. 6.1C). This optimum length is close to the 1.7 mm length of the high density plateau in the experimental plasma. The dephasing energy obtained at this length is also the maximum energy gain for the given parameters. Electron energy spread increases again with further propagation as the particles are decelerated, unless the plasma is terminated at this point. Peak electron energy remains nearly constant as the particles are mixed to fill all phases in the wake, but the number of electrons at high energy is reduced after 2.2 mm propagation (Fig. 6.1D). The bunch dissipates more slowly than it forms since the laser pulse is depleting its energy into the wake as it propagates, resulting in reduced wake amplitude and slower deceleration, and monoenergetic features are present from  $\sim 1.3$  to 1.9 mm, with the energy of the peak varying from 80 to 220 MeV. The asymmetry may be even greater in three dimensions, where filamentation [12], hosing [3, 88, 89], and other instabilities may further disperse the laser, leading to observation of low energy spread well beyond the dephasing length. Hence we expect that, for plasmas shorter than the dephasing length, low energy beams with continuous distributions would be observed, while at the dephasing length higher energies and structure (i.e. monoenergetic bunches of narrow energy spread) in the distribution would be present. After the dephasing limit, peak energy should not increase, and structure in the distribution and density of particles at high energy should be reduced.

Wake buckets behind the first one also trap particles, but these do not contribute to the highest energy beam. The difference may be due to transverse wave breaking and laser envelope effects. The variation of  $\lambda_p$  with density leads to longer plasma wavelength on the channel axis where the density is lowest (Chapter 2), and the non-linear equations for the plasma wake show that the plasma wave period also lengthens

with increasing amplitude [3, 77]. Both effects lead to longer plasma wavelength on axis, and hence curvature of the wake phase fronts, as visible in Fig. 6.2. Curvature increases with increasing distance behind the laser pulse, and this curvature reduces the threshold for trapping through transverse wave breaking for buckets far behind the pulse [65]. It also increases focusing region in the wakefield [3, 77], and in highly nonlinear wakes such as those in the present experiment the simulations show that nearly the entire accelerating region is also focusing. The trapping threshold has also recently been shown to increase for buckets within the laser envelope (i.e., the first bucket) [118]. Consistent with this, simulations indicate that the wave breaks and picks up particles early and at low wave amplitude in buckets far behind the laser pulse. The peak energy obtainable from the wakefield rises with wave amplitude [3] (Eq. 2.48), so these particles dephase early and at low energy, and do not contribute to the high energy beam. However, as each bucket dephases, its electrons are bunched at the dephasing energy for that bucket. These energies range from 13-100 MeV, compatible with the observation of structure in the experimental energy spectrum at lower energies. Such structure may result when fluctuations in guide quality terminate the wake early, near the dephasing of a particular bucket, or due to fluctuation in laser and plasma parameters.

The parameters of the accelerated bunch are close to those in the experiment, except possibly for the trapped charge. The peak energy observed in simulations and the length over which the beam dephases are reasonably compatible with the experiment. Monoenergetic features are observed in the simulations over distances compatible with the length of the experimental plateau. Energy is 220 MeV for the simulations, not much higher than the experimental observation of 170 MeV. Energy spread is  $\pm 1 - 2\%$  FWHM, in agreement with the experiment. Using the slab calculation of bunch charge, there are  $6 \times 10^8$  electrons in the high energy bunch, lower than the experimental value by a factor of three. Using the cylindrical method, bunch

charge is  $1.5 \times 10^8$  electrons, less than 1/10th of the charge found in experiments. As noted above (Section 6.1), these two estimates provide upper and lower limits on beam loading so that the three-dimensional charge expected is between these values. Studies varying simulation parameters (Chapter 7) suggest that the low charge observed in the simulations is likely due to a combination of simulation resolution and three-dimensional effects neglected in these simulations due to available computer time. There is also sensitivity to variations of physical parameters within the range of experimental fluctuations (such as laser intensity and plasma density) and this may also explain to the the discrepancies (Section 7.4). Because the experimental diagnostics did not observe from zero to full energy in a single shot, it is also possible that the experimentally observed bunches near 86 MeV (Fig. 5.4) may be the lower energy bunch from the second wake bucket. This bunch has a trapped charge of approximately  $3 \times 10^9$  electrons (slab) near 70 MeV after 1.5 mm propagation, compatible with the experimental values, but broader energy spread. Again, sensitivity physical and simulation parameters may explain the discrepancy in energy spread (Chapter 7). The essential physics of electron bunch formation is however consistent for all these simulations, indicating that the description given here is appropriate.

### 6.3 Particle Tracking

Tracking the particles in the simulation allows some of the details of bunch formation to be seen. In the present simulations, this was done by weighting the particles with variable charge (but fixed charge:mass ratio) as described in Chapter 7, then using the particle weight to track the particles from frame to frame. The trajectories of a randomly sampled subset of the particles that were accelerated to high energy were tracked through the simulation, providing information on particle position and

velocity, as well as the fields at the particle locations as a function of propagation distance and simulation time.

Particle coordinate data shown in Fig. 6.3 verify the bunch formation mechanisms discussed above, and provide additional information on the particle trajectories. The particles are colored by injection order, with red particles being those injected first (at the shortest propagation distance), and blue last. The particle acceleration trajectories, Fig. 6.3A, verify that bunching in energy does occur when the front of the bunch (first injected particles) decelerate, while those at the tail (injected later) continue to accelerate. The transverse origin and subsequent behavior of the particles are shown in Fig. 6.3B, indicating that the particles are injected from a radius of approximately  $5 \mu\text{m}$ , rather than being injected on axis. This reflects the strong ponderomotive blowout by the laser pulse which excludes on axis electrons. A similar effect has also been seen in [64], though in much narrower channels where there was also interaction with the channel-vacuum interface. The result of injection from off axis is that particles subsequently execute large transverse oscillations in the wake field. Early and late injected particles are injected from similar radii and follow similar transverse trajectories. This oscillation is being modeled as a potential source of x-ray radiation [34, 119].

The electric fields at the particle locations, shown in Fig. 6.4, help to further distinguish how trapping turns on and off again. As above, the particles are colored by injection order, with red particles being those injected first. As shown in Fig. 6.4A, late injected particles see a much lower initial accelerating electric field than early injected particles, and it is likely that this reduction is what eventually terminates trapping, resulting in the formation of an isolated electron bunch. It is this formation of an isolated bunch which allows the eventual bunching in energy to form a low energy spread bunch. Transverse electric fields are also lower at time of injection for late injected particles, which helps turn off trapping since the transverse field is

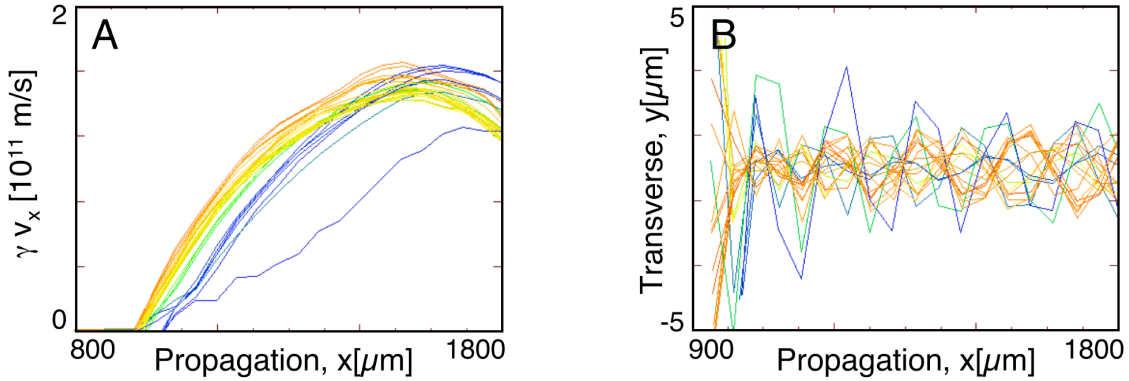


Figure 6.3. Tracks of representative particles in momentum vs. propagation distance (A) and transverse coordinate vs. propagation distance (B). Particles are color coded by injection order, with red particles injected first, blue last. Bunching of the particles at dephasing is evident in the crossing of late injected particles from below to above the energy of the first injected particles near the dephasing point, approximately 1.5 mm of propagation (A). Early and late injected particles follow similar transverse trajectories (B).

required in order to bring the particles from their initial off axis position to the center where the accelerating field is large. Both of these changes indicate beam loading, as described in the previous Section.

## 6.4 Laser Pulse Modulation

The laser pulse is strongly modified by self-modulation and focusing in the simulations at high power, and some features of the modification are consistent with the experiment. Strong radial self-modulation results in high intensity out to much larger radii than at low power (Fig. 6.5). Indeed, after 1.7 mm propagation, intensity at the edge of the simulated plasma at  $r = 30 \mu\text{m}$  is  $\sim 7\%$  of on-axis intensity, and order of a percent of the input intensity. The intensity profile from 10 -30 micron is nearly linear, implying percent level intensities would persist out to the edge of the experimental plasma near  $50\mu\text{m}$ . This intensity is more than sufficient to ionize neutral gas outside the waveguide, consistent with the experimental observation

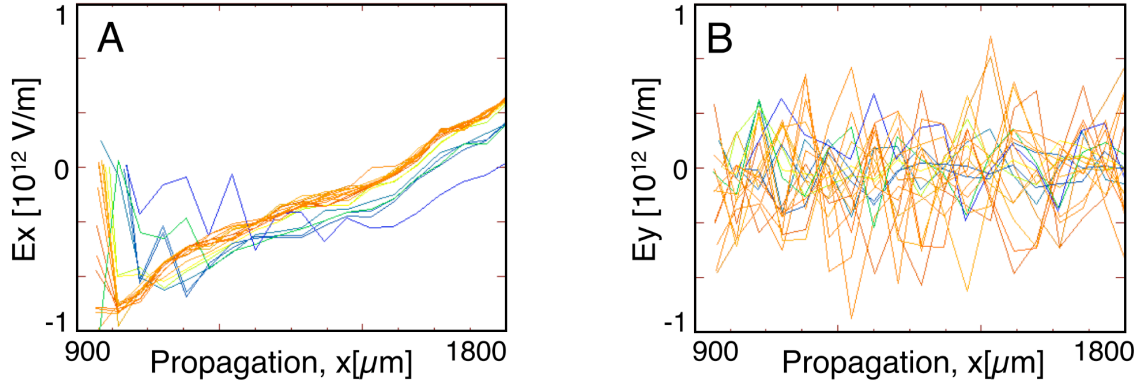


Figure 6.4. Electric fields experienced by representative tracked particles as a function of propagation distance. Particles are color coded by injection order, with red particles injected first, blue last. Late injected particles experience lower accelerating field (negative  $E_x$ ) early on, near injection (A). Later in propagation, the late injected particles are still accelerated while the early injected particles dephase and are decelerated, bunching the particles in energy. Transverse fields (B), required to inject the particles from their initial large radius into the accelerating field on axis, are also lower at time of injection for late injected particles. The declining axial and transverse fields for late injected particles, due to beam loading, eventually turn off of injection, producing the isolated bunch.

that plasma was ionized outside the guide at high powers. The simulation results suggest that this is due not simply to the increased power in the guide, but also due to the altered mode structure resulting from self-modulation. In contrast to the experiment, where the optical pulse is sometimes observed to break up into many filaments, especially at high power, the simulated pulse remains as a single spot. The spot width FWHM also remains less than that of the injected spot, in contrast to the experiment where we always observed the output spot to be larger than the input spot at high power. These discrepancies may be due to differences in the filamentation [12] and hosing [3, 88, 89] instabilities between the (two-dimensional) simulations and (three-dimensional) experiment. Depletion of laser energy is also less than in the experiment, 60% compared to 90%. This reduced depletion may be because self-modulation is more efficient in three dimensions, and may also be part of the reason

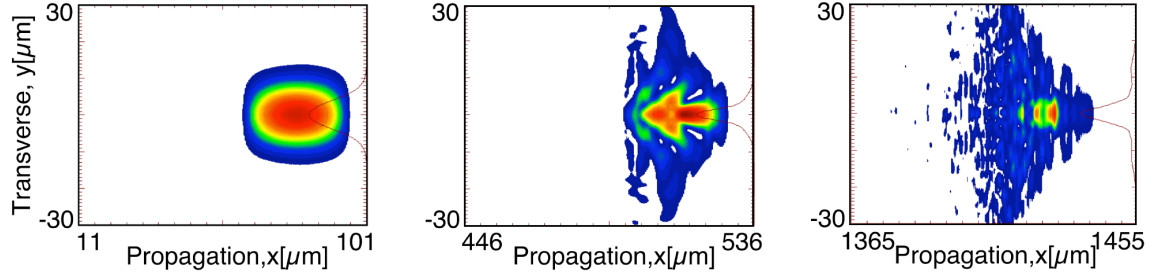


Figure 6.5. Simulated laser mode evolution as a function of propagation distance at a laser power of 9 TW (color: blue to red). Each panel shows a contour plot of amplitude ( $a_0$ ) and a lineout of intensity ( $a_0^2$ ) integrated along the propagation axis. Strong radial self-modulation results in a mode profile with significant intensity at large radius. This is consistent with the appearance of ionization in the neutral gas surrounding the experimental channel at high powers. The distortion of the mode is apparent in comparison to the nearly Gaussian transverse envelope of the guided beam at lower power (Fig. 4.8).

why a smaller number of electrons were trapped in the simulation as compared to the experiment.

## 6.5 Summary

The simulations described in this Chapter make it clear that the high quality beams observed in the experiments are formed when electrons self-trapped by the wake load the wake [16, 17], reducing its amplitude. This in turn prevents further injection, resulting in an isolated electron bunch which is concentrated in energy when the leading edge dephases and is decelerated while the trailing end of the bunch is still accelerating.

Other simulations have also observed the formation of structure in the energy distribution over long propagation distances using self-trapped electrons [61–64]. Previous simulations [63] had indicated that a high energy few-cycle optical pulse (not available experimentally) would be required to produce low beam divergence relatively small energy spread, about  $\pm 10\%$ . Trapping was also continuous in these simulations,

as a result of the very strong laser pulse, so that beam loading did not fully turn off injection. The simulations presented here show that a bunch of narrow spread can be produced by longer laser pulses through self-modulation, as used in the experiments. In addition, it is seen that for specific laser and plasma parameters, beam loading can turn off self-trapping, resulting in bunch isolated in phase space and therefore exhibiting  $\pm 1 - 2\%$  percent energy spread, as observed in the experiments. We discuss the effects of parameter variation further in Section 7.4, which shows that obtaining this small energy spread bunch requires tuning of laser energy and plasma parameters within a few percent. Energy spread of about  $\pm 10\%$  has also been observed for 50 fs laser pulses with a plasma radius of  $7 \mu\text{m}$  and density of  $3 \times 10^{18}$ , and published simultaneously with the results herein [64]. These simulations showed injection from off axis, consistent with the tracking results above. Compression of bunch energy spread at dephasing was also observed, also consistent with the results here. As is shown in Chapter 7, interaction with the channel walls in such narrow channels increases trapping relative to the experimental case. All of these simulations observe transverse beam loading, and the simulations presented here indicate that for the experimental parameters longitudinal loading is also important.

The simulations reproduce many of the important features of the experiment, including laser modulation/guiding features, the length over which the electron bunch is formed, and many of the characteristics of that bunch. Energy and energy spread are near experimental values. Trapped charge is a factor of a few below experimental values, most likely due to a combination of three-dimensional and simulation resolution effects as well as variation in physical parameters as discussed above and in the following Chapter. We now turn to the numerical and physical validations that underlay these simulations and which show the level of confidence that can be expected.



# Chapter 7

## Simulation Numerical and Physical Parameters

This Chapter describes the results of more than one hundred simulation runs which explored the effects of numerical and physical parameters on the simulation results. These simulations were conducted to validate and elaborate on the simulations of electron bunch formation described in Chapter 6. Initial checks were first made to determine the simulation box size, boundaries, and particle load that would produce initially usable results. Where possible, the simulations were checked against analytic models. Dependence of simulation results on numerical parameters was next studied to evaluate whether the simulations are converged, and which parameters are most important. Numerical parameters included longitudinal and transverse box size and resolution, particle resolution and weighting, particle load, and time step. Lastly, the effect of variation in physical parameters on the simulations was evaluated. Physical parameters included pulse shape and energy, plasma density and longitudinal and transverse profile. All simulations described are two-dimensional particle-in-cell (PIC) simulations [70] using the code VORPAL [74]. Considerations relating the

two-dimensional simulations to the three-dimensional experiments are presented in Section 6.1.

## 7.1 Initial Simulation Design

The initial simulations were designed based on previous laser plasma PIC simulations [73,74], which suggested appropriate starting parameters, as well as the physical parameters of the experiment. The initial numerical resolution was chosen to well resolve the characteristic scales of variation in each axis. To first order this is the laser wavelength  $\lambda$  in the propagation direction, and the laser spot size  $w_0$  in the transverse direction. Given the experimental parameters of  $\lambda = 0.8 \mu\text{m}$  and  $w_0 \sim 7 \mu\text{m}$ , using 16 cells/period as a starting point (both from previous PIC work and as a generally reasonable number to describe a curve) indicated a cell spacing of 16 cells/ $\lambda$  longitudinally, and 2 cells/ $\lambda$  in the transverse direction. These parameters were used for the initial runs, and further checks on the effects of resolution are described below.

In order to provide reasonable computation time, the simulation window co-moved with the laser pulse and only a few plasma periods behind the laser pulse were resolved in the longitudinal direction. As we have seen in Chapter 6, this region covers the important physics of beam formation. The moving window moves at  $c$ , as it is then physical to assume that unperturbed plasma flows in the front of the box, and nothing from behind the box can propagate forward into it. Hence the longitudinal box size was chosen to accommodate both several plasma periods and slippage of the laser pulse in the box due to its group velocity in the plasma being less than  $c$ . Considering the group velocity, we have (Eq. 2.29)  $v_g = c\sqrt{1 - \omega_p^2/\omega^2} \sim 0.995c$  for a plasma of density  $1.8 \times 10^{19} \text{ cm}^{-3}$ . Over 2 mm propagation, the laser pulse will then slip back by  $10 \mu\text{m}$  relative to a frame moving at  $c$ . With a plasma period near  $8 \mu\text{m}$ , and a pulse length of  $16 \mu\text{m}$  as in the experiment, a box at least  $40 \mu\text{m}$  long is needed.

Runs with box lengths of 40, 60, and 90  $\mu\text{m}$  showed that a 90  $\mu\text{m}$  box was sufficient to resolve the wake periods that participate in beam generation, and this size was used for the remaining simulations.

The transverse boundary conditions available in the code were reflecting for electromagnetic waves, and this necessitated a box large enough that reflections from the boundary did not re-enter and interfere with the simulation. At a transverse dimension of 40  $\mu\text{m}$ , the laser field amplitude is down to less than 0.1% of peak value for a Gaussian pulse with  $w_0 = 7 \mu\text{m}$ , and this was used as an initial value. Even though the laser is weak at this radius, reflection from the wall still resulted in unacceptable perturbation of the simulation. Runs using transverse box sizes of 80 and 120  $\mu\text{m}$  showed that perturbation was small at the latter size for channeled simulations over 2 mm propagation distances.

Subsequent simulations showed that a smaller transverse box could be used by leaving a narrow strip of vacuum (no particles) near the edge of the box. This low density region effectively acted as a ‘channel’ at the edge of the simulation, helping to prevent unwanted boundary reflections from returning to the simulation. Both a sudden cut off in the density profile and a cosine ramp to zero density were tried: for densities near  $2 \times 10^{19} \text{ cm}^{-3}$ , there was little difference, but for higher densities the cosine ramp showed less reflection due to the smoother profile. These results are consistent with the guiding theory of Section 2.5.1, which showed that light is diffracted away from high density toward low density regions. Use of a partial transverse load allowed use of a smaller box, now 90  $\mu\text{m}$  long and 80  $\mu\text{m}$  wide, without destructive perturbation by reflections. This in turn reduced computational requirements for a given resolution.

Increased simulation efficiency was also obtained by using variably weighted particles to represent the channel. In a PIC code, each simulated particle represents

many physical particles (typically, a few  $10^7 - 10^8$  particles are simulated, versus a few  $10^{14}$  in the physical problem). The plasma is least dense on the axis of laser propagation, so that using constant weight ( $N_{real}/N_{simulated}$ ) results in more particles per cell off axis. This is inefficient, since only the center of the plasma interacts strongly with the laser, and hence the largest number of particles (and computational time) is spent in areas not important to acceleration. The variable weight scheme used loads a constant number of particles per cell, changing the particle weight to represent varying density. For channeled problems as discussed here, this saved approximately 50% in computation time for a given number of particles per cell on axis. This in turn allowed higher particle resolution on axis, where it is needed most. The variable weighting may however affect trapping, as discussed in the following Section.

Since the particles are variably weighted, and the density varies with radius due to the channel, the particle weight can be used to track individual particles if the weights (that is, transverse positions) are not re-used. The quiet source loader [70,74] used for these simulations prevents re-use of positions in order to reduce particle noise induced seeding of high frequency modes. However, if the simulation center is on a cell boundary or center, the negative of a position is also used, resulting in two particles for each weight. This was rectified by choosing the simulation center to be slightly off of the cell boundary (i.e. by making the transverse limits slightly asymmetric: -60.2 to 59.8 rather than -60 to 60), and by using double precision to represent the weights and positions. In this case, only one particle per weight is generated, enabling particle tracking by weight. No difference was found in simulation output between runs with the offset center and runs with the center on a cell boundary, so that this change does not affect the result. Tracking the particles allowed the positions as a function of time to be analyzed in order to determine injection mechanisms, as shown in Chapter 6.

The simulations were run with a cold (zero velocity) initial plasma load, in or-

der to prevent grid-induced self-heating. Due to the numerical dispersion relation, a warm plasma will self-heat [70] until the Debye length is about equal to the grid spacing. For grid parameters such as those used here, this indicates plasma temperatures of keV, much greater than the 30 eV experimental temperatures. Using a zero temperature load, which does not self-heat, is then more accurate. A grid fine enough to produce accurate temperatures at self-heating saturation was not possible due to computational time. However, temperature would be a parameter of interest for future simulations - in the current work the plasma was left at hundred-eV temperatures after the passage of the laser, and this temperature depended on resolution, indicating that it is not physical and may affect results.

No significant difference was found between runs using or not using a Hamming filter to smooth current deposition, or between different versions of the code.

## 7.2 Checks Against Analytic Fluid Models

The simulations were checked against analytic models by running at low  $a_0$  and short pulse lengths. In this case the analytic formulae for laser guiding, pulse propagation, and wake generation derived in Chapter 2 are valid, and can be compared against the simulations. This provides confidence for subsequent scaling to higher intensities where the simulations must stand on their own. To do this, a simulation was run with a laser amplitude  $a_0 = 0.22$ , Gaussian transverse profile with spot size  $8.5 \mu\text{m}$  FWHM, and a sine pulse shape of length of 12 fs FWHM. The pulse length was chosen to match the plasma period for the density on the channel axis ( $1.8 \times 10^{19} \text{cm}^{-3}$ ) providing operation in the linear standard wakefield regime covered by analytic models. The plasma transverse profile was matched to guide the laser pulse, and 10 particles per cell were used, with variable weight to represent the guiding channel. This simulation used a grid of 1800 x 300 cells in a co-moving window 90 x 80  $\mu\text{m}$

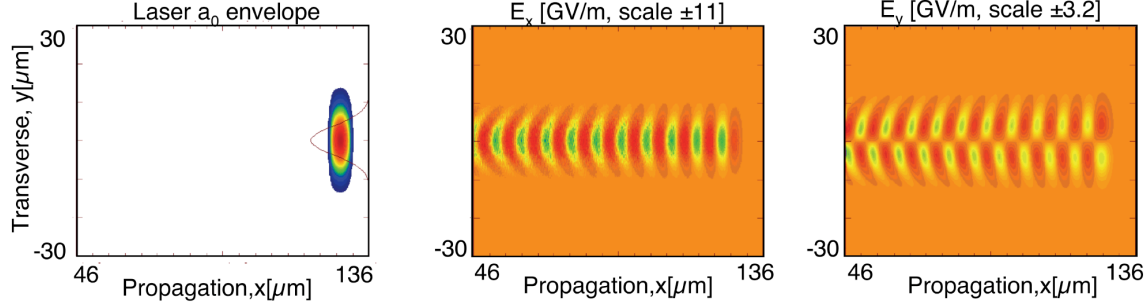


Figure 7.1. The laser pulse (left) and axial (center) and transverse (right) wake structures for a simulation comparing to fluid calculations (color: blue to red). The evolution of the laser spot, and the generation of the wake, are close to fluid formulae for this low intensity case.

in size. The time step was 0.997 times the Courant condition  $dt_c$  (see below for details on time step). The laser pulse length and intensity were reduced to match the linear regime, and the plasma channel density rise was increased to make a matched channel, relative to runs reproducing the experiment (Chapter 6). Spot size, plasma channel axial density, and simulation size are the same as in runs reproducing the experiment, maximizing the relevance of the checks. The wake structure and laser spot profile from this simulation are shown in Fig. 7.1.

Over 300  $\mu\text{m}$  of propagation, well more than  $Z_R$ , the laser spot diameter remained within 0.4  $\mu\text{m}$  of the initial 8.5  $\mu\text{m}$ . The small oscillation present seems to originate from the slight expansion of the laser pulse from where it is launched in the simulation to where it enters the plasma 40  $\mu\text{m}$  later. This results in a small mismatch to the guide, but the discrepancy is within one cell of transverse resolution and hence is within the expected precision in any case. For reference, an unguided beam expands to 15  $\mu\text{m}$  over the same distance, as described by Eq. 2.21 and verified by simulations run without a plasma. Hence, the simulated laser transverse properties match the expected analytic guiding model in the low intensity limit.

The laser group velocity in the simulations matched fluid theory calculations. For the density used here, Eq. 2.29 indicates  $v_g = c\sqrt{1 - \omega_p^2/\omega^2} \sim 0.995c$ . Group velocity

is affected by the channel structure and the dispersion then becomes:  $\omega^2/c^2 - k^2 = k_p^2 + 2/w_0^2$  [52]. We then use  $k_p^2 + 2/x_0^2$  in place of  $k_p^2$  to account for the channel in Eq. 2.29, and the group velocity is then:  $c\sqrt{1 - (k_p^2 + 2/x_0^2)/k^2} = 0.994c$ . The laser pulse in the simulation slipped back with respect to the moving window, traveling at  $c$ , by  $1.2 \mu\text{m}$  over  $196 \mu\text{m}$  of propagation, indicating a velocity of  $0.994 c$  which is matched to the channel theory result.

The simulated wake can be compared to analytic fluid models, since for these parameters agreement should be close with the fluid model derived in Section 2.2. Plasma wavelength is  $7.6 \mu\text{m}$ , very close to the  $7.8 \mu\text{m}$  calculated from the plasma frequency and group velocity. The discrepancy may be due to channel plasma density variation across the channel, as well as the measurement resolution. The fluid model predicts peak accelerating electric field of (Eq. 2.17)  $7.7 \times 10^9 \text{ V/m}$  for the laser intensity launched into the simulation. However, the variation of spot size due to coupling, described in Section 7.2, slightly reduces  $a_0$ , and using the amplitude present in the plasma we obtain  $7.4 \times 10^9 \text{ V/m}$  which compares well to the observed  $7.3 \times 10^9$  in the simulation. The radial wake also has the structure expected from the Panofsky-Wenzel theorem, Eq. 6.1, and the ratio of peak transverse electric field to peak longitudinal field matches the theorem at 20% (for the spot size used). This indicates that focusing forces will be well represented by the simulations. Overall, we obtain agreement within a few percent with simple fluid models for this low intensity case, indicating that the simulations reasonably reproduce the desired quantities. Increasing resolution to 2700 by 300 grid points improved agreement with the analytic models slightly, though agreement was already very good. Peak axial field increased from  $7.3$  to  $7.4 \times 10^9 \text{ V/m}$ , the latter being in agreement with the fluid model. Group velocity and pulse propagation were similar. We can then use the simulations to explore higher intensity phenomena not accessible by analytic formulae. However, as discussed below, quantities such as particle trapping are much more sensitive than

the linear accelerating field, and require higher resolution for convergence than the 16-24 by 3 cells/ $\lambda$  indicated by these checks.

### 7.3 Numerical Convergence and Parameters

We next turn to the details of numerical parameters which influenced the output for simulations of high intensities similar to the experiment, as described in Chapter 6. The simulations probe regimes not accessible to the analytic checks, and small perturbations can be important, so that numerical checks on convergence are required. Important numerical parameters include time step as well as grid and particle resolution.

Due to numerical dispersion, the time step in the simulations must be selected appropriately to yield accurate results. PIC codes use a ‘leap frog’ finite differencing scheme, in which electric field ( $\mathbf{E}$ ) and charge density ( $\rho$ ) are known at integer time steps, magnetic field ( $\mathbf{B}$ ) and current density ( $\mathbf{J}$ ) at half integer. Applying finite differencing to the wave equations in one dimension then produces the wave equation solved by the code [70]. For a light wave in vacuum, it is found that  $\Omega = c\kappa$ , where  $\Omega$  and  $\kappa$  are the numerical  $\omega$  and  $k$  respectively, only for a specific time step known as the Courant condition  $cdt_c = dx$ . At this time step, a light wave propagates in vacuum at  $c$ . For longer timesteps, the method is unstable. Shorter timesteps result in unphysical dispersion, yielding phase and group velocities smaller than the physical values. For stability, one then wishes to run at time steps less than but as close as possible to  $dt_c$ . The deviations for various time steps are plotted in Fig. 7.2. Due to the mismatch in the numerical dispersion relation between  $k$  and  $\omega/c$ , both group and phase velocity differ from  $c$ . This is most pronounced for coarse grid spacings and timesteps significantly smaller than  $dt_c$ . The simulations compared with the experiments (Chapter 6) used 24 cells/ $\lambda$ , and a timestep of  $0.997 dt_c$ , resulting in

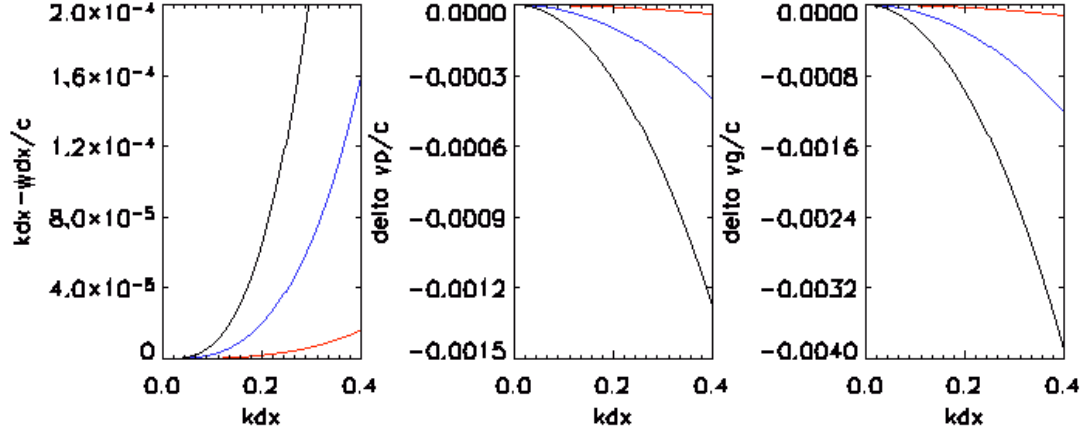


Figure 7.2. Plot of numerical dispersion for timesteps of 0.9 (black), 0.97 (blue) and 0.997 (red) times the Courant condition timestep  $dt_c$ . Due to the mismatch in the numerical dispersion relation between  $k$  and  $\omega/c$ , both group and phase velocity differ from  $c$  (delta  $vg$ ,  $vp$ ). This effect is most pronounced for coarse grid spacings ( $kdx$  large) and for timesteps significantly different from  $dt_c$ . The simulations used for comparison with experiments were conducted at 24 cells/ $\lambda$  or  $kdx = 0.26$ , and a timestep of 0.997  $dt_c$ , resulting in a group velocity error of  $5 \times 10^{-5}$  which is very small compared to the plasma modification ( $5 \times 10^{-3}$ ).

a group velocity error of  $5 \times 10^{-5}$ , which is very small compared to the plasma modification ( $5 \times 10^{-3}$ ).

The group velocity has been confirmed by observing the propagation of the laser pulse and confirming that it propagates at the expected velocity. Using a time step of 0.997 to 0.995  $dt_c$ , the pulse propagated at the rate indicated by the fluid calculation (previous section) for 16 or more cells/ $\lambda$ . Smaller time steps resulted in a non-physically slow group velocity, and this affected trapping, laser propagation and other simulation results. This effect was modest for timesteps as short as 0.97  $dt_c$  and large for steps of 0.9  $dt_c$ . Most significantly, at a resolution of 16 cells/ $\lambda$ , trapping and acceleration to high energies was observed in the first bucket for powers of 4 TW with a time step of 0.97  $dt_c$ , whereas this trapping does not occur for timesteps of 0.997  $dt_c$  due to the (correct) higher velocity of the wake. This illustrates the importance of dispersion to accurate simulations. Changing from 0.997 to 0.995  $dt_c$

at 9 TW and 16 cells/ $\lambda$  increased trapping only 5%, which is reasonably converged. Since the physical group velocity becomes higher with decreasing plasma density, future simulations of standard laser wakefield accelerators at densities near  $10^{18} \text{ cm}^{-3}$  will have to pay close attention to dispersion to ensure accurate results, as a very small numerical dispersion can then be problematic.

Grid cell spacing is important as it determines how well the laser and wake are resolved, and also plays into laser propagation velocity as indicated above. Runs were conducted with longitudinal spacings of 16, 24, and 32 cells/ $\lambda$  (1800, 2700, and 3600 cells total), with a transverse resolution of 3 cells/ $\lambda$  (300 cells total) and 10 particles per cell in all cases (Fig. 7.3). The wake and laser pulse structure changed only slightly. Particle trapping and bunch formation changed dramatically however, indicating the importance of higher resolution to accurately analyze self-trapping. Trapped charge using the cylindrical approximation of Section 6.1 increased twofold from  $1.2$  to  $2.4 \times 10^8$  electrons when longitudinal resolution was increased from 16 to 24 cells/ $\lambda$ . Using the slab charge approximation, charge also increased nearly a factor of two, from  $6 \times 10^8$  to  $1 \times 10^9$ . Energy spread of the bunch decreased from  $\pm 12\%$  to  $\pm 2\%$  FWHM and bunch energy increased from 166 to 200 MeV. Note that this is true even though numerical dispersion is less significant in the latter case, which should cause trapping to decrease due to increased group velocity, all other parameters being constant. This indicates the sensitivity of self-trapping to precise details of particle phase space, which are better resolved in the high resolution case, even though the gross properties such as longitudinal field are, as indicated in the previous Section, essentially invariant with resolution. Increasing resolution from 24 to 32 cells/ $\lambda$  had only a 10 % effect on trapping and almost no effect on energy or energy spread, indicating that the simulations are approaching convergence in longitudinal resolution.

The effect of changing transverse resolution on trapping (for longitudinal spacing

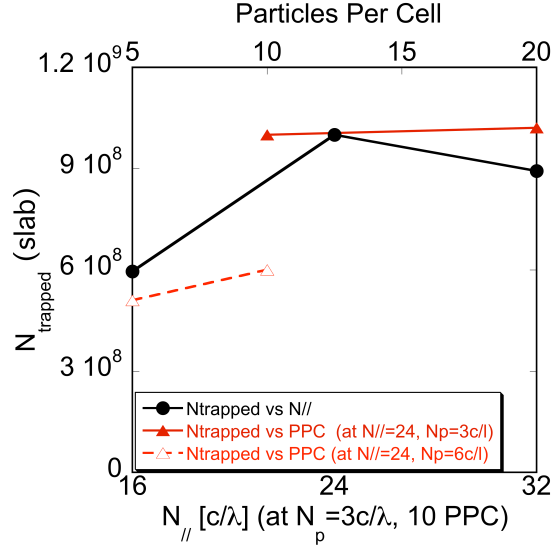


Figure 7.3. Trapped particle number versus simulation longitudinal resolution ( $N_{\parallel}$ ) and particles per cell (PPC). Transverse resolution is denoted  $N_p$ . Trapped charge increases with particles per cell, and appears to peak near 24 cells/ $\lambda$  for longitudinal resolution. Changes at the highest resolutions are small (10% level or less), indicating that these are approaching the needed resolution.

of 24 cells/ $\lambda$ ) also significant. An increase from 3 to 6 cells/ $\lambda$  reduced energy spread by approximately a factor of two to  $\pm 1\%$  FWHM and trapped charge by 35% to  $1.5$  or  $6 \times 10^8$  for the cylindrical and slab calculations respectively. Bunch energy rose slightly to 220 MeV. Below 3 cells/ $\lambda$ , the wake structure is also affected, with reduced transverse field. At 1 cell/ $\lambda$ , there was little trapped charge and the bunch was very poorly formed and broad in energy spread. These changes are likely due to the need to resolve fine transverse structure in the wake near the trapping point (Fig. 7.5, below). Micron scale transverse structures form at the edge of the wake due to the near complete blow-out of the plasma by the laser pulse. This in turn requires resolution of much smaller structures than the laser spot size, which is the characteristic scale at lower intensities. These results indicate that runs with higher transverse resolutions would be desirable.

The number of particles per cell determines, among other things, the smoothness of the plasma density. Because a small number of particles are simulated relative to

the physical system, there is more high frequency noise in the simulated density, but this decreases as the number of simulated particles increases. For particle trapping, number of particles per cell also in effect sets the minimum ‘fraction’ of that cell’s charge that can be trapped - if one uses 10 particles per cell for instance, then the options are 0, 10, 20... up to 100 %. Bunch charge increased 20%, and energy spread decreased slightly, with increasing particle resolution in comparing runs with 5 and 10 particles per cell at a grid resolution of  $2700 \times 600$  (Fig. 7.3). Bunch energy was not affected. This may be due to smoother resolution of fine wake structures and of trapping. Increasing to from 10 to 20 particles per cell at  $2700 \times 300$  cells did not did not affect trapping significantly.

Variable or constant weighting of the macro particles also appears to have an effect. A run using constant weight particles at a resolution of  $1800 \times 300$  cells and 10 particles per cell on the channel axis trapped twice the charge of a run using variable weight particles and with otherwise identical parameters, yielding a bunch charge of  $1.3 \times 10^9$  electrons (slab approximation) even in this low resolution case. Energy was lower at 150 MeV and spread greater at  $\pm 15\%$  FWHM, than the comparable variable weight case which showed 166 MeV  $\pm 12\%$ . The increase in trapped particles is much more than expected based on the results versus particles per cell above and the slightly larger number of particles off axis (due to the channel profile) in the constant weight case. Noise in the density distribution appears somewhat higher in the constant weight case, which may affect trapping, but the reason for the differences observed is not known.

It is clear from these simulations that particle trapping results are changing with resolution in both grid and particles, and that with higher resolution the results are more closely approaching those of the experiments. This is true despite the fact that general wake parameters change little, indicating the sensitivity of the trapping problem. Substantially higher resolution simulations are then desirable in order to

provide replication of the experiments. This will rely on the availability of computer time and on future algorithm developments which may afford efficiency gains.

## 7.4 Physical Parameters

Having considered the numerical parameters important to the results, we next turn to the ‘physical’ parameters which influence the simulation output. While the results of the previous Section illustrate the accuracy and limits of the simulation results, here we consider how the simulations can give insight into the effect of variation in the laser pulse and plasma.

The polarization of the laser pulse is very important to trapping and acceleration. This difference suggests the importance of three-dimensional effects and of physics not covered by the ponderomotive model used in Section 2.2 (since that model is symmetric with laser polarization). Runs with the laser pulse polarized in the plane of the simulation trapped approximately two times the charge compared to out of plane polarized simulations, yielding approximately  $2 \times 10^9$  electrons at 120 MeV (slab calculation). The energy spread of the bunch was much broader at  $\pm 15\%$  FWHM, and as a result the bunch density was actually lower for the in-plane polarized runs. Peak energy is lower, most likely due to increased beam loading [16,17] from the larger trapped charge, resulting in lower accelerating field. This is shown in figure 7.4. The differences are likely associated with the oscillation of the electrons in or out of the simulation plane; though the general structure of the wakes are similar, high frequency features appear at the laser frequency in the longitudinal field in the case where the laser is polarized in plane. These runs were conducted with  $2700 \times 300$  grid points at a time step of  $0.997 dt_c$ , with 10 particles per cell. The resolution scalings above hence suggest that a high resolution constant weight run with in plane polarization might produce a bunch with energy spread and charge close to the experiment.

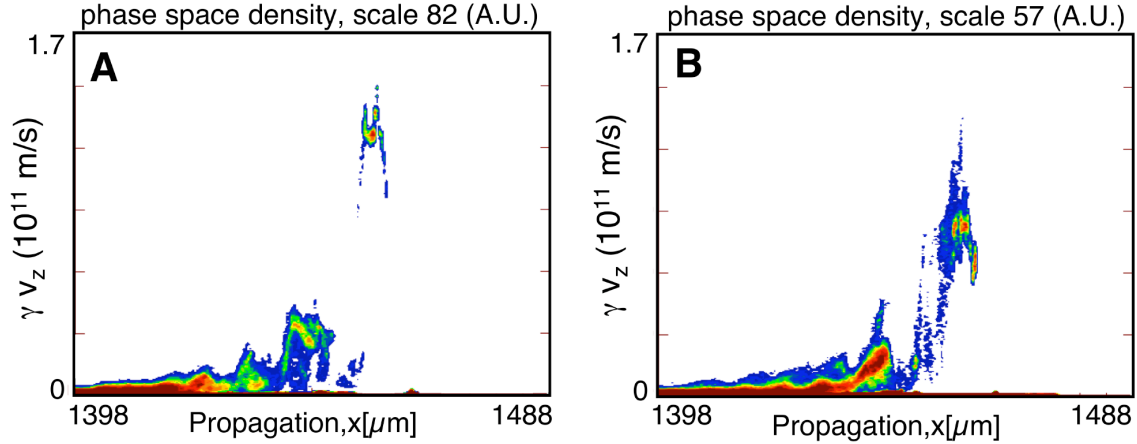


Figure 7.4. Electron phase space density (A.U.) for runs with opposite laser polarizations (color: blue to red). Polarization out of the simulation plane (A) results in trapping of less charge ( $1 \times 10^9$  electrons using slab calculation) but a narrower energy spread, and as a result the phase space density is high. Polarization in the simulation plane (B) traps more charge ( $2 \times 10^9$  electrons, slab) but broad energy spread results in a lower phase space density.

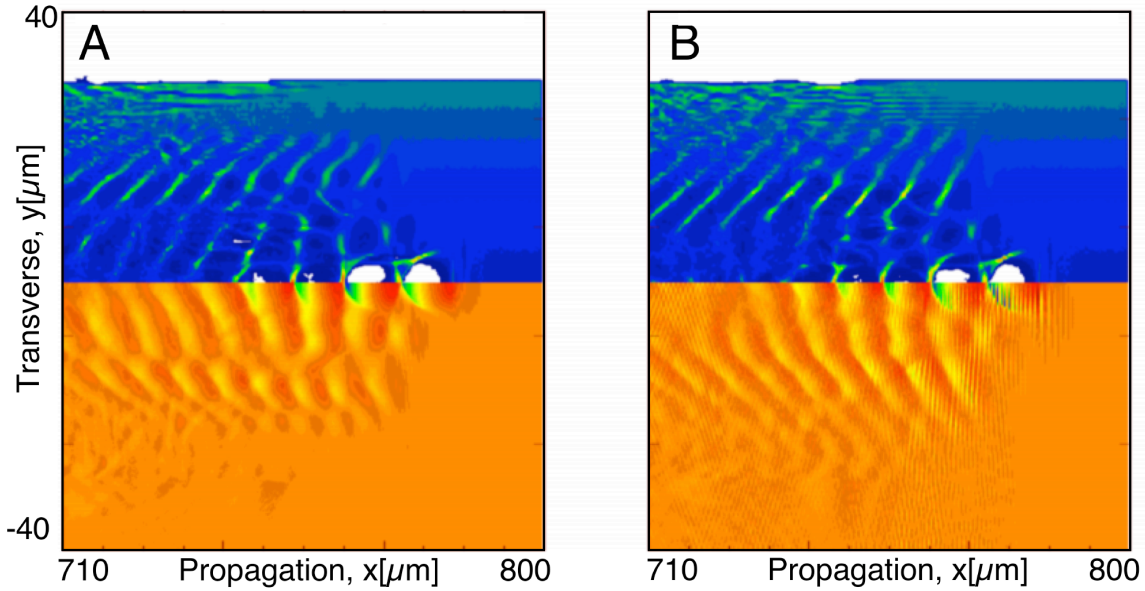


Figure 7.5. Electron density (top half plane, scale  $8 \times 10^{19} \text{ cm}^{-3}$ ) and longitudinal field (lower half plane, scale 800 GV/m) for runs with opposite laser polarizations (color: blue to red). Density is smoothed over the laser period but electric field is not, showing that while the general wake structure is very similar, polarization in the simulation plane results in high frequency features at the laser frequency.

Laser amplitude strongly affects trapping. Increasing laser intensity by 15% increased trapped charge nearly threefold to near  $2 \times 10^9$  (slab) in simulations using  $1800 \times 300$  grid points at a time step of  $0.997 dt_c$ , with 10 particles per cell. Energy spread also increased from  $\pm 10$  to 25% because trapping did not turn off fully, producing a bunch less cleanly isolated in phase space. This indicates the severe sensitivity of self trapping to laser amplitude and the need for stabilization in order to generate reproducible electron beams. Due to experimental fluctuations in laser power and plasma density of  $\sim 10\%$ , this also indicates that the simulation results are likely compatible with the experimentally observed spectra and trapped charge (which have a few times the charge of the simulation results for the nominal laser parameters).

Several variables in the plasma profile have been simulated, including the density, channel transverse shape and size, and the length of the ‘ramp’ or region over which the plasma rises from vacuum to the plateau density. Plasma ramp length had a small effect on the results for ramp lengths of 30-150  $\mu\text{m}$ , with trapped charge and bunch energy changing only  $\sim 10\%$  at a resolution of  $1800 \times 300$  cells and 10 particles per cell. The primary effect seems to be due to the diffraction of the laser pulse (which is launched at focus at the wall in all cases), which causes a slightly larger injected spot size for the longer ramp. This in turn delays self-modulation and wake generation, requiring longer propagation distance for the same wake development. Further studies using a launcher able to focus at the edge of the plasma density plateau, as done in the experiment, would be of interest, but these results indicate that the shorter ramp used in the simulations is not likely responsible for differences between experiment and simulation. This is reasonable, as a large wake is not driven in the ramp region since the laser has not yet self-modulated. The important trapping and acceleration physics occurs only after  $\sim 1$  mm propagation, well beyond the ramp.

The transverse shape and size of the plasma is also important. Trapped charge

is very sensitive to the channel density rise; use of a matched channel satisfying Eq. 2.37 reduced trapped charge by a factor of two compared to simulations with the experimental profile, which has a 40% reduced rise in density. These simulations had a resolution of  $1800 \times 300$  cells and 10 particles per cell. In narrow plasmas it appears that interaction of the wake with the plasma wall increases trapping. Reducing plasma diameter from 60 to 38  $\mu\text{m}$  increased trapping nearly twofold, with minimal impact on energy spread, at a (lower) resolution of 1800 cells longitudinally and 1 cell/ $\lambda$  transversely (=100 cells for the 60 micron width). Large trapping in thin plasma columns has also been observed by other simulations [64,120]. These simulations give an idea as to which plasma factors are important, and indicate the potential for future simulations with more variations of parameters to optimize results. Structure within the plasma, such as a change in density with propagation, could also be important, and has not yet been explored.

## 7.5 Summary

The simulations described in this Chapter provide insight into the numerical behavior of the simulations and also the response to physical parameters. The simulations are not converged in resolution, though the changes are becoming small at the highest resolutions tested. Comparison of various runs suggests that trapped charge increases, peak energy decreases, and energy spread decreases with increasing resolution for most numerical parameters, bringing the results closer to the experiments. Bunches of up to  $0.3$  to  $1 \times 10^9$  electrons (lower and upper limits from cylindrical and slab calculations respectively) in few percent energy spread near 200 MeV were observed in simulations using the nominal experimental parameters and out of plane polarization, and these are close to the experimental results. Runs varying numerical and physical parameters indicated that the lower charge and higher energy in

the simulations resulted from a combination of resolution and three-dimensional effects as well as uncertainty in physical parameters within the experimentally observed fluctuations.

Variation of physical parameters such as plasma and laser shapes in the simulations gave a controllable way of evaluating the effects these quantities. Comparisons indicated that polarizing of the laser pulse in the plane of the simulation increased trapping, implying that three-dimensional effects are important. This is also indicated by the lower energy depletion of the laser into the wake in the simulations than in the experiments (noted in Chapter 6). Bunch charge up to  $2 \times 10^9$  (cylindrical and slab approximately equal in this case) electrons was observed with polarization in plane, compatible with the experiments, but with energy spread of 15%, broader than the experiment. Dramatic sensitivity to laser amplitude and transverse channel profile were observed, with as much as a factor of three increase in trapped charge for a 15% increase in intensity, which is close to the experimental laser fluctuations. The sensitivity of dependence on these quantities points to a large space available for optimization and to the need for precise specification of parameters to match the simulation and experimental results. The effect of the plasma ramp length was weak.

Due to available computer time, most of the simulations described here were performed on a desktop computer (dual G5 2 GHz with 2.5 GB memory), with the highest resolution runs performed on the NERSC supercomputer Seaborg using 128 processors. Indeed, three-dimensional simulations done by other researchers have reported trapping and acceleration of  $10^9$  electrons to 80 MeV, similar to the experimental results [121]. However, these simulations required  $\sim 100$  G5 CPU's to run even with only 2 particles per cell and  $32 \times 4$  cells/ $\lambda$ . Energy spread was large in these 3D simulations, which the results described here imply may be related to numerical resolution and tuning of physical parameters.

Despite the limits on accuracy imposed by resolution, the basic features of the results are robust; self-trapping injects electrons into the wake, beam loading suppresses further trapping, and particles are subsequently concentrated in a small energy range at the dephasing point. This gives good confidence that while the details may vary, the essential physics is correct. In addition, the dephasing length is close to 1.5 mm in all the simulations, so that this parameter is likely predicted accurately (except for possible three-dimensional effects). This value is also close to the length of the experimental plasma flat top  $\sim 1.7$  mm. Peak energies, trapped charge, and energy spread similar to the experiments have also been observed, though not all in the same simulation. Based on the results above, it appears likely that higher resolution and inclusion of three-dimensional effects, coupled with further variation of parameters within the experimental uncertainty (including details of plasma and laser shape/amplitude), could reproduce a bunch similar to that formed in the experiment.

# Chapter 8

## Optimization of Beam Quality at Dephasing

The experiments of Chapter 5 demonstrated production of high quality electron bunches with small energy spread, and the simulations of Chapter 6 indicated that these were formed when electrons were bunched in energy at the dephasing length. In this Chapter we describe experiments which demonstrated the dependence of electron bunch energy and energy spread on dephasing by changing the length and density of the plasma target [59,60]. Use of various target conditions allowed evaluation of accelerator performance for accelerator lengths greater than, equal to, and less than the dephasing length.

Variation of gas jet density was accomplished by variation of the backing pressure, while length was varied by using shaped nozzles (Appendix B). The jets were supersonic to produce short edge gradients and a plateau region of nearly constant density whose length was determined by the nozzle size Fig. 8.1. We used a slit gas jet which provided a plateau of either 600  $\mu\text{m}$  or 4 mm long depending on rotation with respect to the laser axis. For intermediate length, a cylindrical jet with a 1.8

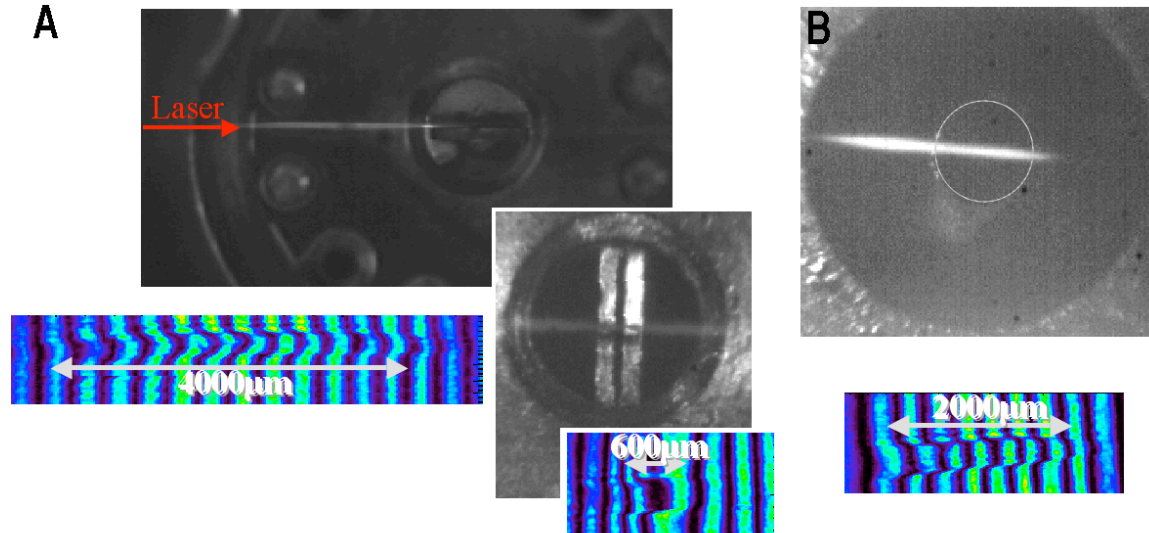


Figure 8.1. Use of different gas jets and densities provided targets to evaluate acceleration before, at, and after dephasing. A slit gas jet (A) provided a plateau of 600  $\mu\text{m}$  at up to  $4 \times 10^{19} \text{ cm}^{-3}$ , or 4 mm at up to  $2 \times 10^{19} \text{ cm}^{-3}$ , depending on rotation with respect to the laser axis. For intermediate length, a cylindrical jet (B) with a 1.8 mm plateau and density up to  $4 \times 10^{19} \text{ cm}^{-3}$  was used.

mm plateau was used. Operating height of the laser above the jets was 0.5-1 mm, selected to avoid burning the jet with the laser, and was greatest for the longer jets to allow for laser divergence. These selections gave us plasmas 0.6 or 1.8 mm long at  $4 \times 10^{19} \text{ cm}^{-3}$ , and 0.6 or 4 mm long at  $2 \times 10^{19}$ . Only the lower density was possible in the 4 mm long plasma, because the greater operating height required for the long plasma allowed the gas to expand further.

To allow evaluation of the electron beam statistics, no slit was used in the magnetic spectrometer. In this case, the spectrometer subtends 30 mrad solid angle so that (according to the BPS data in Chapter 5) most beams produced are within its acceptance. Momentum resolution is reduced, but bunching in the energy spectrum is still visible.

Laser and target conditions were similar to the experiments of Chapter 5. The laser was focused to an intensity of  $1.1 \times 10^{19} \text{ W/cm}^2$  in a spot of  $8.5 \mu\text{m}$  FWHM in hydrogen gas jets. The pulse length was 55 fs, a few times the linear plasma period

for the densities used, in the self-modulated regime [20]. As the laser entered the gas, its front edge ionized a plasma. As in the experiments of Chapter 5, the pulse modulated into sub-pulses at the plasma period as it propagated, trapping particles and accelerating them [4, 10, 22]. Channeling and pre-ionization were not used for these experiments, so that they also provide a further comparison between channeled and unchanneled operation.

## 8.1 Acceleration and Dephasing Lengths

Using the available jet lengths and densities, acceleration experiments were conducted with plasma length greater than, equal to, or less than the dephasing length. This allowed us to experimentally evaluate the evolution of structure in the electron beam energy spectrum. In order to allow electron trapping from the background plasma, the experiments were in the self-modulated regime. In this regime, the analytic solution for the dephasing length,  $L_d = \lambda_p^3/\lambda^2$  where  $\lambda_p$  is the plasma wavelength (Eq. 2.47), is not adequate because of the need to account for modulation and trapping, and the dephasing length was therefore evaluated using simulations.

The simulations described in Chapter 6 were repeated without guiding for plasma densities of 2 and  $4 \times 10^{19} \text{ cm}^{-3}$ . Numerical parameters included a moving window co-propagating with the laser pulse, 90  $\mu\text{m}$  long in the longitudinal direction by 80  $\mu\text{m}$  transversely. The grid was  $1800 \times 300$  cells with 10 particles per cell. Timestep was  $0.997 dt_c$ , and the pulse was a half sine shape with the experimental spot width, intensity, and pulselength. Electron beam behavior in these simulations is qualitatively similar to that described in Chapter 6. Self modulation occurs more quickly without channeling, as the focusing effect of the channel suppresses radial modulation. Self-modulation and dephasing are also faster at higher densities, so that the length over which the particles are accelerated and dephase decreases, and the peak energies

drop (consistent with Section 2.6). However, structure still appears in the energy distribution, with appearance of a narrow energy spread feature near the dephasing length. At  $2 \times 10^{19} \text{ cm}^{-3}$ , dephasing length is  $1200 \mu\text{m}$ . At  $4 \times 10^{19} \text{ cm}^{-3}$ , dephasing length drops further to  $600 \mu\text{m}$ . Chapter 7 indicated that the simulations are well converged in dephasing length, so that these numbers should be reliable within  $\sim 100 \mu\text{m}$ . However, self modulation is faster in three-dimensions, which cannot be described by the two dimensional simulations, and this may shorten the dephasing length in the experiment somewhat relative to these numbers.

Comparing the dephasing lengths from the simulations to the available gas jet lengths and densities, we find that at a density of  $4 \times 10^{19} \text{ cm}^{-3}$ , lengths of  $0.6 \text{ mm} \approx L_{deph}$  and  $1.8 \text{ mm} > L_{deph}$  were available, allowing comparison of beams at and after dephasing. Using a second density of  $2 \times 10^{19} \text{ cm}^{-3}$ , lengths of  $0.6 \text{ mm} < L_{deph}$  and  $4 \text{ mm} > L_{deph}$  allowed additional comparison of pre- and post-dephasing beams. Data from the two densities together characterize the nature of the beam before, at, and after dephasing.

## 8.2 Electron Spectra versus Acceleration Length

Experiments were conducted with plasma length equal to, greater than, and less than the dephasing length using the densities and plasma lengths provided by the gas jets described above. As shown in Section 3.3.3 and Chapter 5, the energy spectrum over all energies was obtained by scanning the magnet current over many laser shots. This gave the shot averaged spectrum, from which peak energy could be derived. Analysis of individual images then showed whether there was structure in the distribution. Comparison of the energy spectra showed the dependence of bunch quality on the accelerator and dephasing lengths

The electron energy spectrum of the accelerator operated at a plasma density of  $4 \times 10^{19} \text{ cm}^{-3}$  is shown in Fig. 8.2, for plasma lengths of 0.6 mm and 1.8 mm. The 1.8 mm plasma corresponds to the same gas jet conditions as in the channeled experiment. In contrast to the guided accelerator, there is little structure in the electron energy distribution, and the peak energy is lower - below 40 MeV (similar to Fig. 5.9). The divergence of the beam is also much broader, as shown in Fig 5.3. Comparing the unchanneled results from the 0.6 and 1.8 mm plasmas, we find that the peak energies observed in the averaged spectrum are similar at both plasma lengths, indicating that no acceleration occurred beyond 0.6 mm. There is also more charge at energies above 18 MeV in the 0.6 mm plasma. Individual phosphor images (Fig 8.2 inset) show that there is substantially more structuring of the spectrum in the short plasma. Both features are consistent with a dephasing length near 0.6 mm at this density, which is also close to the 0.6 mm dephasing length seen in simulations. Beyond that length there should be little energy gain, and structure in the distribution and density of electrons at high energy should be reduced, as observed.

With a plasma density of  $2 \times 10^{19} \text{ cm}^{-3}$  the character of the energy spectra changed (Fig. 8.3), consistent with the increased dephasing length at the lower density. The averaged experimental energy spectrum for a plasma length of 0.6 mm shows low peak energies, while the individual phosphor images (inset) show no structure in the distribution. This is consistent with the electron beam being extracted well before dephasing. In contrast, the averaged spectrum at 4 mm plasma length shows that high energies are produced. Individual images show the appearance of monoenergetic structures in the spectrum at high energy. These features indicate the beam is extracted at or after dephasing. This data is also consistent with the dephasing length of  $1200 \mu\text{m}$  observed in simulations at this density.

The scaling of peak energy observed with density is roughly consistent with the theoretical scaling of maximum energy gain at dephasing. At dephasing, energy gain

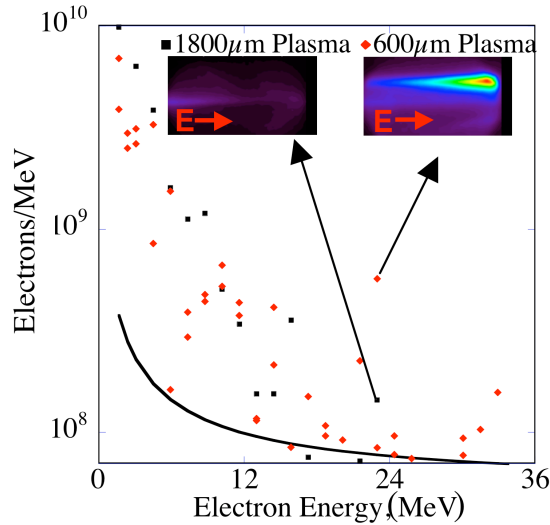


Figure 8.2. Electron energy spectrum for the unchanneled accelerator operated at a density of  $4 \times 10^{19} \text{ cm}^{-3}$ , obtained by scanning the magnet current over many shots. Each point is one shot. For a plasma length of 0.6 mm, near the dephasing length calculated in simulations, there is several times more charge at high energy than for a 1.8 mm long plasma, which is longer than the dephasing length. The insets show individual phosphor images, demonstrating that the spectrum is also more structured at the dephasing length, consistent with simulation (color: black to red). Fluctuation in the spectrum appears to be due to fluctuations in self-guiding and in laser parameters shot-to-shot.

is proportional to the reciprocal of plasma density for constant  $E_{max}/E_0$ , where  $E_{max}$  is the maximum accelerating field and  $E_0$  is the wave breaking field [3] (Section 2.6). The peak energy observed at  $2 \times 10^{19} \text{ cm}^{-3}$  was above 90 MeV at 4mm propagation distance, compared to  $\sim 40$  MeV at  $4 \times 10^{19} \text{ cm}^{-3}$ . This ratio is close to the factor of two predicted by the scaling of energy with density for constant  $E_{max}/E_0$ . The same scaling of energies is observed in the simulations, which also show that  $E_{max}/E_0$  is close to the same for the two cases.

The peak energies observed experimentally are roughly 60% of those obtained in simulations. In part this may be because the two dimensional simulations do not adequately model instabilities such as filamentation [12] and hosing [88] that can disrupt the drive beam. The phosphor screen used in the spectrometer also has a high

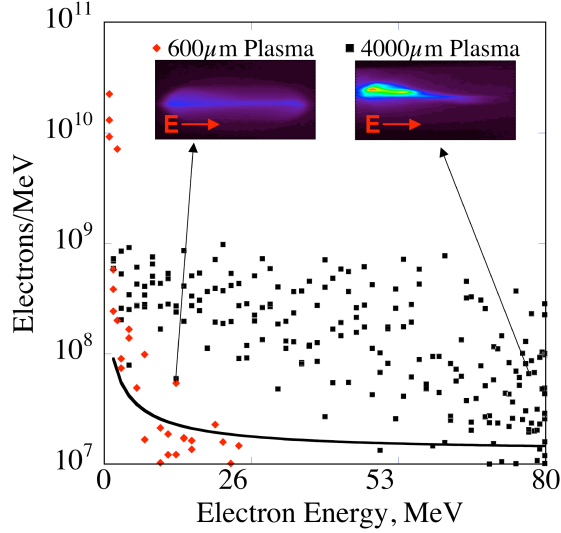


Figure 8.3. Electron energy spectrum for the unchanneled accelerator operated at a density of  $2 \times 10^{19} \text{ cm}^{-3}$ , obtained by scanning the magnet current over many shots. Each point is one shot. For a plasma length of 0.6 mm, before the dephasing length calculated in simulations, very low energies are produced compared to a 4 mm plasma, which is longer than the dephasing length. The insets show individual phosphor images, demonstrating that the spectrum is also unstructured and smooth before the dephasing point, consistent with the explanation that particles are bunched in energy at dephasing (color: black to red). Fluctuation in the spectrum appears due to fluctuations in self-guiding and in laser parameters shot-to-shot.

detection threshold of a few  $10^7$  electrons, which limits detection. Lastly, the trapped charge in the simulations is less than in the experiments (Chapter 6), reducing the effect of beam loading and increasing final energy.

Charge and energy of the beams fluctuated significantly in the unchanneled accelerator using the low density plasma. This may be due to instabilities in relativistic self-guiding [12, 22, 88], which was used to guide the laser pulse over the several mm ( $\approx 10$  diffraction ranges) required to achieve the dephasing condition in this case. Analysis of the laser mode transmitted through the plasma was performed using the mode imager camera. This showed that the transmitted laser profile was in fact highly unstable, as expected, often breaking into many beamlets. The instabilities in self guiding are stronger in three dimensions, and hence were not well modeled by the two-dimensional simulations, which showed propagation of a single laser spot

through the plasma. The instability of the beam may in fact be partly responsible for the production of high energy beams in the long plasma; even if the plasma is longer than the dephasing length, drive beam breakup and depletion may have stopped acceleration near dephasing on some shots. Hence, while the single beam experiment demonstrates the dephasing physics, in order to obtain stable beams at high energy use of a guiding channel appears to be important in order to obtain stable propagation.

### 8.3 Comparison of Channeled and Unchanneled Results

Comparing the single beam experiments to experiments performed with the same laser and plasma density but using a guiding channel [45](Chapter 5), we find that the stability of the beam at high energy was greatly increased by the guiding channel. An averaged spectrum of the channeled accelerator was taken with no slit in the spectrometer to allow evaluation of beam statistics and comparison with the unchanneled experiments. In the unchanneled case at a density of  $2 \times 10^{19} \text{ cm}^{-3}$ , most shots produced no detectable charge at 80 MeV (detection threshold  $10^7$  electrons using the phosphor screen of the magnetic spectrometer), and fluctuation in charge was two orders of magnitude. In the channeled accelerator, by contrast, at the same density almost all shots showed substantial charge at high energy, and fluctuation was less than one order of magnitude. Charge at high energy was also at least two times higher. This is illustrated by the multi-shot, averaged energy spectra shown in Fig. 8.4, and is consistent with the mode image observations in the last Section and Chapter 5. These measurements indicated that the plasma channel greatly improved the intensity and reproducibility of the output optical mode image, which measures

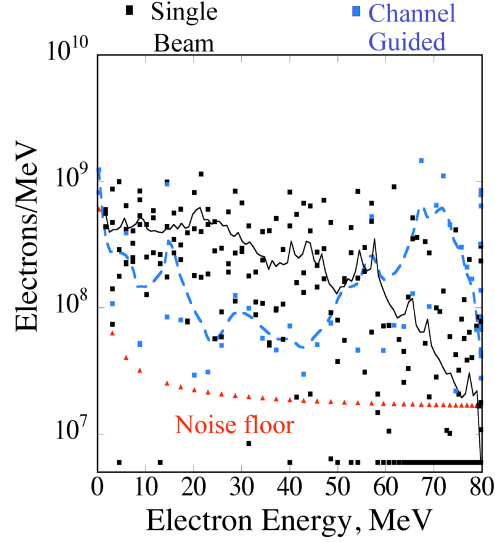


Figure 8.4. Electron energy spectrum for the unchanneled and channeled accelerators operated at densities near  $2 \times 10^{19} \text{ cm}^{-3}$ , obtained by scanning the magnet current over many shots, demonstrates the advantages of channeling. The channeled accelerator shows much higher charge at high energy (fit), and almost all shots (each point one shot) show charge at high energy. In contrast, the unchanneled accelerator produces charge at high energy rarely. Residual fluctuation in the channeled case is likely due to beam pointing jitter which changes the guide efficiency shot to shot. No slit was used in the spectrometer.

how effectively the drive pulse focus (and hence plasma wave amplitude) was retained through the plasma. Remaining fluctuation in the channeled case appears to result primarily from pointing jitter of the laser spot into the channel, and it should therefore be possible to reduce this fluctuation further with stabilization. Some jitter also results from the electron bunch pointing jitter, which is still slightly larger than the spectrometer acceptance.

Consistent with the explanation presented here, monoenergetic beams have also been observed in experiments at other laboratories using a large laser spot size to increase  $Z_R$  and hence the focused propagation distance of the laser pulse [61, 62]. Like the unchanneled experiments described in this Chapter, that method was less efficient than use of a plasma channel in terms of amount of charge accelerated and electron bunch energy per laser power. To obtain long  $Z_R$ , a large laser spot was

required, reducing laser intensity. This in turn reduced the wake amplitude and hence the electron bunch energy at a given density (Eq. 2.48). Self-trapping is also highly sensitive to laser intensity (Fig. 2.6B), so lower charge is expected. The large spot size also reduces transverse wave breaking, further lowering trapping [65]. Experiments using the same laser power and energy as the channeled experiments described in Chapter 5 but without a guiding channel [62] observed approximately half the peak energy and 10% of the charge obtained in the channeled experiments.

## 8.4 Summary

The single beam experiments described in this Chapter indicate that structure in the energy spectrum can be obtained in the unguided case via control of gas jet length and density. Extraction of the beam at or near dephasing appears to be the important parameter, consistent with simulations and channeled experiments. High quality beams can then be generated with the desired energy by adjusting plasma length and density. Structure in the distribution is also observed after dephasing, and this may be due to depletion or breakup of the drive laser pulse. Self guiding extended propagation beyond  $Z_R$  in the single beam experiments, but this was less reliable than channel guiding. The resulting electron beams from unchanneled experiments were never as high in quality or energy as those from channel guided experiments (Chapter 5, Fig. 5.4). Hence channeling remains an important mechanism for optimizing performance, since it offers reproducible control over laser propagation and allows the use of smaller spot size and hence less laser power to reach the required intensities.

# Chapter 9

## Conclusions

This thesis has demonstrated the use of a plasma channel to extend the interaction length in laser wakefield accelerators, and the tuning of such accelerators to produce low energy spread high quality electron beams by using beam loading of the wake to control electron trapping and by matching the acceleration length to the dephasing length over which the electrons outran the wake. Here, we summarize the results, and present directions for future work and prospects.

### 9.1 Summary

The primary experiments in this dissertation were conducted to explore the guiding of high power laser pulses and the resultant effect on laser acceleration, and were based on past experiments and theoretical scalings (Chapter 2). Supporting experiments and simulations were subsequently conducted to clarify the mechanisms of beam formation. Technical development and construction of laser and diagnostic systems, control systems, and gas targets, enabled these experiments (Chapter 3, Appendix A, B).

Guiding experiments [46, 60] (Chapter 4) demonstrated that the mode of a laser pulse can be maintained without aberration over many diffraction ranges using a plasma channel for powers at or above the self-guiding threshold, and at intensities relevant for acceleration. High intensities were guided without self-trapping of electrons. Data on depletion and spectral shifting of the laser pulse, as well as simulations and analytic estimates indicate that a large plasma wave was excited without trapping of electrons, providing a high gradient long scale length dark current free structure for acceleration. This was confirmed by increasing laser power, and observing the trapping and acceleration of electrons.

Electrons were trapped and accelerated from the background plasma when the guided pulse power exceeded 4 TW, and bunches with several  $10^9$  electrons within a few MeV energy spread at energies above 80 MeV were produced at a power of 9 TW [45, 59, 60] (Chapter 5, Fig. 5.4). This represents a qualitative improvement from previous experiments, including those shown in this dissertation, which used no guiding channel and showed 100% energy spread. Acceleration of electrons up to  $\sim 170$  MeV was observed, though diagnostic limitations prevented analysis of energy spread at energies above 92 MeV. Initial measurements indicate the emittance of these beams is close to state of the art conventional facilities. Pre-ionized but unchanneled experiments did not differ significantly from experiments in un-ionized gas jets, indicating that the channel and not ionization is the important factor. Acceleration performance was well correlated to guided mode intensity and spectral features, confirming the importance of the channel. Experiments on nuclear activation and  $\gamma - n$  reactions as well as cross calibration of charge transformers (ICT's) were used to verify the performance of the magnetic spectrometer used in these experiments.

Simulations [45, 59, 60] (Chapter 6) indicated that the high quality electron beams were obtained from self-trapped electrons by taking advantage of beam loading, and dephasing. Loading of the wake by the injected bunch [16, 17] turned off trapping after

the loading of an initial bunch of electrons into the wake, producing a self-consistent phased injection of the electrons. These electrons were then grouped in energy at the dephasing length, where the front of the bunch (initially at higher energy than the tail since it was injected first and thus accelerated longer) was decelerated while the tail was still accelerating. Simulations also indicated that only one wake ‘bucket’ contributed to the high energy bunch, so that bunch length was  $< \lambda_p \sim 7.5\mu\text{m}$  providing for ultrafast applications.

While computational resources were not available to fully reproduce the experimental parameters, the physics of bunch formation was consistent over a wide range of runs. Convergence studies (Chapter 7) indicated that the simulations are not converged, and there is significant variation in results with grid and particle resolution, indicating the need for high resolution simulations. Three-dimensional effects also appear to be important based on the variation of results with laser polarization and low resolution three-dimensional runs. Results are however approaching experimental conditions as particle and grid resolution are increased, and the essential features of trapping, loading, and dephasing are robust, giving confidence in the physical picture derived from the simulations. It appears likely that high resolution three-dimensional simulations, coupled with further variation of parameters within the experimental uncertainty, could reproduce a bunch similar to that formed in the experiment.

Experiments varying gas target density and length indicated that the low energy spread beams were obtained by matching the acceleration length to the length over which the electrons dephase from the wake, consistent with simulations [59,60] (Chapter 8). At high densities this can be done using a very short gas jet, but this leads to low peak energies and low efficiency. At lower density, longer acceleration distances and higher peak energies are obtained. The long acceleration distance at low densities requires maintaining the intensity of the drive laser over mm scales, and

channeled experiments then demonstrate clear advantage in beam charge, quality, and stability.

In summary, the experiments and simulations described herein demonstrate that high quality beams can be formed from self-trapped electrons self-consistently by appropriately tuning the plasma profile to control laser propagation and to match acceleration length to the dephasing length. The plasma channel maintains the laser focus over long distance, and controls propagation, providing much greater performance for a given laser power than reported by similar experiments which used a large spot or self-guiding size to extend propagation distance [62] (Chapter 8).

## 9.2 Prospects and Future Work

The beams from channel guided accelerators such as those described here open up a new class of experiments with laser accelerators. The experiments and simulations herein demonstrate production of high energy beams with small energy spread, which are a qualitative improvement from the previous state of the art exponential electron spectra. This allows consideration of laser-plasma accelerators for a wide variety of applications that demand high-quality electron bunches. Further work on injection, stabilization, efficiency, and other topics promise further advances in the development of high-gradient accelerators.

Beams with high spectral density at high energy will enable more efficient use of these accelerators as radiation sources for physics, chemistry and biology. A laser can be scattered from the electron beam, producing a compact high brightness femtosecond x-ray source [30–33]. In addition, the bunch radiates as it exits the plasma, producing THz emission which may be brighter than conventional sources [29, 34]. The bright and intrinsically ultrafast nature of the beams in particular may enable

probing of time resolved phenomena with unprecedented resolution. Even before the beams are stabilized, production of radioisotopes and other applications can immediately benefit from the higher average charge at high energy [28].

Improvements in laser stability as well as controlled electron injection will be needed to further stabilize and improve the properties of the electron bunches. Simulations and experimental observations indicated that small jitter in laser pointing, energy, or plasma density could significantly affect electron bunch properties. This indicates the need for laser pointing, energy, and pulse length stabilization. Higher efficiency lasers (such as diode pumped systems) are also required for high repetition rate accelerators, since current flash lamp drivers develop excessive heat and would consume excessive energy at collider repetition rates. Driving the wake in the standard regime (non self-modulated, Section 2.2) or controlling the instability by seeding it with a second laser pulse [122] may also help to reduce variation by reducing fluctuation in wake formation.

Techniques such as colliding pulse injection [44,48,49] externally impose injection, and simulations indicate such schemes are less sensitive to laser variation than self-trapping. Additionally, the control offered may allow further narrowing of the energy spread. These techniques will be made more practical by the existence of the long scale length dark current free structure demonstrated here in the guiding experiments below 4 TW. The setup for such experiments was developed as part of this work, and injection studies are now under way.

If injection and laser performance can be stabilized, producing bunches of reproducible energy and emittance, staging and beam propagation issues must then be addressed. This begins with long scale low density guiding and acceleration experiments which will extend the range of the channeling technique. The structure developed in this dissertation can provide energy gains up to  $\sim 170$  MeV, limited by

length and by the relatively slow phase velocity at the high density used. Simulations indicate that channeling over cm scales at densities near  $10^{18} \text{ cm}^{-3}$  using a 100 TW-class driver could achieve energies of 1 GeV or greater per stage due to the high dephasing energy at low density [37, 40]. These experiments are now under way using capillary waveguides at LBNL. Staging and electron beam transport will then need to be explored.

As issues of stability and reproducibility are addressed, and energy is increased, the beams from laser accelerators based on plasma channels may be of suitable quality to serve high energy physics and light source applications. Due to their good emittance, these beams may offer focusability competitive with state of the art RF accelerators. Such beams may be injected into and post accelerated in subsequent laser accelerator stages to produce compact multi stage electron linacs. Given the gradients demonstrated, it may be possible to construct a TeV linac in a distance of a few hundred meters, rather than 10's of kilometers. The high gradients and ultrashort nature of the beams may enable construction of more compact light sources and free electron lasers, since there would be reduced need for pre-bunching, and the linac distance would be greatly reduced. Hence experiments that require large facilities may become possible in the laboratory or medical clinic. It is hence believed that the plasma channel technique demonstrated here, together with the extraction of the beam at the dephasing length, provides the basis for a new generation of compact, bright, ultrashort electron sources with broad applications.

# Appendix A

## Control System

Optimization and development of laser accelerators requires characterizing the interactions of many factors including plasma density and structure, laser focal location and spotsize, and laser chirp and power [10, 123]. To do this, experiments at high repetition rates are needed in order to scan parameters and to investigate their effects on performance. Because of radiation hazards associated with high rep rate operation, such experiments must be operated remotely. Data must also be collected and saved synchronously from many detectors at high speed. To accomplish this, a control system was developed for the 10 Hz L'OASIS laser which allows high rep rate experiments [123]. Such a control system is increasingly important as experiments become more complex, with multiple laser pulses and exploration of detailed physics and optimization, and was vital to the experiments described in this manuscript [45, 46, 59, 60].

## A.1 Control System Architecture

The control system is based on a network of personal computers running custom and commercial control, data collection, and analysis programs, which are coordinated over a 100Base-T Ethernet network. It is installed at the 10 Hz multi arm Ti:Sapphire laser of the L'OASIS laser facility at LBNL, which delivers up to five laser pulses on target, and which is equipped with a large array of diagnostics for wakefield acceleration experiments [91,94](Chapter 3). Fig. A.1 shows a selection of major detectors and controlled systems in the target chamber (center) and one representative compressor out of three. Acquisition of data from over fifteen instruments and nearly a hundred data channels is possible at several-Hz rep rates, as is control over more than sixty controls and motors. A master control program (written in LabVIEW) running on a main computer coordinates data collection and control of all systems, both by direct interfaces and by remote control over subsidiary computers which control cameras and other diagnostics. Ethernet addressable GPIB and serial controllers are used to provide operation of devices over long distances.

Fig. A.2 shows the system layout and flow of data. Each diagnostic or computer receives a trigger from a timing box (SRS DG535), timed to assure that all acquire data on the same shot of the laser and gas jet. The main control program configures the subsidiary machines and diagnostics according to user instructions. In operation, the control program sets a user defined group of the diagnostics to acquire for the each shot over the network. After acquiring the shot, by default each diagnostic reverts to a no acquire mode until signaled again. This avoids the need for a hardware triggering system. In fact, the system runs on the same hardware required to do individual shot experiments with manual saving of the data, allowing greatly improved data collection efficiency at little cost. Diagnostics capable of keeping pace with the shot rate - currently all but the Photometrics digital CCD cameras - are acquired every

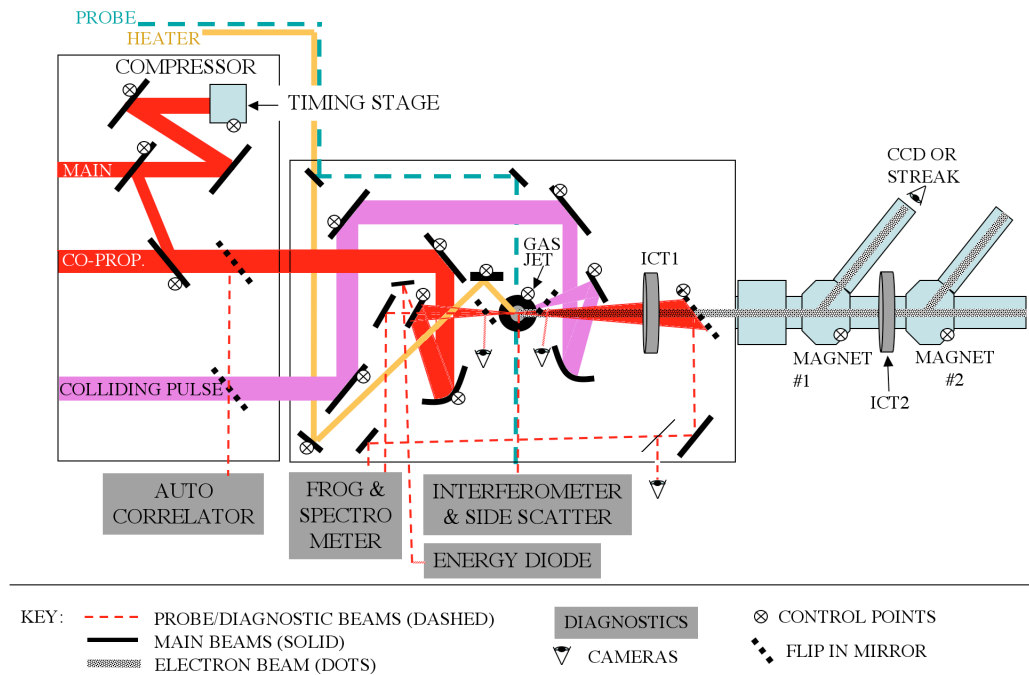


Figure A.1. Experimental arrangement of the target chamber (center) and one compressor chamber, showing a selection of major detectors and controlled systems. Radiation detectors are distributed around the area. Nuclear activation targets and THz detectors are not shown.

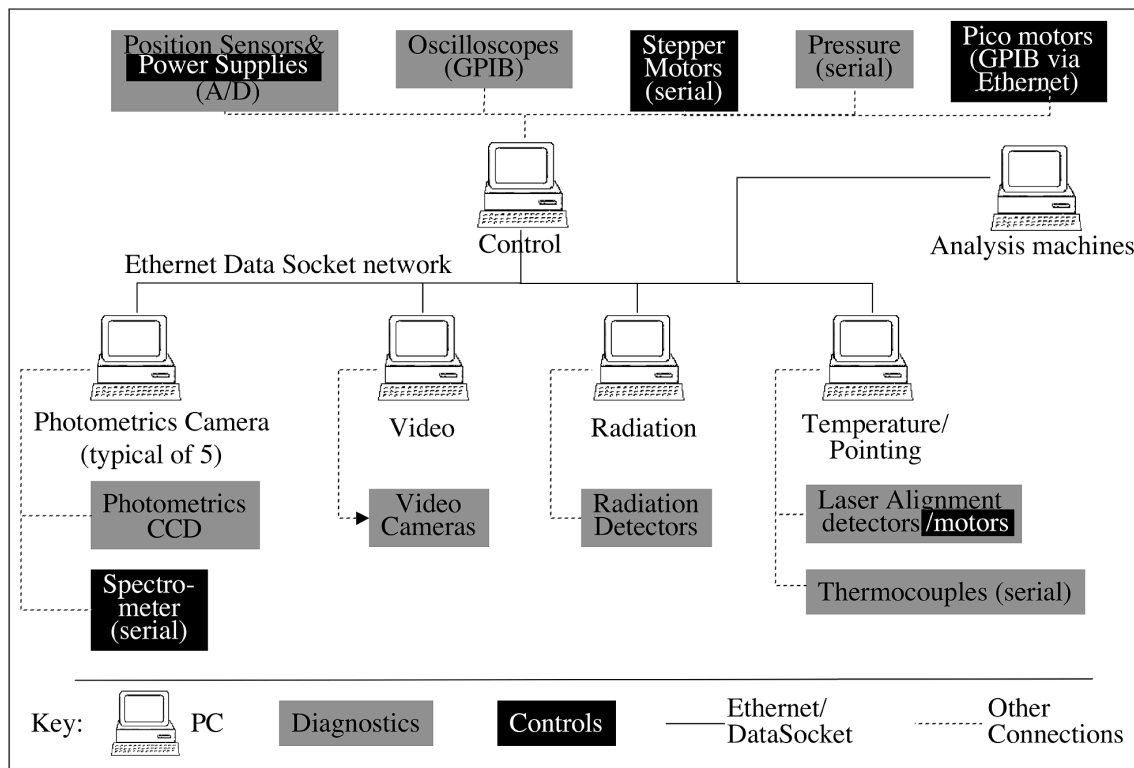


Figure A.2. Schematic diagram of the control system, showing representative machines as well as the data and control connections. Not all machines are shown.

shot. Slow diagnostics are sub-cycled; they are fired all at once, and fired again only when all of them have finished acquiring. This maximizes the number of shots on which all diagnostics acquire at once.

The control program uses the DataSocket protocol, an Ethernet based messaging system, to communicate with LabVIEW programs running on the subsidiary machines in order to control the system. For diagnostics and controls with interfaces compatible with LabVIEW, these programs collect data directly. DDE, a Microsoft Windows inter-process communication tool, is used to communicate with commercial acquisition programs for systems which need specialized software, such as V++ for Photometrics CCD cameras. In this case, the control system uses DataSocket to signal over the network to a LabVIEW program on the target machine, which in turn controls other acquisition software using DDE. This combination provides

faster communication than using DDE over the network directly. Control systems are distributed in the same way.

Using higher level languages and protocols such as LabVIEW and DDE, as well as taking advantage of commercial software such as V++ where available, minimized coding time and allowed the system to be put on line by the author. This reduced costs and provides flexibility for on going modifications. The system is written to allow expansion by plugging in modules for new detectors or controls; recent addition of a new controller supporting twenty motion control points took less than three hours.

## **A.2 Diagnostics and Controls**

A variety of diagnostics and controls are supported. These include five digital CCDs, two video CCDs, three oscilloscopes, eight radiation detectors, two vacuum gauges, two laser pointing readouts/controls, three temperature monitors, and over 60 motors and actuators.

The main control program (Fig. A.3) directly acquires data over GPIB from up to three Tektronix oscilloscopes which read laser energy diodes, beam charge transformers, and other sensors. It also acquires data from position sensors using an A/D board (which also provides triggering) as well as chamber pressure data via a serial interface to a gauge controller. Eight radiation detectors, which are used as indicators of high energy electron production, are operated by a second computer and collected over a serial link. Two RS170 analog video frame-grabbers with a LabVIEW interface reside on another machine (Fig. A.4). A laser pointing system that uses feedback from quadrature detectors to compensate for laser drift, and a room temperature logging system are also incorporated.

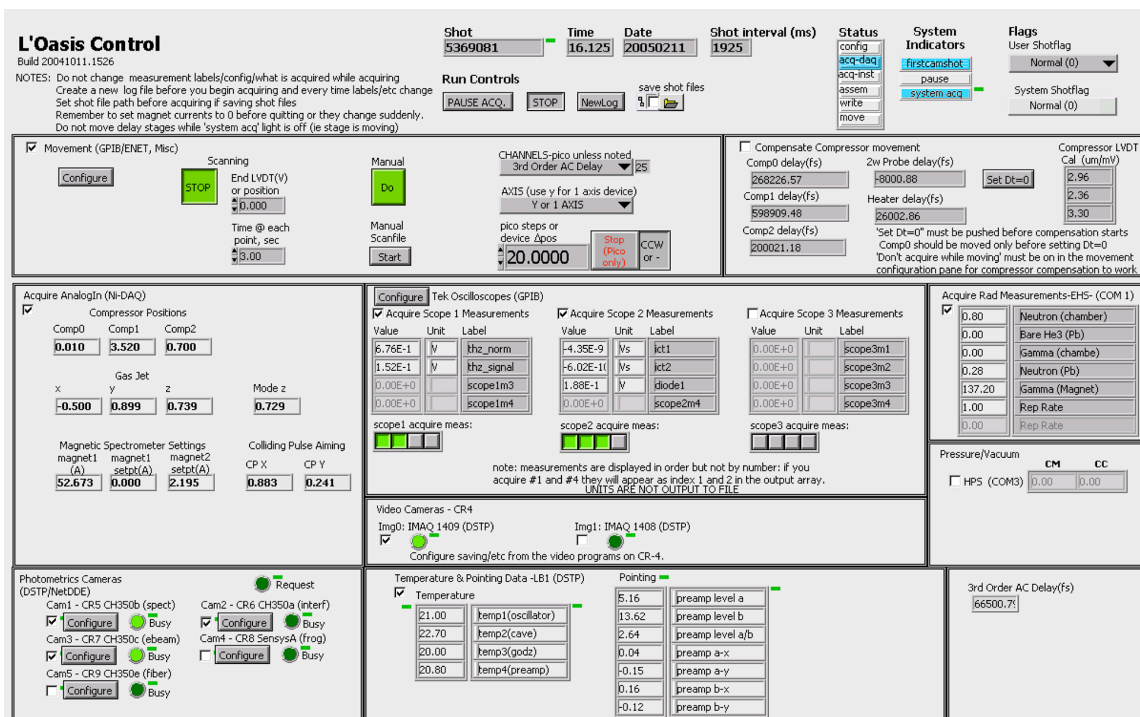


Figure A.3. The front panel of the master control program, showing movement controls (top left) with scanning, as well as displays for various acquired diagnostics and checkboxes to acquire and configure cameras.

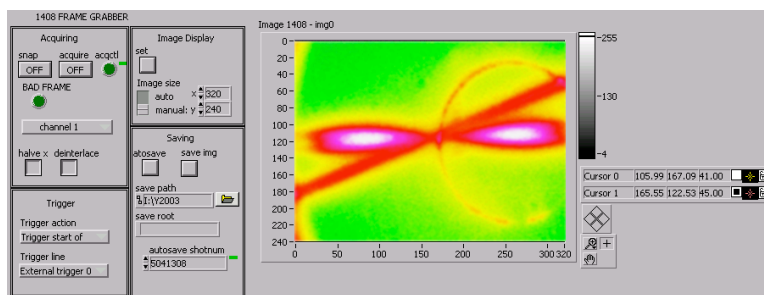


Figure A.4. One of two video CCD frame grabbers, typically used for alignment cameras. Acquisition of triggered signals and de-interlacing of the images for pulsed signals is provided. Shown is an image of the gas jet from above, illuminated by the recombination radiation of backfill gas ionized two crossing laser pulses being aligned for an injection experiment.

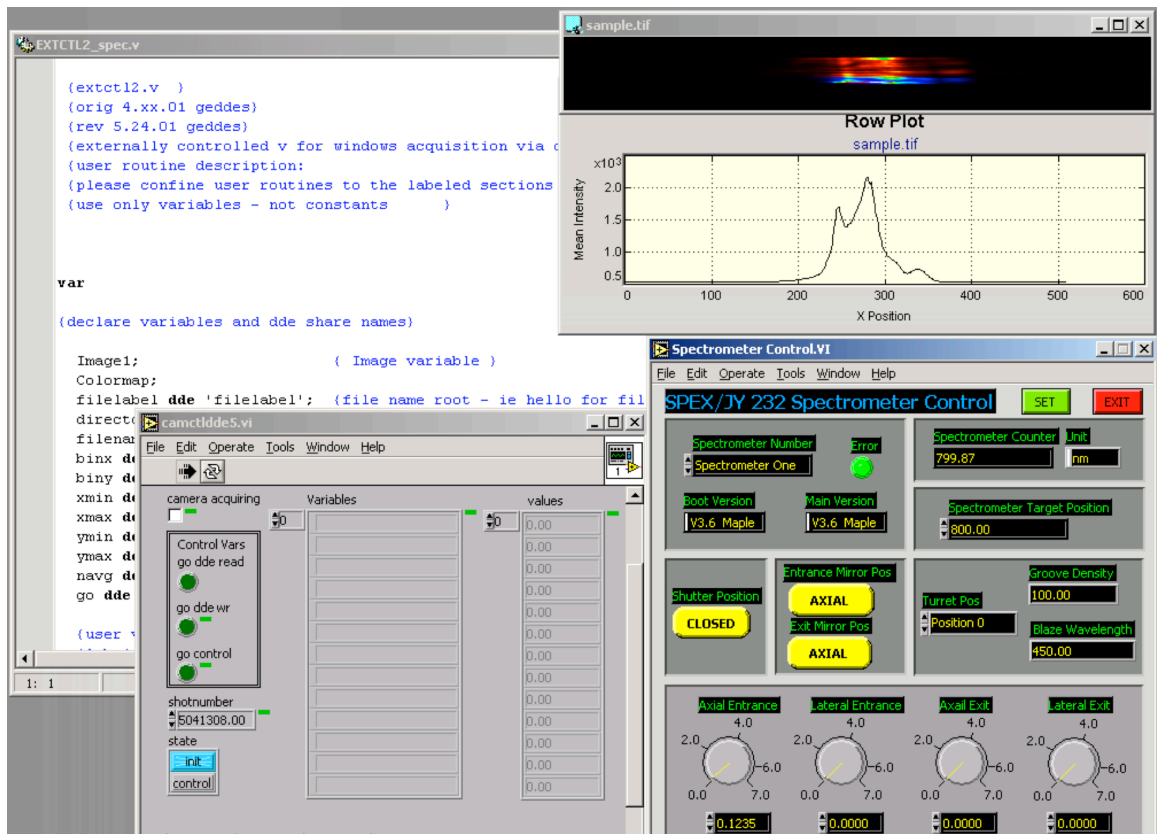


Figure A.5. Each of five Photometrics CCD cameras, such as this one for the optical spectrometer, are controlled by a custom script in the V++ language (EXTCTL2-spec.v, back pane). This script acquires images and displays lineouts and other processing (top right). Acquisition is configured by the control program using a DDE interface to set variables in this script through an intermediary LabVIEW program (CAMCTLDDE5, bottom left). The spectrometer itself is controlled by a serial link by a separate program (bottom right).

Up to 5 Photometrics digital CCD cameras, each with its own controller computer, are supported via a DataSocket to DDE conversion LabVIEW program (above) which allows the control program to remotely drive the operation of Photometrics proprietary V++ driver software. Scripts for these cameras have been developed which allow remote configuration by the control system, allowing on the fly changes to camera binning, region of interest, and other parameters. Both the image and user selectable preliminary analysis (i.e. lineouts, integrated counts, or filtered images) can be displayed shot by shot (Fig. A.5).

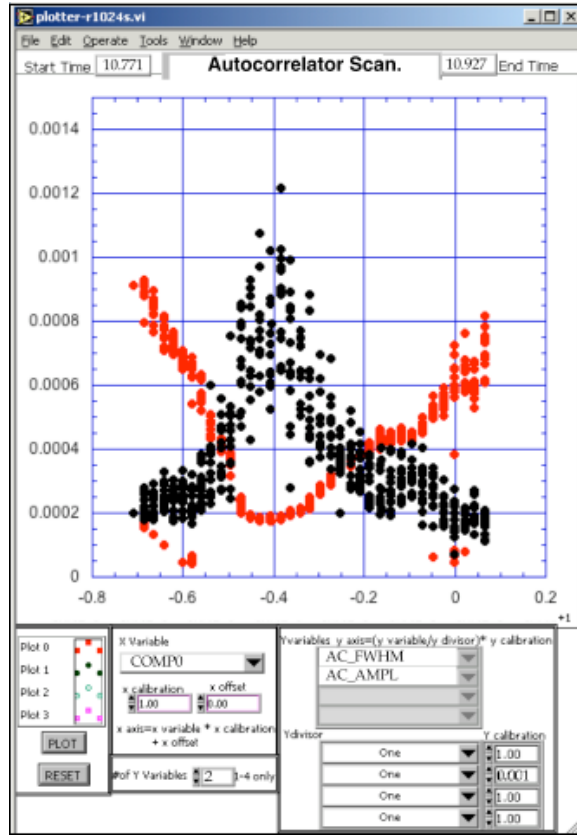


Figure A.6. Numeric data is collected by the master control program and re-distributed over the network, allowing online plots of experimental parameters from anywhere in the lab. A plotter program (shown) allows plotting of up to 4 variables or ratios at once. Shown is an autocorrelator scan indicating laser pulsewidth as a function of grating position.

Numeric data acquired is re-distributed over DataSocket allowing on line plots/analysis from anywhere on the network, as shown in Fig. A.6, and is saved to a flat-file database for later use. Images are saved directly to a file server, and are tagged with a shot number given by the control program so that synchronized data can be retrieved.

The control portion of the system regulates more than sixty motors and power supplies to allow remote operation of the experiment. Each laser pulse is independently and remotely timed and pointed by timing stages and motorized mirrors. Compressor grating position is adjustable to control pulse length and chirp. All pulses have inde-

pendent timing provided by stepper driven stages with 10 fs precision, and automatic compensation to maintain timing during compressor movements is provided by sensing the compressor position and moving the timing stage to compensate. The pulses can also be pointed remotely, and the pointing can be monitored via top and side imagers, or via flip in mirrors with microscope objectives (Chapter 3). This allows for controlled injection experiments using the colliding pulse concept [44] as well as guiding experiments using plasma channels (Chapters 4, 5). The gas jet can be moved in three axes to provide scans of plasma density, scale length, and laser waist location with respect to the gas profile. Power supplies for magnetic spectrometers are controlled to allow profiling of the electron bunch energy spectrum. Motors, position sensors, and other subsystems are also automated. Picomotors are used for movement of mirrors and light equipment, with position read out via LVDT indicators providing  $\mu\text{m}$  precision where required. API and Silvermax stepper motors are supported for heavy positioning and delay stages. Newport ES300 motion controllers are supported for high precision positioning, with both motion control and readout over serial link.

### A.3 Acquisition and Analysis

The control system provides synchronous acquisition and control at shot rates up to 3 Hz, which is limited by diagnostic speed, network set up time required to prepare for a shot, and the time taken to save data across the network. Time required to set up the Photometrics cameras for each shot using the DataSocket/DDE interface is the principal limit, at about 300 ms. The oscilloscopes and serial interfaces are relatively fast, taking  $\approx 100$  ms total in parallel with the cameras. The video cameras, on a separate machine, take about 200 ms to process and save data (limited by processor speed). This allows acquisition consistent with the present limits on our gas jet rep rate set by pumping capacity. Further improvement is available in a straightforward

way by hardware triggering the Photometrics cameras and providing a faster computer for the video cameras, which should bring the system to 5 Hz. Improvement beyond this point would rely on faster response from diagnostics such as oscilloscopes in next generation instruments.

Positions controlled by the system can be scanned, allowing automated collection of a series of data points at various parameter values. Logging of manual movement is also supported, allowing the user to log scans of parameters not controlled by the system (i.e. gas jet backing pressure). To provide accurate data collection, the control program includes self-checks which make sure that data is not acquired while the system is moving motors and magnets.

Large amounts of data are generated using this system (a few  $10^4$  shots/day), so that categorization and analysis of the data are also important. To this end, the user can designate 'scan' files, which save the data from a particular scan (for instance of gas jet position) in a separate file in addition to the main database. Data analysis routines in the IDL language allow data files to be processed and relevant data extracted quickly. Batch processing of image files allows relevant parameters to be extracted and plotted from image files including integrals, peak values, spot locations, and more. Batch filtering and analysis allows trends and correlations to be extracted from data that may not be evident from single shots (see for instance Fig. 5.6). Movies can be made and exported to MPEG format, where each frame includes a display of all image data from that shot, as well as a plot of selected numeric data for the run with a marker indicating the shot's position (Fig. A.7). This allows data to be rapidly scanned visually.

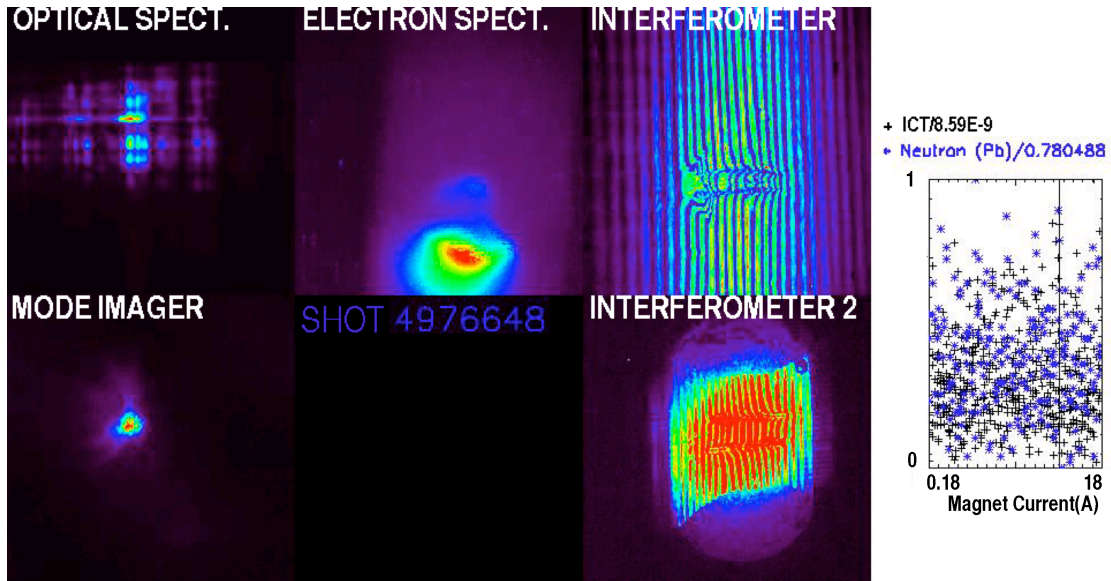


Figure A.7. Large quantities of shot correlated data are gathered by the system, requiring analysis tools to match the controls. Here, a frame from a movie displaying the various cameras acquired on each shot together with the position of the shot on a plot of numeric parameters (right) is shown.

## A.4 Summary

A control and data collection system has been implemented at the L’OASIS laser using Ethernet network messaging to coordinate operation of more than 10 computers and many diagnostics. Use of network coordination allowed the system to be developed at essentially no cost relative to uncoordinated data collection computers, but provides several-Hz synchronous acquisition and control, allowing high repetition rate experiments. This ability provided the detailed data required for the complex channeled acceleration studies described herein.



# Appendix B

## Gas Target Development

Gas target development, which provided the plasmas required for the channeled accelerator experiments, is described in this Appendix. The general profile of the plasma will follow that of the gas target from which the plasma is created (with detailed structuring available through hydrodynamic techniques such as channeling [51–54]). Consideration of the plasma requirements for wakefield acceleration then sets the target requirements for the gas plume. Target density, uniformity, and edge gradients of the target can all be used to optimize performance. The target must also present reasonable loads on the vacuum system. Hence design of the gas target is an integral part of accelerator development.

Supersonic gas jets were designed and built to provide the required gas targets. An adiabatic flow code was written which gives a reasonable model of flow through the jet nozzle. Two interferometers were built which allow characterization of the gas density by different methods, providing cross checking. The adiabatic flow code and diagnostics were then used to design and test nozzles, and experimental variation of shape was used to obtain gas jets meeting the target requirements.

## B.1 Target Requirements

Because the plasma is ionized from a neutral gas plume, the structure of the neutral gas will be generally mirrored by the plasma. Important parameters for wakefield acceleration include plasma density, the density scale length over which the density ramps up from vacuum to full density, and the length of the plasma (Sections 2.1, 2.3, 2.6). Though changes can be made after ionization (for instance using hydrodynamic shock, see Chapter 4) this requires laser energy, and is expensive and difficult. Hence the gas target profile should be as close to the required plasma as possible.

Plasma density selects the regime of operation, and for these experiments was in the range of one to six  $10^{19}$   $\text{cm}^{-3}$ . This provided operation in the self-modulated regime for the 50 fs laser pulses available [20](Section 2.5.3) and allowed self-trapping of electrons (Chapters 2,5). Densities quoted in this Appendix are the electron density of the fully ionized plasma, since this is what is relevant for wakefield acceleration. To obtain the neutral gas atomic density, divide by  $Z$ , the atomic number for the gas used. Operation in the standard wakefield regime (using controlled injection [44, 47] rather than self-trapping) would use densities near  $1 \times 10^{18}$   $\text{cm}^{-3}$  for the 50 fs laser pulse available. The desired densities are at or below the fully ionized electron density of helium gas at room pressure.

Density scale length and uniformity considerations were set by consideration of laser propagation and wake generation (Section 2.7), and we review these here. Avoiding ionization induced refraction of the laser pulse [92, 93] requires use of a low  $Z$  (hydrogen or helium) plasma which rises from near zero density to the desired interaction density over less than  $\approx 2Z_R$ , where  $Z_R$  is the diffraction range over which the laser pulse remains focused (Eq. 2.21). For the present experiments,  $2Z_R \approx 450$   $\mu\text{m}$ , which sets the scale length requirement for the edge of the gas. The requirement

on plasma density uniformity was set by the fact that changing density changes the wake wavelength, which can dephase electrons and spoil acceleration. To avoid this, density must be maintained within  $\pm 5\%$  tolerance, or within 10% of the maximum value.

Gas targets were developed to meet these requirements, with the goal of 10% uniformity over distances of 0.6 - 2 mm at densities of a few  $10^{19}$  and with edge scale lengths of a few hundred micron.

## B.2 Supersonic Nozzles and Flow

Supersonic gas jets were designed to meet the target requirements outlined above. Such nozzles can in principle provide short edge scale lengths coupled with easy diagnostic access and reasonable gas loads. Because the gas expands at the sound speed in the direction orthogonal to flow after exiting the nozzle, the edge scale length a height  $h$  above the nozzle can be estimated as  $L_s \approx 2 * h/M$  where  $M = v/c_s$  is the Mach number and  $v, c_s$  are the fluid and sound speeds respectively. The factor of 2 results from the fact that the disturbance propagates both outward and inward at the sound speed in a manner analogous to a Mach cone [124]. We then expect a flat-top in density approximately  $L_s$  shorter than the nozzle diameter. Distance from the nozzle,  $h$ , must be large enough that the laser pulse does not clip the jet, accounting for spreading of the laser pulse as it propagates the length of the nozzle. At the L'OASIS facility, the laser was focused with an f/4 off axis parabola and the desired nozzle length was near 2.2 mm, predicting  $h \geq 0.3$  mm. In practice, plasma effects such as ionization diffraction [92, 93] can spread the pulse further so that  $h \approx 1$  mm was typically found to be safe for 2.2 mm nozzles. For a nozzle at Mach 1, the expansion velocity matches the flow velocity. For distances at or beyond approximately the nozzle radius, nearly Gaussian gas distributions with no flat-top

and long gradients result [109], which is not satisfactory. To satisfy the gradient scale length criteria indicated above at operating height, we require  $M \geq 5$ . In turn, to avoid discontinuity in flow direction at the lip of the nozzle, the opening angle of the nozzle  $\theta_N$  should match the natural expansion angle of the gas derived above. This gives  $\theta_N \leq 12$  degrees for  $M \geq 5$ . Hence the nozzle will be on the order of 5 mm long for a 2 mm wide opening.

Supersonic flow is obtained with a converging - diverging nozzle design which expands from a high pressure reservoir into near vacuum [124] (Fig. B.1A). At very low Mach number, the flow can be considered incompressible because perturbations are communicated efficiently upstream against the flow. Hence at Mach number less than 1, decreasing area causes increasing velocity in order to meet the continuity and momentum equations. Once Mach 1 is reached disturbances cannot propagate against the flow, so that the change in area cannot be communicated to the gas upstream, and increasing area then expands the gas rather than drawing more from the reservoir (fully compressible flow). Because of the equation of state of the gas, this results in increasing flow velocity with increasing area at velocities greater than Mach 1. Mach 1 is then obtained at the point of smallest area,  $A = A^*$ . Because a full simulation of the valve, which would include transonic gas flow in three dimensions with viscous effects and realistic surface roughness, was not available, simple calculations and simulations were used to guide a program of experimental nozzle evaluation. These simple calculations are found to be reasonably accurate.

The basic properties of nozzle flow can be derived from the ideal gas equation [124]. Ignoring viscosity and heat conduction to the wall, expansion through the nozzle can be modeled as adiabatic. If the gas pulse is not long enough to substantially deplete the reservoir, expansion can be evaluated from a stationary reservoir at constant pressure. The validity of these assumptions will be evaluated once the nozzle is designed (below). By inserting the equation of state into the continuity and momentum equa-

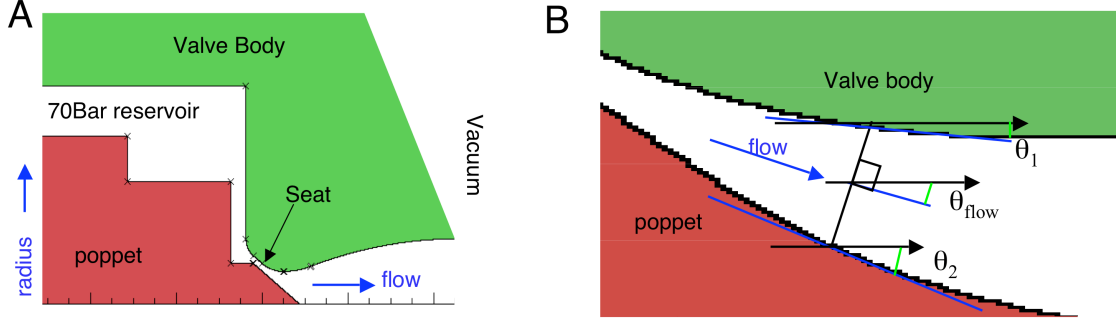


Figure B.1. Gas flow in a convergent - divergent nozzle results in a supersonic jet suitable for wakefield experiments. Due to the need for short gas pulses at high pressure, the valve seat is located at the throat of the nozzle (A), necessitating calculation of flow properties as the gas streams around the poppet. This is accomplished with a code which calculates the direction of flow at every location through the jet (B), and evaluates adiabatic gas expansion for the resulting profile.

tions, the flow properties may be expressed for a perfect gas in the adiabatic limit as follows [124]:

$$T/T_0 = (1 + ((\gamma - 1)/2) * M^2)^{-1} \quad (\text{B.1})$$

$$P/P_0 = (1 + ((\gamma - 1)/2) * M^2)^{-\gamma/(\gamma-1)} \quad (\text{B.2})$$

$$\rho/\rho_0 = (1 + ((\gamma - 1)/2) * M^2)^{-1/(\gamma-1)} \quad (\text{B.3})$$

$$A/A^* = \frac{1}{M} \left( \frac{1 + ((\gamma - 1)/2) * M^2}{(1 + \gamma)/2} \right)^{(\gamma+1)/(2*(\gamma-1))} \quad (\text{B.4})$$

where  $\gamma = C_p/C_v$  is the ratio of specific heats, T is temperature, P pressure,  $\rho$  density, and A area. This determines the parameters for every Mach number M, referenced to the conditions in the reservoir (subscripts  $_0$ ). Mach number, density, and other parameters can then be determined as a function of cross sectional area referenced to the minimum or throat area  $A^*$ , allowing evaluation of flow through the nozzle. If the desired outlet density and size are known, the required throat size and obtainable Mach number can be read off for a given backing pressure. For instance to obtain Mach 5 flow from a 2 mm diameter nozzle at a density of a few  $10^{19}$ , as required to satisfy the plasma needs outlined above, a clear throat area of  $\approx 0.4\text{mm}^2$  with

a reservoir density near 70 bar at room temperature are required for ideal flow in helium.

Due to the requirement to minimize gas load on vacuum pumps, the gas pulse should be as quick as possible, which means using a fast valve and locating the valve seat at the nozzle in order to minimize the reservoir to be depleted after closing. This resulted in a nozzle and valve seat of the form illustrated in Fig. B.1A. In order to obtain the densities required, this valve also had to handle large pressures and the largest available opening stroke. A General Valve series 9 solenoidal valve was used, which allowed operating pressures up to 70 bar with pulses as short as 600  $\mu$ s. An opening stroke of approximately 200  $\mu$ m on an 0.8 mm diameter seat gave an open aperture near 0.5 mm<sup>2</sup>, compatible with the estimated needs above. With the valve seat forming part of the nozzle, the flow pattern becomes more complex than a standard converging - diverging nozzle. The flow is no longer purely axial, but follows the contour of the valve poppet for part of the distance, so that this must be accounted for.

A code which evaluates ideal gas flow for the desired nozzle geometries was implemented and used to evaluate possible nozzle profiles. To facilitate realistic machining, the profiles are specified as a series of radiused and straight sections. As input, the code accepts contours of the valve body, nozzle, and the valve poppet (Fig. B.1A). Flow direction is approximated by the area-weighted mean between inner and outer wall angles when the flow is non-axial (Fig. B.1B). The code calculates flow area at each z location along the flow axis, then uses the flow equations above to determine Mach number, density, etc. This allowed quick evaluation of potential profiles and adjustment of the profile to obtain the smoothest acceleration of the flow possible, as well as matching of the opening angle to Mach number and other desired parameters.

The basic valve and nozzle parameters derived above were used to evaluate the

validity of the assumptions used in the model; inviscid flow, adiabatic expansion, and steady flow from a stationary reservoir. The effects of viscosity are roughly characterized by the Reynolds number:  $N_{Re} = (LV\rho)/\mu$  where  $L$  is the duct width,  $V$  the fluid velocity,  $\rho$  the density, and  $\mu$  the fluid viscosity. Reynolds numbers less than 2000 correspond to laminar flow, while values greater than a few times this are turbulent [125,126]. The helium gas can be modeled as a monoatomic ideal gas [127] and the parameters can then be derived. The viscosity for the ideal gas takes the form  $\mu = (nm c_s L_{mfp})/2$  where  $n$  is the number density,  $m$  the mass,  $c_s$  is the thermal speed, and  $L_{mfp}$  the mean free path. These quantities were evaluated at the throat where the diameter is smallest and hence the effects of viscosity greatest. The thermal speed  $c_s = \sqrt{(\frac{3}{2}kT)/(\frac{1}{2}m)}$  where  $T$  is temperature, is near 1200 m/s at room temperature. The mean free path can be evaluated as  $L_{mfp} = 1/(\sqrt{2}n\sigma_0) = 1/(\sqrt{2}n\pi d^2)$ , where  $d$  is the diameter of the gas atom, yielding  $L_{mfp} \approx 1.5 \times 10^{-8}$  m. Inserting these into the expression for the Reynolds number, we find  $N_{Re} \approx 1 \times 10^5 \times L$  (mm), indicating that flow is turbulent down to approximately 40  $\mu\text{m}$ , and that the width of the laminar layer should be near 20  $\mu\text{m}$ . With a 200  $\mu\text{m}$  valve opening, viscous effects will hence be moderate, so that the inviscid model should give useful general predictions. Due to the relative size of the laminar layer and throat, we would expect the inviscid model to overestimate flow by 20-30 %.

Heat flow is slow compared to the transit time of the gas across the nozzle, so that the adiabatic assumption should be valid. The gas cools as it expands through the room temperature nozzle, and heat flow was evaluated by calculating the specific heats and conductivities of the nozzle and gas respectively. The nozzle consists of roughly 1  $\text{cm}^{-3}$  of steel, giving it a heat capacity of 3.5 J/ $^\circ\text{C}$  with a conductivity of 40 W/m/ $^\circ\text{C}$  [125]. With our valve, the gas flowed through an aperture (above) of 0.5  $\text{mm}^2$  at Mach speed for 600  $\mu\text{s}$ , yielding a total flow volume of  $\sim 400$   $\text{mm}^3$ . From the ideal gas flow calculations (Eq. B.4), the density at the Mach point was about

60% of the reservoir density, so that the total flow was as much as 1 millimole. For a monoatomic ideal gas, the heat capacity is  $\approx 12.5 \text{ J/mol/}^\circ\text{C}$  [127] so that the gas volume had a capacity of  $12 \text{ mJ/}^\circ\text{C}$ . Even total isothermal expansion would therefore not greatly affect the nozzle temperature, which can be assumed to remain constant at room temperature. The heat conduction of an ideal gas is  $\kappa = \frac{C_V \mu}{m_m} \approx 0.2 \text{ W/m/}^\circ\text{C}$  where  $C_V$  is the molar heat capacity at solid volume,  $m_m$  is the molar weight, and  $\mu$  is the viscosity [127]. The change in gas temperature can then be written:

$$\Delta T_{gas} = \frac{\Delta E_{gas}}{C_V} = \frac{\Delta T_{(gas-wall)} \kappa A dt}{C_V dx} \quad (\text{B.5})$$

$E_{gas}$  is the energy of the gas,  $T_{gas-wall}$  is the temperature difference between the gas and wall, which is near  $100 \text{ }^\circ\text{C}$  at the Mach point. The passage was narrowest and heat flow most severe at this point so that evaluating here gave an upper limit on heat flow effects.  $A$  is the area over which heat flows, taken as the interior area of the entire nozzle  $\approx 20 \text{ mm}^2$  to give an upper limit,  $dt$  is the time of flow set by the time of gas transit through the nozzle  $\approx 4 \text{ } \mu\text{s}$ , and  $dx$  is the distance over which the temperature gradient is held, taken to be the narrowest dimension  $0.2 \text{ mm}$ . Using these values, we found an upper limit on heat flow effects of  $\Delta T_{gas} \approx 10^{-3} \text{ }^\circ\text{C}$ , which is insignificant compared to the  $\approx 100 \text{ }^\circ\text{C}$  variation due to adiabatic expansion. The adiabatic model was very well satisfied. Note also that the transit time was short compared to the opening time of the nozzle, while the amount of gas flowed was much less than the reservoir volume of about  $1 \text{ cm}^3$ . The assumption of steady flow from a reservoir should therefore be valid as well. This is especially true since the first half of the gas pulse was generally used.

These calculations indicated that supersonic gas jets can in principle meet the target requirements, and established the basic properties of a nozzle suitable for our experiments. Such a nozzle would be approximately  $2 \text{ mm}$  in outlet diameter, with an outflow Mach number near  $5$  and an outlet wall angle near  $12^\circ$ , matched to the

Mach expansion angle at this speed. This in turn indicates a throat area near 0.5 mm<sup>2</sup> with a reservoir at 70 bar. Flow in nozzles relevant to the experiments will be reasonably well modeled by an adiabatic ideal gas expansion model. A code was written which calculates this model for the desired geometries, providing a first order tool for designing nozzles with the desired flow properties. However, because these calculations give only the general form of flow, experimental characterization and optimization was required, and this is addressed in the following sections.

### B.3 Gas Jet Characterization

In order to characterize nozzles built, two interferometers were constructed and an analysis program was written to recover the data. One of the interferometers analyzed the neutral gas plume while the second analyzed the plasma, providing two independent measurement methods which were cross checked. These diagnostics allowed comparison of different gas jets so that an appropriate design could be selected.

A gas jet test stand was built to measure nozzle neutral gas profiles quickly (Fig. B.2). This facility consists of an interferometer to measure gas density and a gas jet mounted in a dedicated vacuum chamber together with driver and gas supply systems and vacuum pumps. The interferometer is a Mach-Zehnder type using a stabilized single mode helium- neon gas laser and  $\lambda/20$  aluminum mirrors to provide high phase front quality. One arm of the interferometer passes through the gas plume from the jet, and measures the line integral of the refractive index change due to the gas plume. The interferogram is imaged at the plane of the gas jet by a singlet achromat onto an 8 bit video CCD which is acquired by the same video frame grabber used for the main control system, allowing triggered data acquisition.

A phase recovery routine was written which allowed automatic analysis of multiple

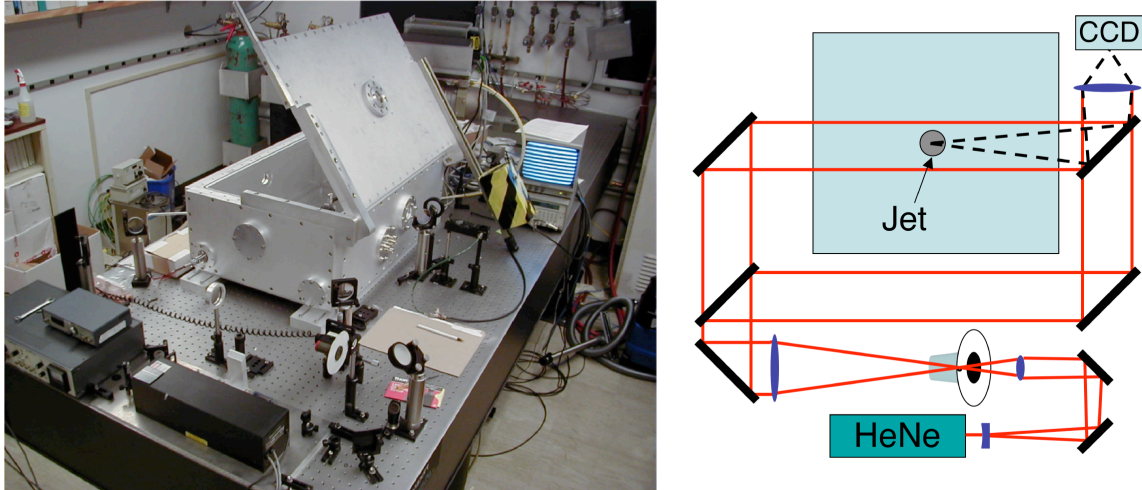


Figure B.2. A gas jet test stand enabled fast measurement of jet density profiles. The picture at left and diagram at right show the frequency stabilized HeNe laser (foreground) pulsed by a chopper wheel (white disk) that is the light source for a Mach-Zehnder interferometer. One arm of the interferometer passes through the gas jet in the vacuum chamber (center top). The interferogram is acquired by a CCD then analyzed by custom software, and density is recovered by Abel or algebraic inversion.

interferograms, returning average density as well as RMS fluctuations. Fringe tracing, skeletonization, and Fourier [128] phase recovery were all implemented allowing comparison and the use of the optimal method for given data. After phase retrieval, the data can be smoothed, rotated, and background subtracted to optimize signal to noise. For cylindrical jets, a two-dimensional map of density was obtained by Abel inversion [108,109], assuming the flow was also cylindrically symmetric. The assumption of cylindrical symmetry was checked using the plasma interferometer (below). For non-symmetric nozzles, multiple interferograms were taken at various angles and the density map was recovered using a simultaneous algebraic reconstruction technique (SART) [129]. Fig. B.3 shows that the typical shot-to-shot deviation of the interferometer was below 0.06 radian RMS, probably limited by variation in the HeNe laser and by fluctuations in the air. Fringe shift due to the gas plume was typically order of 4 radian for diatomic gasses (nitrogen, hydrogen), so that error was a few percent at full density, and more near the edges where density is low. Monoatomic gasses such

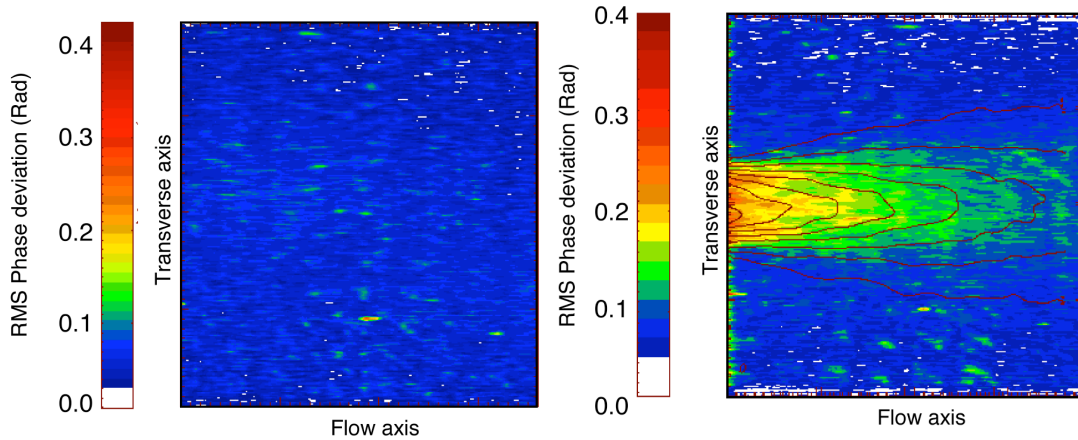


Figure B.3. The interferometer and gas jet deviations are measured by taking the RMS deviation of each point in the phase map over 10 shots. With the jet off (left), the background phase map shows a typical deviation of less than 0.06 radian, setting the limit on accuracy of the measurement. With the jet on (right), deviation is near 0.2 radian (colorbar), while the value of the phase shift is near 4 radian (overplotted contours, max contour scale = 4 radian) indicating a variation in gas flow of approximately 5% shot-to-shot.

as Helium produce 5 times less phase shift, making precise analysis more difficult. There was also additional error near the axis of symmetry due to the nature of the Abel inversion, which sometimes caused non-physical features in the calculated density profile near axis. However, the general profile was recovered accurately. Because the entire profile was obtained on a single shot and without requiring use of the main laser and vacuum system, this allowed quick nozzle characterization, which was important for design and optimization. Spatial resolution was about  $30 \mu\text{m}$ , set by the resolution of the CCD. Analysis of multiple interferograms (Fig. B.3) showed that the fluctuation with the gas jet on was near 5%, implying a 5% RMS fluctuation of mass flow and indicating the reproducibility of the gas jet. This fluctuation measurement is convolved with the timing jitter (see below), but the latter was found to be less significant.

To measure the fast gas pulses produced by the model 9 valve ( $\sim 600 \mu\text{s}$  long), a time resolution of better than  $\pm 50 \mu\text{s}$  was required. To achieve this, an SRS chopper

wheel was used to pulse the HeNe laser. A 60  $\mu\text{m}$  Coherent laser pinhole was mounted to the otherwise opaque disk. The laser was then focused onto this pinhole with an f/4 lens allowing the laser to pass through when the pinhole was aligned to the beam. The disc spun at up to 19 revolutions per second, the upper limit being set by the clock of the video camera and the requirement to have only one pulse on each frame. This produced a 12  $\mu\text{s}$  pulse width. The gas jet driver was triggered from the laser pulse using a diode. Jitter in the rotation speed of the disc introduced a timing jitter of  $\pm 40 \mu\text{s}$  min-max. By scanning the timing of the laser arrival with respect to the jet trigger, density variation was measured to be  $\pm 3\%$  min-max when timing was changed by  $\pm 100 \mu\text{s}$ . No variation was detectable on 40  $\mu\text{s}$  time scales during the middle 200  $\mu\text{s}$  of the pulse where flow was used for experiments, indicating that the resolution obtained was adequate. Outside this time window the flow ramped up and then back down with a time scale of 200-300  $\mu\text{s}$ .

A second measurement of density was obtained by measuring the plasma density using the folded wave interferometer on the main experimental chamber after the laser pulse ionized the jet (Fig. 3.5). Measuring the plasma rather than neutral gas yields larger fringe shift, but only measures the part of the jet that was ionized. Because it required use of the main laser and vacuum system, and because care was required to obtain the appropriate intensity to fully ionize the gas but not modify the profile (i.e. through filamentation), this method was time consuming. It was used as a check on the neutral gas interferometer. Here we obtain the density along the one-dimensional ‘line’ that the laser ionized. The ‘ignitor’ pulse was used for this measurement, as it ionized essentially the full length of the jet due to its long diffraction range. To avoid jet damage, the laser propagated perpendicular to the flow axis, parallel to the top of the jet. The height of the laser above the jet could be set between 1-3mm. The spatial resolution was on the order of 20  $\mu\text{m}$ . The same software used for the neutral gas interferometer also accommodated these interferograms. Fig. B.4 shows

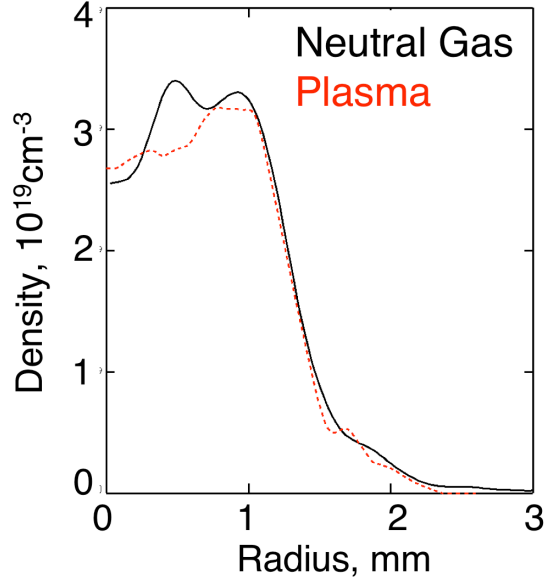


Figure B.4. Comparison of electron density from the neutral density and plasma interferometers. Full ionization of hydrogen was assumed to obtain plasma density from neutral gas data. The general profiles are similar, confirming the usefulness of the neutral gas method for the bulk of the profile. Note the sudden unphysical drop in the profile derived from the neutral gas measurement near  $R=0$ , resulting from inaccuracy of the Abel inversion at this point and indicating a region where care should be taken in interpreting the results.

a comparison between the plasma and neutral gas interferometers. As expected from the characteristics of the Abel inversion, fluctuations of density near the flow axis observed in the neutral gas data are not present in the plasma interferometer data, indicating that they are non-physical. The general profile is very well reproduced however, confirming the neutral gas measurements.

The development and verification of the diagnostics described here, and the automated analysis software written to accompany them, resulted in the ability to quickly measure gas jet profiles with few percent accuracy. This in turn allowed the evaluation of many gas jet designs in order to improve performance. In the acceleration experiments, the laser intensity was well above the ionization threshold for the gasses used. Hence the gas was typically fully ionized, and the density profiles that follow

are therefore the electron density assuming full ionization of hydrogen, the gas most commonly used.

## B.4 Cylindrical Nozzle Designs and Results

Using the tools described in the previous Section, a variety of nozzles were designed and tested. For compatibility with the valve used, all follow the general form shown in Fig. B.5. The fitting of the valve requires the nozzle platform to be 1.8 cm in diameter. To provide clearance for the laser at  $f/4$ , this required that the nozzle extend about 6 mm out from the poppet. The nozzle in the figure is similar to the ‘standard’ straight pipe nozzle supplied by General Valve, and was in use at the start of experiments. Because of the straight outlet pipe, this nozzle was of nearly sonic output velocity. Measurement confirmed a profile with no flat-top and long gradient scale length. Two simple variations of this nozzle were also evaluated, flaring the output either in a spherical cup or a 45 degree cone at the outlet. The 45 degree and cupped nozzle gas profiles were similar to that of the straight nozzle. This is as expected since both output sections are reasonably matched to the natural Mach 1 expansion of the gas, and therefore offer no acceleration or supersonic benefit. The gas profiles of these nozzles are shown in Fig. B.6

A nozzle designed using one-dimensional adiabatic flow is shown in Fig. B.7. This nozzle has an outlet flared at 10 degrees to match the divergence angle of the plume at the design exit velocity of Mach 6, and was designated nozzle 03B-01. Outlet diameter was 2.2 mm. The straight section was retained to keep the length sufficient for the required mount to the valve, and the nozzle was machined of stainless steel. The seat of the valve was matched in angle to the angle of the poppet. This angle is reasonably optimized as a trade off between flow area and turbulence. A flat poppet will provide the largest opening for a given valve stroke, but the flow then collapses

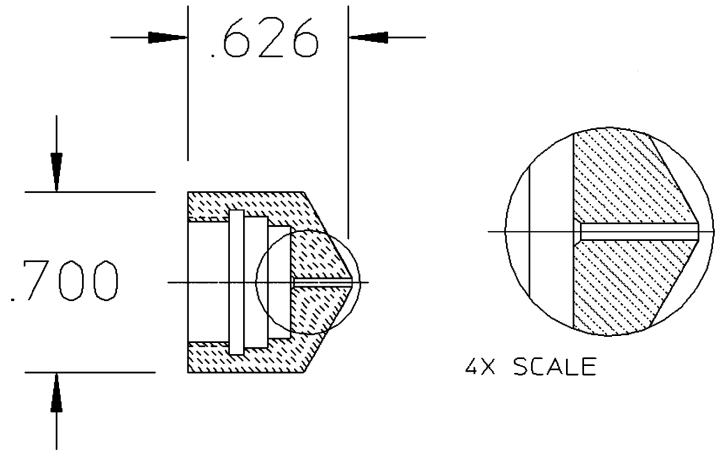


Figure B.5. The general form of the gas jet, showing the dimensional constraints determined by fitting to the valve (left). A close up of the initial, sonic flow nozzle is shown at right.

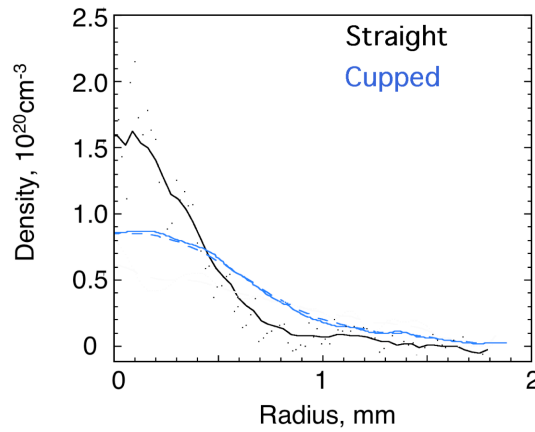


Figure B.6. The plasma density profiles of the straight and cupped nozzles at a height of  $800 \mu\text{m}$  above the nozzle, as a function of radial distance from the jet axis. Both profiles are essentially Gaussian, reflecting sonic outflow. The cupped nozzle profile is wider, consistent with the longer distance from the end of the straight section for the same distance above the tip in this nozzle. The cupped section hence seems to have no nozzle effect. To obtain plasma density from neutral gas data, full ionization of hydrogen was assumed.

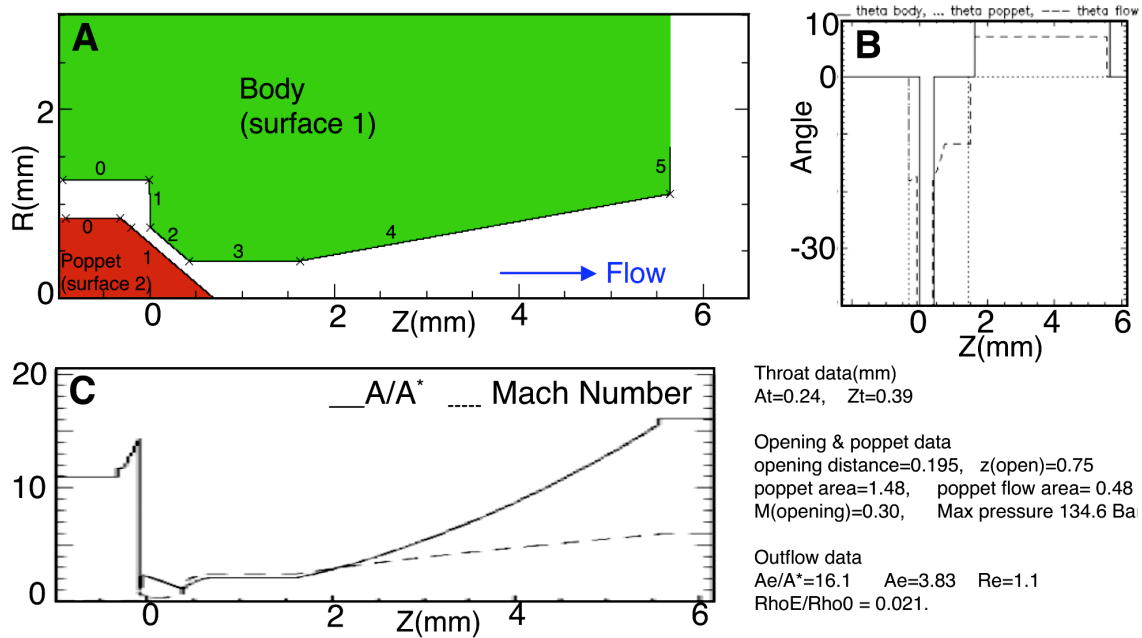


Figure B.7. A supersonic nozzle (A) designed using the ideal flow code uses a 10 degree expansion angle matched to the outflow Mach expansion angle of the plume at the calculated exit speed in order to suppress shocks at the output. The code outputs the angles of flow (B) and area and Mach numbers (C) as a function of axial position to aid in design. Calculated nozzle parameters are shown at the lower right.

on the axis and must turn sharply, losing speed. A very shallow angle minimizes turning of the flow but gives a very small opening. The length of the seat is a trade off between flow and durability (see below). The code predicted output of this nozzle at Mach 6 with a density as high as  $7.5 \times 10^{19}$  from a 70 bar reservoir. From the Mach number, we expect an edge scale length of approximately 300-400  $\mu\text{m}$  at 1 mm height, and a flat-top where the density remains constant of approximately 1.8mm. Scale length would be increased by the effects of viscosity, which will create a subsonic boundary layer. Such a layer would be expected to spread rapidly, creating a broad low density halo around the main jet.

The measured supersonic nozzle density profile (Fig. B.8) had a relatively flat-top region 1.6 to 1.8 mm long, where the density remained within  $\sim 10\%$  of the peak value, reasonably consistent with the predictions of Section B.2. The edge gradient

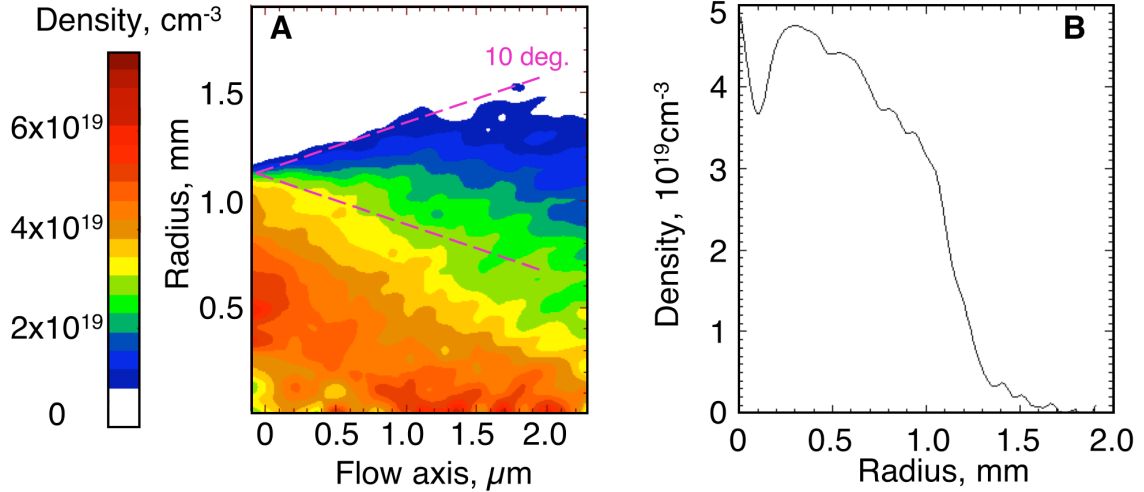


Figure B.8. The plasma density profile of the supersonic nozzle obtained with the neutral density interferometer. Full ionization of hydrogen was assumed to obtain plasma density from neutral gas data. The contour plot (A) shows expansion roughly along the expected 10 degree Mach lines. A line profile taken 700  $\mu\text{m}$  from the jet opening (B) shows a nearly flat-top region extending 7-900  $\mu\text{m}$  from axis, with a further 450  $\mu\text{m}$  gradient from 90% to 10% of peak density. The dip near  $R=0$  is, as shown in Fig. B.4, non-physical and due to instability in the Abel inversion algorithm. The observed parameters are reasonably consistent with one-dimensional flow calculations.

was composed of an approximately 450  $\mu\text{m}$  slope from 90% to 10% of full density, and a further 300  $\mu\text{m}$  of low density plasma. The observed gradients were reasonably consistent with the expected 300-400  $\mu\text{m}$  from the code with the addition of a low density contribution from the viscous layer. The divergence of the plume was near the expected 10 degrees, and the density was approximately 30% lower than the one-dimensional prediction, roughly consistent with the expected size of the viscous layer relative to the throat. Even in the ‘flat-top’ region of this nozzle there was some variation of density. While this would be less than ideal for a single pulse experiment, it was found that the channel creation process flattened the density profile due to the non-homogeneous nature of the heater pulse, creating a 1.7 to 1.8 mm flat-top nearly ideal for those experiments (Chapter 4).

We evaluated accelerator performance with these nozzles in the unguided self-

modulated regime. Accelerator output was optimized for both the straight and 10 degree flared nozzle gas profiles, and the supersonic nozzle displayed much higher performance as shown in Fig. B.9. Electron beam charge was measured using an integrating current transformer for these experiments, and electron energy was diagnosed using radiation detectors mounted near the beam pipe (Chapter 3). These detectors measured forward directed gamma radiation produced by Bremsstrahlung when the electrons slowed in the target. Gamma ray yield increases with increasing electron energy, and the ratio of gamma yield to charge hence provided a rough diagnostic of accelerator performance. Gas jet density, height of the laser above the jet, and laser pulse length were first tuned to maximize charge and radiation yields with the laser focus positioned over the upstream edge of each gas jet (known to be near the optimal position from previous scans). The gas jet was then scanned with respect to the laser focus to find the optimum location. In both cases, as expected from the discussion of Section B.1, the yield fell off sharply for a laser focus location much more than  $\approx 2Z_R$  into the jet. While peak charge in the two cases was similar, the gamma yield was nearly 5 times greater for the supersonic profile, indicating that electrons were accelerated to higher energy. This is reasonable, as the flat-top began little more than  $2Z_R$  into the supersonic profile. Hence the laser pulse may have reached the flat-top region in the supersonic profile allowing more efficient acceleration, while this region did not exist at all for the straight jet.

The 10 degree supersonic nozzle design demonstrated performance close to optimal for the desired experiments, and was a large improvement over previous nozzles. A series of tests were next done to determine what parameters influenced nozzle output, and to explore potential optimizations.

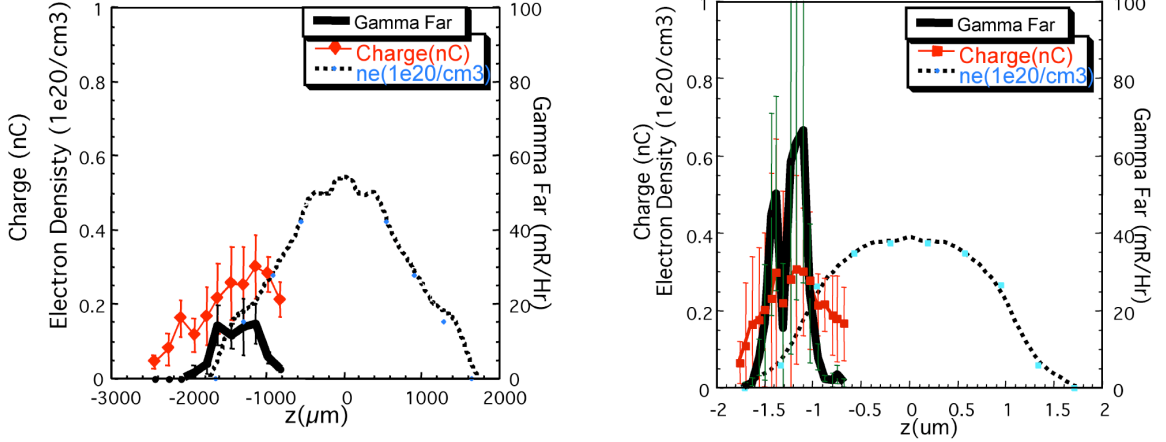


Figure B.9. The performance of the unchanneled self-modulated laser wakefield accelerator was parameterized by charge and yield of gamma rays, which indicate high energy electrons. As the gas jet position was scanned with respect to the laser waist ( $Z=0$  indicates the waist centered above the jet), optimum performance for both profiles yielded similar charge. Gamma-ray yield was five times greater for the flat-top supersonic jet, indicating production of higher energy electrons. Laser chirp, jet backing pressure, and other parameters were optimized prior to these scans.

## B.5 Cylindrical Nozzle Shape, Surface, and Environmental Variations

As a result of the improvements made using the initial supersonic design, a variety of new shapes as well as variations of material were tried in pursuit of further optimization. In order to determine which factors were important, the profile of the nozzle and its surface roughness were varied.

Surface roughness on scales comparable to the laminar layer (above) can increase wall friction [124], while larger bumps also may induce turbulence, making surface finish important for nozzle output. To test these effects, a set of 10 degree flared nozzles was machined in aluminum designated 03B-03 through -05. The softer material resulted in fewer tool ‘digs’, or scratches during machining. However, aluminum cannot be electro-polished to obtain the mirror finish used in the stainless nozzle. As a result, the steel nozzle 03B-01 had no detectable small scale roughness, but several

large, smooth circumferential scoring marks created by tooling which were approximately  $100\ \mu\text{m}$  in size. The aluminum nozzles all had a sandpaper like finish with a grain size of approximately  $15\ \mu\text{m}$  which is near the width of the laminar layer. Using a pick, controlled scratches were then made in some of the nozzles to allow comparison of the effects of small and large scale surface roughness. Nozzle 03B-04 had a few and 03B-05 had many digs at the  $100 - 150\ \mu\text{m}$  scale. Gas flow in the aluminum nozzles is shown in Fig. B.10 and can be compared to the steel nozzle in Fig. B.8. As expected, the rougher small scale surface finish of the aluminum nozzles resulted in reduced flow (overall density) due to increased wall friction when compared to the steel nozzle. More surprising is the appearance of a shock wave, evidenced by high density at the edge and a hole in the center, in nozzle 03B-03, which has no large scale wall perturbations. This shock wave was reduced in amplitude and then eliminated in the nozzles which have increasing amounts of  $100\text{-}150\ \mu\text{m}$  wall roughness, indicating that large scale roughness may mix the flow, preventing large shocks from forming. Hence the tool marks which were initially thought problematic may be beneficial to obtaining shock free flow.

A variety of nozzles were next constructed to evaluate the impact of various changes to the profile of the generally successful 03B-01 design. Elements of the design were changed piecewise to allow evaluation (Fig. B.11). Changing the poppet seat flare had a modest effect, slightly increasing flow but reducing poppet life several fold (not shown). Lengthening the straight section (03D) was found to be detrimental, which is reasonable given that this region does not contribute to expansion and only adds wall drag. Machining a  $150\ \mu\text{m}$  step (03F) in the expanding section modestly increased the flat-top region, supporting the conclusions regarding roughness reached above. Eliminating the straight section showed the largest gain, producing a nozzle with a good flat-top and short edge gradients (03E). This is the smoothest flat-top profile obtained at a fixed distance of  $1\ \text{mm}$  from the nozzle tip, but the shortened

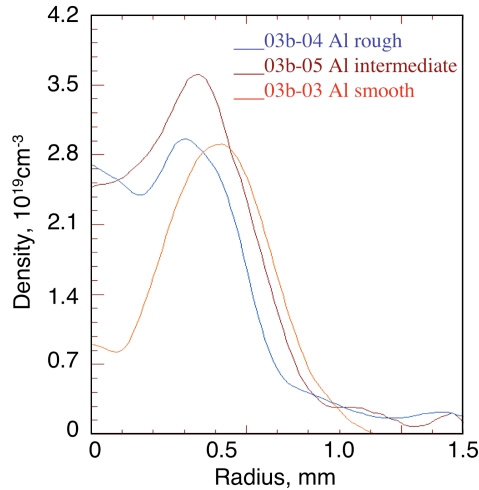


Figure B.10. Variation of nozzle surface finish in aluminum nozzles showed that nozzle surfaces with roughness at scales larger than the laminar layer may suppress formation of shocks and produce more uniform gas profiles. Compared to the steel nozzle (Fig. B.8), the greater small scale roughness of these nozzles appears to have reduced flow volume.

length of this jet due to elimination of the straight section did not allow as much clearance for the laser, requiring greater operating height in practice. At that increased height, performance was not better than the original (03B-01). Alternatively, continuing expansion at 10 degrees to a nozzle aperture of 4.4mm (03F) rather than the standard 2.2mm also produced a somewhat flat distribution, but the density was unsuitable for self-modulated experiments. There is also a small amplitude shock evident in the higher density edge/low density center of this jet, which is likely because the 10 degree cone angle is not matched to the exit velocity of the jet at the higher expansion ratio. This was confirmed by varying the expansion angle of the cone from 6 to 15 degrees with a fixed outlet diameter of 2.2 mm (Fig. B.11) to evaluate the impact of mismatch between the cone angle of the nozzle and the sonic expansion angle of the gas plume. Using a cone with a narrower or wider expansion angle than that of the gas plume resulted in a flow with shocks present, which are absent in the (matched) 10 degree case.

A classic bell shaped nozzle [124] designated 06, designed with similar output

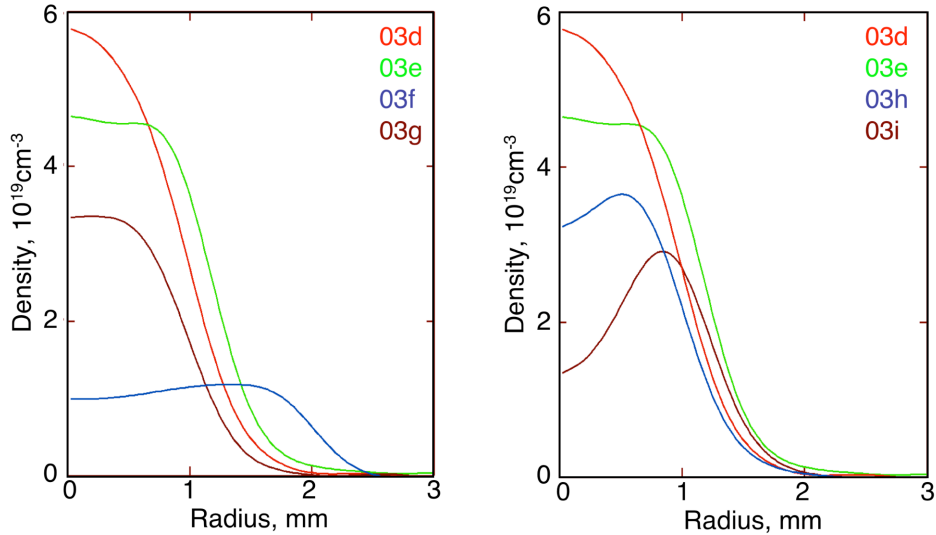


Figure B.11. Variations of gas jet shape based on the 10 degree supersonic nozzle (Fig. B.8). Extension of the straight section (03D, left) reduced the flat-top region. A step in the expansion section (03G, left) slightly extended the flat-top in agreement with Fig. B.10. Eliminating the straight section (03E, left) extended the flat-top region, as did expansion to larger aperture (03F, left). Changing cone angle (right) to 6 degrees (03h) or 15 degrees (03i) induced shocks as the nozzle no longer matched the gas expansion angle.

parameters as the 10 degree nozzle, but with a smoother acceleration profile  $dM/dz$  due to the curved surfaces was evaluated next (as illustrated in Fig. B.1). This nozzle displayed generally similar flow volume to the 10 degree nozzle, but had a shock wave in the flow which resulted in a low density on the flow axis, and which made the density profile unsuitable. The poor performance of this nozzle indicated that while the one-dimensional flow method gets general parameters right, smooth acceleration is not necessary or sufficient to ensure a smooth output profile. As indicated by the tests above, the shock wave in this case probably resulted from the fact that the outlet nozzle cone angle (0 degrees) was not matched to the divergence of the plume.

A further set of shapes were evaluated which had been designed to produce a very smooth acceleration contour through the Mach point, by either shaping the throat around the poppet or by moving the throat downstream of the poppet. Doing this

required using a larger poppet seat to obtain the same expansion ratio, and the result was a set of nozzles which had reasonably smooth profiles, but which could not open at the full pressure required. Expansion from a larger throat at lower pressure reduced Mach number and increased edge scale length, making these nozzles undesirable.

The sensitivity of the jet to various environmental and maintenance events was evaluated to assess the long term reliability of the target for experiments. Factors influencing jet reproducibility include vacuum chamber back pressure, setting of the poppet stroke, poppet wear and replacement, and driver function. Gas profiles were taken before and after a run to assess the impact of wear on the poppet. For  $10^4 - 10^5$  shots using poppets made of hard Kel-F plastic, differences were at the few percent level, which is acceptable. Softer Teflon poppets deformed visibly into the throat over this number of shots, restricting gas flow and making them unusable. Vacuum chamber back pressure had a negligible effect on the gas profile for relevant pressures, and less than 10% variation was observed at pressures up to 1/2 Torr, which is a thousand times the pressure during experiments. However, measurements at atmospheric pressure were not usable due to shocks driven in the ambient gas. Gas profiles were also comparable for small changes to the driver current pulse profile or changes from one driver box to another. The stroke of the valve must be set precisely to obtain reproducible flow, and this was done by observing the DC voltage at which the valve opened with no pressure applied. Setting the voltage at 1 volt precision gave  $\sim 10 \mu\text{m}$  resolution on the valve stroke (as measured using thin shim wedges inserted between the valve and nozzle), and resulted in reproducible gas profiles when the poppet was changed. Over 1 year of operation, measurements of gas jet density indicated fluctuations of  $\lesssim 10\%$ , resulting in reproducible experiments.

Based on these tests, it was evident that the base design 10 degree stainless steel nozzle 03B-01 had a reasonably optimized design, and displayed the best performance. This design was retained for channeled acceleration experiments. In the long term,

revisiting a design without a straight section as in 03E may be of interest if laser clearance issues can be resolved (i.e. with a different mount to the valve). A smooth profile which matches the wall angle at each  $Z$  to the local Mach expansion angle of the gas would also be of interest based on the findings here. The findings that a relatively simple cone nozzle geometry is adequate, and that bell profiles can induce density non-uniformity, agrees with other numerical and experimental studies [130].

## B.6 Slit Gas Jet

To make longer acceleration distances practical, a slit shaped jet providing a long narrow plasma was implemented. Although cylindrical nozzles are simple to machine, they become impractical as accelerator length increases in order to reach higher energies because the large area of the nozzle requires a large (slow) valve, and the resulting high gas flow overwhelms pumping systems. In addition, the thick gas plume of even mm-scale cylindrical nozzles is an impediment to controlled injections schemes which rely on a second laser pulse incident from the side [44, 47, 49]. This motivates the development of long narrow ‘slit’ jets.

A 200  $\mu\text{m}$  transverse slit size was chosen to give acceptable side access and gas density. The laser  $f/\text{number}$  dictates an operating height of at least  $\approx 1$  mm (Section B.2) and the available valve dictates a Mach number of less than 5 for the desired density, so that the plume from such a slit will be 600  $\mu\text{m}$  wide at operating height. This is narrow enough to allow injection of a laser pulse from the side through  $\approx 2Z_R$  of gas, providing reasonable access for injection experiments. At the same time, the slit is wide enough that the spreading of the plume does not drive density down too far to be useful (as shown below). The nozzle was chosen to have a cylindrical valve seat and throat, which allows good sealing of the poppet to the seat, and an asymmetrical flare to a rounded rectangular opening.

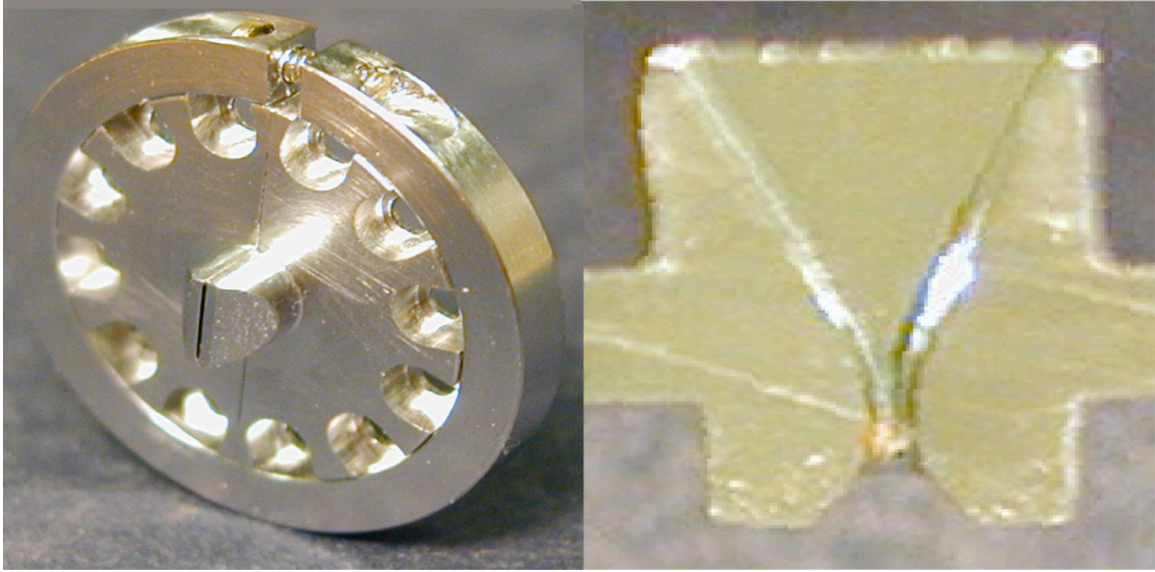


Figure B.12. Assembly and cutaway pictures of the slit gas jet. The jet was CNC machined in two pieces then joined and polished to obtain the desired profile.

A version of the gas flow code described in Section B.2 was implemented to deal with this profile, and it was found that reasonable expansion was possible up to a  $4 \text{ mm} \times 0.2 \text{ mm}$  aperture with an output Mach number of 3.5 and density above  $10^{20} \text{ cm}^{-3}$ . Extrapolating the expansion of the plume to an operating height of 1 mm above the jet, predicted a density of  $7 \times 10^{19} \text{ cm}^{-3}$  and a plume width of 6-800  $\mu\text{m}$ , which fit the requirements for injection experiments. Viscosity is more important for the long thin jet, and the design density was picked high to compensate for the resulting drop in density expected. The design was iterated between gas flow considerations (to produce a reasonable throat and a expansion angle matched to the Mach number) and machining constraints to produce a buildable design. The resulting nozzle is pictured in Fig. B.12.

Due to its complexity, this profile was manufactured in two halves using a CNC mill at the Design Center of LBNL. The halves were then joined by press fit clamp rings (not shown), and the valve seat was polished and plated to produce a smooth surface. The resulting valve seat sealed reasonably, producing an acceptable back

pressure of  $5 \times 10^{-4}$  torr with the valve closed but pressurized, which is 1/10th of the pressure produced by puffing the valve at 0.5 Hz. One piece cylindrical nozzles did not leak significantly, allowing back pressures as low as  $10^{-5}$ . No effect on acceleration was observed for back pressures up to several  $10^{-3}$  indicating that these are reasonable performance numbers. Poppet wear rate was approximately twice as fast as for cylindrical valves, likely because the smoothness of the poppet seat is still somewhat worse. The raw seat produced by joining the two halves without processing did not seal adequately.

The gas plume of the slit nozzle was profiled using the gas jet test stand. The interferometer pulse was passed through the gas plume at four angles; 0, 30, 60, and 90 degrees to the slit axis. The resulting phase data was used to tomographically reconstruct the gas density distribution using algebraic reconstruction [129]. The gas plume at operating height, shown in Fig. B.13, is  $1 \text{ mm} \times 4.5 \text{ mm}$  in size, reasonably consistent with calculation. The density obtained (assuming double ionization of helium or hydrogen) was up to  $2 \times 10^{19} \text{ cm}^{-3}$  at 1 mm height with a 4 mm flat-top length, allowing low density self-modulated or resonant wakefield experiments. Density increased for smaller operating heights, with  $n \sim 4 \times 10^{19} \text{ cm}^{-3}$  at 3-500  $\mu\text{m}$  and  $2.4 \times 10^{19} \text{ cm}^{-3}$  at 700  $\mu\text{m}$ . As with the cylindrical nozzles, the densities obtained with the neutral gas interferometer were checked using the plasma interferometer. These densities are significantly lower than the adiabatic flow prediction, reflecting the greater importance of viscosity for the slit shape. The scale length was approximately 400  $\mu\text{m}$ , which is acceptable. The flat-top uniformity was excellent, better than the cylindrical nozzles.

Variable plasma length was obtained by rotating the jet. Operating with the laser aligned along the slit gave plasma flat-top lengths of 4 mm and densities up to  $2 \times 10^{19} \text{ cm}^{-3}$ , restricted by the requirement to operate the laser at least 1 mm above the jet to avoid burning it. If the laser was operated at 90 degrees to the slit rather than

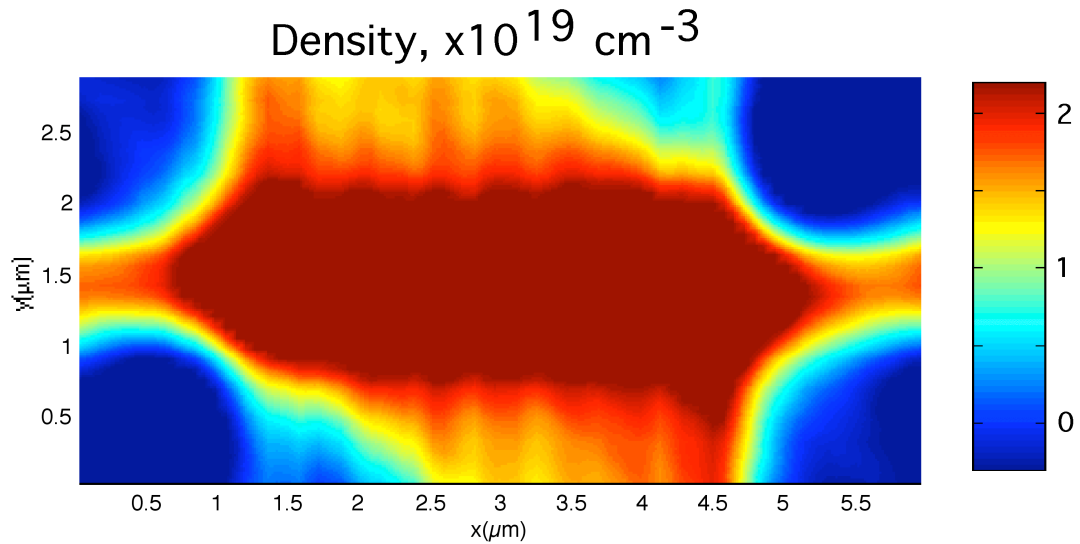


Figure B.13. The two-dimensional plasma profile of the slit nozzle in a plane 1 mm from the nozzle, obtained with the neutral density interferometer. This shows a homogeneous plume with little density variation and a size of 4 x 1 mm suitable for injection and long scale length experiments. To obtain plasma density from neutral gas data, full ionization of hydrogen was assumed.

along it, the height of operation above the jet could be reduced and densities of up to  $4 \times 10^{19}$  were obtained in plasmas as short as 600  $\mu\text{m}$ . This variability allowed testing of the effect of plasma length on the acceleration process. These experiments and their results are described in Chapter 8.

## B.7 Summary

Gas jet targets have been developed which meet the requirements for wakefield acceleration, including channeled and unchanneled experiments. Simple supersonic cylindrical jets provide reasonably flat density profiles with short edge scale lengths. Variation of shape indicated that matching of exit cone angle to Mach angle was the most important parameter, and that internal nozzle shape and roughness can be tuned to provide further improvements. Superior performance and variable length

plasmas were obtained using CNC machined slit gas jets. Such nozzles will enable long scale accelerators in the future, and provided data on the effect of acceleration length for these experiments.

# Bibliography

- [1] S. Humphries. *Principles of charged particle acceleration*. John Wiley & Sons, Hoboken NJ, or <http://www.fieldp.com/cpa/cpa.html>, 1999.
- [2] T. Tajima and J. M. Dawson. Laser electron accelerator. *Phys. Rev. Lett.*, 43(4):267–70, 1979.
- [3] E. Esarey, P. Sprangle, J. Krall, and A. Ting. Overview of plasma-based accelerator concepts. *IEEE Trans. Plasma Sci.*, 24(2):252–288, 1996.
- [4] A. Modena, Z. Najmudin, A. E. Dangor, C. E. Clayton, K. A. Marsh, C. Joshi, V. Malka, C. B. Darrow, C. Danson, D. Neely, and F. N. Walsh. Electron acceleration from the breaking of relativistic plasma waves. *Nature*, 377:606–608, 1995.
- [5] K. Nakajima, D. Fisher, T. Kawakubo, H. Nakanishi, A. Ogata, Y. Kato, Y. Kitagawa, R. Kodama, K. Mima, H. Shiraga, K. Suzuki, K. Yamakawa, T. Zhang, Y. Sakawa, T. Shoji, Y. Nishida, N. Yugami, M. Downer, and T. Tajima. Observation of ultrahigh gradient electron acceleration by a self-modulated intense short laser pulse. *Phys. Rev. Lett.*, 74:4428–4431, 1995.
- [6] D. Umstadter, S.-Y. Chen, A. Maksimchuk, G. Mourou, and R. Wagner. Non-linear optics in relativistic plasmas and laser wake field acceleration of electrons. *Science*, 273(5274):472–5, 1996.
- [7] C.I. Moore, A. Ting, K. Krushelnick, E. Esarey, R. F. Hubbard, H. R. Burris, C. Manka, and P. Sprangle. *Phys. Rev. Lett.*, 79:3909, 1997.
- [8] D. Gordon, K. C. Tzeng, C. E. Clayton, A. E. Dangor, V. Malka, K. A. Marsh, A. Modena, W. B. Mori, P. Muggli, Z. Najmudin, D. Neely, C. Danson, and C. Joshi. *Phys. Rev. Lett.*, 80:2133, 1998.
- [9] V. Malka, S. Fritzler, E. Lefebvre, M. M. Aleonard, F. Burgy, J. P. Chambaret, J. F. Chemin, K. Krushelnick, G. Malka, S. P. D. Mangles, Z. Najmudin, M. Pittman, J. P. Rousseau, J. N. Scheurer, B. Walton, and A. E. Dangor. Electron acceleration by a wake field forced by an intense ultrashort laser pulse. *Science*, 298(5598):1596–1600, 2002.

- [10] W. P. Leemans, P. Catravas, E. Esarey, C. G. R. Geddes, C. Toth, R. Trines, C. B. Schroeder, B. A. Shadwick, J. van Tilborg, and J. Faure. Electron-yield enhancement in a laser-wakefield accelerator driven by asymmetric laser pulses. *Phys. Rev. Lett.*, 89:4802, 2002.
- [11] D. Nicholson. *Introduction to Plasma Theory*. John Wiley and Sons, New York, 1983.
- [12] William L. Kruer. *The Physics of Laser Plasma Interactions*. Addison-Wesley, Redwood City, CA, 1988.
- [13] F. F. Chen. *Plasma Physics and Controlled Fusion*. Plenum Press, New York, 1984.
- [14] A. I. Akhiezer and R. V. Polovin. Theory of wave motion in an electron plasma. *Sov. Phys. JETP*, 3:696, 1956.
- [15] John M. Dawson. Nonlinear electron oscillations in a cold plasma. *Phys. Rev.*, 113(2):383–387, 1959.
- [16] T. Katsouleas, S. Wilks, P. Chen, J. M. Dawson, and J. J. Su. Beam loading in plasma accelerators. *Part. Accel.*, 22(1):81–99, 1987.
- [17] T. C. Chiou and T. Katsouleas. High beam quality and efficiency in plasma-based accelerators. *Phys. Rev. Lett.*, 81(16):3411–14, 1998.
- [18] Phillip Sprangle, Eric Esarey, Jonathan Krall, and G. Joyce. Propagation and guiding of intense laser pulses in plasmas. *Phys. Rev. Lett.*, 69(15):2200–2203, 1992.
- [19] J. Krall, A. Ting, E. Esarey, and P. Sprangle. Enhanced acceleration in a self-modulated-laser wake-field accelerator. *Phys. Rev. E*, 48(3):2157–61, 1993.
- [20] E. Esarey, J. Krall, and P. Sprangle. Envelope analysis of intense laser pulse self-modulation in plasmas. *Phys. Rev. Lett.*, 72:2887–2890, 1994.
- [21] C. D. Decker, Warren B. Mori, Kuo-Cheng Tzeng, and Thomas C. Katsouleas. Modeling single-frequency laser-plasma acceleration using particle-in-cell simulations: The physics of beam breakup. *IEEE Trans. Plasma Sci.*, 24(2):379–392, 1996.
- [22] E. Esarey, P. Sprangle, J. Krall, and A. Ting. Self-focusing and guiding of short laser pulses in ionizing gases and plasmas. *IEEE J. Quantum Electron.*, 33(11):1879–914, 1997.
- [23] Z. Najmudin, K. Krushelnick, E.L. Clark, S.P.D. Mangles, B. Walton, A.E. Dangor, S. Fritzler, V. Malka, E. Lefebvre, D. Gordon, F.S Tsung, and C. Joshi. Self modulated wakefield and forced laser wakefield acceleration of electrons. *Phys. Plasmas*, 10(5):2071–2077, 2003.

- [24] B. Saleh and M. Teich. *Fundamentals of Photonics*. Wiley, New York, 1984.
- [25] A.G. Litvak. *Sov. Phys JETP*, 30:344, 1969.
- [26] P. Sprangle, C. M. Tang, and E. Esarey. Relativistic self-focusing of short-pulse radiation beams in plasmas. *IEEE Trans. Plasma Sci.*, PS-15:145–153, 1987.
- [27] W. B. Mori. The physics of the nonlinear optics of plasmas at relativistic intensities for short-pulse lasers. *IEEE J. Quantum Electron.*, 33(11):1942–1953, 1997.
- [28] W. P. Leemans, D. Rodgers, P. E. Catravas, C. G. R. Geddes, G. Fubiani, E. Esarey, B. A. Shadwick, R. Donahue, and A. Smith. Gamma-neutron activation experiments using laser wakefield accelerators. *Phys. Plasmas*, 8:2510–2516, 2001.
- [29] W. P. Leemans, C. G. R. Geddes, J. Faure, Cs. Toth, J. van Tilborg, C. B. Schroeder, E. Esarey, G. Fubiani, D. Auerbach, B. Marcellis, M. A. Carnahan, R. A. Kaindl, J. Byrd, and M. C. Martin. Observation of terahertz emission from a laser plasma accelerated electron bunch crossing a plasma-vacuum boundary. *Phys. Rev. Lett.*, 91:4802, 2003.
- [30] P. E. Catravas, E. Esarey, and W. P. Leemans. Femtosecond x-rays from thomson scattering using laser wakefield accelerators. *Meas. Sci. Tech.*, 12(11):1828–34, 2001.
- [31] R. W. Schoenlein, W. P. Leemans, A. H. Chin, P. Volfbeyn, T. E. Glover, P. Balling, M. Zolotarev, K. J. Kim, S. Chattopadhyay, and C. V. Shank. Femtosecond X-ray pulses at 0.4 a generated by 90 degrees Thomson scattering: a tool for probing the structural dynamics of materials. *Science*, 274(5285):236–8, 1996.
- [32] W. P. Leemans, R. W. Schoenlein, P. Volfbeyn, A. H. Chin, T. E. Glover, P. Balling, M. Zolotarev, K. J. Kim, S. Chattopadhyay, and C. V. Shank. X-ray based subpicosecond electron bunch characterization using 90 degrees thomson scattering. *Phys. Rev. Lett.*, 77(20):4182–5, 1996.
- [33] W. P. Leemans, S. Chattopadhyay, E. Esarey, A. Zholents, M. Zolotarev, A. Chin, R. W. Schoenlein, and C. V. Shank. *Les Comptes Rendus de l'Académie des Sciences*, IV:279–296, 2000.
- [34] W. P. Leemans, E. Esarey, J. van Tilborg, P. A. Michel, C. B. Schroeder, Cs. Toth, C. G. R. Geddes, and B. A. Shadwick. Radiation from laser accelerated electron bunches: Coherent terahertz and femtosecond x-rays. *IEEE Transactions on Plasma Science*, 33(1):8–22, 2005.
- [35] X. J. Wang, X. Qiu, and I. Ben-Zvi. Experimental observation of high-brightness microbunching in a photocathode rf electron gun. *Phys. Rev. E*, 54(4):R3121–4, 1996.

- [36] E. Esarey, P. Sprangle, J. Krall, A. Ting, and G. Joyce. Optically guided laser wakefield acceleration. *Phys. Fluids B*, 5:2690–2697, 1993.
- [37] W. P. Leemans, C. W. Siders, E. Esarey, N. E. Andreev, G. Shvets, and W. B. Mori. Plasma guiding and wakefield generation for second-generation experiments. *IEEE Trans. Plasma Sci.*, 24:331–342, 1996.
- [38] H. M. Milchberg, C. G. Durfee III, T. M. Antonsen, and P. Mora. Channel guiding for advanced accelerators. pages 247–57, 1996.
- [39] T. C. Katsouleas, T. C. Chiou, W. B. Mori G, J. S. Wurtele, and G. Shvets. Studies of intense laser propagation in channels for extended length plasma accelerators. In *Particle Accelerator Conference*, IEEE Conf. Proc., pages 773–5. IEEE, 1995.
- [40] R. F. Hubbard, D. Kaganovich, B. Hafizi, C. I. Moore, P. Sprangle, A. Ting, and A. Zigler. Simulation and design of stable channel guided laser wakefield accelerators. *Phys. Rev. E*, 63(3):036502–1, 2001.
- [41] A. J. W. Reitsma, W. P. Leemans, E. Esarey, C. B. Schroeder, L. P. J. Kamp, and T. J. Schep. Simulation of electron postacceleration in a two-stage laser wakefield accelerator. *Phys. Rev. ST Accel. Beams*, 5(5):051301, 2002.
- [42] T. Katsouleas, C. Joshi, J.M Dawson, F.F. Chen, C.E. Clayton, W.B. Mori, C. Darrow, and D. Umstadter. Plasma accelerators. In *AIP Conference Proceedings- Laser Acceleration Particles*, pages 63–98, 1985.
- [43] Eric Esarey and Mark Pilloff. Trapping and acceleration in nonlinear plasma waves. *Phys. Plasmas*, 2(5):1432–1436, 1995.
- [44] E. Esarey, R. F. Hubbard, W. P. Leemans, A. Ting, and P. Sprangle. Electron injection into plasma wake fields by colliding laser pulses. *Phys. Rev. Lett.*, 79(14):2682–2685, 1997.
- [45] C. G. R. Geddes, Cs. Toth, J. van Tilborg, E. Esarey, C. B. Schroeder, D. Bruhwiler, C. Nieter, J. Cary, and W. P. Leemans. High quality electron beams from a laser wakefield accelerator using plasma channel guiding. *Nature*, 431(7008):538–541, 2004.
- [46] C. G. R. Geddes, Cs. Toth, J. van Tilborg, E. Esarey, C. B. Schroeder, J. Cary, and W. P. Leemans. Guiding of relativistic laser pulses by preformed plasma channels. *Submitted to Phys. Rev. Lett.*, 2004.
- [47] D. Umstadter, J. K. Kim, and E. Dodd. Laser injection of ultrashort electron pulses into wakefield plasma waves. *Phys. Rev. Lett.*, 76(12):2073–6, 1996.
- [48] C. B. Schroeder, P. B. Lee, J. S. Wurtele, E. Esarey, and W. P. Leemans. Generation of ultrashort electron bunches by colliding laser pulses. *Phys. Rev. E*, 59(5):6037–6047, 1999.

- [49] G. Fubiani, E. Esarey, C. B. Schroeder, and W. P. Leemans. Beat wave injection of electrons into plasma waves using two interfering laser pulses. *Physical Review E*, 70(1):016402–12, 2004.
- [50] C.I. Moore, A. Ting, S.J. McNaught, J. Qiu, H.R. Burris, and P. Sprangle. A laser-accelerator injector based on laser ionization and ponderomotive acceleration of electrons. *Phys. Rev. Lett.*, 82:1688, 1999.
- [51] C. G. Durfee III and H. M. Milchberg. Light pipe for high intensity laser pulses. *Phys. Rev. Lett.*, 71:2409–2411, 1993.
- [52] P. Volfbeyn, E. Esarey, and W. P. Leemans. Guiding of laser pulses in plasma channels created by the ignitor-heater technique. *Phys. Plasmas*, 6:2269–2277, 1999.
- [53] K.Y. Kim, I. Alexeev, J. Fan, E. Parra, and H.M. Milchberg. Plasma waveguides: addition of end funnels and generation in clustered gasses. In *Advanced Accelerator Workshop, Mandalay bay 2002*, page 646, New York, 2002. AIP.
- [54] E. W. Gaul, S. P. Le Blanc, A. R. Rundquist, R. Zgadzaj, H. Langhoff, and M. C. Downer. Production and characterization of a fully ionized he plasma channel. *Appl. Phys. Lett.*, 77(25):4112–14, 2000.
- [55] A. Butler, D. J. Spence, , and S. M. Hooker. Guiding of high-intensity laser pulses with a hydrogen-filled capillary discharge waveguide. *Phys. Rev. Lett.*, 89:185003, 2002.
- [56] A. Zigler, Y. Ehrlich, C. Cohen, J. Krall, and P. Sprangle. Optical guiding of high intensity laser pulses in a long plasma channel formed by a slow capillary discharge. *J. Opt. Soc. Am. B.*, 13:68–71, 1996.
- [57] Y. Kitagawa, Y. Sentoku, S. Akamatsu, W. Sakamoto, R. Kodama, K. Tanaka, K. Azumi, Y. Norimatsu, T. Matsuoka, H. Fujita, and H. Yoshida. Electron acceleration in an ultraintense laser-illuminated capillary. *Phys. Rev. Lett.*, 92(20):205002/1–4, 2004.
- [58] M. Borghesi, A. J. Mackinnon, R. Gaillard, , O. Willi, and A. A. Offenberger. Guiding of a 10-tw picosecond laser pulse through hollow capillary tubes. *Phys. Rev. E*, 57(5):R4899–R4902, 1998.
- [59] C. G. R. Geddes, Cs. Toth, J. van Tilborg, E. Esarey, C. B. Schroeder, D. Bruhwiler, C. Nieter, J. Cary, and W. P. Leemans. Production of high quality electron bunches by dephasing and beam loading in a laser plasma accelerator. *Phys. Plasmas*, *in press*, 2005.
- [60] C. G. R. Geddes, Cs. Toth, J. van Tilborg, E. Esarey, C. B. Schroeder, D. Bruhwiler, C. Nieter, J. Cary, and W. P. Leemans. Laser guiding at relativistic intensities and wakefield particle acceleration in plasma channels. In *Proc. of the 2004 Advanced Accelerator Concepts Workshop*. AIP, 2004.

- [61] J. Faure, Y. Glinec, A. Pukhov, S. Kiselev, S. Gordienko, E. Lefebvre, J.-P. Rousseau, F. Burgy, and V. Malka. A laser-plasma accelerator producing monoenergetic electron beams. *Nature*, 431(7008):541–544, 2004.
- [62] S. P. D. Mangles, C. D. Murphy, Z. Najmudin, A. G. R. Thomas, J. L. Collier, A. E. Dangor, E. J. Divall, P. S. Foster, J. G. Gallacher, C. J. Hooker, D. A. Jaroszynski, A. J. Langley, W. B. Mori, P. A. Norreys, F. S. Tsung, R. Viskup, B. R. Walton, and K. Krushelnick. Monoenergetic beams of relativistic electrons from intense laserplasma interactions. *Nature*, 431(7008):535–538, 2004.
- [63] A. Pukhov and J. Meyer-ter-Vehn. Laser wake field acceleration: the highly non-linear broken-wave regime. *Appl. Phys. B*, 74:355–61, 2002.
- [64] F. S. Tsung, R. Narang, W. B. Mori, C. Joshi, R. A. Fonseca, and L. O. Silva. Near gev energy laser wakefield acceleration of self-injected electrons in a cm scale plasma channel. *Phys. Rev. Lett.*, 93, 2004.
- [65] S. V. Bulanov, F. Pegoraro, A. M. Pukhov, and A. S. Sakharov. Transverse-wake wave breaking. *Phys. Rev. Lett.*, 78(22):4205–4208, 1997.
- [66] Jerry B. Marion and Stephen T. Thornton. *Classical Dynamics*. Saunders College Publishing, Fort Worth TX, USA, 1988.
- [67] P. Sprangle, E. Esarey, A. Ting, and G. Joyce. Laser wakefield acceleration and relativistic optical guiding. *Appl. Phys. Lett.*, 53:2146–2148, 1988.
- [68] E. Esarey, A. Ting, P. Sprangle, and G. Joyce. The laser wakefield accelerator. *Comments Plasma Phys. Controlled Fusion*, 12:191–204, 1989.
- [69] Denis Teychenn, Guy Bonnaud, and JeanLouis Bobin. Wave-breaking limit to the wake-field effect in an underdense plasma. *Phys. Rev. E*, 48(5):R3248R3251, 1993.
- [70] C. K. Birdsall, A. B. Langdon, V. Vehedi, and John Paul Verboncoeur. *Plasma Physics via Computer Simulations*. Adam Hilger, Bristol, Eng., 1991.
- [71] B. A. Shadwick, G. M. Tarkenton, E. H. Esarey, and W. P. Leemans. Fluid simulations of intense laser-plasma interactions. *IEEE Trans. on Plasma Sci.*, 30(1):38–9, 2002.
- [72] K. C. Tzeng, W. B. Mori, and T. Katsouleas. Electron beam characteristics from laser-driven wave breaking. *Phys. Rev. Lett.*, 79(26):5258–61, 1997.
- [73] D. Bruhwiler, J.Cary, private communication.
- [74] C. Nieter and J.R. Cary. Vorpil: a versatile plasma simulation code. *J. Comp. Phys.*, 196(2):448–473, 2004.
- [75] W.K.H. Panofsky and W.A. Wenzel. *Rev. Sci. Instrum.*, 27:967, 1956.

- [76] Ruth RD, Chao AW, Morton PL, and Wilson PB. A plasma wake field accelerator. *Particle Accelerators*, 17:171–89, 1985.
- [77] C. Joshi, W. B. Mori, T. Katsouleas, J. M. Dawson, J. M. Kindel, and D. W. Forslund. Ultrahigh gradient particle acceleration by intense laser-driven plasma waves. *Nature*, 311:525–9, 1984.
- [78] Unger. *Planar Optical Waveguides and Fibers*. Clarendon Press, Oxford, 1977.
- [79] C. G. Durfee III, J. Lynch, and H. M. Milchberg. Mode properties of a plasma waveguide for intense laser pulses. *Opt. Lett.*, 19:1937–1939, 1994.
- [80] T. C. Chiou, T. Katsouleas, C. Decker, W. B. Mori, G. Shvets, and J. S. Wurtele. Laser wake-field acceleration and optical guiding in a hollow plasma channel. *Phys. Plasmas*, 2:310–318, 1995.
- [81] T. C. Katsouleas, T. C. Chiou, , C. Decker, W. B. Mori G, J. S. Wurtele, G. Shvets, and J.J. Su. Laser wakefield acceleration and optical guiding in a hollow plasma channel. In *Advanced Accelerator Concepts. Third Workshop*, volume 279 of *AIP Conf. Proc.*, pages 480–9, New York, 1993. Amer. Inst. Phys.
- [82] G. Shvets, J. S. Wurtele, T. C. Chiou, and T. C. Katsouleas. Excitation of accelerating wakefields in inhomogeneous plasmas. *IEEE Trans. Plasma Sci.*, 24(2):351–62, 1996.
- [83] P. Volfbeyn, P. B. Lee, J. Wurtele, W. P. Leemans, and G. Shvets. Driving laser pulse evolution in a hollow channel laser wakefield accelerator. *Phys. Plasmas*, 4(9):3403–10, 1997.
- [84] P. Sprangle, A. Ting, and C. M. Tang. Radiation focusing and guiding with application to the free-electron laser. *Phys. Rev. Lett.*, 59:202–205, 1987.
- [85] C. D. Decker, W. B. Mori, K.-C. Tzeng, and T. Katsouleas. The evolution of ultra-intense, short-pulse lasers in underdense plasmas. *Phys. Plasmas*, 3(5):2047–2056, 1996.
- [86] Y. Ehrlich, C. Cohen, A. Zigler, J. Krall, P. Sprangle, and E. Esarey. Guiding of high intensity laser pulses in straight and curved plasma channel experiments. *Phys. Rev. Lett.*, 77:4186–4189, 1996.
- [87] A. B. Borisov, A. V. Borovskiy, O. B. Shiryayev, V. V. Korobkin, A. M. Prokhorov, J. C. Solem, T. S. Luk, K. Boyer, and C. K. Rhodes. Relativistic and charge-displacement self-channeling of intense ultrashort laser pulses in plasmas. *Phys. Rev. A*, 45:5830–5845, 1992.
- [88] P. Sprangle, J. Krall, and E. Esarey. Hose-modulation instability of intense laser pulses in plasmas. *Phys. Rev. Lett.*, 73:3544–3547, 1994.

- [89] G. Shvets and J. S. Wurtele. Instabilities of short-pulse laser propagation through plasma channels. *Phys. Rev. Lett.*, 73(26):3540–3543, 1994.
- [90] A. Ting, E. Esarey, and P. Sprangle. Nonlinear wakefield generation and relativistic focusing of intense laser pulses in plasmas. *Phys. Fluids B*, 2:1390–1394, 1990.
- [91] W. P. Leemans, P. Volfbeyn, K. Z. Guo, S. Chattopadhyay, C. B. Schroeder, B. A. Shadwick, P. B. Lee, J. S. Wurtele, and E. Esarey. Laser driven plasma based accelerators: Wakefield excitation, channel guiding, and laser triggered particle injection. *Phys. Plasmas*, 5:1615–1623, 1998.
- [92] R. Rankin, C. E. Capjack, and N. H. Burnett and P. B. Corkum. Refraction effects associated with multiphoton ionization and ultrashort-pulse laser propagation in plasma waveguides. *Opt. Lett.*, 16(11):835–7, 1991.
- [93] W. P. Leemans, C. E. Clayton, W. B. Mori, K. A. Marsh, P. K. Kaw, A. Dyson, C. Joshi, and J. M. Wallace. Experiments and simulations of tunnel-ionized plasmas. *Phys. Rev. A*, 46:1091–1105, 1992.
- [94] Cs. Toth, J. van Tilborg, C.G. R. Geddes, G. Fubiani, C. B. Schroeder, E. Esarey, J. Faure, G. Dugan, and W. P. Leemans. Powerful, pulsed, thz radiation from laser accelerated relativistic electron bunches. In *High Power Laser Ablation V, Taos NM*, Bellingham WA, 2004. SPIE.
- [95] D. Strickland and G. Mourou. Compression of amplified chirped optical pulses. *Opt. Comm.*, 56(3):219–21, 1985.
- [96] R. Trebino, K. W. DeLong, D. N. Fittinghoff, J. N. Sweetser, M. A. Krumbu gel, , and B. A. Richman. Measuring ultrashort laser pulses in the time-frequency domain using frequency-resolved optical gating. *Rev. Sci. Instrum.*, 68, 1997.
- [97] W. P. Leemans, D. Rodgers, P. E. Catravas, G. Fubiani, C. G. R. Geddes, E. Esarey, B.A. Shadwick, G. J. H. Brussard, J. van Tilborg, S. Chattopadhyay, J. S. Wurtele, L. Archambault, M. R. Dickinson, S. DiMaggio, R. Short, K. L. Barat, R. Donahue, J. Floyd, A. Smith, and E. Wong. Laser wakefield accelerator experiments at LBNL. In P. Colstock and S. Kelley, editors, *Proceedings of the Advanced Accelerator Concepts Workshop*, pages 136–145, New York, 2000. AIP.
- [98] H. M. Milchberg, T. R. Clark, C. G. Durfee III, and T. M. Antonsen. Development and applications of a plasma waveguide for intense laser pulses. *Phys. Plasmas*, 3(5):2149–2155, 1996.
- [99] T. R. Clark and H. M. Milchberg. Time- and space-resolved density evolution of the plasma waveguide. *Phys. Rev. Lett.*, 78(12):2373–2376, 1997.
- [100] L.D. Landau and E.M. Lifshitz. *Quantum Mechanics*. Pergamon Press, London, 1978.

- [101] L.V. Keldysh. *Sov. Phys. JETP*, 20:1307, 1965.
- [102] S. Augst, D. Strickland, D.D. Meyerhofer, S.L. Chin, and J.H. Eberly. Tunneling ionization of noble gasses in a high intensity laser field. *Phys. Rev. Lett.*, 63(20):2212–15, 1989.
- [103] S. Augst, D.D. Meyerhofer, D. Strickland, and S.L. Chin. Laser ionization of noble gasses by coulomb barrier suppression. *JOSA-B*, 8(4):858, 1991.
- [104] Dawson and C. Oberman. *Phys. Fluids*, 5:517, 1962.
- [105] G. Shvets and N. J. Fisch. Electron-ion collisions in intensely illuminated plasmas. *Phys. Plasmas*, 4(2):428, 1997.
- [106] <http://online.physics.uiuc.edu/courses/phys402/exp/A2/A2.pdf>.
- [107] F. Martin. Folded-wave interferometer for laser-matter interaction studies. *Applied Optics*, 19(24):4230–2, 1980.
- [108] I.H. Hutchinson. *The principles of plasma diagnostics*. Cambridge University Press, New York, 1987.
- [109] A. Behjat, G.J. Talents, and D. Neely. The characterization of a high density gas jet. *J. Phys. D.*, 30:2872–9, 1997.
- [110] MIL-STD-150A, Section 5.1.1.7, Resolving Power Target. On the web at: [www.efg2.com/Lab/ImageProcessing/TestTargets/](http://www.efg2.com/Lab/ImageProcessing/TestTargets/).
- [111] G. Dugan, A. Misuri, and W. Leemans. Design and performance estimates for the l’oasis experiment magnetic spectrometers, November 2001.
- [112] K. Nakamura, private communication.
- [113] J. F. Briesmeister. MCNP - a general monte carlo n-particle transport code, version 4 c. *LA-13709-M, Los Alamos National Lab*, 2000.
- [114] E. Esarey, G. Joyce, and P. Sprangle. Frequency upshifting of laser pulses by copropagating ionization fronts. *Phys. Rev. A*, 44:3908, 1991.
- [115] G. Fubiani, E. Esarey, and W. P. Leemans. Studies of space-charge effects in ultrashort electron bunches. In P. Colestock and S. Kelly, editors, *Advanced Accelerator Concepts*, volume 569, pages 423–435. AIP Conf. Proc, 2001.
- [116] G. Fubiani, E. Esarey, C. B. Schroeder, and W. P. Leemans. *In preparation*.
- [117] B.A. Shadwick, private communication 2004.
- [118] C. B. Schroeder, E. Esarey, B. A. Shadwick, and W. P. Leemans. Trapping and dark current in plasma-based accelerators. In V. Yakimenko, editor, *Advanced Accelerator Concepts*, pages 564–570, New York, 2004. AIP.

- [119] A. Rousse, K. Ta Phuoc, R. Shah, A. Pukhov, E. Lefebvre, V. Malka, S. Kiselev, F. Burgy, J.P. Rousseau, D. Umstadter, and D. Hulin. Production of a kev x-ray beam from synchrotron radiation in relativistic laser-plasma interaction. *Phys. Rev. Lett.*, 93(13):135005/1–4, 2004.
- [120] J. Cary, private communication, 2004.
- [121] F. Tsung and W.B. Mori, private communication, 2004.
- [122] M. Fomytskyi, C Chiu, M. Downer, and F. Grigsby. Controlled plasma wave generation and particle acceleration through seeding of the forward raman scattering instability. *Phys. Plasmas*, 12:023103–1/10, 2005.
- [123] C. G. R. Geddes, P.E. Catravas, J. Faure, Cs. Toth, J. van Tilborg, and W. P. Leemans. Accelerator optimization using a network control and acquisition system. In C. E. Clayton and P. Muggli, editors, *Proc. of the 2002 Advanced Accelerator Concepts Workshop*, volume 647, pages 796–801, NY, 2002. AIP.
- [124] R. Zucker and O. Biblarz. *Fundamentals of Gas Dynamics*. John Wiley & Sons, Hoboken NJ, 2002.
- [125] D. Giancoli. *Physics*. Prentice Hall, Englewood Cliffs NJ, 1985.
- [126] Available electronically, [http://www.engineeringtoolbox.com/21\\_237.html](http://www.engineeringtoolbox.com/21_237.html).
- [127] F. Reif. *Fundamentals of Statistical and Thermal Physics*. McGraw Hill, New York, 1965.
- [128] M. Takeda, H. Ina, and S. Kobayashi. Fourier transform method of fringe pattern analysis for computer based tomography and interferometry. *J. Opt. Soc. Am.*, 72(1):156–60, 1982.
- [129] R. Azambuja, M. Eloy, G. Figueira, and D. Neely. Three dimensional characterization of high density non-cylindrical pulsed gas jets. *J. Phys. D*, 32(8):L35–43, 1999.
- [130] S. Semushin and V. Malka. High density gas jet nozzle design for laser target production. *Rev. Sci Instrum.*, 17(7):2961–5, 2001.